

TREND

Trapped Radiation Environment Model Development

Technical Note 5

Flight Data Comparisons

ESTEC Contract No. 10725/94/NL/JG(SC)¹

D. Heynderickx (BIRA)

M. Kruglanski (IASB)

V. Pierrard (IASB)

August 1998

¹ESA Technical Management: E.J. Daly

Contents

List of symbols	xiii
Preface	xv
Acknowledgments	xix
Introduction	xxi
The AZUR/EI-88 data base and model	xxi
The SAMPEX/PET data base and model	xxi
The UARS/PEM data base and model	xxii
Model comparisons	xxii
I The AZUR data base and model	1
1 The AZUR mission	3
1.1 Mission goals	3
1.2 The EI-88/1 and EI-88/2 proton telescopes	6
1.2.1 Measurement principle	6
1.2.2 Detector layout and energy range	8
2 The AZUR/EI-88 data base	13
2.1 Retrieval of the data sets	13
2.2 Cleaning of the data sets	18
2.2.1 Rejection criteria	18
2.2.1.1 Calibration mode	18
2.2.1.2 Quality flag	21
2.2.1.3 Pitch angle not defined	21
2.2.1.4 Mixed mode records	21

2.2.1.5	Satellite conditions	21
2.2.1.6	Deviation from neighbouring values	21
2.2.1.7	Abnormally high values	22
3	Model construction	23
3.1	Conversion to fluxes	23
3.1.1	General formulation	23
3.1.2	Single element telescope	25
3.1.3	Multi-element telescope	26
3.2	Geometric factor correction	26
3.3	Application to the EI-88 telescopes	28
3.4	Model building	30
3.4.1	Data binning	30
3.4.2	Selection of bin sizes	32
3.4.3	Correction for telescope field of view	35
3.4.4	Final flux map	39
3.4.5	Comparison to AP-8	39
II	The SAMPEX data base and model	49
4	The SAMPEX mission	51
4.1	Spacecraft configuration	51
4.2	Attitude control	51
4.3	Instrument complement	54
4.3.1	Low Energy Ion Composition Analyzer (LEICA)	54
4.3.2	Heavy Ion Large Telescope (HILT)	55
4.3.3	MAss Spectrometer Telescope (MAST)	55
4.3.4	Proton/Electron Telescope (PET)	55
4.4	Detailed description of the PET telescope	56
4.4.1	Analysis modes	57
4.4.2	Calibrations	59
5	The SAMPEX/PET data base	61
5.1	Retrieval of the data sets	61
5.2	File descriptions	62
5.2.1	SEPHxxxxx.DAT	62

5.2.2	SALFxxxxx.DAT	63
5.2.3	PTLVxxxxx.DAT	63
5.2.4	PKTSxxxxx.DAT	63
5.2.5	QCORxxxxx.DAT	63
5.2.6	BVECxxxxx.DAT	65
5.2.7	SMAGxxxxx.DAT	65
5.2.8	SQUAxxxxx.DAT	65
5.2.9	SCEWxxxxx.DAT	65
5.3	Generation of a new ephemeris data set	66
6	Model construction	69
6.1	Data binning	69
6.2	Correction for telescope field of view	69
6.3	Final flux map	71
6.3.1	Comparison to AP-8	79
7	Statistical analysis of the SAMPEX/PET data	81
7.1	Analysis of the countrate	81
7.2	Analysis of the counts	83
7.3	Analysis of the livetimes	88
7.4	Calculation of the mean countrate	90
7.5	Energy spectra	93
7.6	Conclusions	93
III	The UARS data base and model	95
8	Mission and detector description	97
8.1	The UARS mission	97
8.2	Particle Environment Monitor	98
8.3	The HEPS instrument	100
8.4	Data archive	102
9	Data processing	105
9.1	Data retrieval	105
9.2	Geographic and geomagnetic coordinates	106
9.2.1	Cleaning of the data sets	108

9.3	Geometric factor correction	111
9.4	Data binning	111
9.4.1	Flux at the reference points	114
9.4.2	Processing algorithm	115
10	Proton PEM/UARS model	117
10.1	Model coverage	117
10.2	Detector field of view	129
10.3	Corrected flux	134
10.4	Proton flux model	135
IV	Model comparisons	151
11	Intercomparisons of the models	153
11.1	Comparisons of the models for a LEO mission	153
11.2	Comparisons of the models for a GTO mission	155
11.3	Conclusions	168
	References	171
A	Telemetry file for the HEPS/PEM/UARS data	175
A.1	Header format	175
A.2	Body format	176
A.3	First level file	177
A.4	Second level	178
A.4.1	Ephemeris data	178
A.4.2	Measurement data	181
A.5	Binned data	182
B	List of IDL subroutines related to UARS data	183

List of Figures

1.1	Cross section of the AZUR satellite	4
1.2	Representation of the orbital attitude of the AZUR satellite	5
1.3	Cross section of the EI-88 instrument	7
1.4	Cross section of the EI-88 sensors	9
1.5	Energy deposited in the EI-88 detectors as a function of incident particle energy	10
2.1	Sample of the raw EI-88/1 channel 4 count rates in data file TAPE4.DAT . .	19
2.2	Sample of the EI-88/1 channel 4 count rates in data file TAPE4.DAT after running the cleaning programme	20
3.1	Measured effective area for the EI-88 detectors [from Achtermann et al. (1970)]	29
3.2	Effective area for the EI-88 detectors approximated by the analytical function described in the text	29
3.3	$F_{10.7}$, $F_{10.7A}$, R_Z , and K_p for the duration of the AZUR mission	31
3.4	Cumulative distribution of AZUR EI-88/1 measurements in α_0 bins	33
3.5	(L, α_0) Map of the number of measurements for channel 1	33
3.6	Uncorrected flux averages (\square) for EI-88/1 channel 1, $L = 1.2$. The symbols $+$ represent the flux predicted by means of Eq. (3.19), and the symbols \diamond are the corrected bin averages.	36
3.7	Same as Fig. 3.6, for channel 6 and $L = 1.2$	36
3.8	Same as Fig. 3.6, for channel 1 and $L = 1.4$	37
3.9	Same as Fig. 3.8, for channel 6 and $L = 1.4$	37
3.10	Same as Fig. 3.8, for channel 1 and $L = 2.0$	38
3.11	Same as Fig. 3.8, for channel 6 and $L = 2.0$	38
3.12	Comparison of the equatorial pitch angles subtended by the EI-88/1 and EI-88/2 detectors	39
3.13	(L, α_0) Map of the PAB97 model and AP-8 MAX for channel 1	40
3.14	(L, α_0) Map of the ratio of AP-8 MAX to the PAB97 model for channel 1 . . .	40
3.15	(L, α_0) Map of the PAB97 model and AP-8 MAX for channel 2	41

3.16	(L, α_0) Map of the ratio of AP-8 MAX to the PAB97 model for channel 2 . . .	41
3.17	(L, α_0) Map of the PAB97 model and AP-8 MAX for channel 3	42
3.18	(L, α_0) Map of the ratio of AP-8 MAX to the PAB97 model for channel 3 . . .	42
3.19	(L, α_0) Map of the PAB97 model and AP-8 MAX for channel 4	43
3.20	(L, α_0) Map of the ratio of AP-8 MAX to the PAB97 model for channel 4 . . .	43
3.21	(L, α_0) Map of the PAB97 model and AP-8 MAX for channel 5	44
3.22	(L, α_0) Map of the ratio of AP-8 MAX to the PAB97 model for channel 5 . . .	44
3.23	(L, α_0) Map of the PAB97 model and AP-8 MAX for channel 6	45
3.24	(L, α_0) Map of the ratio of AP-8 MAX to the PAB97 model for channel 6 . . .	45
3.25	World map of the PAB97 >50 MeV proton flux at 500 km	46
3.26	World map of the AP-8 MAX >50 MeV proton flux at 500 km	46
4.1	Mechanical design of the SAMPEX spacecraft and physical layout	52
4.2	Pointing strategy for the SAMPEX spacecraft in two illustrative orbit planes .	53
4.3	Schematic of the PET telescope	56
6.1	Effective areas of the SAMPEX/PET sensors	71
6.2	(L, α_0) Map of the PSB97 model and AP-8 MIN for channel 1	72
6.3	(L, α_0) Map of the PSB97 model and AP-8 MIN for channel 2	72
6.4	(L, α_0) Map of the PSB97 model and AP-8 MIN for channel 3	73
6.5	(L, α_0) Map of the PSB97 model and AP-8 MIN for channel 4	73
6.6	(L, α_0) Map of the PSB97 model and AP-8 MIN for channel 5	74
6.7	(L, α_0) Map of the PSB97 model and AP-8 MIN for channel 6	74
6.8	(L, α_0) Map of the PSB97 model and AP-8 MIN for channel 7	75
6.9	(L, α_0) Map of the PSB97 model and AP-8 MIN for channel 8	75
6.10	(L, α_0) Map of the PSB97 model and AP-8 MIN for channel 9	76
6.11	(L, α_0) Map of the PSB97 model and AP-8 MIN for channel 10	76
6.12	(L, α_0) Map of the PSB97 model and AP-8 MIN for channel 11	77
6.13	(L, α_0) Map of the PSB97 model and AP-8 MIN for channel 12	77
6.14	(L, α_0) Map of the PSB97 model and AP-8 MIN for channel 13	78
6.15	(L, α_0) Map of the PSB97 model and AP-8 MIN for channel 14	78
6.16	(L, α_0) Map of the PSB97 model and AP-8 MIN for channel 15	79
6.17	World map of the PSB97 >50 MeV proton flux at 500 km	80
6.18	World map of the AP-8 MAX >50 MeV proton flux at 500 km	80
7.1	Distribution in (B, L) space of the average countrate observed in PET energy channel PHI32 from Jul 1992 to Dec 1995	82

7.2	Histograms of PET proton count rates in the energy channel 37.4–45.8 MeV (PHI32) for the 6 bins shown in Fig. 7.1	84
7.3	Histograms of PET PHI32 proton counts (solid lines) fitted by Poisson distributions (dashed line) with the χ^2 method, for the 6 (B, L) bins shown in Fig. 7.1	86
7.4	Histograms of livetimes in the PET PHI32 channel for the 6 (B, L) bins shown in Fig. 7.1	87
7.5	Histograms of PET PHI32 proton counts in bin 1 ($B = 0.19, L = 1.24$) when the livetime interval is subdivided in 5 equal subintervals	89
7.6	Differential unidirectional spectrum in the 6 (B, L) bins shown in Fig. 7.1	92
8.1	Line drawing of the UARS observatory showing the placement of the various instruments	98
8.2	Diagram of the HEPS1 and HEPS2 telescopes	101
9.1	Flow chart of the transformation of IDFS files into ‘.eph’ and ‘.flx’ files	108
9.2	Deviation between VMAG and IGRF on 1–2 November 1991	110
9.3	Deviation between VMAG and IGRF on 3–4 November 1991	110
9.4	UARS/PEM data coverage	113
9.5	Flow chart of IDL procedures to produce the ‘.bin’, ‘.cor’ and ‘.res’ files	116
10.1	Iso-contours of L at 585 km	118
10.2	Iso-contours of the magnetic field intensity at 585 km	118
10.3	Local pitch angle of the HEPS2/T2 telescope with azimuth angle \mathcal{A} (ascending leg)	120
10.4	Local pitch angle of the HEPS2/T2 telescope with azimuth angle $\mathcal{A} + 180^\circ$ (ascending leg)	120
10.5	Local pitch angle of the HEPS2/T2 telescope with azimuth angle $180^\circ - \mathcal{A}$ (descending leg)	121
10.6	Local pitch angle of the HEPS2/T2 telescope with azimuth angle $360^\circ - \mathcal{A}$ (descending leg)	121
10.7	Local pitch angle of the HEPS1/T2 telescope with azimuth angle \mathcal{A} (ascending leg)	122
10.8	Local pitch angle of the HEPS1/T2 telescope with azimuth angle $\mathcal{A} + 180^\circ$ (ascending leg)	122
10.9	Local pitch angle of the HEPS1/T2 telescope with azimuth angle $180^\circ - \mathcal{A}$ (descending leg)	123
10.10	Local pitch angle of the HEPS1/T2 telescope with azimuth angle $360^\circ - \mathcal{A}$ (descending leg)	123

10.11	Local pitch angle of the HEPS1/T1 telescope with azimuth angle \mathcal{A} (ascending leg)	124
10.12	Local pitch angle of the HEPS1/T1 telescope with azimuth angle $\mathcal{A} + 180^\circ$ (ascending leg)	124
10.13	Local pitch angle of the HEPS1/T1 telescope with azimuth angle $180^\circ - \mathcal{A}$ (descending leg)	125
10.14	Local pitch angle of the HEPS1/T1 telescope with azimuth angle $360^\circ - \mathcal{A}$ (descending leg)	125
10.15	Local pitch angle of the HEPS2/T1 telescope with azimuth angle \mathcal{A} (ascending leg)	126
10.16	Local pitch angle of the HEPS2/T1 telescope with azimuth angle $\mathcal{A} + 180^\circ$ (ascending leg)	126
10.17	Local pitch angle of the HEPS2/T1 telescope with azimuth angle $180^\circ - \mathcal{A}$ (descending leg)	127
10.18	Local pitch angle of the HEPS2/T1 telescope with azimuth angle $360^\circ - \mathcal{A}$ (descending leg)	127
10.19	Iso-contours of the equatorial pitch angle when $\alpha = 90^\circ$ at 585 km	128
10.20	Raw $E \approx 100$ MeV proton flux at $1.295 < L < 1.305$ measured by the HEPS1/T2, HEPS1/T1, HEPS2/T2 and HEPS2/T1 telescopes as a function of the equatorial pitch angle for the period of time from October to December 1991	130
10.21	Distribution of the local pitch angle of the HEPS1/T2, HEPS1/T1, HEPS2/T2 and HEPS2/T1 telescopes as a function of α_0 at $1.295 < L < 1.305$ for the period of time from October to December 1991	130
10.22	First simulation of the reponse of detector HEPS2/T1	131
10.23	Second simulation of the reponse of detector HEPS2/T1	131
10.24	Simulation of detector measurements as a function of α_0 at different local pitch angles	133
10.25	Correction factor of the HEPS1/T1 measurements for the same conditions as Fig. 10.20	134
10.26	UARS/HEPS Differential flux as a function of the equatorial pitch angle for 17.2–24.4 MeV protons	136
10.27	UARS/HEPS Differential flux as a function of the equatorial pitch angle for 31.7–42.1 MeV protons	136
10.28	UARS/HEPS Differential flux as a function of the equatorial pitch angle for 94.0–122.5 MeV protons	137
10.29	UARS/HEPS Differential proton flux spectra at $L = 1.2$	137
10.30	UARS/HEPS Differential proton flux spectra at $L = 1.3$	138
10.31	UARS/HEPS Differential proton flux spectra at $L = 1.4$	138

10.32	UARS/HEPS Differential proton flux spectra at $L = 1.5$	139
10.33	UARS/HEPS Differential proton flux as a function of the parameter L at $\alpha_0 = 73^\circ$	139
10.34	UARS/HEPS Differential proton flux as a function of the parameter L at $\alpha_0 = 52^\circ$	140
10.35	UARS/HEPS Differential proton flux as a function of the parameter L at $\alpha_0 = 41^\circ$	140
10.36	(L, α_0) map of the integral perpendicular proton flux at $E > 5.6$ MeV.	141
10.37	(L, α_0) map of the integral perpendicular proton flux at $E > 6.8$ MeV.	142
10.38	(L, α_0) map of the integral perpendicular proton flux at $E > 7.9$ MeV.	142
10.39	(L, α_0) map of the integral perpendicular proton flux at $E > 10.4$ MeV.	143
10.40	(L, α_0) map of the integral perpendicular proton flux at $E > 13.1$ MeV.	143
10.41	(L, α_0) map of the integral perpendicular proton flux at $E > 17.2$ MeV.	144
10.42	(L, α_0) map of the integral perpendicular proton flux at $E > 24.4$ MeV.	144
10.43	(L, α_0) map of the integral perpendicular proton flux at $E > 31.8$ MeV.	145
10.44	(L, α_0) map of the integral perpendicular proton flux at $E > 42.1$ MeV.	145
10.45	(L, α_0) map of the integral perpendicular proton flux at $E > 56.8$ MeV.	146
10.46	(L, α_0) map of the integral perpendicular proton flux at $E > 71.4$ MeV.	146
10.47	(L, α_0) map of the integral perpendicular proton flux at $E > 94.0$ MeV.	147
10.48	(L, α_0) map of the integral perpendicular proton flux at $E > 122.4$ MeV.	147
10.49	(L, α_0) map of the integral perpendicular proton flux at $E > 145.8$ MeV.	148
10.50	(L, α_0) map of the integral perpendicular proton flux at $E > 160.9$ MeV.	148
11.1	World map of the PAB97 directional proton flux above 30 MeV for the LEO orbit described in the text	154
11.2	World map of the PUB97 directional proton flux above 30 MeV for the LEO orbit described in the text	154
11.3	World map of the PSB97 directional proton flux above 30 MeV for the LEO orbit described in the text	155
11.4	World map of the AP-8 MAX directional proton flux above 30 MeV for the LEO orbit described in the text	156
11.5	World map of the AP-8 MIN directional proton flux above 30 MeV for the LEO orbit described in the text	156
11.6	Integral PAB97 trapped proton fluxes above 30 MeV for the LEO orbit described in the text	157
11.7	Integral PUB97 trapped proton fluxes above 30 MeV for the LEO orbit described in the text	158

11.8	Integral PSB97 trapped proton fluxes above 30 MeV for the LEO orbit described in the text	159
11.9	Integral AP-8 MAX trapped proton fluxes above 30 MeV for the LEO orbit described in the text	160
11.10	Integral AP-8 MIN trapped proton fluxes above 30 MeV for the LEO orbit described in the text	161
11.11	PAB97 Integral and differential trapped proton spectrum for the LEO orbit described in the text	162
11.12	PUB97 Integral and differential trapped proton spectrum for the LEO orbit described in the text	163
11.13	PSB97 Integral and differential trapped proton spectrum for the LEO orbit described in the text	164
11.14	AP-8 MAX Integral and differential trapped proton spectrum for the LEO orbit described in the text	165
11.15	AP-8 MIN Integral and differential trapped proton spectrum for the LEO orbit described in the text	166
11.16	World map of the PAB97 directional proton flux > 30 MeV for the GTO orbit described in the text	167
11.17	World map of the PUB97 directional proton flux > 30 MeV for the GTO orbit described in the text	167
11.18	World map of the PSB97 directional proton flux > 30 MeV for the GTO orbit described in the text	168
11.19	World map of the AP-8 MAX directional proton flux > 30 MeV for the GTO orbit described in the text	169
11.20	World map of the AP-8 MIN directional proton flux > 30 MeV for the GTO orbit described in the text	169

List of Tables

1.1	Orbital elements of the AZUR satellite	6
1.2	Detector and absorber characteristics of the EI-88 instruments	8
1.3	Energy channels of the EI-88 instruments for protons and α particles	11
2.1	Directory structure of the AZUR data files and processing routines	13
2.2	List of IDL routines used for the AZUR data analysis	14
2.3	Record structure of the AZUR tape identification files	14
2.4	Content of the AZUR tape pass header records	15
2.5	Content of the AZUR tape data records	16
2.5	(continued)	17
2.5	(continued)	18
3.1	Geometric factors and surface areas of the EI-88 sensors [from Häusler (1972)]	28
3.2	(E, L, α_0) Bin limits for the PAB97 model grid	34
4.1	SAMPEX Scientific Instruments	54
4.2	PET Detector, ADC, and discriminator characteristics	57
4.3	PET Response	58
5.1	SAMPEX/PET Data set file description	61
5.2	PET Channel characteristics	64
5.3	Description of the EPH structure	66
6.1	(E, L, α_0) Bin limits for the PET model grid	70
7.1	Probability P (in %) that the histogram of counts is distributed according to a Poisson law (null hypothesis) for six (B, L) bins and for the 15 energy channels of the PET telescope	83
7.2	Mean countrates calculated by different methods for the detector PHI32 during July 1994	91

8.1	List of the UARS experiments	99
8.2	List of the PEM instruments	99
8.3	Characteristics of the HEPS detectors	100
8.4	Differential number flux uncertainties for protons from 5 to 150 MeV	102
8.5	List of the UARS sensors used from the IDFS database	103
8.6	Possible value of the IDFS quality indicator for the magnetometer and proton detectors	104
9.1	Proton energy (MeV) channels of the EP1 and EP2 sensors of the HEPS detectors	107
9.2	Bin limits (L, α_0)	112
A.1	List of metavariables	176
A.2	List of type codes for the record field	176
A.3	List of additional first-level metavariables	177
A.4	Definition of the first-level body structure	178
A.5	Description of the metavariables and body structure for the ephemeris files . . .	179
A.6	Description of the body structure for the measurement files	181
A.7	Metavariables for the binned data files	181
B.1	List of IDL subroutines related to UARS data	184

List of symbols

A Detector surface area

α Pitch angle

α_0 Equatorial pitch angle

β Azimuthal angle defined in the local mirror plane

B Geomagnetic field intensity

\mathbf{B} Geomagnetic field vector

B_m Mirror point geomagnetic field intensity

B_0 Equatorial geomagnetic field intensity

B_c Geomagnetic field intensity at the atmospheric cutoff

C Counting rate

E Particle energy

ϵ Detector efficiency

$F_{10.7}$ Solar radio flux at 10.7 cm

G Geometric factor (cm^2sr)

Γ Telescope gathering power

h Effective detector area

j Differential particle flux

J Integral particle flux

L McIlwain's (1961) parameter (R_E)

λ Wavelength (\AA)

- ω Solid angle (sr)
- ϕ Geocentric longitude or azimuth angle
- φ Angle introduced by Daly & Evans (1993)
- \mathbf{r} Position vector
- R Telescope directional response function
- S Total area
- $d\sigma$ Element of surface area
- t Time
- T Total observation time
- θ Polar angle
- Z Atomic number

Preface

The models of the Earth's trapped radiation environment in common use in the West are the NASA models AP-8 and AE-8 (Vette 1991b), which were developed in the late sixties. These models represent the trapped particle environment as measured by a series of instruments on satellites that flew in the sixties and early seventies. The NASA models have been used—more or less exclusively—for more than twenty years now and have become a generally accepted standard.

Only fairly recently has the interest in the trapped radiation environment been rekindled, mainly since the Combined Release and Radiation Effects (CRRES) mission which has emphasized several aspects of the old models which are in need of updating or replacement:

1. The NASA models are static. Two versions were released, for conditions of solar minimum and solar maximum, respectively, but effects of variations in the trapped particle environment on shorter time scales can not be evaluated with the current models. Consequently, the NASA models only allow for estimates of the average effect of the trapped radiation for missions of six months or longer.
2. The input to the NASA models consisted of measurements obtained with a variety of detectors, calibration techniques, orbital data, etc., so that the internal consistency and errors are difficult to estimate.
3. Instrument design has advanced enormously over the last decades, so that more accurate and comprehensive measurements are now possible.
4. Several instruments used as input to the NASA models were plagued by severe background contamination. In addition, cross-calibration of the various instruments was not always feasible.
5. The measurements were unavoidably contaminated by Starfish and other atmospheric nuclear detonations.
6. Extrapolations were used to model the low- and/or high-energy parts of the particle spectra, both at low altitudes and near the geostationary environment.
7. The NASA models do not contain directional information, since only omnidirectional fluxes are given. In view of describing the low altitude environment, where the East-West asymmetry plays an important role for protons, directional data are needed.

8. The interaction of the Earth's atmosphere with the radiation belts was included as an arbitrary cut-off value for L . New low-altitude models should provide a more realistic description of atmospheric effects.
9. The data were organised in function of magnetic field models with epoch 1960 or 1970. The secular variation of the Earth's magnetic field over the period following the development of the NASA models introduces severe difficulties in applying these models to the actual near-Earth environment (Heynderickx et al. 1996ab).
10. No attempt was made to include the contributions of external sources to the geomagnetic field.
11. The organisation of the flux maps in terms of L and B/B_0 introduces large interpolation errors for low altitudes where the particle flux varies rapidly with B/B_0 .

The TREND (Trapped Radiation ENvironment Development) study identified weaknesses in the existing models and methods and identified suitable satellite data sets for updating the models (Lemaire et al. 1990). During the TREND-2 study, additional data sets were acquired and analysed, and new coordinate systems investigated (Lemaire et al. 1995). The aim of the TREND-3 study, of which this Technical Note is a part, is to derive new proton and electron models from these data sets, using the coordinate systems identified as most suitable during TREND-2. This Technical Note presents the results of the study of the low altitude trapped proton environment using three data sets:

1. AZUR/EI-88: this data set was used to construct the AP-8 MAX low altitude model (Sawyer & Vette 1976). The measurements made by this instrument are unidirectional, but the official release of AP-8 MAX only contains an omnidirectional flux map [an unofficial release of a directional flux map based on the omnidirectional AP-8 MAX was later issued by Vette (unpublished report), a copy of which was made available to BIRA/IASB by A. Konradi]. The data of the AZUR mission are of a very high quality, but unfortunately cover no more than about three months. The AZUR/EI-88 data were obtained from NSSDC with the help of J. King, and were analysed at BIRA/IASB (using documentation provided by D. Hovestadt). The result of this analysis (described in Part I of this Technical Note) is a new unidirectional low altitude trapped proton model which may replace the low altitude part of AP-8 MAX.
2. The SAMPEX mission (Baker et al. 1993) was launched in 1992 and carried, among other instruments, the energetic particle telescope (PET). The satellite is still operational and continues to transmit high quality data. J.B. Blake of Aerospace Corp. has made the PET data available to BIRA/IASB for the development of a new low altitude trapped proton model. One year of data has been analysed in the TREND-3 study, resulting in a new unidirectional trapped proton model for epoch 1995. The construction of this model is described in Part II of this Technical Note. The SAMPEX/PET data were also used to validate a new method of describing the East-West asymmetry in the low altitude proton environment (see Technical Note 6 of the TREND-3 study). In the follow-on study

TREND-4, the SAMPEX/PET data will serve to study the dependence of the low altitude trapped proton environment on the solar cycle.

3. A third data set, UARS/PEM, was acquired in collaboration with SWRI through J.D. Winningham. One year of these directional data were analysed, which resulted in a new low altitude trapped proton model for epoch 1992. This model and its derivation are described in Part III of this Technical Note.

The three new models were compared to the AP-8 models, and were applied to several typical low altitude orbital environments. Part IV of this Technical Note presents the results of these evaluations.

The implementation of the new models in the UNIRAD software suite is described in Technical Note 10.

Acknowledgments

The AZUR radiation belt model for trapped protons could never have been developed without the cooperation of D. Hovestadt, Max Planck Institut für Extraterrestrische Physik, Garching, who was the PI of the EI-88 directional detectors. He provided D. Heynderickx with the necessary documentation for the analysis of the AZUR data and granted permission to use the data set. We wish to acknowledge also the Director of NSSDC, J. King, who has unearthed this historical data set from the archives of the NSSDC, at GSFC, Greenbelt.

We wish to address our special thanks to J.B. Blake, Aerospace Corporation, Los Angeles, and R.A. Mewaldt, CALTECH, Pasadena, for offering the TREND project manager to make use of the proton flux measurements of the Proton Electron Telescope (PET) obtained onboard of the SAMPEX satellite, in order to build a new trapped proton environment model. R.A. Mewaldt and J.B. Blake are PI's for this comprehensive experiment. We thank also M.D. Looper, research assistant at Aerospace Corporation for implementing the unique PET dataset during two visits at BIRA/IASB, and for many long and fruitful discussions.

The TREND team at BIRA/IASB has also been given access to the PEM proton flux measurements obtained onboard of the UARS satellite. We are very grateful to J.D. Winningham and J.R. Sharber, South West Research Institute, San Antonio, PI and Co-I of PEM, for allowing M. Kruglanski to visit SwRI, and to use the PEM observations to build a database for trapped energetic protons. The TREND project manager also thanks the SwRI personnel, especially R.A. Frahm, for allowing us to retrieve and partly process these data on their computer facilities. This database has been used by M. Kruglanski, with the assistance of M.M. Echim (visiting BIRA/IASB from the Institute of Gravitation and Space Sciences, Bucharest), to build the PEM/UARS proton environment model.

During the TREND-3 modelling effort the ESA Technical Manager E.J. Daly has closely followed the progress of the data analysis and model development. His experience and advice have been very stimulating and greatly appreciated by all TREND team members. We also benefited from H. Evans' useful suggestions and comments.

We thank J. Lemaire, the TREND-3 project manager, for carefully reading the manuscript and providing many helpful comments and suggestions. The collaboration with Aerospace Corp. and SWRI would not have been possible without his contacts and efforts.

The technical support of our system manager L. Fedullo has been invaluable throughout the TREND programme. He has installed and maintained the VMS cluster and software that constitute the platform on which the BIRA/IASB part of the TREND work has been performed.

Finally, we acknowledge P. Simon, Director of BIRA/IASB, and his predecessor, Baron M. Ackerman, who gave full support to the TREND study and who facilitated its realisation. The logistic and administrative personnel of BIRA/IASB is also generally acknowledged for its efficient help and good collaboration.

Introduction

This Technical Note describes the data processing of three satellite data sets: AZUR/EI-88, SAMPEX/PET, and UARS/PEM. In the first three parts, the data bases of the three instruments are described, including the processing procedure and the final format of the data bases. The binning of the data into flux maps is discussed as well.

The implementation of the new flux maps in the UNIRAD package is described in Technical Note 10. In Part IV of this document, the three resulting proton models are applied to evaluate several typical low altitude orbital environments.

The AZUR/EI-88 data base and model

Part I of this Technical Note is devoted to AZUR/EI-88 data base analysis. Chapter 1 describes the AZUR mission and instrumentation, with special emphasis on the EI-88 instruments. The installation and treatment of the data base forms the subject of Chapter 2: this includes the “cleaning of the data set” (i.e. identification and removal of contaminated or otherwise invalid measurements), the calculation of magnetic coordinates B , L , and α_0 , and the creation of the final data set used in the modelling.

Once the final data base is established, the measured fluxes have to be corrected for the finite opening angle of the EI-88 telescopes. Chapter 3 starts out with a general description of this correction procedure, which has been applied to the SAMPEX/PET and UARS/PEM data as well. The rest of the chapter is devoted to the application of the opening angle correction and the binning of the corrected data into an (E, L, α_0) flux map, which constitutes the new AZUR/EI-88 model. Finally, the final flux map is compared to the AP-8 MAX flux map. The implementation of the new flux map in the UNIRAD software suite is described in Technical Note 10.

The SAMPEX/PET data base and model

The analysis of the SAMPEX/PET data base and the development of a new low altitude trapped particle model is described in Part II of this Technical Note. A detailed description of the SAMPEX mission and instruments, with special emphasis on the PET instrument, is given in Chapter 4. The installation of the data base on the BIRA/IASB hardware forms the subject of

Chapter 5. This includes a description of the data processing routines and of the format of the final data set.

The construction of the new model is described in Chapter 6. The correction of the flux measurements for the finite opening angle of the PET telescope is analogous to the correction applied to the AZUR/EI-88 data, described in Chapter 3. The corrected data have been binned into an (E, L, α_0) flux map, which constitutes the new SAMPEX/EI-88 model. Finally, the final flux map is compared to the AP-8 MIN flux map. The implementation of the new flux map in the UNIRAD software suite is described in Technical Note 10.

The UARS/PEM data base and model

The analysis of the UARS/PEM data base and the development of a new low altitude trapped particle model is described in Part III of this Technical Note. A detailed description of the UARS mission and instruments, with special emphasis on the PEM instrument, is given in Chapter 8. The installation of the data base on the BIRA/IASB hardware forms the subject of Chapter 9. This includes a description of the data processing routines and of the format of the final data set.

The construction of the new model is described in Chapter 10. The correction of the flux measurements for the finite opening angle of the PEM telescope is analogous to the correction applied to the AZUR/EI-88 data, described in Chapter 3. The corrected data have been binned into an (E, L, α_0) flux map, which constitutes the new UARS/PEM model. Finally, the final flux map is compared to the AP-8 MAX flux map. The implementation of the new flux map in the UNIRAD software suite is described in Technical Note 10.

Model comparisons

In Part IV, the three models developed in Parts I–III are applied to evaluate the trapped proton environment for several typical low altitude orbital configurations. For each set of orbits, the predictions of the three models for the trapped proton fluxes at each orbital point, as well as for the total mission fluence, are compared.

Part I

The AZUR data base and model

Chapter 1

The AZUR mission

The AZUR satellite was launched on November 8, 1969, into a 102.9° inclination, sun-synchronous polar orbit with apogee 3145 km and perigee 384 km. The last telemetry data were recorded on June 18, 1970. Unfortunately, the data gathered after March 5, 1970 have been lost.

A cross sectional view of the AZUR satellite is shown in Fig. 1.1. The satellite was magnetically stabilized, with one axis aligned along the magnetic field direction, as shown in Fig. 1.2. The full orbital parameters are given in Table 1.1. The AZUR satellite has international reference 1969-097A No. 4221.

The instrument complement included detectors to measure the directional and omnidirectional fluxes of protons and electrons. These instruments and the high quality of the resulting measurements made the AZUR mission particularly well suited for the study of the trapped radiation environment, despite the short duration of the mission. The energetic proton measurements, which were collected during the maximum of Solar Cycle 20, were the basis for the low altitude part of the NASA model AP-8 MAX (Sawyer & Vette 1976).

1.1 Mission goals

The mission goals were the measurements of the following quantities:

1. directional proton intensities in several energy intervals between 0.25 and 100 MeV (two particle telescopes EI-88/1 and EI-88/2, PI D. Hovestadt);
2. directional intensity of alpha particles in the energy range 6.5–19 MeV;
3. omnidirectional proton intensities in two energy ranges: 20–45 MeV and 40–80 MeV;
4. omnidirectional integral electron intensity above two thresholds: 1.5 and 4.0 MeV;
5. directional integral intensity of charged particles parallel, antiparallel and perpendicular to magnetic field lines, above 40 keV for electrons and 0.7 MeV for protons;

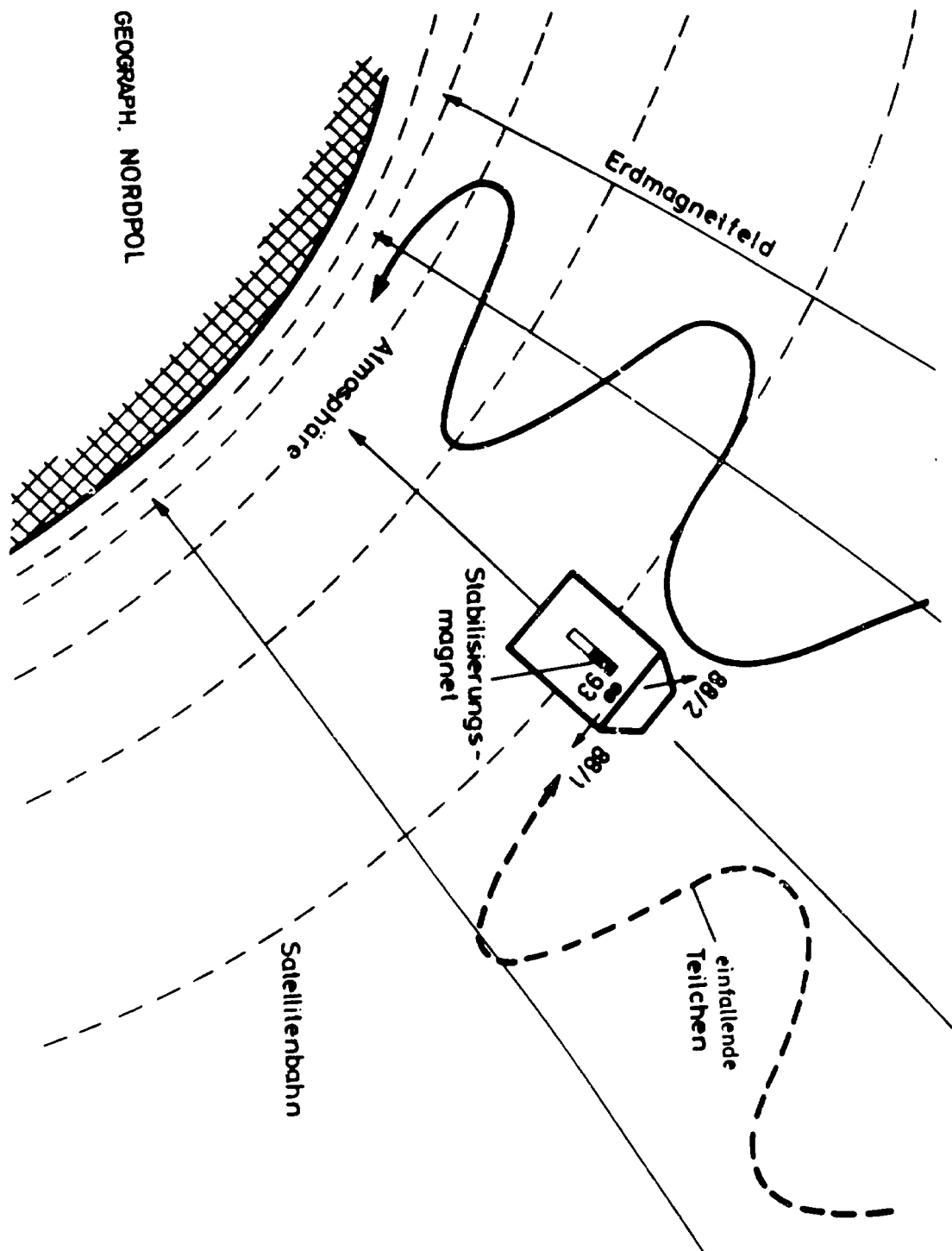


Figure 1.2. Representation of the orbital attitude of the AZUR satellite

Table 1.1. Orbital elements of the AZUR satellite

Orbital Element	Nominal Orbit	First Orbit
Semi-major axis (km)	8179.09	8142.80
Eccentricity	0.17337	0.16957
Inclination (deg)	102.671	102.975
Argument of perigee (deg)	161.801	161.906
Right ascension of ascending node (deg)	125.490	126.564
Period (m)	122.688	121.87603
Perigee height (km)	382.69	383.84
Apogee height (km)	3218.72	3145.43
Geocentric perigee latitude at injection (deg)	17.741 N	17.617 N
Precession of perigee (deg/day)	1.667	1.671
Precession of node line (deg/day)	0.96	

6. omnidirectional integral intensity of charged particles above two thresholds: 12 and 30 MeV for protons, 0.7 and 3.2 MeV for electrons;
7. optical emission by N_2^+ ($\lambda = 3914 \text{ \AA}$) and $OI-N_2$ ($\lambda = 2972 \text{ \AA}$);
8. transverse hydromagnetic waves with amplitudes above 5γ (magnetometer EI-15, PI G. Musmann).

The payload consisted of seven instruments. Descriptions of each instrument package can be found in Achtermann et al. (1970). In this study, we only use the measurements made by the two directional proton telescopes (EI-88/1 and EI-88/2), which are described below, and the magnetometer data.

1.2 The EI-88/1 and EI-88/2 proton telescopes

1.2.1 Measurement principle

The EI-88 experiment measures the directional proton flux in the energy range 1.5–100 MeV. Figure 1.3 is a cross section of the instrument. The aperture opening is constructed with a number of Al and Ta collimators and is continued through a plastic scintillator surrounding the detectors and absorbers. The scintillator is connected to a photomultiplier by means of a plexiglass light conductor. The detectors respond to particle beams through the aperture opening. The energy dependent reach of the incident particles determines the number of detectors and absorbers they penetrate. Through the implementation of seven detectors and a treatment of the detector signal logic the total measurement range is divided into six energy ranges for protons and one channel for α particles. The anticoincidence rates are referred to as channel 8.

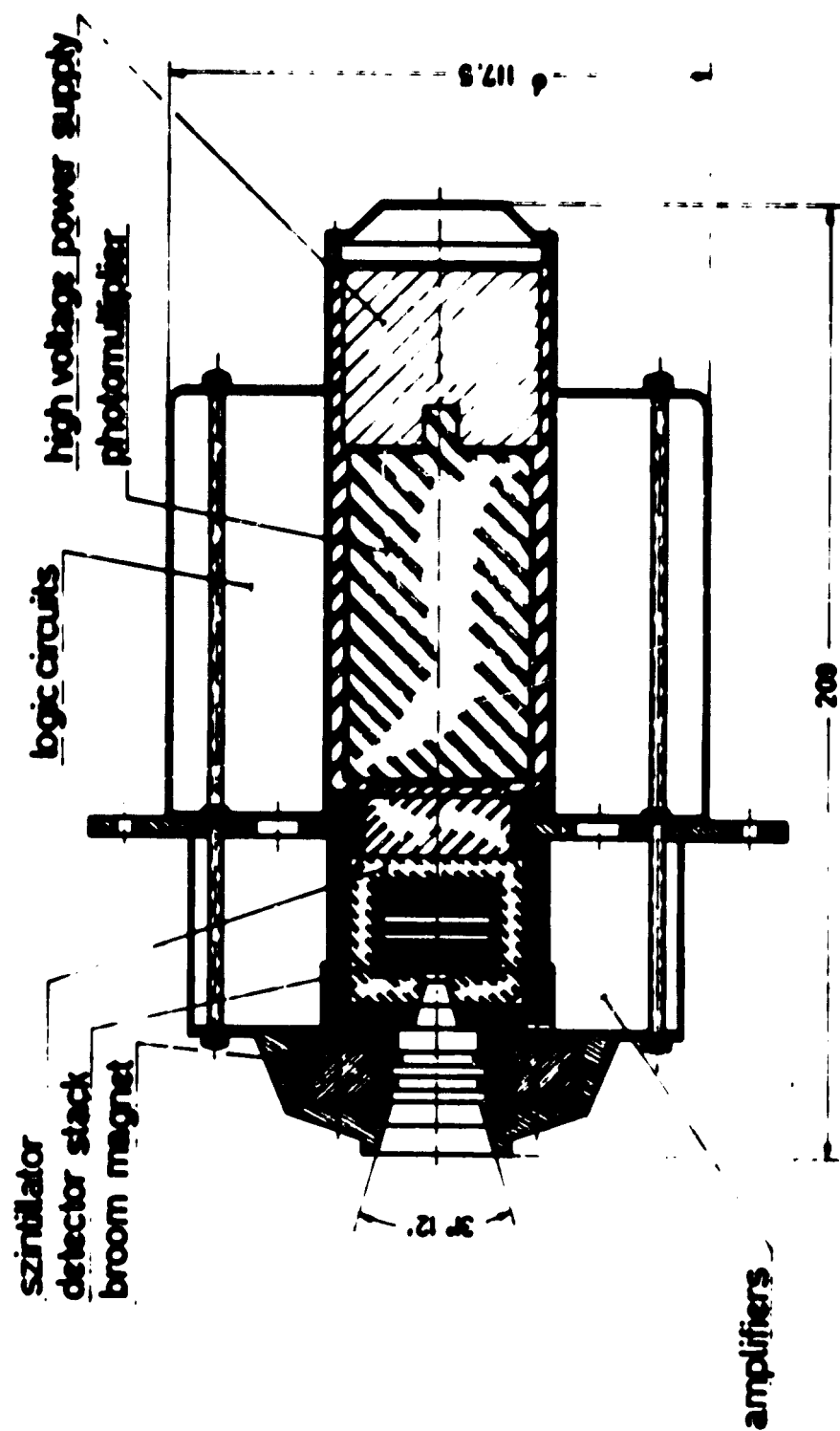


Figure 1.3. Cross section of the EI-88 instrument

Table 1.2. Detector and absorber characteristics of the EI-88 instruments

Detector	Absorber	Thickness (μ)	Electronics threshold (keV)
	Ni	1	
A		20	300, 900
B		50	500, 2300
C		100	600
	Al	30	
D		300	900
	Al	200	
E		400	700
	Cu	565	
	Al	30	
F		400	400
	Ta	1750	
G		400	400
	Ta	7050	

The lower limit of the detector range is determined by the thickness of the Ni foil placed before the scintillator, the thickness of the first detector, and the electronic threshold of the second detector. The Ni foil with thickness $1 \mu \sim 8.9 \times 10^{-4} \text{ g cm}^{-2}$ serves to shield the scintillator and the detectors from incoming light. The upper energy limit of the instrument is given by the absorption thickness of the combined detector cage up to the aft inner wall of the scintillator. In addition to its role as upper energy limit for particles coming in through the aperture, the scintillator also tags particles that penetrate from outside the aperture through the combined shielding. An anticoincidence switch between scintillator and detectors prohibits these particles to be measured. In order to limit the impulse rate of the scintillator and, correspondingly, the dead time of the instrument, the electronics are constructed around the scintillator and the photomultiplier to provide additional shielding.

The electronic thresholds of the semiconductor detectors (see Table 1.2) are chosen sufficiently high so that electrons penetrating the aperture without scattering do not produce a signal. This arrangement does not rule out electrons undergoing multiple scattering and pile-up effects. Therefore, the instruments are equipped with a sweeping magnet which ensures that the influence of electrons on the ion count rates is negligible (Achtermann et al. 1970).

1.2.2 Detector layout and energy range

Figure 1.4 shows a cross section through the EI-88 sensors. The plastic scintillator surrounds an Al cage that contains the seven detectors and the three absorbers. The detector connectors are fed through holes in the scintillator and the closest Ta shield to the amplifiers, which are

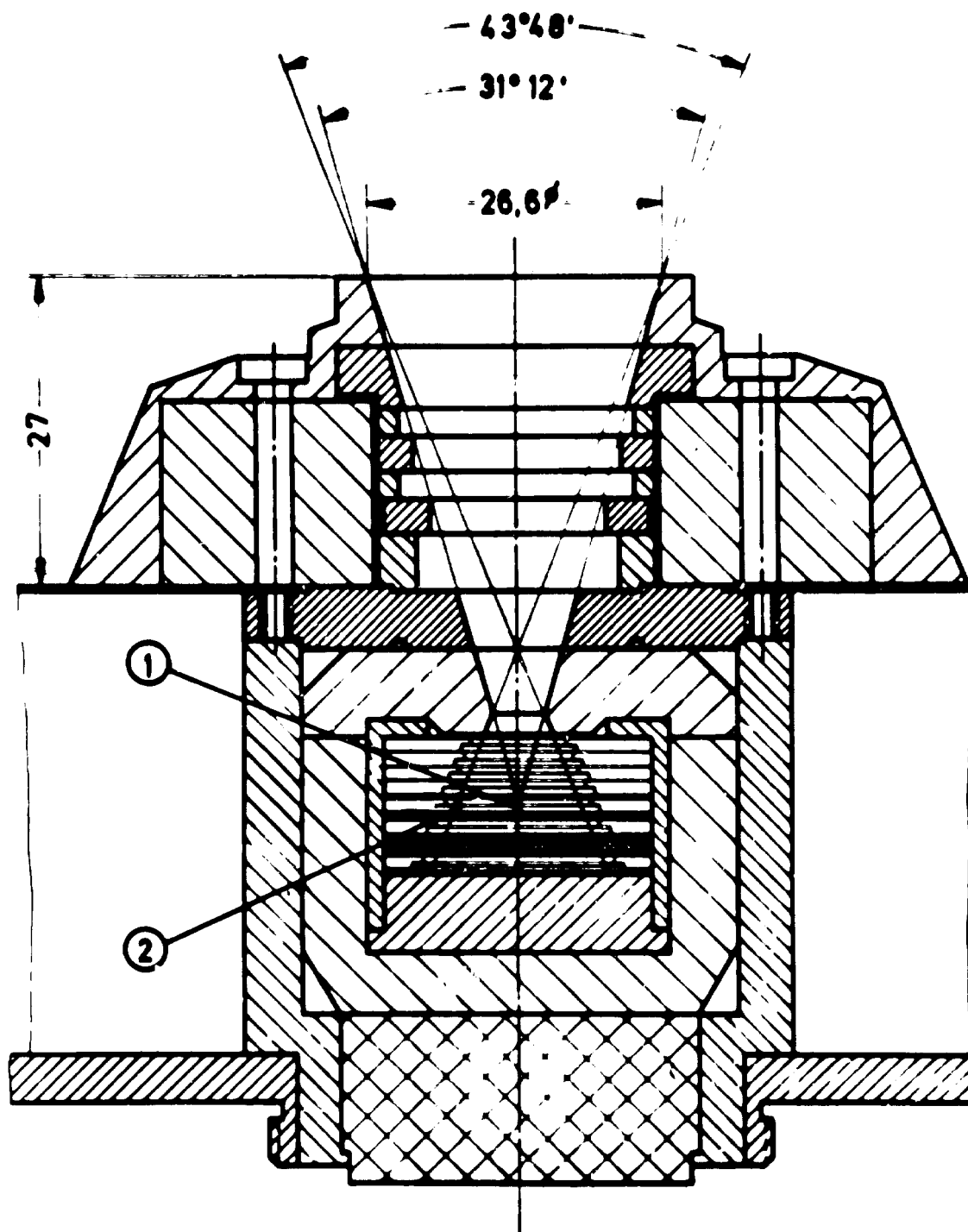


Figure 1.4. Cross section of the EI-88 sensors

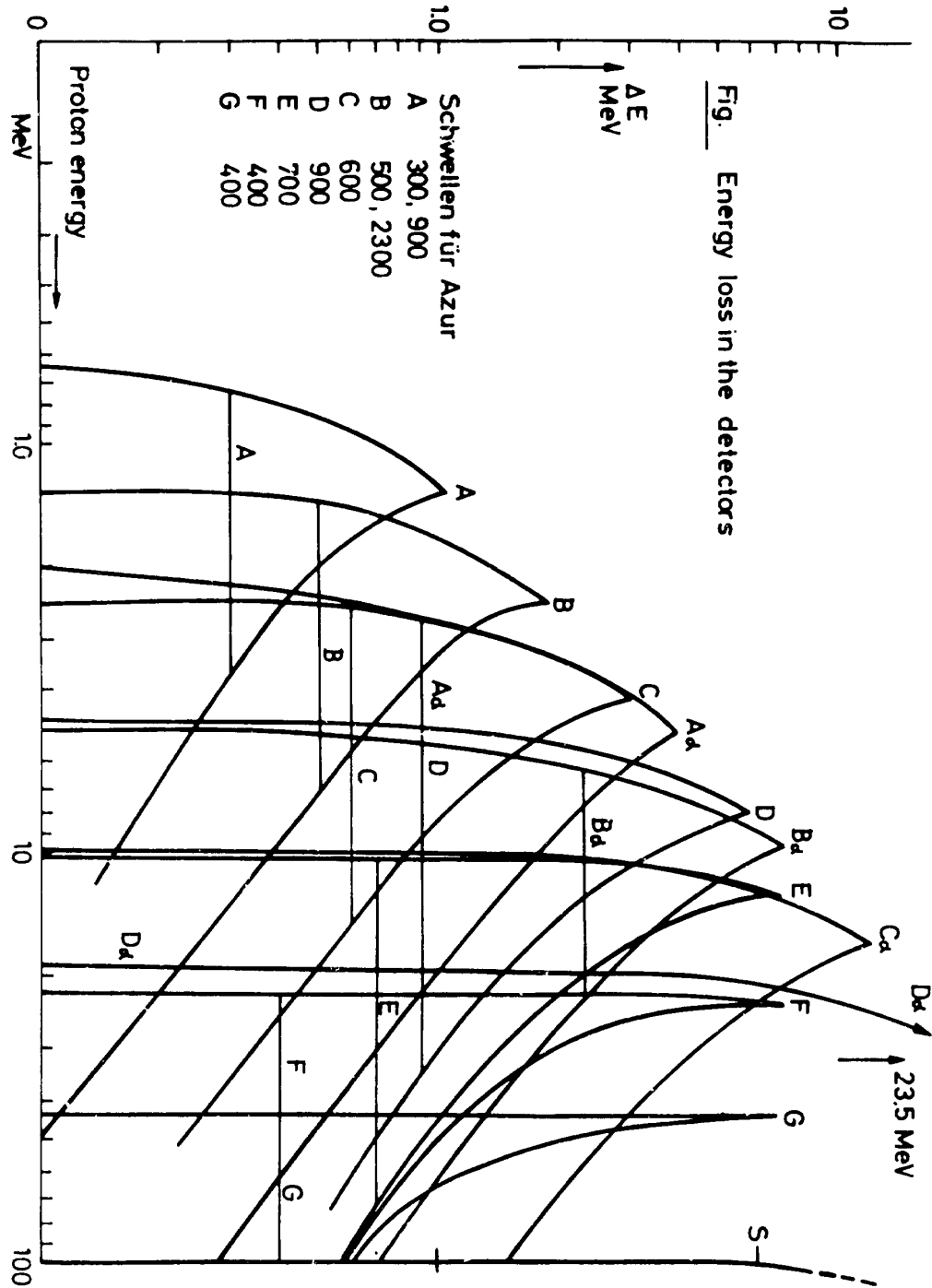


Figure 1.5. Energy deposited in the EI-88 detectors as a function of incident particle energy

Table 1.3. Energy channels of the EI-88 instruments for protons and α particles

Channel	Logic	Particle	Energy range (MeV)
1	A B \bar{C} \bar{S}	protons	1.5–2.7
2	A B \bar{D} \bar{S}	α	6.0–19.0
3	B C \bar{D} \bar{S}	protons	2.7–5.2
4	C D \bar{E} \bar{S}	protons	5.2–10.4
5	D E \bar{F} \bar{S}	protons	10.4–22.0
6	E F \bar{G} \bar{S}	protons	22.0–48.8
7	F G \bar{S}	protons	48.8–104.0
8	S	anticoincidence	

arranged around the detector cage. Figure 1.5 shows the energy deposited in the detectors as a function of the energy of the incident proton. The detector thresholds and switching logic yield the energy ranges for protons and α particles listed in Table 1.3.

The detectors EI-88/1 and EI-88/2 are identical except for a small difference in aperture angle, and thus geometric factor. The angular response function of the telescopes is discussed in Sect. 3.3. The integration time for both instruments is fixed at 10 s. Due to the slow spin rate of the satellite, this rather long integration time does not compromise the quality of the directional measurements.

Chapter 2

The AZUR/EI-88 data base

In this chapter we describe the downloading of the data sets to a DEC Alpha workstation running OpenVMS. The data analysis is performed with a series of IDL programmes and one FORTRAN programme [to calculate (B, L) values]. The different steps in the analysis procedure are outlined and the format of the final data base is described. Table 2.1 shows the directory structure of the AZUR data base and processing routines. The IDL routines are listed in Table 2.2.

2.1 Retrieval of the data sets

The data were sent to BIRA/IASB by NSSDC in the form of two magnetic tapes. Originally, the data were sent to NSSDC by MPE on 14 tapes, each tape containing a data file and a tape identification file. NSSDC merged the data set to two tapes containing 28 binary files in total: 14 data files and 14 identification files. The tapes are 9 track, 800 bpi, unlabelled, with

Table 2.1. Directory structure of the AZUR data files and processing routines

Directory name	Contents
BIN45	Bin means for EI-88/2 data
BIN90	Bin means for EI-88/1 data
DETCOR45	Geometric correction factors for EI-88/2 data
DETCOR90	Geometric correction factors for EI-88/1 data
FORTTRAN	Magnetic field model routines
IDL	IDL routines
MODELS	Final model maps
TAPE	Original CYBER binary data files

Table 2.2. List of IDL routines used for the AZUR data analysis

Name	Function
TAPE_ASCII.PRO	Convert CYBER binary format to ASCII format
CLEAN.PRO	Extract valid data points from the ASCII files
CHECKBIN.PRO	Derive the optimal bin size
BINNING.PRO	Bin the measurements in (E, L, α_0) bins
MODEL.PRO	Create the (E, L, α_0) model data file
DETCOR.PRO	Calculate the corrections to the geometric factors
MODCOR.PRO	Check the model file for inconsistencies
MODPLOT.PRO	Plot the new model and compare to AP-8
MODWORLD.PRO	Produce world maps of the new model and compare to AP-8

Table 2.3. Record structure of the AZUR tape identification files

Word	Content
1	1
2	Satellite Id. Nr. 6909701
3	Experiment Id. Nr. 889293
4	Tape Nr.
5–81	Spares

RECFM=VBS and BLKSIZE=9844. These two tapes were read at BIRA/IASB on an Apollo workstation and the 28 files were then transferred by binary FTP to the Alpha workstation.

The tapes were written by a CYBER machine. The internal representation of floating numbers on this architecture differs from the representation on the Alpha hardware. In addition, alphanumeric information is coded in EBCDIC on the CYBER. The IDL programme `tape.pro` reads in each data file, transforms the binary code to Alpha format and writes the resulting values to a set of new files in ASCII format. These files have names `TAPEnn.DAT` and reside in the main directory. Odd-numbered files are tape identification files (see Table 2.3 for their contents) and are not used in the data processing.

The even-numbered files contain the actual data (100 orbits per file). The data in each file are organised in passes (or contacts) between different ground stations. Each pass begins with a pass header record and is followed by the normal data records in chronological order. Each record, of both types, consists of 81 four byte words. The content of word nr. 1 specifies the record type. The contents of the pass header records and data records are given in Tables 2.4 and 2.5, respectively.

Table 2.4. Content of the AZUR tape pass header records

Word Nr.	Content	Representation
1	Type of record	Integer
2	Year of begin of pass	Integer
3	Day of begin of pass	Integer
4	Second of begin of pass	Integer
5	Year of end of pass	Integer
6	Day of end of pass	Integer
7	Second of end of pass	Integer
8	Orbit number at begin of pass	Integer
9	First character of station name	Character
10	Second character of station name	Character
11	Third character of station name	Character
12	Fourth character of station name	Character
13	Fifth character of station name	Character
14	K_p	Float
15–81	Spare	

Word 2 of the data records identifies the data quality:

```

Word 2 = 0:  good
        = 1:  average
        = 2:  bad

```

Records flagged as bad were rejected in the data analysis. Words 3 to 40 contain auxiliary data. Words 41 to 66 contain the counting rates of the scientific data channels. The channels contain the counting rates plus 1, i.e. 1 means zero counts.

Words 67 to 81 contain housekeeping data of the experiments and the logical condition. Word 74 indicates normal mode (=0) or calibration mode (=1). Words 68 and 70 contain the mode of operation of EI-88/1 and EI-88/2, respectively:

```

Word 68 (70) = 0:  data channels of EI-88/1 and EI-88/2
                   contain count rates of Table~1.3
                = 1:  channels contain single rates of
                   detectors A to G and anticoincidence

```

The modes of operation alternate in a fixed sequence of a period of 16 formats (10s each): 14 formats designated with 0 are followed by 2 formats designated 1. The first format with a 1 and the first format with a 0 are a mixture of coincidence and single rates and can therefore not be used. For the final data base all formats with a 1 were rejected.

Table 2.5. Content of the AZUR tape data records

Word Nr.	Content	Representation
1	Type of record (pass header or data)	Integer
2	Quality	Integer
3	Year	Integer
4	Day	Integer
5	UT (ms)	Integer
6	LT hour	Integer
7	LT min	Integer
8	MLT hour	Integer
9	MLT min	Integer
10	Orbit Nr.	Integer
11	Spare	
12	Geographic latitude (deg)	Float
13	Geographic longitude (deg)	Float
14	Geographic distance (R_E)	Float
15	Right ascension (deg)	Float
16	Declination (deg)	Float
17	Magnetic latitude (deg)	Float
18	Magnetic longitude (deg)	Float
19	L (R_E)	Float
20	B (gauss)	Float
21	Λ (invariant latitude, deg)	Float
22	R (R_E)	Float
23	Angle between satellite axis and \mathbf{B} (deg)	Float
24	Azimuth with respect to \mathbf{B} (deg)	Float
25	Aspect angle to sun (deg)	Float
26	Azimuth angle with respect to sun (deg)	Float
27	γ_1 Spin axis (geocentric, deg)	Float
28	γ_2 Spin axis (geocentric, deg)	Float
29	γ_3 Spin axis (geocentric, deg)	Float
30	B_x Magnetic field vector component (geocentric, deg)	Float
31	B_y Magnetic field vector component (geocentric, deg)	Float
32	B_z Magnetic field vector component (geocentric, deg)	Float
33	Spare	
34	Spare	
35	Spare	
36	Station (abbreviation to one character)	Character

Table 2.5. (continued)

Word Nr.	Content	Representation
37	Orbit counter	Integer
38	Record counter	Integer
39	Corrected orbit counter	Integer
40	Corrected record counter	Integer
41	EI-88/1 Channel 1 counts plus 1	Integer
42	EI-88/1 Channel 2 counts plus 1	Integer
43	EI-88/1 Channel 3 counts plus 1	Integer
44	EI-88/1 Channel 4 counts plus 1	Integer
45	EI-88/1 Channel 5 counts plus 1	Integer
46	EI-88/1 Channel 6 counts plus 1	Integer
47	EI-88/1 Channel 7 counts plus 1	Integer
48	EI-88/1 Channel 8 counts plus 1	Integer
49	EI-88/2 Channel 1 counts plus 1	Integer
50	EI-88/2 Channel 2 counts plus 1	Integer
51	EI-88/2 Channel 3 counts plus 1	Integer
52	EI-88/2 Channel 4 counts plus 1	Integer
53	EI-88/2 Channel 5 counts plus 1	Integer
54	EI-88/2 Channel 6 counts plus 1	Integer
55	EI-88/2 Channel 7 counts plus 1	Integer
56	EI-88/2 Channel 8 counts plus 1	Integer
57	EI-93 Channel 1 counts plus 1	Integer
58	EI-93 Channel 2 counts plus 1	Integer
59	EI-93 Channel 3 counts plus 1	Integer
60	EI-93 Channel 4 counts plus 1	Integer
61	EI-92 Channel 1 counts plus 1	Integer
62	EI-92 Channel 2 counts plus 1	Integer
63	EI-92 Channel 3 counts plus 1	Integer
64	EI-92 Channel 4 counts plus 1	Integer
65	EI-92 Channel 5 counts plus 1	Integer
66	EI-92 Channel 6 counts plus 1	Integer
67	EI-88/1 Detector current	Integer
68	EI-88/1 Logic	Integer
69	EI-88/2 Detector current	Integer
70	EI-88/2 Logic	Integer
71	EI-93 Detector current	Integer
72	EI-92 Detector current	Integer
73	Light in EI-92	Integer

Table 2.5. (continued)

Word Nr.	Content	Representation
74	Calibration mode	Integer
75	EI-88/1 Temperature	Integer
76	EI-88/1 Photomultiplier	Integer
77	EI-88/2 Temperature	Integer
78	EI-88/2 Photomultiplier	Integer
79	EI-93 Temperature	Integer
80	EI-92 Temperature	Integer
81	16 V Voltage	Integer

2.2 Cleaning of the data sets

The next step in the data processing is the “cleaning” of the ASCII data files `TAPEnn.DAT` generated by `TAPE.PRO`. This routine reads in a data file `TAPEnn.DAT`, rejects bad data records and produces an output file `CLEANnn.DAT`. The records of the ASCII files produced by the programme `CLEAN.PRO` do not contain all the words listed in Table 2.5, in particular the data for EI-93 and EI-92 (words 57–66), housekeeping data (words 67–81), and records 1, 11, 33–35, and 37–40 were not copied. The first line in each `CLEANnn.DAT` file consists of column headers.

The effect of the cleaning programme is shown in Figs. 2.1 and 2.2, which show the raw and cleaned count rates for a sample of channel 4 data in file `TAPE4.DAT`.

2.2.1 Rejection criteria

Not all the records in the data files are valid measurement records. Bad or contaminated records and housekeeping records were identified and have not been included in the final data files `CLEANnn.DAT`. Below, we describe the different rejection criteria. The programme `CLEAN.PRO` produces listing files `CLEANnn.LOG` with the number of records rejected by each criterion.

The records rejected by the criteria in Sects. 2.2.1.1–2.2.1.3 are eliminated altogether. The criteria in Sects. 2.2.1.4 and 2.2.1.5 do not remove records, but set the count rates of one or both detectors to -1 . Finally, the criteria in Sects. 2.2.1.6 and 2.2.1.7 act on individual channels of each detector.

2.2.1.1 Calibration mode

Data records with the calibration mode flag (word 74) set to one can be safely rejected.

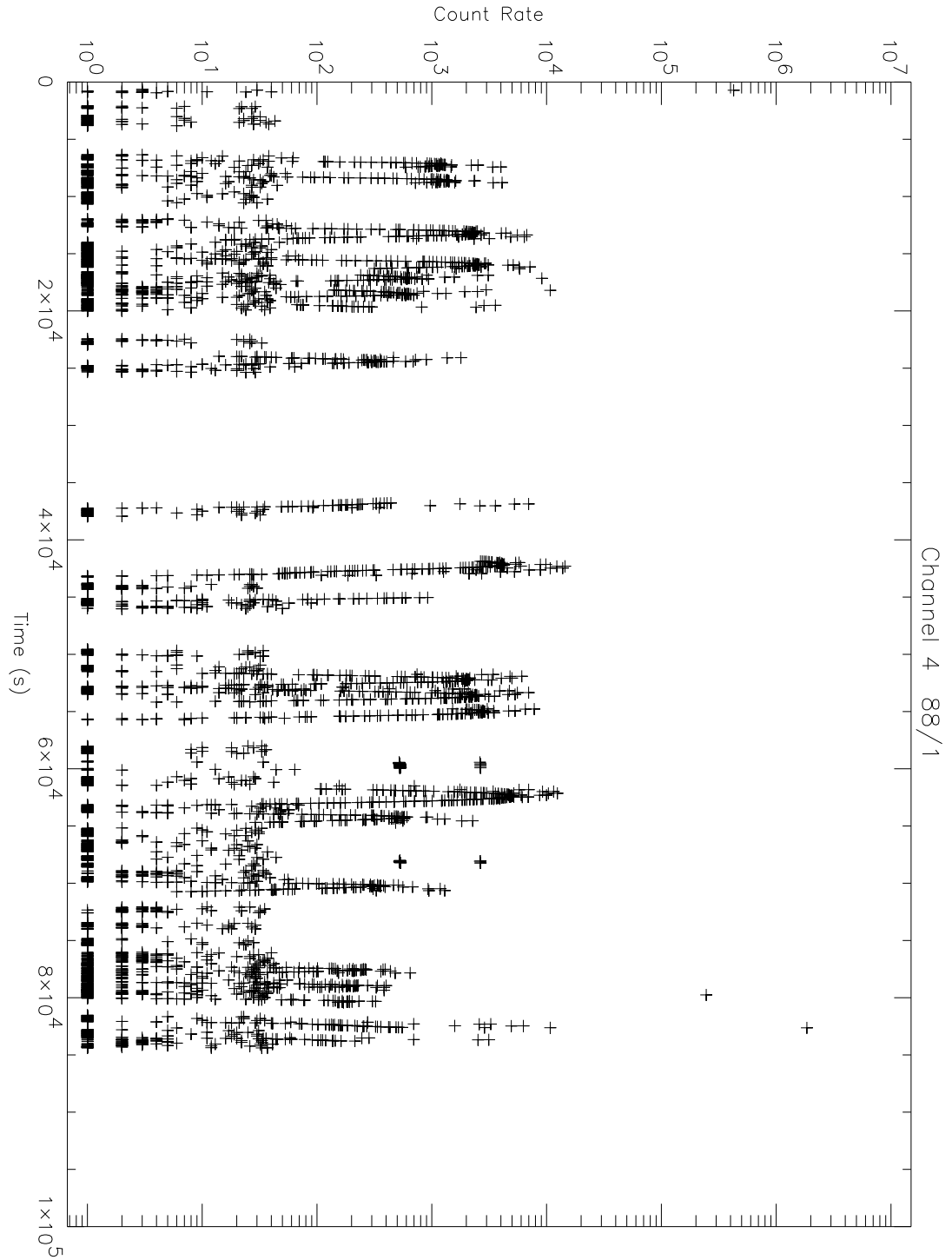


Figure 2.1. Sample of the raw EI-88/1 channel 4 count rates in data file TAPE4.DAT

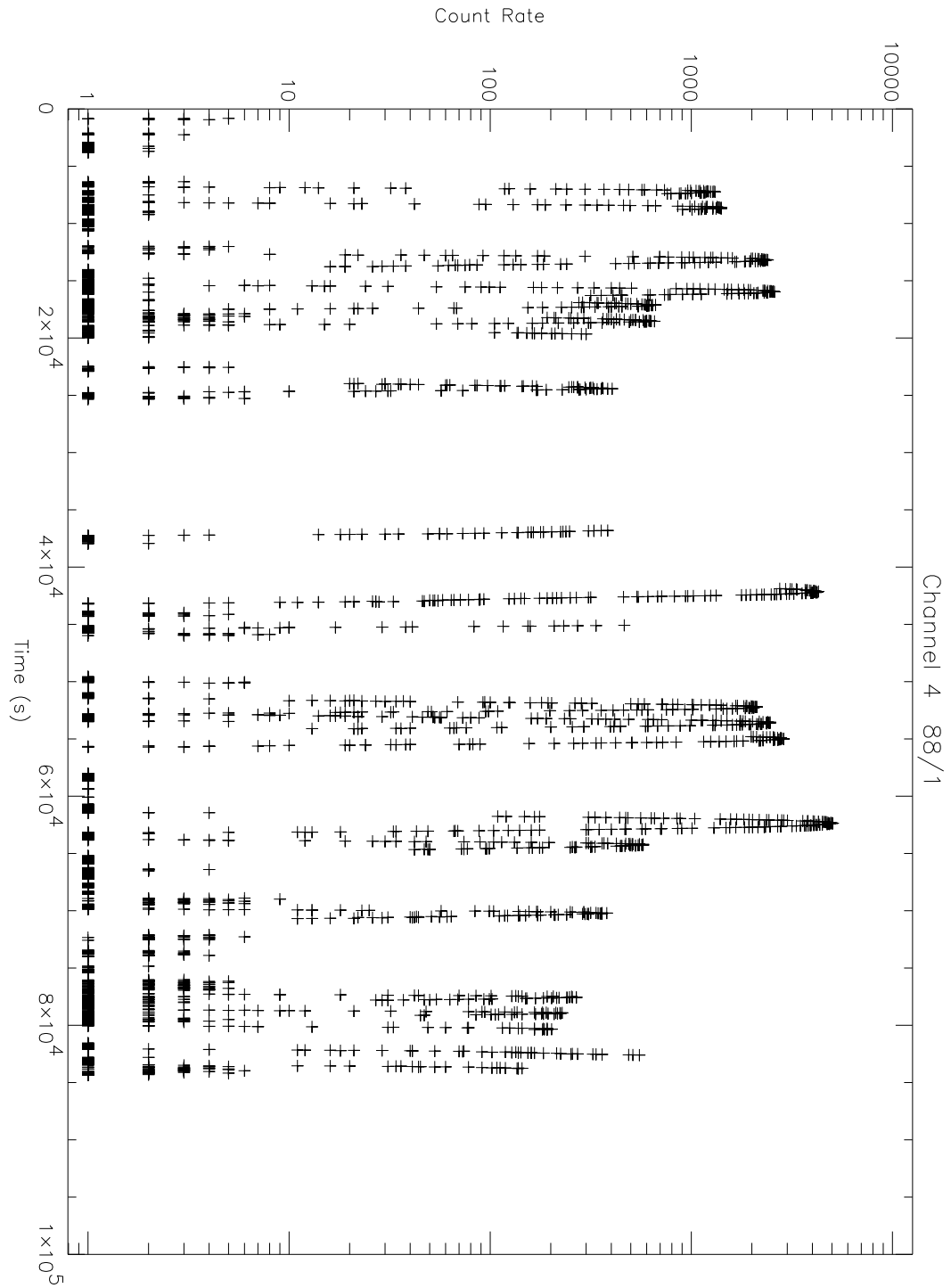


Figure 2.2. Sample of the EI-88/1 channel 4 count rates in data file TAPE4.DAT after running the cleaning programme

2.2.1.2 Quality flag

Data records with quality flag (word 2) equal to two are of bad quality (or don't contain data) and can be safely rejected.

2.2.1.3 Pitch angle not defined

A value -7.0 for the angle between the satellite axis and **B** (word 23) indicates a problem with the magnetometer data. These data records are rejected.

2.2.1.4 Mixed mode records

The modes of operation of EI-88 alternate in a fixed sequence of a period of 16 formats (10 s each): 14 formats designated with 0 are followed by 2 formats designated 1. The first format with a 1 and the first format with a 0 are a mixture of coincidence and single rates and can therefore not be used. For the final data base all records with a 1 in word 68 or 70 were rejected, as well as the first record with a 0. The combined rejection criterion is that each record is rejected for which word 68 differs from word 68 in the previous record, or for which word 70 differs from word 68 in the previous record. The first record in every data file is rejected as well.

2.2.1.5 Satellite conditions

The operational conditions of the satellite and instruments are recorded in the housekeeping records 67–81. Data records for which the actual values of the following parameters deviate too much from the average (over the whole data file, except for the records already flagged as suspect) value of the parameter are flagged, for each EI-88 detector separately: detector current, temperature, photomultiplier current, and 16 V voltage. If the record is flagged, the count rates for the corresponding detector are set to -1 . On visual inspection of the time evolution of the individual data points, it was found that the record preceding a record with deviating conditions was very often erroneous as well. Therefore, the records preceding (while checking that there are no gaps in the telemetry) bad condition records are flagged as well.

2.2.1.6 Deviation from neighbouring values

The above “cleaning” criteria are able to identify most of the measurements that are invalid because of instrumental or telemetric effects. However, after a detailed inspection of time plots and listings of the cleaned data, some spurious data were still found. We did not find a criterion to identify these deviating points unambiguously, and decided on another scheme to remove them: after applying all the above criteria, each count rate (for each channel and detector separately) is compared to the average of the preceding and succeeding count rate. If the middle count rate is more than a factor five (a value of five turned out to be a good compromise between

not rejecting too many data points and not rejecting enough spurious points) above the average count rate, it is set to -1 . In the CLEANnn.LOG files, these points are identified as “remaining suspects”. On average, there are about a few dozen per channel and per data file.

2.2.1.7 Abnormally high values

After applying the selection criteria described above, a small number of data points still deviate from the surrounding points (in contrast to “neighbouring points”, by “surrounding points” are meant points separated from a given point by at least two ten-second interval) when plotted as a function of time, in the sense that these suspect points have count rates in one or more detectors that are much higher (up to two orders of magnitude) than those of the neighbouring points. We inspected time plots of all the data, for each detector separately, and identified the remaining suspect data points by eye. Since there are only very few of these points (a few dozen over the whole data base) and they deviate clearly from the neighbouring points, we feel confident in eliminating them. Also, the averages and standard deviations of the data after removing these points improve substantially. “Removing a point” in this context means that the count rate of the specific detector channel is set to -1 .

Chapter 3

Model construction

In order to construct flux maps, count rates have to be converted to physical units (fluxes) and averaged over two dimensional coordinate grids. The conversion to fluxes is an iterative process because of the finite aperture of the detectors, i.e. the true unidirectional flux has to be derived from the measured count rate in successive approximations, which procedure is described in Sects. 3.1–3.3. In Sect. 3.4 the binning procedure and model construction is outlined.

3.1 Conversion to fluxes

The description of geometric factor and directional response in this section is based on a paper by Sullivan (1971).

3.1.1 General formulation

The coincidence counting rate of any particle telescope depends upon the effective dimensions and positions of the telescope sensors as well as on the sensor efficiencies. For an ideal telescope—whose efficiency for detecting particles of a given type is one in a given energy interval and zero otherwise and whose sensors are mathematical surfaces with no thickness—the factor of proportionality relating the counting rate C to the integral directional particle flux J is defined as the gathering power Γ of the telescope. When the flux is isotropic, i.e. $J = J_0$, the factor of proportionality is called the geometric factor G :

$$C = G J_0 . \quad (3.1)$$

Exact expressions can be obtained for the geometric factor and directional response of cylindrically symmetric telescopes.

The coincidence counting rate of a particle telescope can be expressed as:

$$C(\mathbf{x}, t_0) = \frac{1}{T} \int_{t_0}^{t_0+T} dt \int_S \mathbf{r} \cdot d\sigma \int_{\Omega} d\omega \int_0^{\infty} dE \sum_i \varepsilon_i(E, \sigma, \omega, t) j_i(E, \omega, t) , \quad (3.2)$$

where

C	=	coincidence counting rate (s^{-1}),
\mathbf{x}	=	position vector of the telescope
i	=	label for type of particle,
j_i	=	differential directional flux of particle type i ($\text{s}^{-1}\text{cm}^{-2}\text{sr}^{-1}\text{MeV}^{-1}$),
ε_i	=	detection efficiency for particle type i ,
t	=	time,
t_0	=	time at start of observation,
T	=	total observation time,
$d\sigma$	=	element of surface area of the last sensor to be penetrated,
S	=	total area of the last telescope sensor,
\mathbf{r}	=	unit vector specified by spherical coordinates (θ, ϕ) ,
$d\omega = -d\phi d\cos\theta$	=	element of solid angle around \mathbf{r} ,
Ω	=	domain of Ω defined by the other telescope sensors,
$\mathbf{r} \cdot d\sigma$	=	effective element of area looking into ω .

Equation (3.2) expresses the requirements for the detection of a particle. Although it is quite general, the following implicit assumptions have been made:

1. $d\sigma$, ω , and \mathbf{x} are time independent;
2. no transformation of particle type occurs other than that included in ε_i ;
3. the particle trajectory is a straight line.

Dropping these assumptions severely complicates the treatment of the problem and renders an analytic solution difficult. The first assumption may not be valid for a rapidly spinning satellite and/or long accumulation times.

To simplify the problem further, we consider only ideal telescopes where the efficiency is independent of ω , σ and t , and consider only one particle type (henceforth, we will drop the subscript denoting particle type).

With the assumption that j is independent of t and separates into

$$j(E, \omega) = j_0(E) F(\omega), \quad (3.3)$$

where $F(\omega)$ is normalised so that $\int F(\omega) d\omega = 1$, Eq. (3.2) becomes

$$C = \left[\int_{\Omega} d\omega \int_S F(\omega) \mathbf{r} \cdot d\sigma \right] J \equiv \Gamma_F J, \quad (3.4)$$

where

$$J = \int_0^\infty j_0(E) \varepsilon(E) dE. \quad (3.5)$$

In the case of a detector with well defined energy channels with uniform response

$$\varepsilon_1 = \begin{cases} 1, & E_l \leq E \leq E_u, \\ 0, & E < E_l, E > E_u, \end{cases} \quad (3.6)$$

J is given by

$$J = \int_{E_l}^{E_u} j_0(E) dE, \quad (3.7)$$

which, for small energy ranges, can be approximated by

$$J = j_0[(E_l + E_u)/2] (E_u - E_l). \quad (3.8)$$

The expression in square brackets in Eq. (3.4) is the gathering power Γ_F of the telescope when the intensity has an angular dependence given by $F(\omega)$, i.e.

$$\Gamma_F = \int_{\Omega} d\omega \int_S F(\omega) \mathbf{r} \cdot d\sigma = \int_{\Omega} F(\omega) d\omega \int_S \mathbf{r} \cdot d\sigma. \quad (3.9)$$

The directional response function $R(\omega)$ of a telescope can be defined as:

$$R(\omega) = \int_S \mathbf{r} \cdot d\sigma. \quad (3.10)$$

For a telescope with cylindrical symmetry the effective area h is related to R as:

$$h(\theta) \cos \theta = \int_S \mathbf{r} \cdot d\sigma. \quad (3.11)$$

With this definition Eq. (3.9) can be rewritten as

$$\Gamma_F = \int_0^{2\pi} \int_0^{\theta_1} F(\theta, \phi) h(\theta) \cos \theta \sin \theta d\theta d\phi, \quad (3.12)$$

where θ_1 is the telescope opening half angle. If the flux is isotropic then F is unity and the geometric factor (the gathering power for isotropic flux) depends only on the geometry of the telescope, i.e.:

$$G = \Gamma_1 = 2\pi \int_0^{\theta_1} h(\theta) \cos \theta \sin \theta d\theta. \quad (3.13)$$

3.1.2 Single element telescope

For an ideal telescope consisting of a single planar detector without shielding, $h(\theta) = A$ with A the surface area of the detector, so that the geometric factor is given by

$$G = 2\pi A \int_0^1 (-\cos \theta) d(\cos \theta) = \pi A. \quad (3.14)$$

If particles are incident from both sides then the detector area is doubled, and

$$G = 2\pi A. \quad (3.15)$$

The gathering power and effective area are also easily evaluated from Eqs. (3.9) and (3.11). A single detector embedded in a viewing cone with opening angle smaller than π can be treated as the lower detector of a two-element telescope in which the respective surfaces of both detectors and their separation define the same solid angle as the viewing cone of the single detector.

3.1.3 Multi-element telescope

For a multi-element telescope with cylindrical symmetry, the effective area can be written in an analytical form, although the derivation becomes tedious for more than two detectors. The gathering power and geometric factor can be determined by integration, which may involve elliptical integrals depending on the form of the angular dependence F of the intensity.

For complex geometries a numerical approximation usually is easier than the analytical approach. This technique involves numerical integration of the effective area taking into account the path of an incoming particle through a mathematical description of the detector plates.

3.2 Geometric factor correction

The quantity typically measured by a particle telescope is the number of incoming particles N over the accumulation period T , in the solid angle Ω defined by the telescope configuration and centered around a direction \mathbf{r} , in the energy interval $[E_l, E_u]$ defined by the detector response. The physical quantity that the telescope aims to measure is the differential directional particle flux j .

In general, the trapped particle flux measured by a telescope differs from the true flux because of the finite opening angles of these instruments. A zero-order approximation of the true flux is given by:

$$j^{(0)}(E) = \frac{1}{G} \frac{N}{T} \frac{1}{E_u - E_l}, \quad (3.16)$$

where G is the nominal geometric factor of the detector element and E represents the reference value of the energy interval $[E_l, E_u]$.

The measured flux can be corrected by an iterative procedure:

1. The first step consists of averaging the zero-order fluxes given by Eq. (3.16) over an (E, L, α_0) grid, using the averages of the uncorrected measured flux as the zero-order approximation $j^{(0)}$. This is equivalent to assuming that the ambient flux is isotropic.
2. For step i , evaluate the gathering power Γ_F [Eq. (3.12)] for each measurement (and for each energy channel), using the pitch angle dependence of the last iteration $j^{(i-1)}$.

3. For each measurement (and energy), integrate the zero-order flux (using the bin averaged $j^{(0)}$) over the telescope opening angle using Eqs. (3.12) and (3.4); compute the ratio of this integrated flux defined to $j^{(0)}$ corresponding to the (E, L, α_0) value for each measurement, and multiply the measured flux by this ratio.
4. Re-bin the measured fluxes, applying the correction factor from step 3. The new bin averages constitute the i^{th} order approximation $j^{(i)}$ of the true flux.
5. Repeat from step 2 until convergence is reached. One step should be sufficient.

This procedure ignores the dependence of the flux on azimuth. This approximation is reasonable when the measurements used for the flux averages were taken over the full azimuth range $[0^\circ, 360^\circ]$. Taking into account both pitch angle and azimuth dependence would significantly increase the complexity of the procedure, which is already very demanding in calculation time.

The gathering power [Eq. (3.12)] is determined by integrating the effective area function h over the telescope opening, whereby the flux dependence on α_0 of the previous iteration is used for $F(\theta)$ (we have ignored the dependence of the flux on ϕ). The integration is carried out in the variable θ , the off-axis angle, and the azimuthal angle ϕ measured in the plane perpendicular to the telescope axis. For a measurement point P and a local pitch angle α (corresponding to the pitch angle of the detector axis), the drift shell coordinates (B_m, L) can be evaluated with BLXTRA. The corresponding equatorial pitch angle α_0 is given by

$$\alpha_0 = \arcsin \left(\sqrt{\frac{B_0}{B_m}} \right), \quad (3.17)$$

with

$$B_0 \equiv \frac{0.311653}{L^3}. \quad (3.18)$$

The flux seen by the detector then is

$$j(E, L, \alpha_0) = \int_0^{2\pi} d\phi \int_0^{\theta_1} j^{(0)}[E, L, \alpha'(\theta, \phi)] h(\theta) \cos \theta \sin \theta d\theta, \quad (3.19)$$

where α' is the local pitch angle corresponding to the off-axis angle θ and the azimuthal angle ϕ . $\alpha'(\theta, \phi)$ is given by:

$$\cos \alpha' = \cos \alpha \cos \theta - \sin \alpha \sin \theta \cos \phi. \quad (3.20)$$

A set of IDL routines has been written to carry out the integration in Eq. (3.20) using Gauss quadrature. These routines are contained in the file FOVAPP.PRO.

Table 3.1. Geometric factors and surface areas of the EI-88 sensors [from Häusler (1972)]

Channel	G (cm ² sr)	A (cm ²)	G (cm ² sr)	A (cm ²)
		EI-88/1		
			EI-88/2	
1–5	0.0580	0.1817	0.0595	0.1864
6	0.0612	0.1917	0.0628	0.1967
7	0.0772	0.2418	0.0792	0.2481

3.3 Application to the EI-88 telescopes

The cone shape of the EI-88 detector stacks (see Fig. 1.4) ensures that lower-lying sensors are not obscured by the sensors above them. Therefore, for an ideal detector of this type each sensor should have the same effective area. Plots of the effective areas for different particle energies are shown for the various sensors in Häusler (1972, Figs. 8–10). Figure 8 in Achtermann et al. (1970)—reproduced in Fig. 3.1—shows the analytically derived effective area function that only depends on the detector geometry, and thus is valid (in the ideal case) for each sensor. Figure 10 in Achtermann et al. (1970) shows the measured effective area for 8 MeV protons in channel 4, which corresponds closely to the analytical effective area. From measurements in a particle beam the authors conclude that for the first five channels the effective area is not dependent on energy. However, particles with higher energies (from about 34 MeV on) can penetrate the edge of the telescope shielding and part of the scintillator, and thus cause an enlargement of the geometric factor for channels 6 and 7. Häusler (1972) lists the geometric factors for the respective channels (see Table 3.1).

In the analysis of the AZUR data, we use the functional dependence shown in Fig. 3.1. The documentation does not specify the analytical function used, but we found that the following function accurately reproduces the dependence in Fig. 3.1:

$$h(\theta) = \begin{cases} A \cos \theta & \theta < \theta_1 \\ A \frac{\cos \theta_1}{\theta_2 - \theta_1} (\theta_2 - \theta) & \theta_1 \leq \theta < \theta_2 \\ 0 & \theta_2 \leq \theta \end{cases} \quad (3.21)$$

where $\theta_1 = 15.6^\circ$ and $\theta_2 = 21.9^\circ$ [the angles are expressed in rad in Eq. (3.21)]. This functional dependence is represented in Fig. 3.2. For each channel, the detector surface A is chosen so that the integration of $h(\theta) \cos \theta$ [see Eq. (3.13)] over the solid angle subtended by the telescope yields the geometric factors listed in Table 3.1 (the geometric factors of EI-88/2 are slightly larger than those of EI-88/1 due to small differences in the telescope mountings).

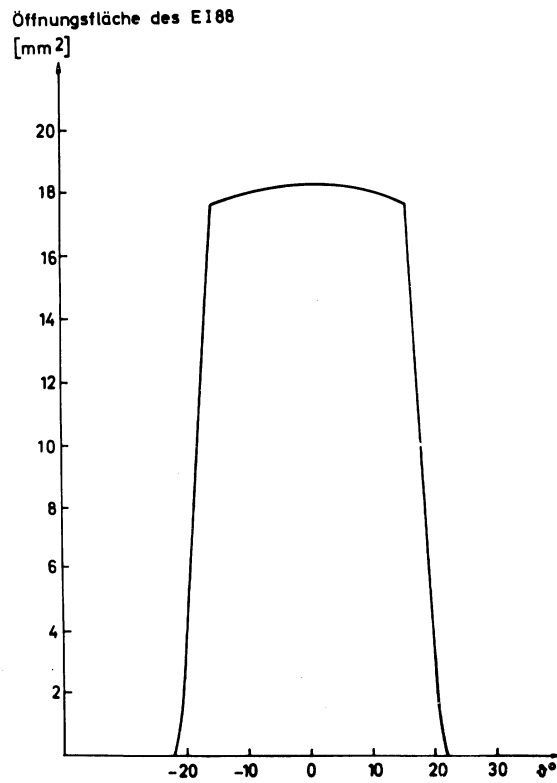


Figure 3.1. Measured effective area for the EI-88 detectors [from Achtermann et al. (1970)]

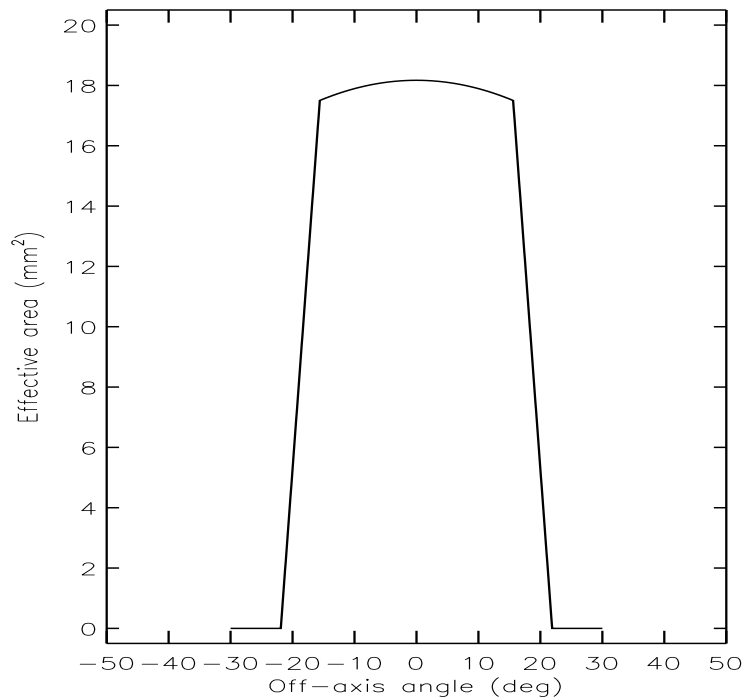


Figure 3.2. Effective area for the EI-88 detectors approximated by the analytical function described in the text

3.4 Model building

Building a flux model or flux map from the AZUR data set (or any other data set) consists of three steps:

1. data binning: averaging the measured fluxes over an (E, L, α_0) grid;
2. correction of the averages for telescope and detector characteristics;
3. creation of the final flux map—including conversion to integral fluxes—and integration of the map into UNIRAD.

The model developed for this study is for protons only, the α particle data have not been used. From here on, the channel numbers refer to proton channels only, i.e. channel two now mean proton channel two (channel 3 in Table 1.3) etc.

3.4.1 Data binning

The data binning consists of averaging the count rates over a three-dimensional coordinate grid. The first coordinate is the AZUR proton channel number (1–6), the second coordinate is L , and the third coordinate is one of the following: α_0 , B , B/B_0 , φ , or n_S . The angle φ was introduced by Daly & Evans (1993) as a means of improving the interpolation in the AP-8 flux maps and is defined as

$$\varphi = \arcsin\left(\frac{B - B_0}{B_c - B_0}\right), \quad (3.22)$$

where B_c is the magnetic field strength at the atmospheric cut-off, for which we used the expression

$$\frac{B_c}{B_0} = 0.65 L^{3.642} \quad (3.23)$$

(Vette 1991a). n_S is the average of the atmospheric density, weighted with the energy-dependent cross sections of collisions with atmospheric constituents, over the drift path of trapped particles (Heynderickx et al. 1995, 1996c).

The values of L and B are calculated for each point in the CLEANnn.DAT files with the Fortran programme BL.FOR which uses the BLXTRA software routines. The outputs consist of:

1. B at the point of measurement;
2. L for the pitch angle corresponding to the orientation of EI-88/1 (close to perpendicular to the magnetic field vector);
3. L for the pitch angle corresponding to the orientation of EI-88/2 (at an angle of about 45° to the magnetic field vector);

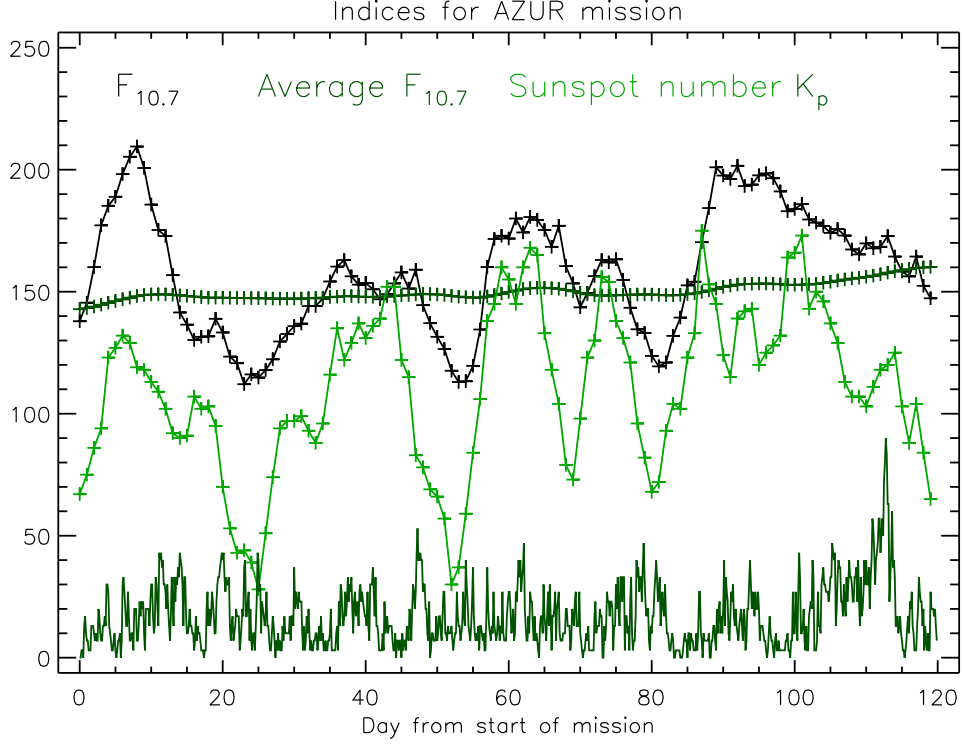


Figure 3.3. $F_{10.7}$, $F_{10.7A}$, R_Z , and K_p for the duration of the AZUR mission. $F_{10.7A}$ is the three-month average of $F_{10.7}$.

These values are written to the ASCII files `BLnn.DAT`. The (B, L) values were calculated with the geomagnetic field model GSFC 12/66 (Cain et al. 1967), extrapolated to epoch 1970.0.

The Fortran programme `AVDENS.FOR` reads the `BLnn.DAT` files, and calculates for each data point the values of:

1. $n_S(E)$ for the mid-point energies of the six proton channels of EI-88/1;
2. the geographic coordinates of the point where the drift shell reaches its minimum altitude;
3. the local average density at the point where the drift shell reaches its minimum altitude;

The calculation is carried out two times per data point, once for each (B, L) pair. The minimum altitudes and the two sets of eight density averages are written to the ASCII files `AVDENSnn.DAT`. The atmosphere models used in this calculation are MSISE-90, IRI-90 and the plasmaspheric extension of Carpenter & Anderson (1992), as specified by Heynderickx et al. (1995).

As the atmospheric density depends on the level of the solar activity through the solar radio flux $F_{10.7}$, we binned the data separately for days when $F_{10.7} \leq 150$ and when $F_{10.7} > 150$ (Fig. 3.3 shows the main indices for the AZUR mission). Due to the short length of the AZUR

mission duration, we did not see any systematic effects of the solar activity on the bin means. Therefore, the final averages were made with all the data.

The binning is carried out by the programme `BINNING.PRO`. It reads the ASCII file `BINLIMS.DAT` which contains the description of the coordinate grids, i.e. the number of intervals for each variable and the interval limits, which do not have to be equidistant. The programme then runs through the `CLEANnn.DAT` files and the corresponding `BLnn.DAT` and `AVDEN-Snn.DAT` files, reads in the respective B , L and n_S values, and calculates for each measurement the values of B/B_0 , α_0 , and φ . Next, the index of the L bin is determined for a data point, as well as the indices of the other coordinate bins. The count rates are accumulated for each energy and coordinate bin separately, as well as the squares of the count rates (in a separate set of bins). The number of values per bin and the accumulated values are written to the binary file `BIN.DAT`, which also contains the number of coordinate bins and the interval limits of the bins.

The bin averages written to the file `BIN.DAT` are based on count rates not corrected for the directional response of the telescope. They serve as the first step in the iterative procedure to correct for the telescope response that is described in Sect. 3.2. The correction is carried out by the IDL programme `DETCOR.PRO`.

3.4.2 Selection of bin sizes

When comparing the distribution of the data over the various coordinate bins (B , B/B_0 , α_0 , φ , n_S as second coordinate), the (L, α_0) and (L, B) grids appeared to be the most adequate. As the equatorial pitch angle always ranges between 0° and 90° , the (L, α_0) bins are rectangular regardless of the L range, which is not the case for the (L, B) . Therefore, we chose the (L, α_0) grid for the final model averages.

The bin limits were chosen so that the measurements are distributed as evenly as possible over the bins. Firstly, a set of L values was selected. The AZUR orbit is such that the magnetic equator is only covered for $L \leq 1.6$. For higher L values, the range of equatorial pitch angles “seen” by the satellite rapidly diminishes with increasing L . Beyond $L = 3$, the coverage is too small to be useful for a radiation belt model, so we limit the model to $L = 3$. The L values chosen as bin limits are listed in Table 3.2.

After selecting the bin limits of the L grid, the whole database was binned in an (L, α_0) grid with equidistant spacing of the α_0 bin limits at 3° . Then, the number of measurements falling in each α_0 bin was summed over the L bins, to obtain the total number of measurements in each α_0 bin. The cumulative number of measurements is shown in Fig. 3.4 as \times symbols, and was fitted by a parabolic curve. Points on this curve which are equidistant in ordinate define a series of α_0 values. We have set the number of α_0 bins to 50, and derived the α_0 values corresponding to 50 equidistant intervals in cumulative number of measurements. The resulting values are the bin limits for a new α_0 grid, which is superimposed on Fig. 3.4, and listed in Table 3.2. In order to close the grid, the values 0° and 90° were added.

The database was then rebinned over the new (L, α_0) grid. The distribution of the measure-

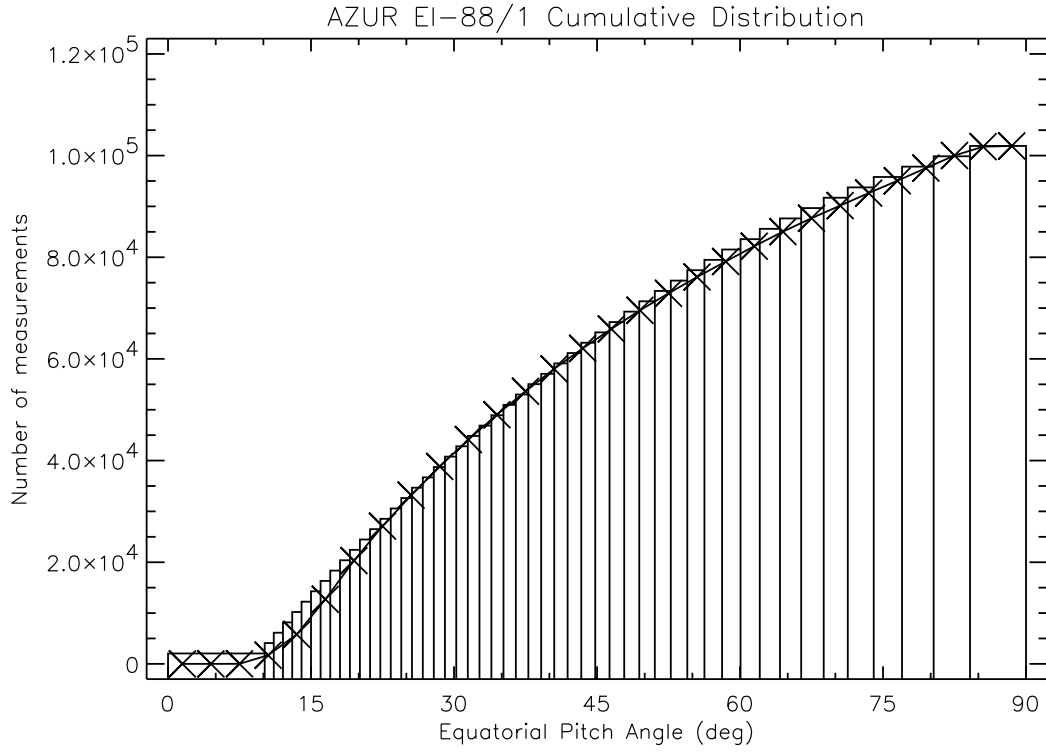


Figure 3.4. Cumulative distribution of AZUR EI-88/1 measurements in α_0 bins. The symbols \times represent evenly spaced bins of width 3° , while the final bins are represented in histogram style.

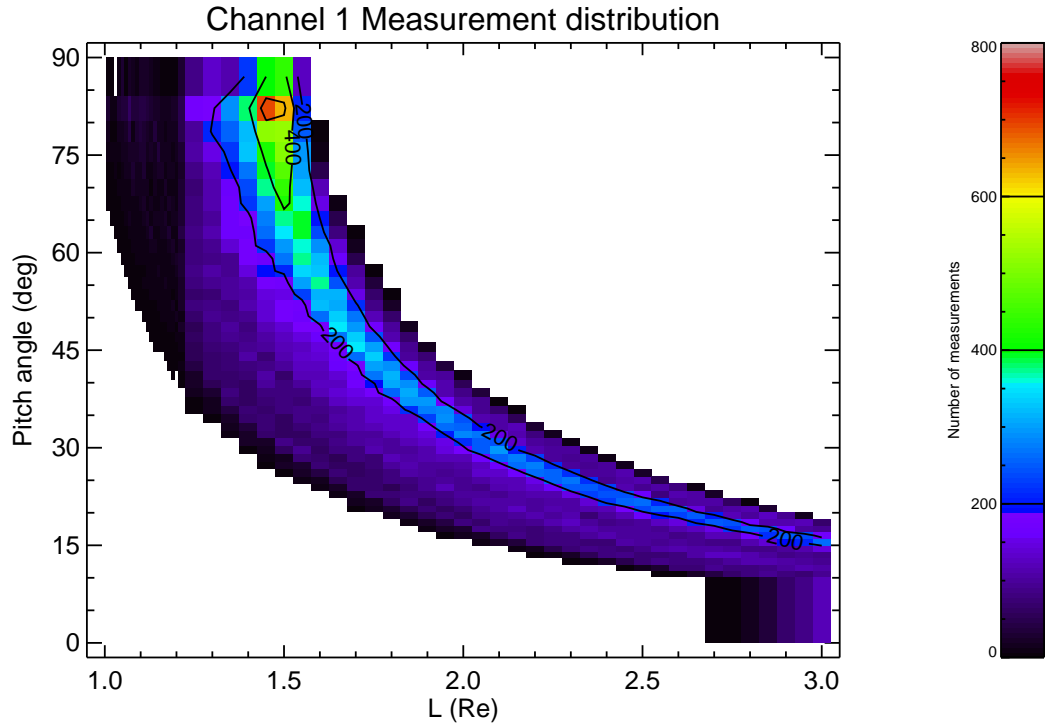


Figure 3.5. (L, α_0) Map of the number of measurements for channel 1

Table 3.2. (E, L, α_0) Bin limits for the PAB97 model grid

E Limits (MeV)	L Limits (R_E)	α_0 Limits (deg)
1.5	1.005	0.0000
2.7	1.015	10.1397
5.2	1.025	11.0914
10.4	1.035	12.0522
22.0	1.045	13.0235
48.8	1.055	14.0045
104.0	1.065	14.9966
	1.075	15.9996
	1.085	17.0134
	1.095	18.0394
	1.105	19.0770
	1.115	20.1277
	1.125	21.1908
	1.135	22.2679
	1.145	23.3591
	1.155	24.4643
	1.165	25.5853
	1.175	26.7215
	1.185	27.8749
	1.195	29.0455
	1.205	30.2336
	1.225	31.4412
	1.275	32.6680
	1.325	33.9164
	1.375	35.1861
	1.425	36.4796
	1.475	37.7977
	1.525	39.1410
	1.575	40.5126
	1.625	41.9128
	1.675	43.3450
	1.725	44.8099
	1.775	46.3115
	1.825	47.8518
	1.875	49.4333
	1.925	51.0610
	1.975	52.7376
	2.025	54.4695
	2.075	56.2616
	2.125	58.1198
	2.175	60.0540
	2.225	62.0722
	2.275	64.1886
	2.375	66.4169
	2.425	68.7793
	2.475	71.3020
	2.525	74.0215
	2.575	76.9961
	2.625	80.3106
	2.675	84.1227
	2.725	90.0000
	2.775	
	2.825	
	2.875	
	2.925	
	2.975	
	3.025	

ments in channel 1 over the (L, α_0) map is shown in Fig. 3.5.

3.4.3 Correction for telescope field of view

The IDL programme `MODEL.PRO` reads in the flux averages created by `BINNING.PRO` and writes the final flux map `AZUR90.DAT` (we have only treated the EI-88/1 data). Since the AZUR data coverage in (L, α_0) space is not uniform, `MODEL.PRO` extends the equatorial pitch angle dependence where necessary to the equator ($\alpha_0 = 90^\circ$). The extension is achieved by fitting, for each E and L bin, the function

$$j(\alpha_0, B_0) = \begin{cases} K \left(\frac{\sin \alpha_0}{\sqrt{B_0}} - \frac{1}{\sqrt{B_c}} \right) \exp \left[-\beta \left(\frac{\sin \alpha_0}{\sqrt{B_0}} - \frac{1}{\sqrt{B_c}} \right) \right] & \alpha_0 \geq \alpha_{0L} \\ 0 & \alpha_0 \leq \alpha_{0L} \end{cases} \quad (3.24)$$

(Badhwar & Konradi 1990, Heynderickx & Lemaire 1993) to the non-zero fluxes in the bin averages, and replacing zero flux values outside the loss cone with the values obtained with the fit function. When not enough bin averages are different from zero, the fit is replaced by the pitch angle dependence of AP-8 MAX, scaled to the flux value of the bin closest to the equator. The extension of the pitch angle coverage is necessary for the application of Eq. (3.19), as the integration in α_0 can extend beyond the equatorial pitch angle range covered by the measurements. `MODEL.PRO` Also has a feature to replace non-zero flux values with the fit function, which is necessary when a bin average clearly deviates from the surrounding points.

Figures 3.6–3.11 show the uncorrected average fluxes (\square) as a function of α_0 for channels 1 and 6 for detector EI-88/1, for three values of L . Superimposed on the figures are the fluxes obtained by means of Eq. (3.19) (+), and the bin means obtained by averaging the fluxes after one iteration of the correction procedure outlined in Sect. 3.2 (\diamond).

The correction for the telescope opening angle clearly depends on the L value and on the energy channel. The correction is largest where the flux dependence on α_0 is steepest, i.e. for the smallest L values and the lowest energy channels.

The reason we have not included the EI-88/2 measurements in the model, is their limited coverage in (L, α_0) space. In addition, these measurements can not be corrected with the method outlined in Sect. 3.2. To illustrate this point, we have used Eq. (3.19) to calculate the flux seen by EI-88/2 for the cases represented in Figs. 3.6–3.11 and superimposed the resulting values in these figures as dashed lines. The fluxes as seen by EI-88/2 are shifted towards the loss cone with respect to the real flux distribution (for $L = 1.2$, EI/88-2 does not see any flux at all). The correction procedure used for EI-88/1 would result in a correction factor equal to zero for almost all measurements. The difference between the integrated fluxes for the respective telescopes is caused by the different α_0 intervals covered by the two instruments, as shown in Fig. 3.12.

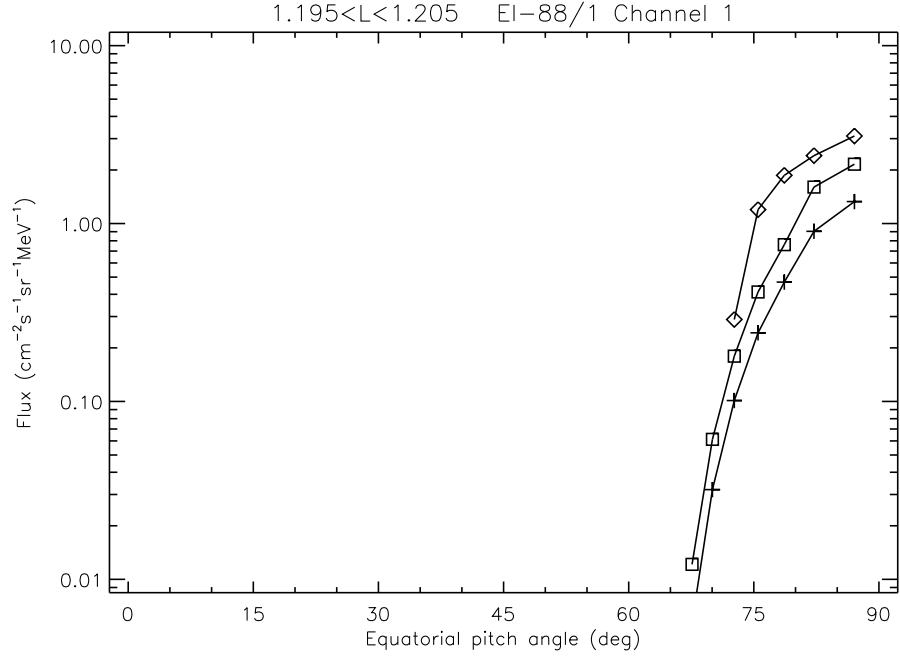


Figure 3.6. Uncorrected flux averages (\square) for EI-88/1 channel 1, $L = 1.2$. The symbols $+$ represent the flux predicted by means of Eq. (3.19), and the symbols \diamond are the corrected bin averages.

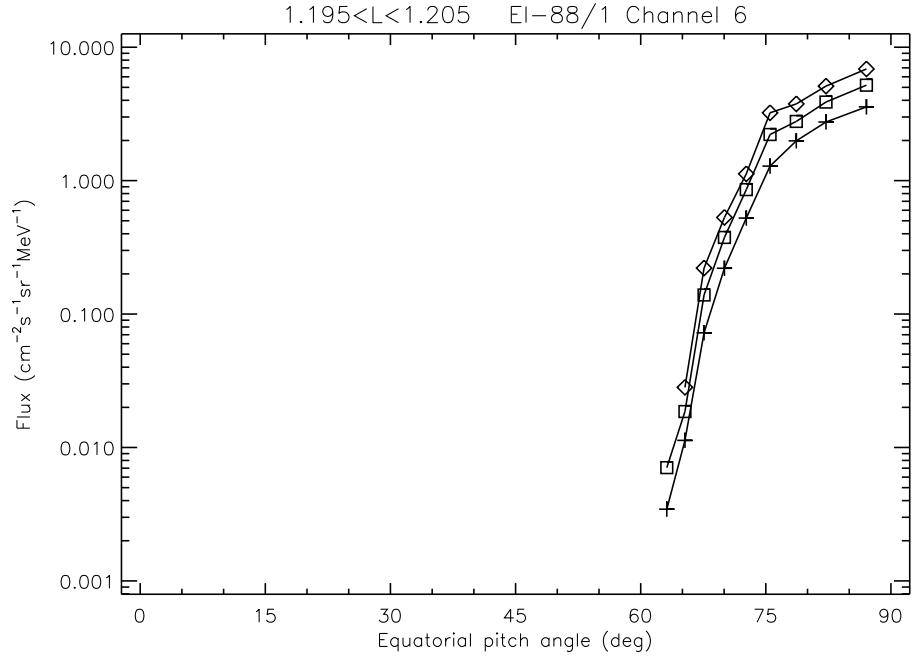


Figure 3.7. Same as Fig. 3.6, for channel 6 and $L = 1.2$

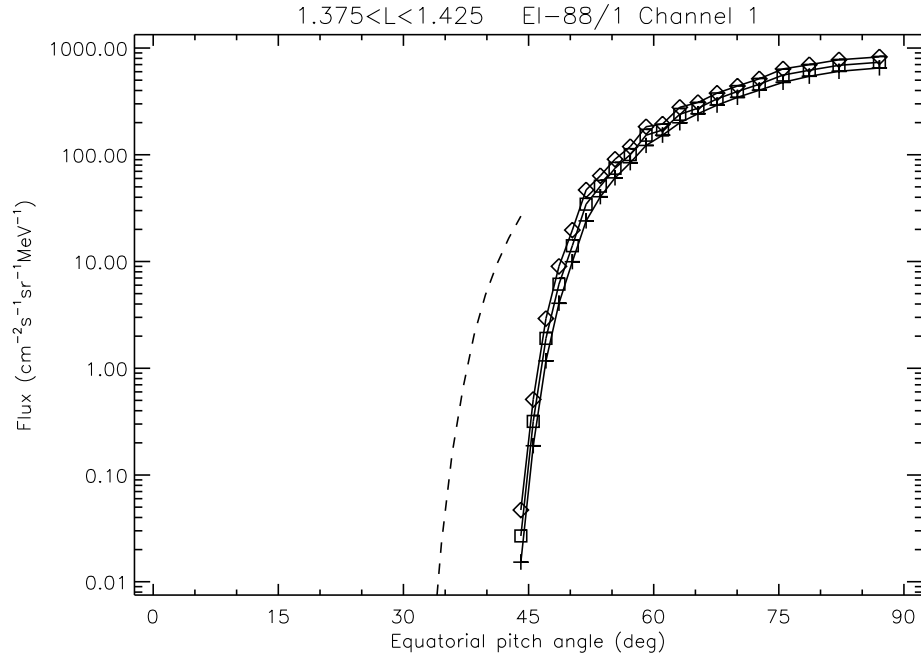


Figure 3.8. Uncorrected flux averages for EI-88/1 (perpendicular to the magnetic field) channel 1, $L = 1.4$. The symbols have the same meaning as in Fig. 3.6. The dashed line represents the flux predicted by means of Eq. (3.19) for detector EI-88/2 (at an angle of 45° to the magnetic field).

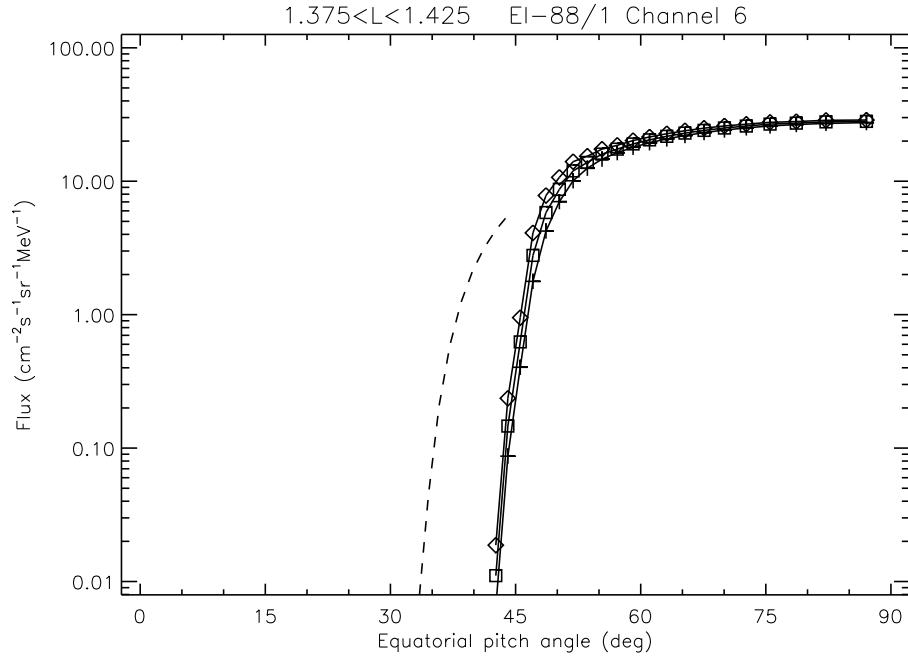


Figure 3.9. Same as Fig. 3.8, for channel 6 and $L = 1.4$

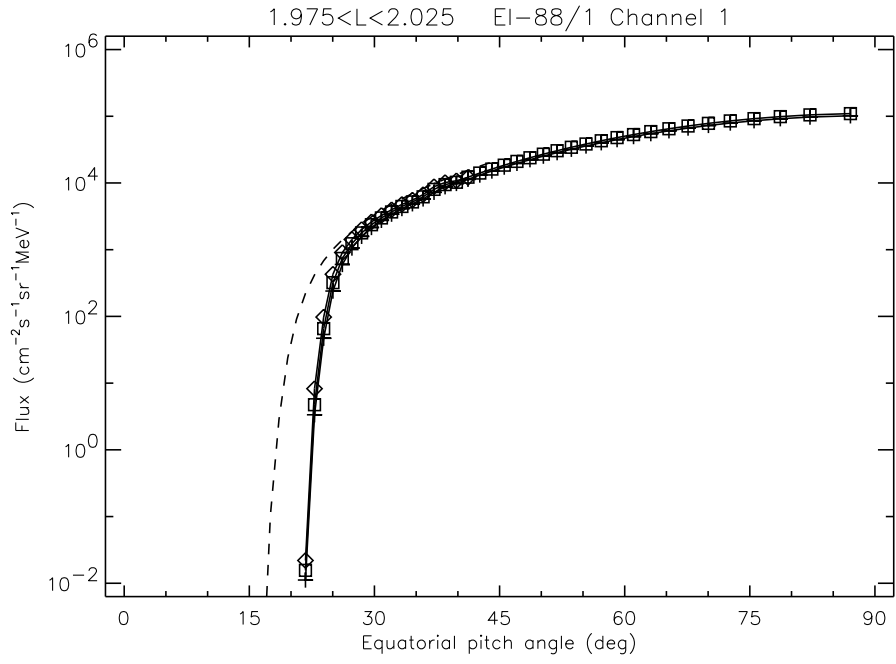


Figure 3.10. Same as Fig. 3.8, for channel 1 and $L = 2.0$

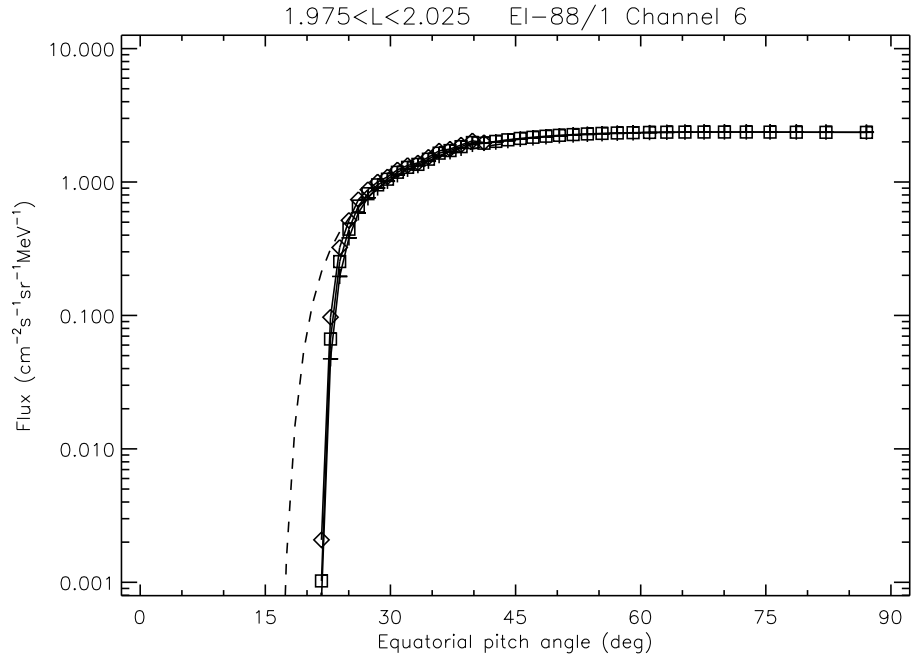


Figure 3.11. Same as Fig. 3.8, for channel 6 and $L = 2.0$

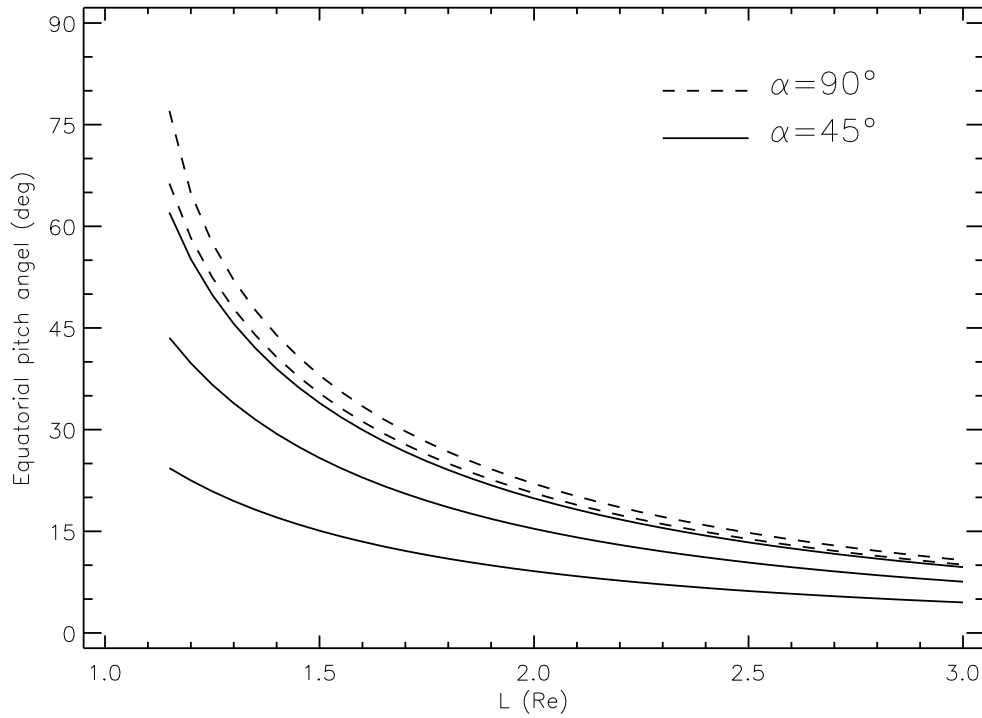


Figure 3.12. Comparison of the equatorial pitch angles subtended by the EI-88/1 and EI-88/2 detectors

3.4.4 Final flux map

The bin averages obtained after one iteration of the procedure outlined above are used to build the final flux map. The α_0 coverage of the final bin averages is not extended toward the equator. Instead, for (L, α_0) bins not covered by the measurements, the flux is set to -1 , so that the software using the model map can exclude the corresponding points. The resulting coverage in (L, α_0) space is illustrated in Figs. 3.13–3.23. The fitting procedure described in Sect. 3.4.3 is applied, however, to correct bin averages that clearly deviate from the pitch angle dependence defined by the other bins (the number of corrections is very small).

The final flux map is then transformed into a BLOCK DATA file by means of the programme MODTOBD.FOR. This programme also transforms differential into integral fluxes. The implementation of the new AZUR model (called PAB97) in UNIRAD is described in Technical Note 10.

3.4.5 Comparison to AP-8

Figures 3.13–3.23 show the flux maps of the PAB97 model in (L, α_0) space, together with the directional AP-8 MAX maps for the same grid values. Figures 3.14–3.24 show the ratios of the AP-8 MAX values to the PAB97 model values. It can be seen that for the lowest L values the PAB97 fluxes are smaller than the corresponding AP-8 MAX fluxes by a factor of about two.

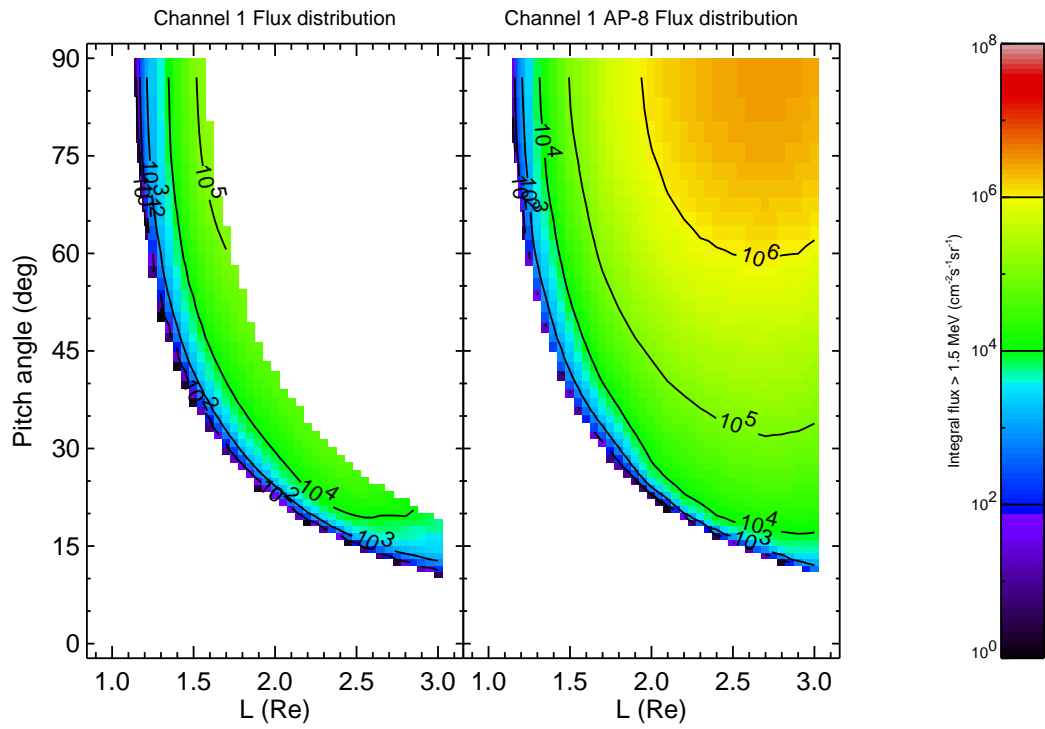


Figure 3.13. (L, α_0) Map of the PAB97 model and AP-8 MAX for channel 1

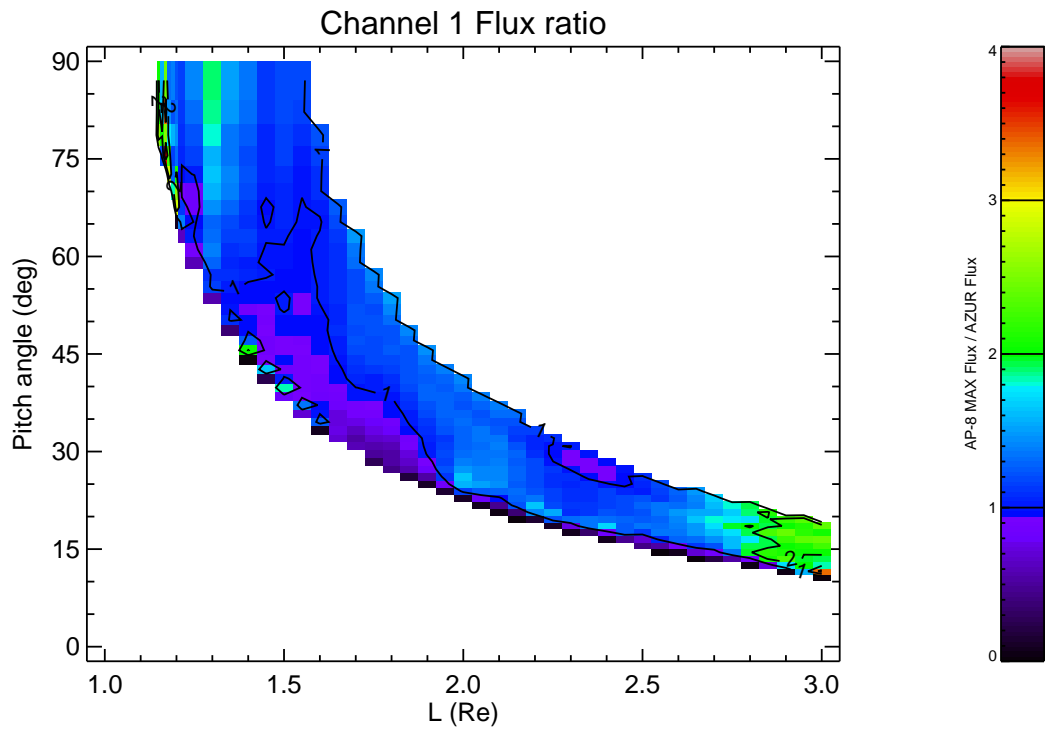


Figure 3.14. (L, α_0) Map of the ratio of AP-8 MAX to the PAB97 model for channel 1

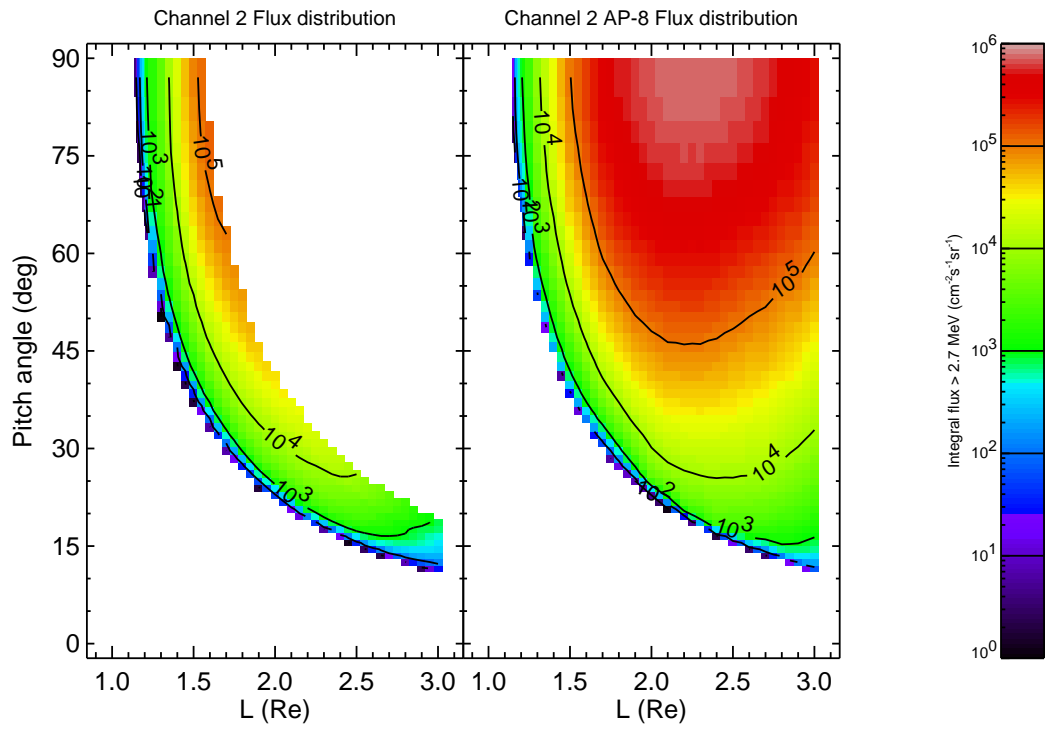


Figure 3.15. (L, α_0) Map of the PAB97 model and AP-8 MAX for channel 2

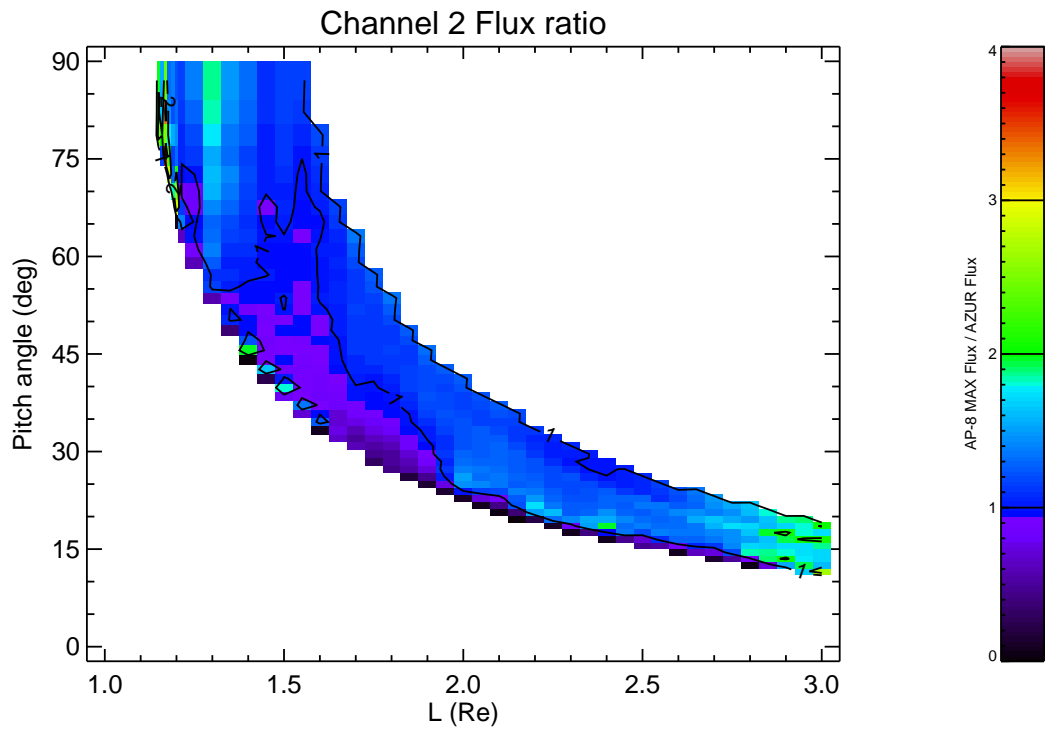


Figure 3.16. (L, α_0) Map of the ratio of AP-8 MAX to the PAB97 model for channel 2

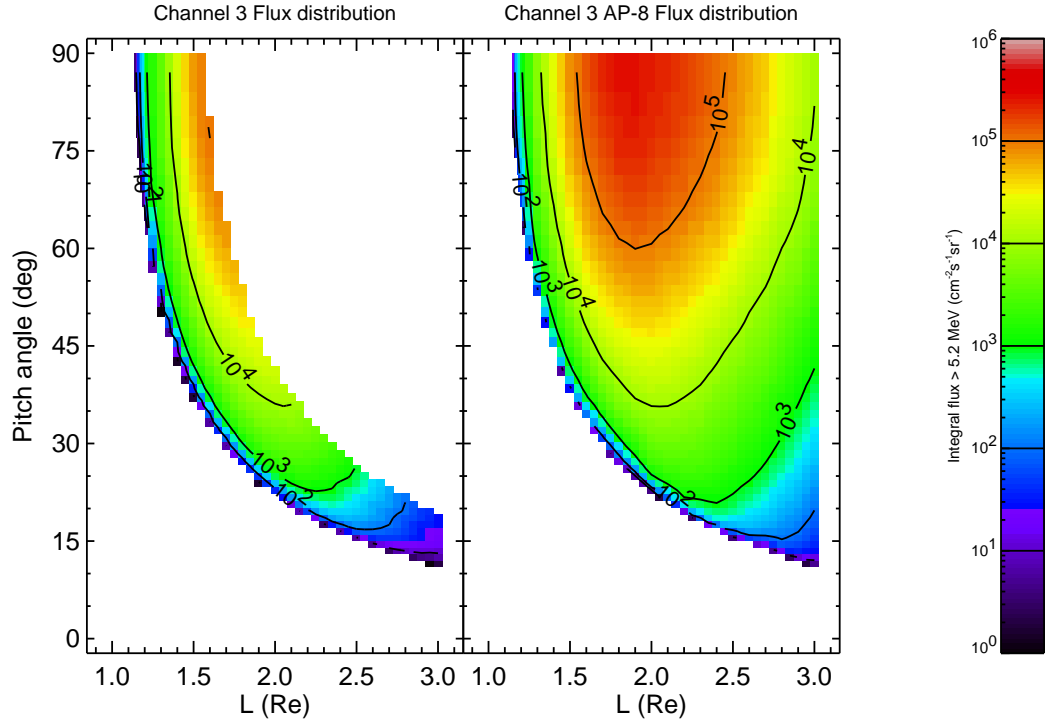


Figure 3.17. (L, α_0) Map of the PAB97 model and AP-8 MAX for channel 3

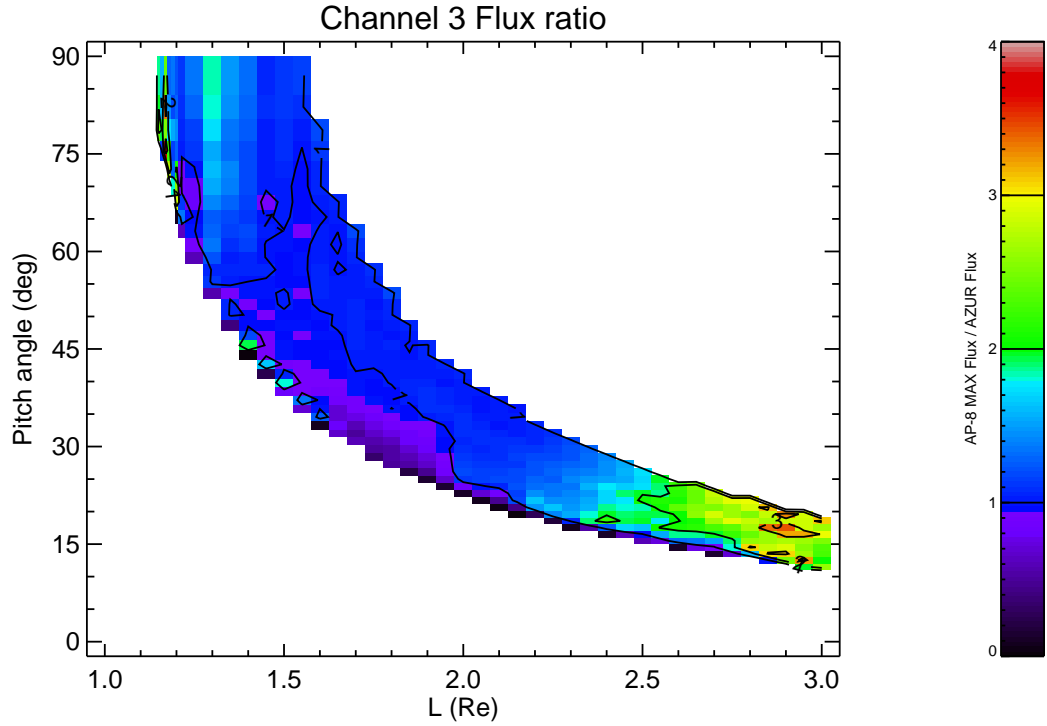


Figure 3.18. (L, α_0) Map of the ratio of AP-8 MAX to the PAB97 model for channel 3

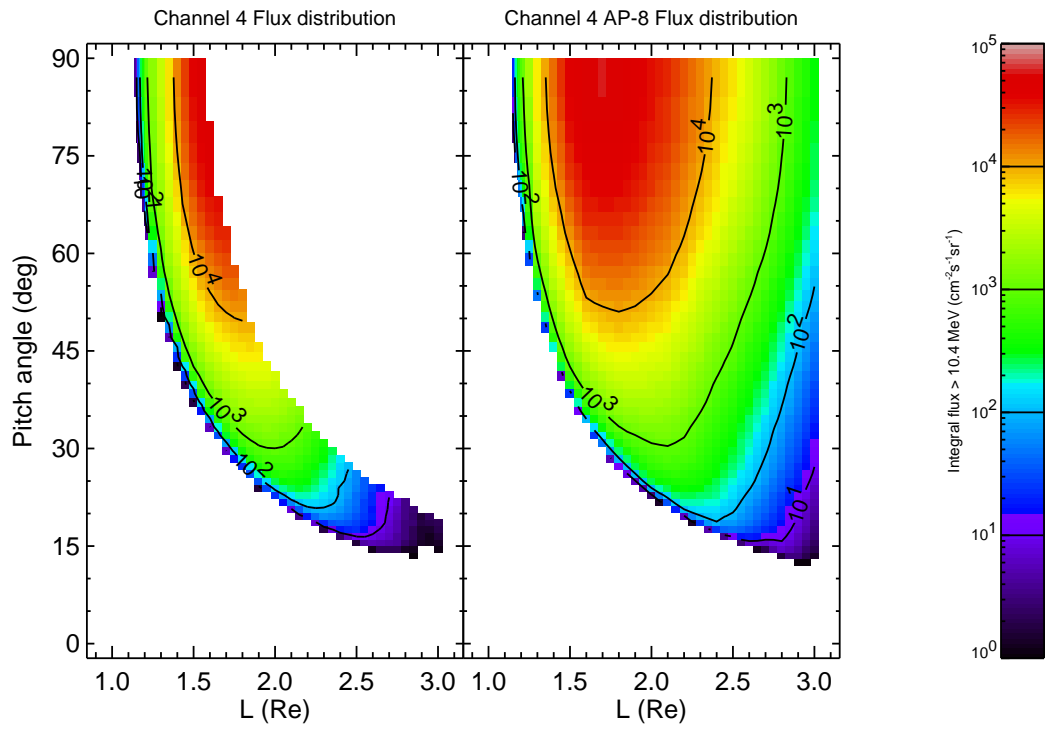


Figure 3.19. (L, α_0) Map of the PAB97 model and AP-8 MAX for channel 4

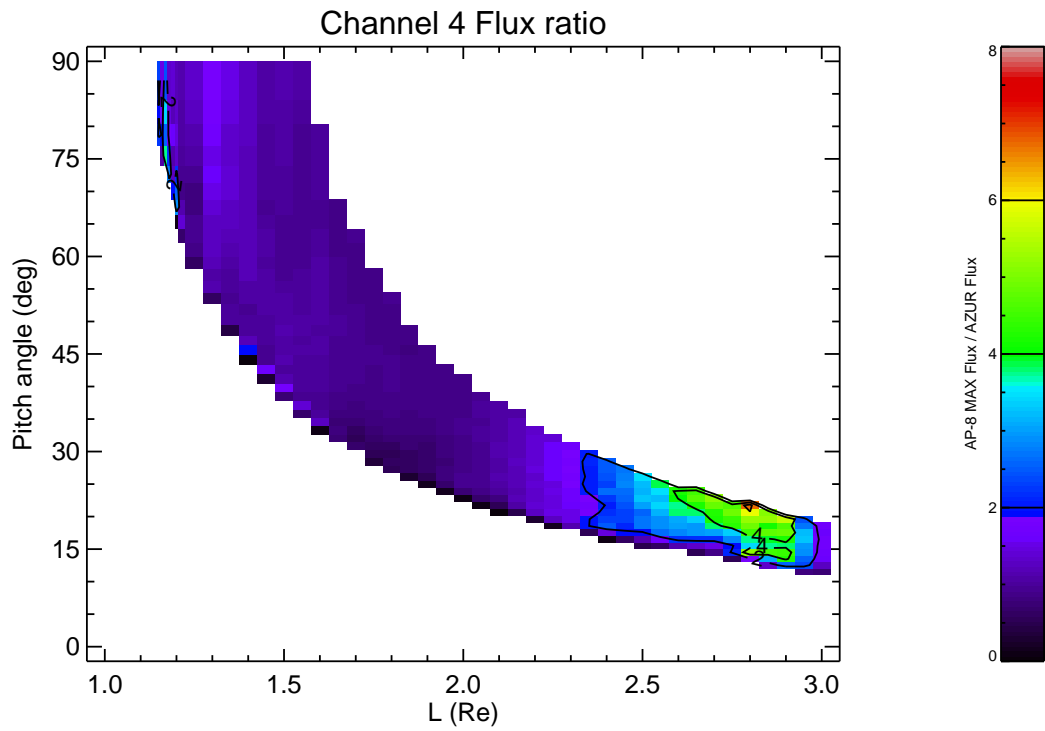


Figure 3.20. (L, α_0) Map of the ratio of AP-8 MAX to the PAB97 model for channel 4

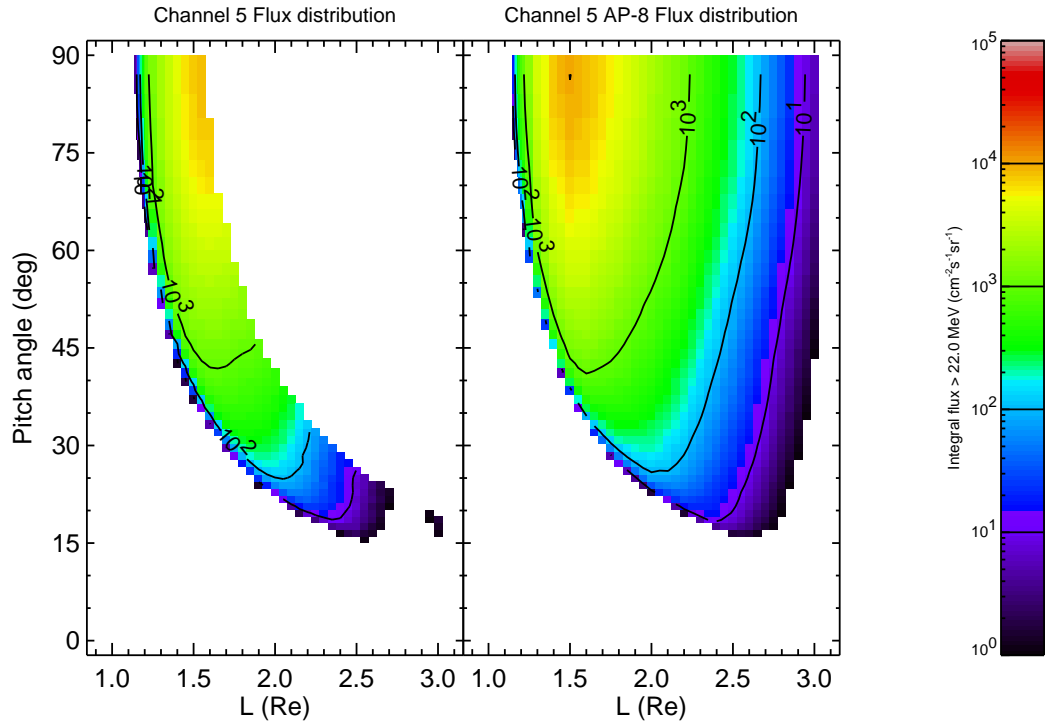


Figure 3.21. (L, α_0) Map of the PAB97 model and AP-8 MAX for channel 5

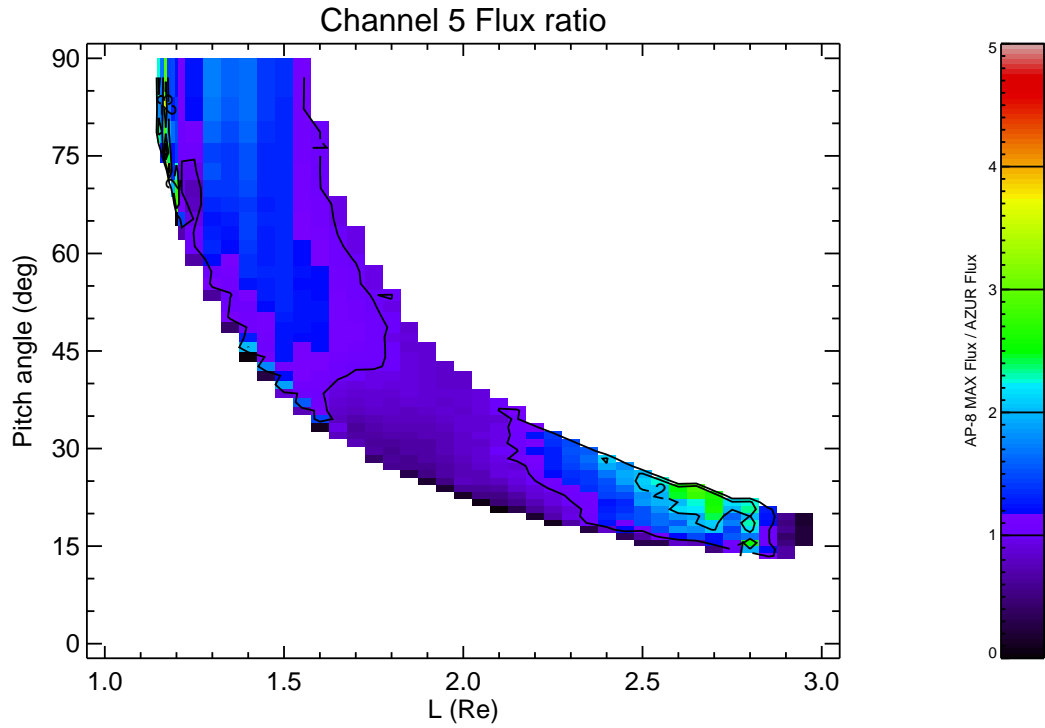


Figure 3.22. (L, α_0) Map of the ratio of AP-8 MAX to the PAB97 model for channel 5

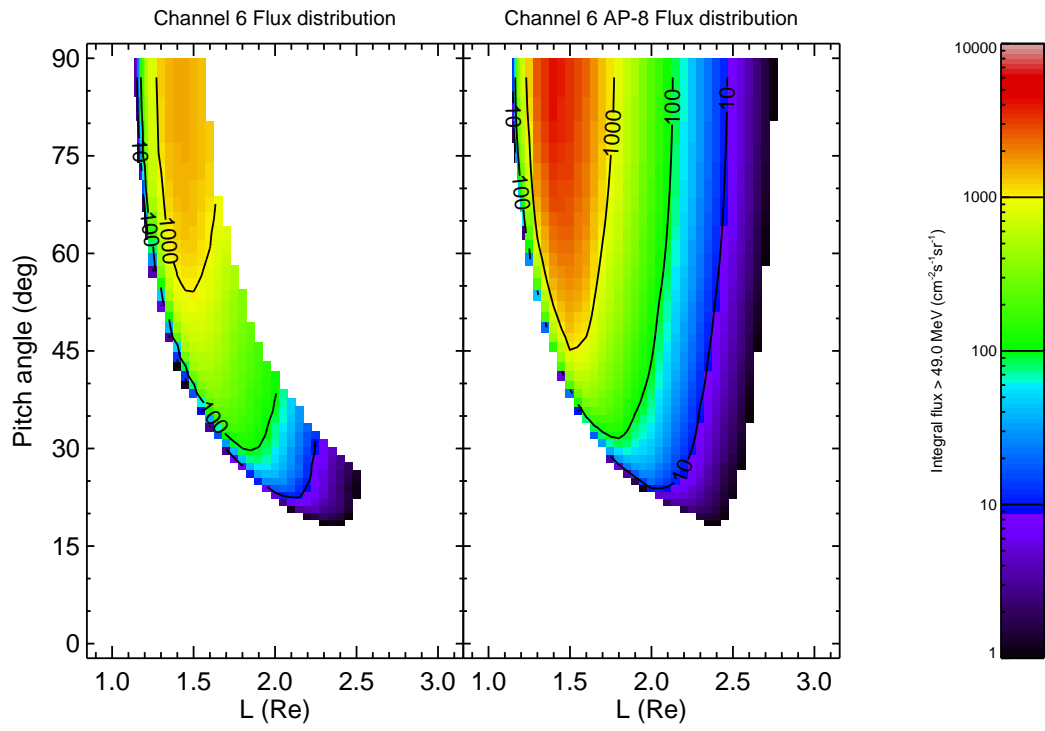


Figure 3.23. (L, α_0) Map of the PAB97 model and AP-8 MAX for channel 6

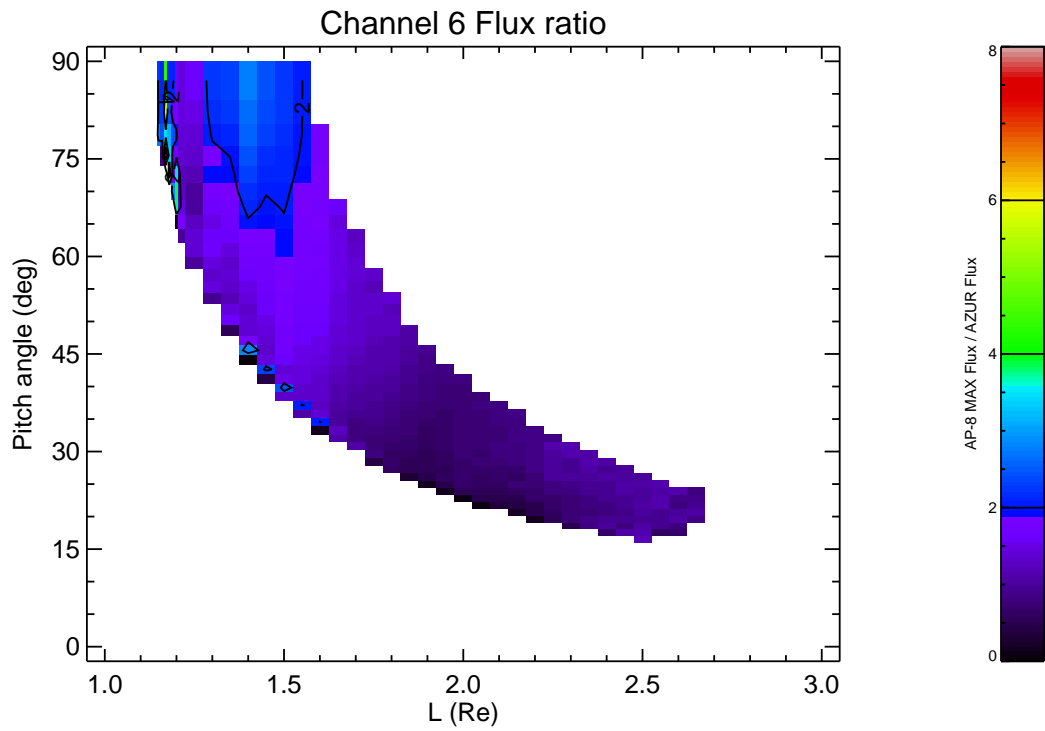


Figure 3.24. (L, α_0) Map of the ratio of AP-8 MAX to the PAB97 model for channel 6

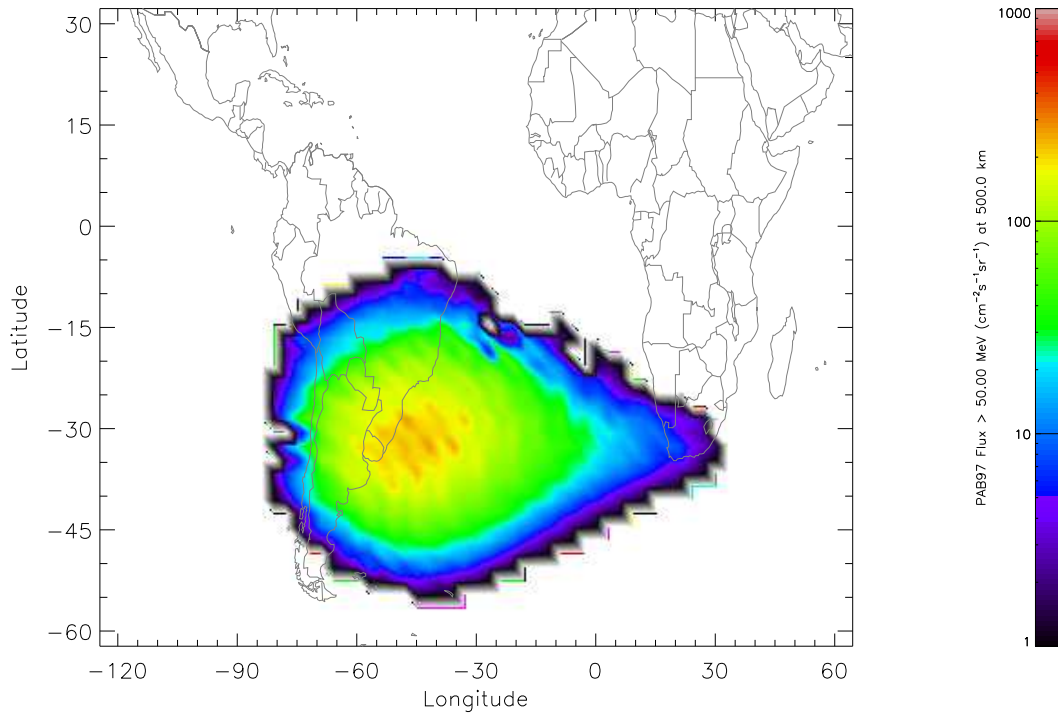


Figure 3.25. World map of the PAB97 >50 MeV proton flux at 500 km

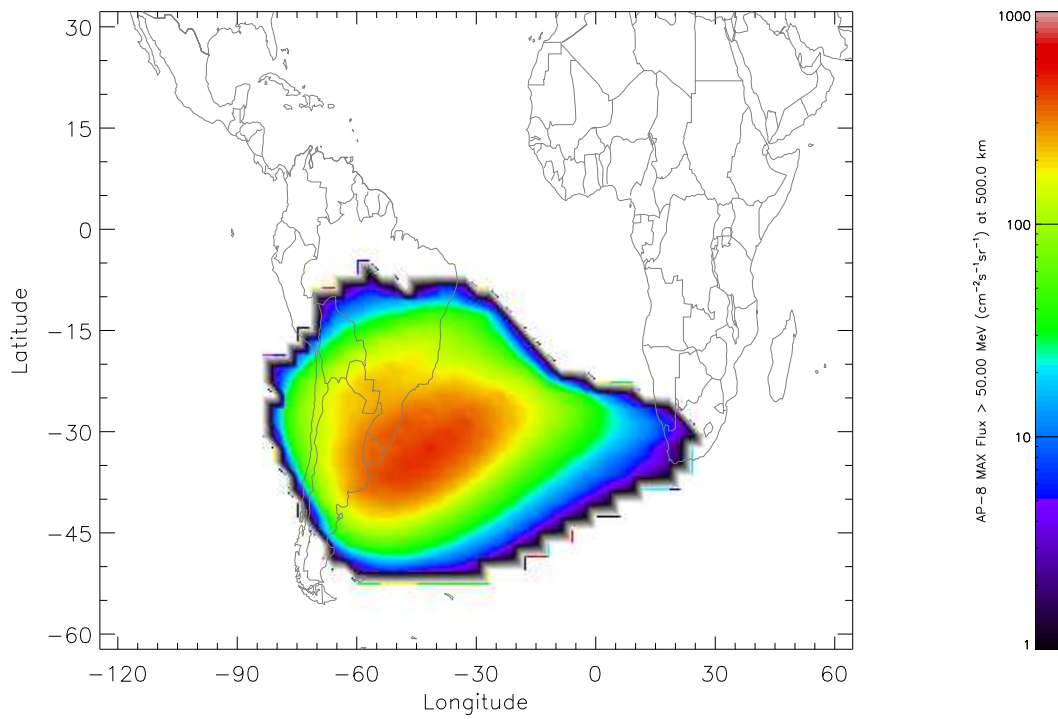


Figure 3.26. World map of the AP-8 MAX >50 MeV proton flux at 500 km

For higher L values, the agreement between the two models is satisfactory.

Another way of comparing the PAB97 model to AP-8 consists of drawing world maps of fluxes at fixed altitude. Figures 3.25 and 3.26 show the distributions of the PAB97 and AP-8 MAX proton flux >50 MeV at an altitude of 500 km, respectively. Again, the PAB97 flux is lower than the AP-8 MAX flux.

Part II

The SAMPEX data base and model

Chapter 4

The SAMPEX mission

The Solar, Anomalous, and Magnetospheric Particle EXplorer (SAMPEX) was the first Small Explorer (SMEX) mission. SAMPEX measures energetic electrons as well as ion composition of particle populations from ~ 0.4 MeV/nucleon to hundreds of MeV/nucleon from a zenith-oriented satellite in near-polar orbit. SAMPEX was successfully launched from NASA's Western Test Range (Lompoc, CA) at 1419 UT on 3 July 1992. The description of the SAMPEX satellite system and instruments has been taken from a series of papers in IEEE Trans. Geosci. Remote Sensing **31**, Nr. 3, 1993.

4.1 Spacecraft configuration

The SAMPEX spacecraft was designed to support a minimum mission duration of 1 year, with a mission goal of 3 or more years (Baker et al. 1993). The SAMPEX mechanical system basically consists of a primary structure, a deployable solar array system, and a yo-yo despin system. SAMPEX is built up of machined aluminium plates which form a box-like structure that houses all of the spacecraft components (see Fig. 4.1).

The SAMPEX orbit has an inclination of 82° , apogee of 670 km and perigee of 520 km. The orbit is non-Sunsynchronous and precesses through all local times (noon-midnight to midnight-noon) in about three months.

4.2 Attitude control

The Attitude Control Subsystem (ACS) is designed as a solar-pointed/momentum bias system. The SAMPEX spacecraft points at the Sun while it rotates about the sunline once per orbit in order to position the instrument lines-of-sight in the zenith direction when overflying the poles. Pointing requirements for the selected experiments are met by choosing sensor, torquers, and system configurations from a standard set of electronics, sensors and actuators. The ACS system utilizes one momentum wheel and three electromagnetic torque rods to orient the experiment

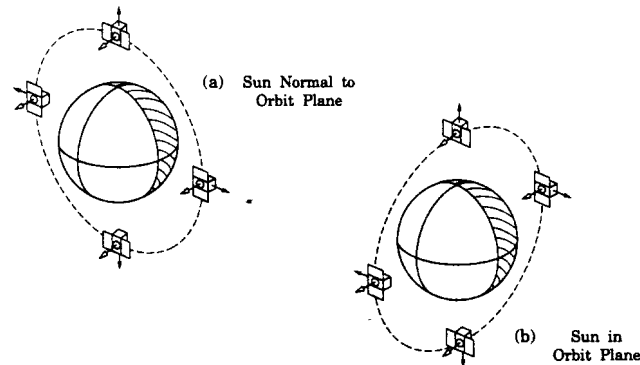


Figure 4.2. Pointing strategy for the SAMPEX spacecraft in two illustrative orbit planes [from Baker et al. (1993)].

viewing axis. Pointing ranges within $\pm 15^\circ$ of vertical over the poles. The attitude computed onboard the spacecraft is known with an accuracy better than 2° (3σ). The pointing strategy for SAMPEX is to point the pitch axis (i.e. the normal to the solar panels) directly at the Sun. Then the yaw axis (parallel to the detector bore sights) rotates about the pitch axis once per spacecraft orbit. The spacecraft views north over the north pole, south over the south pole, and parallel to the equator during the equatorial plane crossings (see Fig. 4.2).

An Attitude Control Electronics (ACE) box which contains signal conditioning electronics and an independent analog safhold mode controls the ACS sensor and hardware. The onboard data system performs closed loop real-time attitude determination and control processing. Three-axis attitude determination is provided by comparing the local measured Sun vector and magnetic field vector with an on-board ephemeris model. Digital control of the spacecraft attitude is completed by sending appropriate command signals across the spacecraft data bus to the actuators.

The spacecraft determines the directions of the Sun and of the local magnetic field (using the Sun sensors and the magnetometer, respectively) with respect to the spacecraft's body-fixed coordinate frame, then compares these measurements with onboard calculations of the same quantities in the GEI coordinate frame in order to relate the two frames. When the magnetic field is nearly parallel or antiparallel to the Sun line, the roll angle about their nearly common line is poorly determined. Therefore, when the angle between these two lines becomes less than 5° (or greater than 175°) while the spacecraft is out of eclipse, or less than 40° (or greater than 140°) while in eclipse, the spacecraft goes into "coast mode" and stops sending attitude information to the telemetry stream until the two lines diverge far enough to resume normal operations. Thus there is a gap in attitude information available on the ground. The time during which attitude is not being updated can add up to a large fraction of a day. The gaps in the attitude data were filled by interpolation, with a quality flag assigned to the interpolated data.

When the spacecraft enters coast mode, the magnetic torque rods shut off if they are running and the rotation speed about the Sun line is reset to a nominal value, which may be significantly slower than before coast mode began. On 27 May 1994, the spacecraft pointing strategy was

Table 4.1. SAMPEX Scientific Instruments

	LEICA	HILT	MAST	PET
Energy range (MeV)				
Electrons	—	—	—	0.4–30
H	0.76–6.1	—	—	18–250
He	0.45–6.1	4.3–38	7–20	18–350 MeV/nuc
C	0.44–11.4	7.2–160	14–210	34–120 MeV/nuc
Si	0.33–5.5	9.6–177	21–330	54–195 MeV/nuc
Fe	0.21–3.1	11.0–90	27–450	70–270 MeV/nuc
Charge range				
Elements	1–25	2–28	2–28	1–2 (1–28*)
Isotopes	2–16	2	2–28	1–2 (1–10*)
Physical characteristics				
Geometric factor (cm ² sr)	0.8	60	7–14	0.3–1.6
Field of view (deg, full angle)	24 × 20	68 × 68	101	58
Mass (kg)	7.4	22.8	8.8	(incl. with MAST)
Power (W)	4.9	5.6	5.3	(incl. with MAST)
Telemetry (kB/s)	1.3	0.9	1.4	0.5

*Commandable high-gain mode

changed to the effect that the instrument line of sight is perpendicular to the magnetic field while the spacecraft is in eclipse.

4.3 Instrument complement

The instruments on the SAMPEX spacecraft are the Low Energy Ion Composition Analyzer (LEICA), the Heavy Ion Large Telescope (HILT), the MAss Spectrometer Telescope (MAST), and the Proton/Electron Telescope (PET). The four instruments onboard have co-aligned bore-sights. A brief description of these instruments is given below. The instrument characteristics are summarised in Table 4.1. In this study, only data from the PET are used. The PET instrument is described in more detail in Sect. 4.4.

4.3.1 Low Energy Ion Composition Analyzer (LEICA)

The LEICA instrument is a time-of-flight mass spectrometer that identifies incident ion mass and energy by simultaneously measuring the time-of-flight and residual kinetic energy of parti-

cles that enter the telescope and stop in an array of four solid state detectors. The time-of-flight is determined by START and STOP pulses from chevron MicroChannel Plate (MCP) assemblies that detect secondary electrons emitted from the entrance foil and a foil in front of the solid state detector, respectively, when the ion passes through them. These secondary electrons are accelerated to approximately 1 keV and deflected onto the MCPs by electrostatic mirrors. The measured energy and velocity are combined to yield the mass of the ion and the energy per nucleon. Details of the LEICA instrument are presented by Mason et al. (1993).

4.3.2 Heavy Ion Large Telescope (HILT)

The HILT sensor is designed to measure heavy ions from He to Fe in the energy range from 8 to 220 MeV/nucleon for oxygen, covering the medium-energy solar energetic ions, the galactic cosmic rays, and the range of maximum intensity of the anomalous cosmic ray component. The sensor consists of a three-element ion drift chamber with two thin multilayer entrance windows followed by an array of 16 solid state detectors and a scintillation counter with photodiodes. The HILT instrument uses a flow-through isobutane system for the drift chamber. The instrument is described in detail by Klecker et al. (1993).

4.3.3 MAss Spectrometer Telescope (MAST)

MAST Is designed to measure the isotopic composition from Li to Ni in the range from approximately 10 MeV/nucleon to several hundred MeV/nucleon (Cook et al. 1993a). MAST consists of a combination of surface barrier and lithium-drifted solid state detectors (11 in total). Combined matrix detector positions determine the particle trajectories, allowing accurate corrections to be made for the pathlength variation with angle and detector response non-uniformities. Although optimised for isotopic analysis of the elements Li to Ni, MAST also performs measurements of stopping He isotopes from approximately 7 to 20 MeV/nucleon. In addition, MAST analyses particles that penetrate the entire stack, providing differential energy spectra of the more abundant elements to well beyond the endpoint energy for stopping particles, and integral flux measurements at higher energies. A priority system ensures that the most interesting events are selected for readout, with stopping $Z \geq 3$ events given the highest priority. However, because MAST is assigned a high telemetry data rate, the pulse heights from essentially all stopping $Z \geq 3$ nuclei can be transmitted, even in very large flares.

4.3.4 Proton/Electron Telescope (PET)

The PET system is designed to complement MAST by measuring the energy spectra and relative composition of protons (18–250 MeV) and helium nuclei (18–350 MeV/nucleon) of solar, interplanetary, and galactic origins, and the energy spectra of solar flare and precipitating electrons from approximately 0.4 to 30 MeV. The instrument measures both trapped and precipitating energetic particles in different parts of the SAMPEX orbit. It also has the capability to look at manmade particle populations such as positrons which are emitted by nuclear reactors that

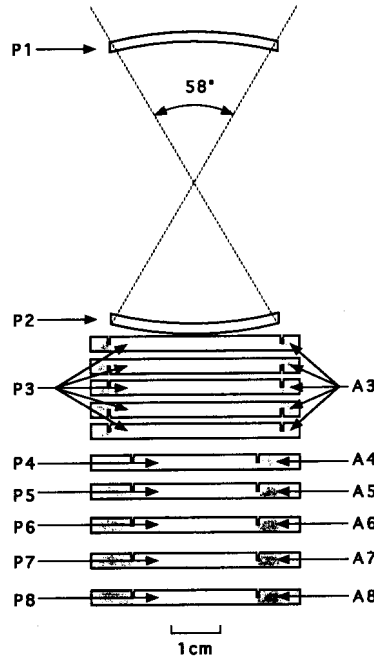


Figure 4.3. Schematic of the PET telescope. The primary analysis mode requires P1 and P2 (58° field of view). A wide angle 90° field of view that requires P2 and P4 but not P1 is also available for electrons. The regions labelled A4 through A8 are annular guard regions used to detect particles that enter or leave through the side of the stack [from Cook et al. (1993b)].

have flown previously in low Earth orbit. The PET system can also duplicate and extend some measurement capabilities of MAST by providing energy spectra and elemental composition of nuclei from Li through Fe using a commandable high gain mode. It provides some isotopic information on nuclei from H to Ne.

4.4 Detailed description of the PET telescope

This section presents the description of PET by Cook et al. (1993b). The PET telescope, shown schematically in Fig. 4.3, consists of a series of eight Li-drifted silicon detectors (P1 to P8) with thicknesses ranging from 2 to 15 mm. The telescope opening aperture is defined by a passive collimator, followed by two curved (spherical) aperture detectors (P1 and P2) designed to minimise pathlength variations over the telescope's 58° opening angle. They are followed by six flat detectors (P3 to P8), where the P3 detector is comprised of five identical devices with a combined thickness of 15 mm. Detectors P3 through P8 are double-grooved devices with a central area for measuring energy loss and an annular guard region (labelled A in Fig. 4.3) used to detect particles that enter or leave through the side of the telescope, a design previously used on Voyager 1, Voyager 2 (Stone et al. 1977), and ISEE-3 (Althouse et al. 1978).

Table 4.2. PET Detector, ADC, and discriminator characteristics

Detector Name	Nominal Thickness (mm)	Central Active Area (cm ²)	Guard Active Area (cm ²)	Nominal ADC Threshold (MeV)	Nominal ADC Full Scale (MeV)	Nominal Discriminator Thresholds (MeV)	Guard Discriminator Thresholds (MeV)
P1	2	8.0	—	0.35	157	P1A=3.1	—
P2	2	8.0	—	0.35	157	—	—
P3	15 (5 × 3) mm	9.2	4.5	0.7	317	P3A=2.8 P3B=12	0.3, 5
P4–P7	3	4.5	8.0	0.36	337	0.23	0.3, 1.2
P8	3	4.5	8.0	—	—	0.3	0.3, 1.2

Particles satisfying the P1·P2 coincidence enter through a 1.5 cm long collimator (not shown in Fig. 4.3) that is nominally 0.75 mm thick at its thinnest point, and that preserves the 58° opening angle. The collimator also supports two windows (each 12.5 μ m thick aluminised Kapton) that provide electrical shielding and protection from sunlight.

Detectors P1, P2, and the centre of P3 are each direct coupled to separate charge-sensitive pre-amplifiers, shaping amplifiers, and 10-bit ADCs. The summed output of the centres of P4 through P7 is fed into a fourth 10-bit ADC. The centre of P8 and the guard regions of P3 to P8 are each connected to pre-amplifiers, shaping amplifiers and discriminators. Each guard signal channel has two discriminators, A1 and A2: A1 is sensitive to minimum ionising particles while the A2 levels are ~ 1.2 MeV for A4–A8 and ~ 5 MeV for A3. Table 4.2 summarises the characteristics of the PET detectors and their analysis chains.

4.4.1 Analysis modes

PET Uses the conventional dE/dx -total energy technique to identify electrons, protons, and heavier nuclei, an approach which is based on the range-energy relations of energetic particles. With this approach a comparison of the rate of energy loss of energetic particles with their total energy loss can be used to identify both the charge and mass of energetic nuclei, as well as measure their kinetic energy. In practice, the rate of energy loss is determined by measuring the energy loss (ΔE) in a detector of known thickness, such as P1 or P2 on PET. In order to minimise the variations in the path length over the telescope's 58° opening angle, P1 and P2 have been constructed from spherical segments of silicon. As a result, PET should be capable of identifying elements from H to Ni, with isotope identification extending through Ne. Although the range-energy characteristics of electrons are not nearly so precise as those of nuclei, electrons are easily separable from protons because of their much lower rate of energy loss.

PET Includes a number of separate analysis modes that are designed to identify electrons and nuclei over selected energy intervals: the primary Lo-Z mode providing differential energy spectra of electrons and of H and He nuclei, and the commandable Hi-Z mode (in which the gain of P1, P2, and P3 is reduced by a factor of ten) in which energy spectra of the elements from Li to Ni can be measured as well. The data used in this study were obtained in the Lo-Z

Table 4.3. PET Response

Particle	Nominal Energy Interval (MeV or MeV/nuc)	Typical Geometry Factor ¹ (cm ² sr)	Detector ^{2,3} Combination	Associated counting rates		
				Name	Res. (s)	Duty Cycle
Electrons	> 0.4	10	P1	P1	0.1	0.5
	~ 1–4	1.8	$P1 \cdot \overline{P1A} \cdot P2 \cdot \overline{P3} \cdot \overline{A}$	ELO	6	1
	~ 4–20	1.7–1.1	$P1 \cdot \overline{P1A} \cdot P2 \cdot P3 \cdot \overline{P4} \cdot \overline{A}$	EHI	6	1
	~ 12–30	0.5–0.3	$P1 \cdot P2 \cdot P4 \cdot \overline{P8} \cdot \overline{A}$	RNG	6	1
	~ 12–30	2.8–0.9	$\overline{P1} \cdot P2 \cdot \overline{P3B} \cdot P4 \cdot \overline{P8} \cdot \overline{A}$	EWG	6	1
H, He	> 4	10	P1	P1	0.1	0.5
	19–28	1.8	$P1A \cdot P2 \cdot \overline{P3} \cdot \overline{A}$	PLO	6	1
	28–64	1.7–1.1	$P1A \cdot P2 \cdot P3 \cdot \overline{P4} \cdot \overline{A}$	PHI	6	1
	64–85	0.5–0.3	$P1 \cdot P2 \cdot P4 \cdot \overline{P8} \cdot \overline{A}$	RNG	6	1
	> 85	0.3	$P1 \cdot P2 \cdot P8 \cdot \overline{A}$	PEN	6	1
$Z \geq 3$ Nuclei ⁴	60–200	1.7–1.1	$P1 \cdot P2 \cdot \overline{P4} \cdot \overline{A}$	PLO, PHI	6	1

¹Based on calculation with straight tracks; accelerator calibration data will modify values for electrons.

²“A” Represents the logical “OR” of the guard rings on P3 to P8.

³P1A, P3A, and P3B are digital discriminators on the P1 and P3 outputs set at 3.1, 2.8, and 12 MeV, respectively.

⁴Commandable mode for $Z \geq 3$ nuclei; energy range indicated is for Si-28.

mode only.

The pulse height of an event is triggered whenever one of the coincidence equations in Table 4.3 is satisfied. The results, along with other information such as the state of various discriminators, are stored in one of five separate event buffers. These event buffers are read out into the telemetry stream by a rotating priority system that ensures that all event types are represented under conditions that range from periods dominated by intense fluxes of solar flare nuclei to periods dominated by trapped protons and electrons.

Because the telemetry rate is insufficient to transmit every event, rate accumulators are used to count events during 6 s intervals. A total of 32 such “counting rates” record instrument live-time, the frequency of electrons and nuclei in several energy intervals defined by the coincidence logic, and the triggering frequency of a variety of discriminator levels. Table 4.3 summarizes some of the counting rates of physical interest. In addition, the “singles” counting rate of the front detector (P1) is sampled for 0.05 s out of every 0.10 s to measure the flux of magnetospheric electrons > 0.4 MeV and protons > 4 MeV on a fast time scale. This “high resolution” rate is recorded whenever the count rate exceeds a (commandable) level of ~ 50 counts/s. All of the coincidence equations and some of the discriminator levels can be modified by command to allow for the possibility of noisy or failed detectors, and to optimise the instrument’s response to the various particles of interest.

4.4.2 Calibrations

The response of PET to electrons has been calibrated over the energy range from ~ 0.3 MeV to ~ 27 MeV with electron beams incident at a variety of energies and zenith angles. At higher energies the linear electron accelerator at the EG&G Santa Barbara facility was operated in a low intensity mode to provide mono-energetic beams at fourteen separate energies from 1.5 to 27 MeV. Calibrations at somewhat lower energies (0.3 to 3 MeV) were carried out with a β spectrometer. PET Was also calibrated with radioactive sources to determine its positron detection efficiency and its response to γ rays that Compton scatter in the telescope producing a possible background for electron and positron measurements. For accelerator calibrations, where beam time is often limited and expensive, PET has a special port that allows events to be read out at rates of several thousand per second.

PET Has a built-in calibrator that can be initiated either periodically (every 6.8 hours) or by command (Cook et al. 1993a). The calibrator includes an 8-bit DAC that supplies reference voltages to the test pulsters of each of the signal channels. The test pulsters can be stimulated either individually or in groups to perform limited tests of the coincidence logic, measure the thresholds of the various discriminators, and the gain, linearity, and long-term stability of the ADCs. Calibration “events” are flagged and stored in a special buffer for read-out and telemetry along with the regular data.

Chapter 5

The SAMPEX/PET data base

In this chapter we describe the installation of the SAMPEX/PET data base on a DEC Alpha workstation running OpenVMS. The data analysis is performed with a series of IDL programmes and the UNILIB library (see TN 10). The different steps in the analysis procedure are outlined and the format of the final data base is described.

5.1 Retrieval of the data sets

The PET data base was delivered to BIRA/IASB by M.D. Looper on optical disks. The data set consists of ephemeris files, attitude information, count rates and livetimes. Table 5.1 lists the files contained on each optical disk side. Each file contains one day of data, with the date forming the second part of the file name as YYDDD. The contents of each file type are described

Table 5.1. SAMPEX/PET Data set file description

Disk label	File names	File contents
XFER00	SEPHxxxxxx.DAT	Ephemeris data
	SALFxxxxxx.DAT	Pitch angle
XFER01	PTLVxxxxxx.DAT	Livetimes
XFER02	PKTSxxxxxx.DAT	Count rates
XFER03	SCEWxxxxxx.DAT	$\Delta L, \Delta B$
XFER04	BVECxxxxxx.DAT	Calculated magnetic field vector components
	QCORxxxxxx.DAT	Corrected attitude information
XFER05	SQUAxxxxxx.DAT	Raw attitude information
	SMAGxxxxxx.DAT	Raw magnetometer data

below. The data delivered to BIRA/IASB cover the period from the start of the mission (day 187 of 1992) up to day 121 of 1996.

5.2 File descriptions

This section contains the descriptions of the contents of the files listed in Table 5.1. The contents of each file correspond to an IDL structure. The structures are defined as:

```
nkts = 14400
seph = replicate({time:01,range:0.,lon:0.,lat:0.,l:0.,
                  bmag:0.},nkts)
salf = fltarr(nkts)
ptlv = replicate({plo:0.,phi:0.,rng:0.,pen:0.},nkts)
pkts = replicate({p21:0b,p22:0b,p23:0b,p24:0b,p31:0b,p32:0b,
                  p33:0b,p34:0b,p4:0b,p5:0b,p67:0b,p81:0b,
                  p82:0b,p83:0b,p84:0b,d31:0b,d32:0b,d33:0b,
                  d34:0b,d4:0b,d5:0b,d67:0b},nkts)
qcor = replicate({qua:fltarr(4),flag:0b},nkts)
bvec = fltarr(3,nkts)
scew = replicate({deltal:0.,deltab:0.},nkts)
smag = replicate({time:01,b:intarr(3)},nmag)
squa = replicate({time:01,qua:fltarr(4)},nqua)
```

nkts Is the number of six second intervals per day, while **nmag** and **nqua** are the number of elements in the **SMAGxxxxx.DAT** and **SQUAxxxxx.DAT** files, respectively. Some files may be missing for some days. The use of IDL structures greatly simplifies the reading of the data files, in that one read statement suffices to read in all data. For instance, to read in an ephemeris file, the following IDL code can be used:

```
nkts=14400
seph=replicate({time:01,range:0.,lon:0.,lat:0.,l:0.,bmag:0.},nkts)
openr,1,'seph93001.dat'
readu,1,seph
close,1
```

5.2.1 SEPHxxxxx.DAT

The **SEPH** structure contains the ephemeris data at the start of each six second interval:

seph.time universal time tag in seconds of start of interval;

seph.range geocentric distance (km);

seph.lon geocentric longitude (deg);

seph.lat geocentric latitude (deg);

seph.l L (R_E) from IGRF 90 model;

seph.bmag B (Gauss) from IGRF 90 model.

5.2.2 SALFxxxxx.DAT

The vector SALF contains the pitch angle of particles entering along the instrument boresight, at the start time of each six second interval.

5.2.3 PTLVxxxxx.DAT

The PTLV structure contains the livetimes in seconds (maximum 6 s) over each six second interval:

ptlv.plo livetime (s) for 2-detector (PLO) events;

ptlv.phi livetime (s) for 3-detector (PHI) events;

ptlv.rng livetime (s) for 4-detector (RNG) events;

ptlv.pen livetime (s) for 8-detector (PEN) events.

5.2.4 PKTSxxxxx.DAT

The PKTS structure contains the counts of protons and deuterons over each six second interval:

pkts.p* counts of proton events from start to end of interval;

pkts.d* counts of deuteron events from start to end of interval.

Table 5.2 associates the count rates in PKTS with the livetimes in PTLV, and gives energy ranges and nominal geometry factors for each channel. When a livetime is zero in the PTLV structure, all associated count rates should be discarded.

5.2.5 QCORxxxxx.DAT

The QCOR structure contains the attitude information at the start of each six second interval:

qcor.qua quaternion for rotation from GEI coordinates into spacecraft body-fixed coordinates, corresponding to the rotation matrix R :

$$\begin{pmatrix} q_0 q_0 - q_1 q_1 - q_2 q_2 + q_3 q_3 & 2 (q_0 q_1 + q_2 q_3) & 2 (q_0 q_2 - q_1 q_3) \\ 2 (q_0 q_1 - q_2 q_3) & -q_0 q_0 + q_1 q_1 - q_2 q_2 + q_3 q_3 & 2 (q_1 q_2 + q_0 q_3) \\ 2 (q_0 q_2 + q_1 q_3) & 2 (q_1 q_2 - q_0 q_3) & -q_0 q_0 - q_1 q_1 + q_2 q_2 + q_3 q_3 \end{pmatrix}$$

Table 5.2. PET Channel characteristics

Channel (PKTS)	Buffer (PTLV)	Energy Range (MeV/nuc)	Nominal Geometric Factor (cm ² sr)
p21	plo	18.5–20.5	1.792
p22	plo	20.5–22.5	1.792
p23	plo	22.5–24.5	1.792
p24	plo	24.5–27.2	1.792
p31	phi	27.2–37.4	1.714
p32	phi	37.4–45.8	1.527
p33	phi	45.8–53.0	1.356
p34	phi	53.0–65.4	1.146
p4	rng	65.4–71.0	0.477
p5	rng	71.0–76.3	0.420
p67	rng	76.3–86.1	0.341
p81	pen	86.1–120.0	0.277
p82	pen	120.0–200.0	0.277
p83	pen	200.0–300.0	0.277
p84	pen	300.0–500.0	0.277
d31	phi	18.4–25.4	1.714
d32	phi	25.4–31.0	1.527
d33	phi	31.0–36.0	1.356
d34	phi	36.0–44.3	1.146
d4	rng	44.3–48.1	0.477
d5	rng	48.1–51.7	0.420
d67	rng	51.7–58.2	0.341

The transformation from GEI to spacecraft components is then given by:

$$\mathbf{X}_{s/c} = R \mathbf{X}_{\text{GEI}} . \quad (5.1)$$

qcor.flag data source flag: 0 if the quaternion is interpolated to the interval start time from two spacecraft-supplied quaternions less than 40 s apart, 1 if the quaternion is determined by calculation using Sun line and magnetic field data in the middle of a period (40 s or more), and 2 if the quaternion is interpolated to the interval start time between two quaternions more than 40 s apart, without reference to measured Sun line and magnetic field data. Data with flag value 0 are successively more trustworthy than data with flag values 1 and 2. In our binning procedures, only data with flag 0 are retained.

5.2.6 BVECxxxxx.DAT

The BVEC structure contains the GEI components of the IGRF 90 magnetic field vector at the spacecraft position at the start of each six second interval.

5.2.7 SMAGxxxxx.DAT

The SMAG structure contains the raw magnetometer data. These data files have a variable number of elements, which is added at the beginning of the files. The SMAG structure is defined as:

smag.time time in seconds from start of day 92001;

smag.b raw magnetometer data of observed magnetic field components in spacecraft body-fixed coordinates. These data have not been corrected for contamination due to the attitude torque rods and are not in units of Gauss.

The SMAG data are not used in this study.

5.2.8 SQUAxxxxx.DAT

The SQUA structure contains the raw attitude data:

squa.time time in seconds from start of day 92001;

squa.qua quaternions sent down from the spacecraft, not corrected or synchronised.

In this study, the QCOR data are used instead of the SQUA data.

5.2.9 SCEWxxxxx.DAT

For the anisotropy study described in TN 6 Part II, the values of L and B calculated at the guiding centre corresponding to each measurement are needed. The SCEW structure contains $\Delta L \equiv L_{GC} - L$ and $\Delta B \equiv B_{GC} - B$ at the start of each six second interval:

scew.deltal difference between the guiding centre L and the spacecraft L (R_E);

scew.deltab difference between the guiding centre B and the spacecraft B (Gauss).

The SCEW data are not used in this study. Instead, we chose to regenerate the values of B , L with the DGRF or IGRF model for the epoch of Jan 1 of each year of measurements. Using the quaternions in the QCORxxxxx.DAT, the look direction of the instrument and the locations of the guiding centres corresponding to each measurement and particle energy E were determined, and the values of B_{GC} and the respective $L_{GC}(E)$ were calculated. Finally, a new value of the

Table 5.3. Description of the EPH structure

Element	Data Type	Definition
eph.time	Long integer	Universal time (s) of start of six second interval
eph.alt	Single precision	Geodetic altitude (km)
eph.lon	Single precision	Longitude (deg)
eph.lat	Single precision	Geodetic latitude (deg)
eph.pa	Single precision	Pitch angle (deg)
eph.b	Single precision	DGRF Magnetic field intensity (Gauss) at spacecraft location
eph.fl	Single precision	L Value (R_E) corresponding to spacecraft location and eph.pa
eph.bc	Single precision	DGRF Magnetic field intensity (Gauss) at the guiding centre of a 100 MeV particle
eph.flc	Single precision	L Value (R_E) corresponding to the guiding centre of a 100 MeV particle and eph.pa
eph.beta	Single precision	Azimuthal angle β (deg)
eph.bv	Single precision (3)	Geocentric spherical DGRF magnetic field vector components (Gauss)
eph.vn	Single precision (3)	Geocentric spherical components of the local curvature vector of the magnetic field line
eph.altm	Single precision	Altitude of the lowest mirror point on the local magnetic field line
eph.flag	Byte	Quality flag

pitch angle for each measurement was derived from the look direction and the direction of the local magnetic field vector. The resulting values are stored in the new ephemeris files described in Sect. 5.3.

5.3 Generation of a new ephemeris data set

In order to simplify the data processing, a new set of ephemeris files was generated: the EPHxxxxxx.DAT files. Each of these files combines all the ephemeris, attitude and magnetic field data for one day. The magnetic field vectors and related quantities were recalculated from the ephemeris data using the UNILIB library and DGRF 90 or IGRF 95 updated to Jan 1 of the year of the measurements (see Sect. 5.2.9).

The IDL structure variable EPH is defined as:

```
eph = replicate({time:01,alt:0.,lon:0.,lat:0.,pa:0.,b:0.,
                fl:0.,bc:0.,flc:0.,beta:0.,bv:fltarr(3),
```

```
vn:fltarr(3),altm:0.,flag:0b},nkts)
```

Table 5.3 lists the definitions of the structure elements. `eph.beta` is the azimuthal angle β defined in TN 6 Part II. The values of L_{GC} and B_{GC} correspond to the guiding centre positions of 103.05 MeV protons (centre of energy channel p81). Storing one value of L_{GC} and B_{GC} is sufficient as they depend linearly on the gyroradius. The curvature vector of the magnetic field lines is stored as it was used in the calculation of `eph.beta`.

Chapter 6

Model construction

In this chapter the data binning procedure is outlined, as well as the conversion from counts and livetimes to fluxes. The model construction procedure is analogous to the procedure followed for the AZUR data (see Chapter 3). The correction procedure for the field of view, described in general terms in Sect. 3.1, is adapted to the PET telescope and sensors.

6.1 Data binning

The PET data for the second half of 1994 and the first half of 1995 have been averaged over a rectangular three dimensional bin in (E, L, α_0) space by means of the IDL programme `BINNING.PRO`. The (E, L, α_0) bin limits of the grid are listed in Table 6.1. The limits of the energy bins correspond to the channel limits in Table 5.2. The L and α_0 bins were selected so as to obtain a uniform distribution of the measurements over the grid. The DGRF magnetic field model for epoch 1995 was used to calculate the magnetic coordinates. No external magnetic field model was used.

Because of the relatively poor statistics of the PET proton counts (only a fraction of the events satisfying detector coincidence conditions are actually processed by the pulse height analysers, and only a few of the twenty analysed events telemetred per second appear in the proton channels; see Chapter 7), it is not possible to convert individual count rates into fluxes without accumulation. For many measurements, the recorded count rate is zero while the corresponding livetime is not, and is lower than the integration time of 6 s. Therefore, it was decided to average the counts and livetimes separately, so that the average flux in each model bin is the ratio of the sum of the counts in that bin divided by the sum of the livetimes.

6.2 Correction for telescope field of view

As for the AZUR data, the PET flux averages are corrected for the telescope field of view by means of the programme `FOVAPP.PRO`. Figure 6.1 shows the effective areas for a subset of

Table 6.1. (E, L, α_0) Bin limits for the PET model grid

E Limits (MeV)	L Limits (R_E)	α_0 Limits (deg)
18.5	1.005	0.0000
20.5	1.015	21.2018
22.5	1.025	22.7340
24.5	1.035	24.2568
27.2	1.045	25.7705
37.4	1.055	27.2751
45.8	1.065	28.7709
53.0	1.075	30.2579
65.4	1.085	31.7364
71.0	1.095	33.2065
76.3	1.105	34.6683
86.1	1.115	36.1220
120.0	1.125	37.5677
200.0	1.135	39.0055
300.0	1.145	40.4356
500.0	1.155	41.8581
	1.165	43.2730
	1.175	44.6806
	1.185	46.0809
	1.195	47.4741
	1.205	48.8602
	1.225	50.2394
	1.275	51.6118
	1.325	52.9774
	1.375	54.3364
	1.425	55.6888
	1.475	57.0348
	1.525	58.3744
	1.575	59.7078
	1.625	61.0350
	1.675	62.3561
	1.725	63.6712
	1.775	64.9803
	1.825	66.2836
	1.875	67.5812
	1.925	68.8730
	1.975	70.1592
	2.025	71.4399
		72.7150
		73.9848
		75.2492
		76.5084
		77.7624
		79.0112
		80.2549
		81.4936
		82.7273
		83.9562
		85.1802
		86.3994
		90.0000

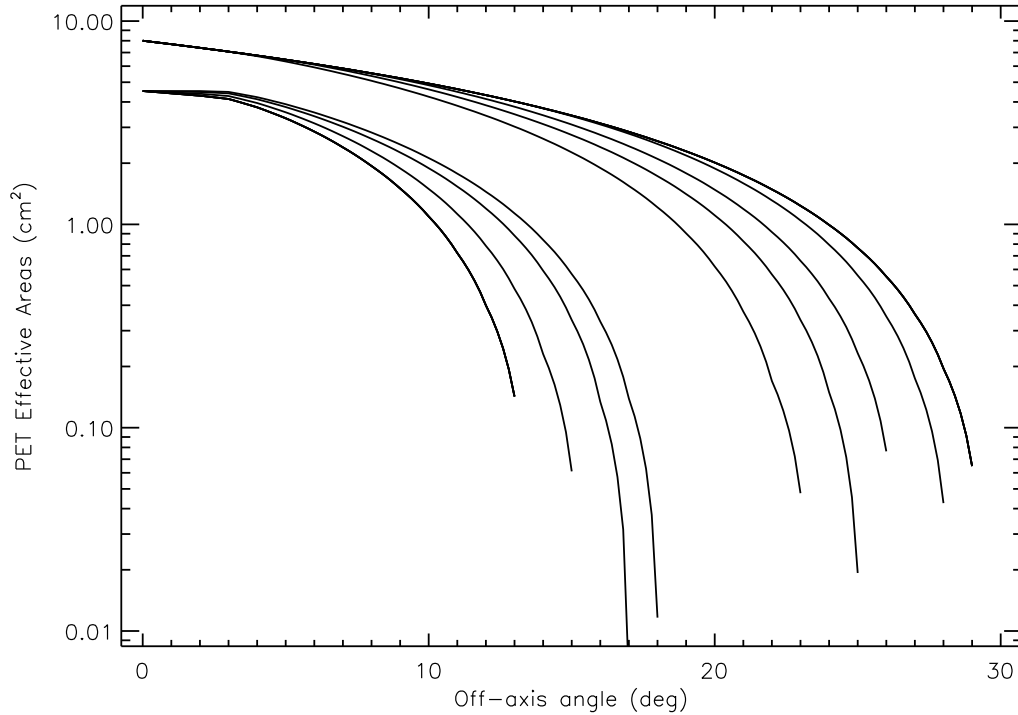


Figure 6.1. Effective areas of the SAMPEX/PET sensors

the PET sensors, which were provided in the form of a table by M.D. Looper.

There are eleven ranges in Fig. 6.1, corresponding to particles stopping in each of the detector wafers from P2 to P8 (counting the P3A, . . . , P3E wafers separately) after passing through all the previous detectors starting with P1. With reference to the channels listed in Table 5.2, p21–p24 are P2 range, p31 is P3A, p32 is P3B, p33 is P3C, p34 is the sum of particles with ranges to P3D and P3E (so its response is taken to be the average of the responses for P3D and P3E), p4 is P4, p5 is P5, p67 is P6 and P7 totalled (and again responses averaged), and p81–p84 are all of P8 range.

The IDL programme `AREAS.PRO` reads the tabulated effective areas and returns the areas for all fifteen proton channels. The field of view correction is carried out by the programme `DETCOR.PRO`, which calls `FOVAPP.PRO` and `AREAS.PRO`.

6.3 Final flux map

The IDL programme `MODEL.PRO` reads in the flux averages created by `BINNING.PRO` and writes the final flux map `SAMPEX.DAT`. This programme is interactive and allows for the correction of spurious points. For grid points where there are no data, the flux is set to -1.0 .

The final flux map is then transformed into a `BLOCK DATA` file by means of the programme

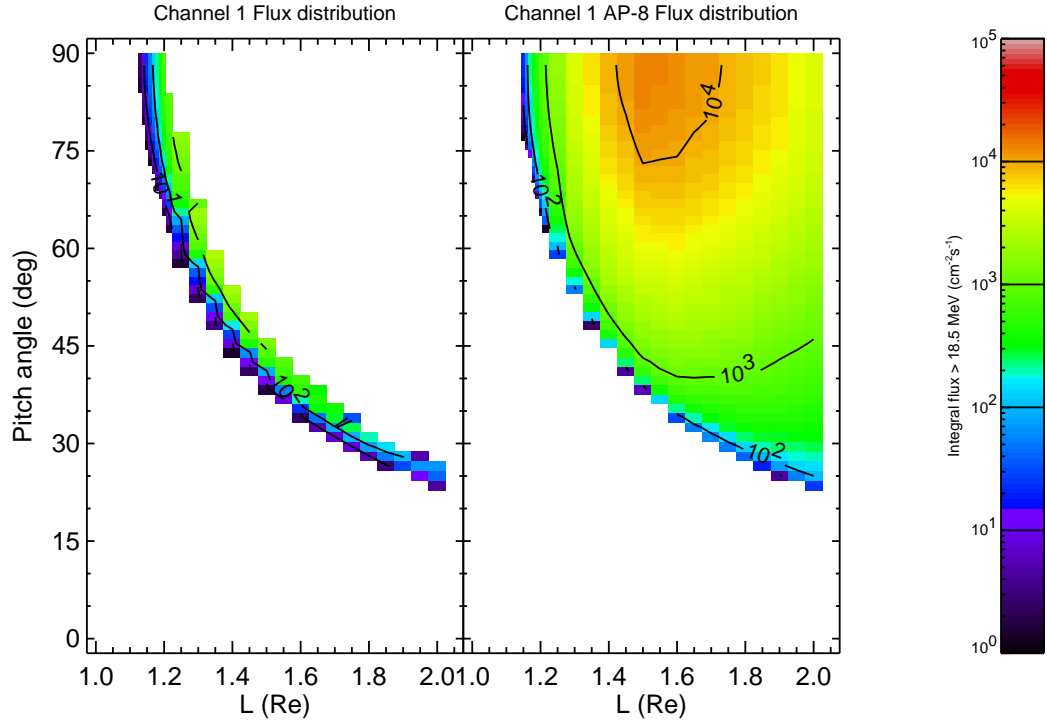


Figure 6.2. (L, α_0) Map of the PSB97 model and AP-8 MIN for channel 1

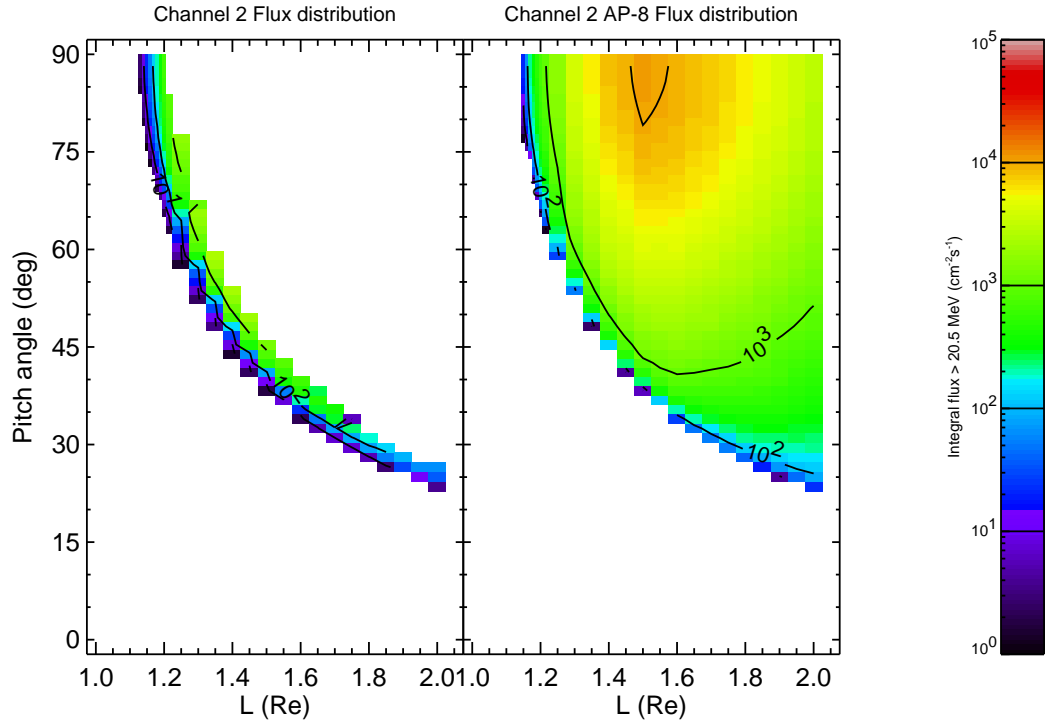


Figure 6.3. (L, α_0) Map of the PSB97 model and AP-8 MIN for channel 2

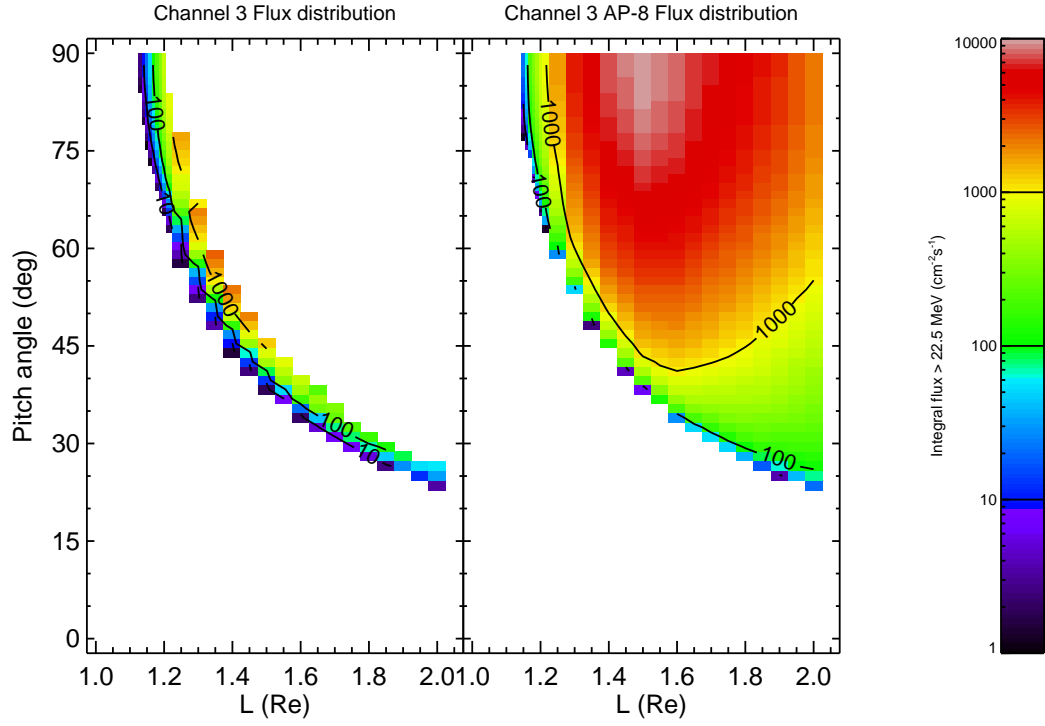


Figure 6.4. (L, α_0) Map of the PSB97 model and AP-8 MIN for channel 3

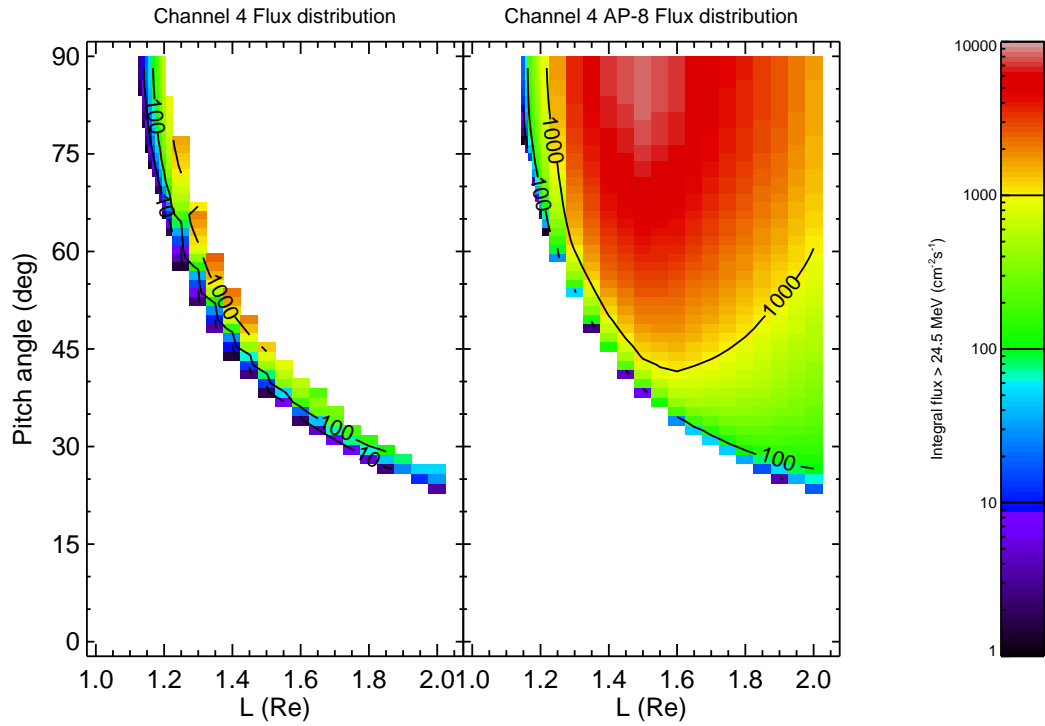


Figure 6.5. (L, α_0) Map of the PSB97 model and AP-8 MIN for channel 4

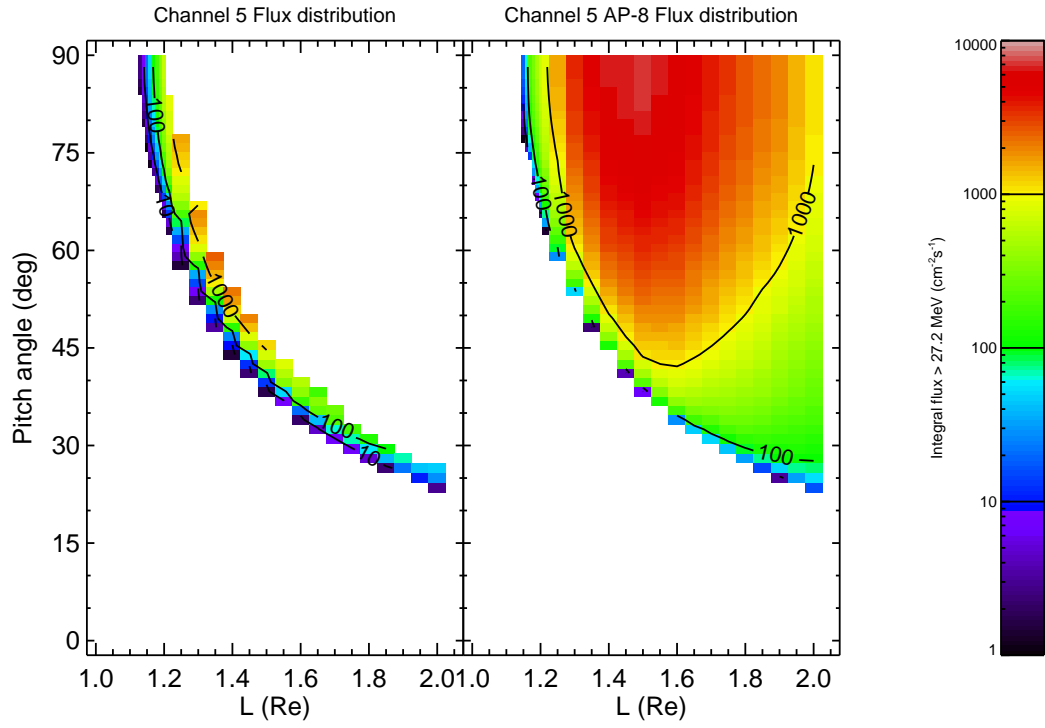


Figure 6.6. (L, α_0) Map of the PSB97 model and AP-8 MIN for channel 5

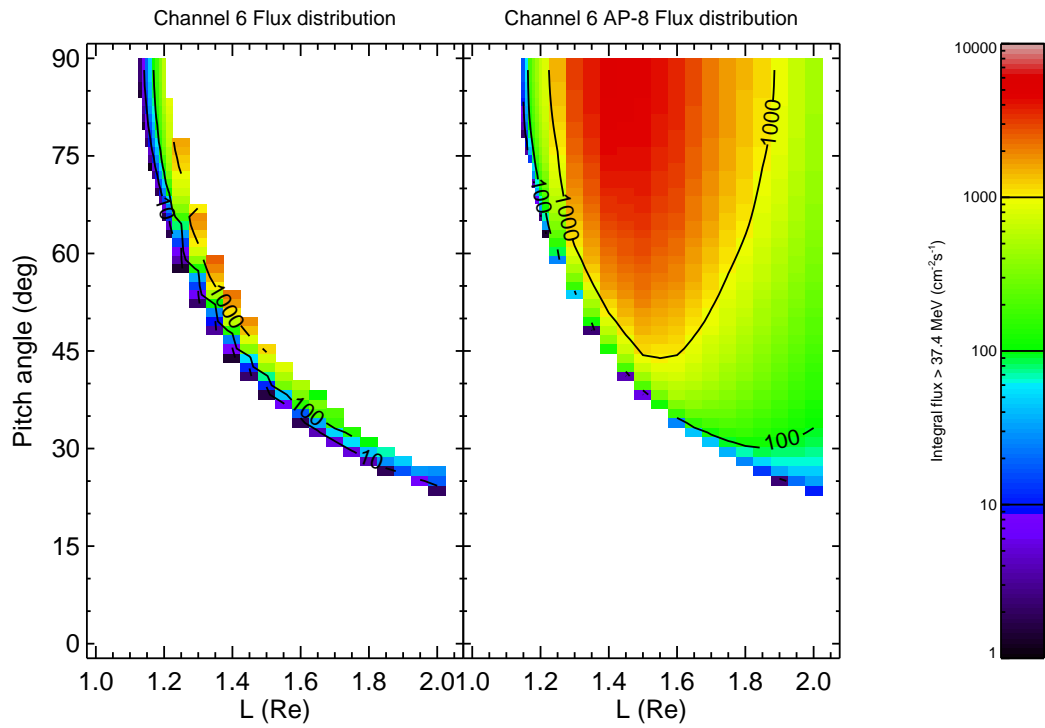


Figure 6.7. (L, α_0) Map of the PSB97 model and AP-8 MIN for channel 6

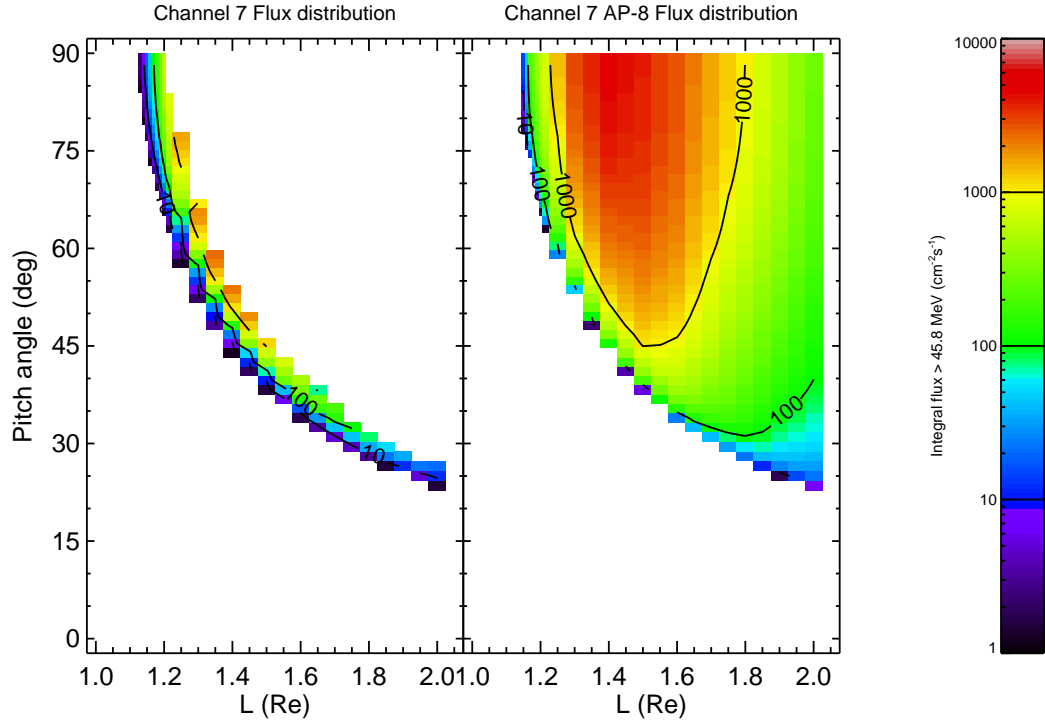


Figure 6.8. (L, α_0) Map of the PSB97 model and AP-8 MIN for channel 7

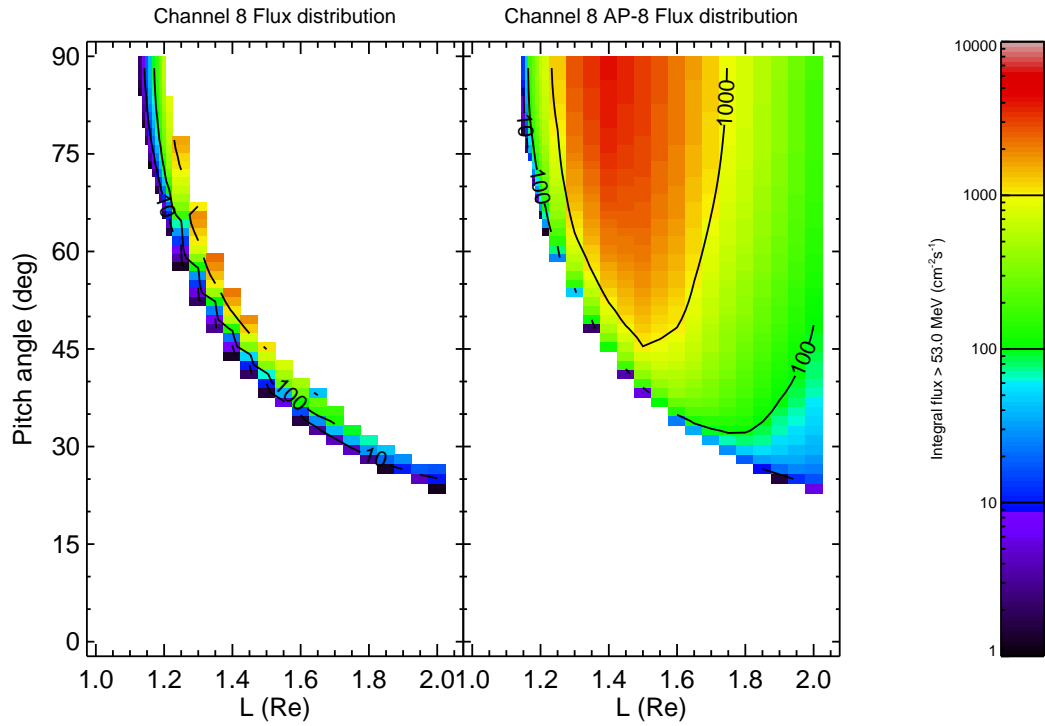


Figure 6.9. (L, α_0) Map of the PSB97 model and AP-8 MIN for channel 8

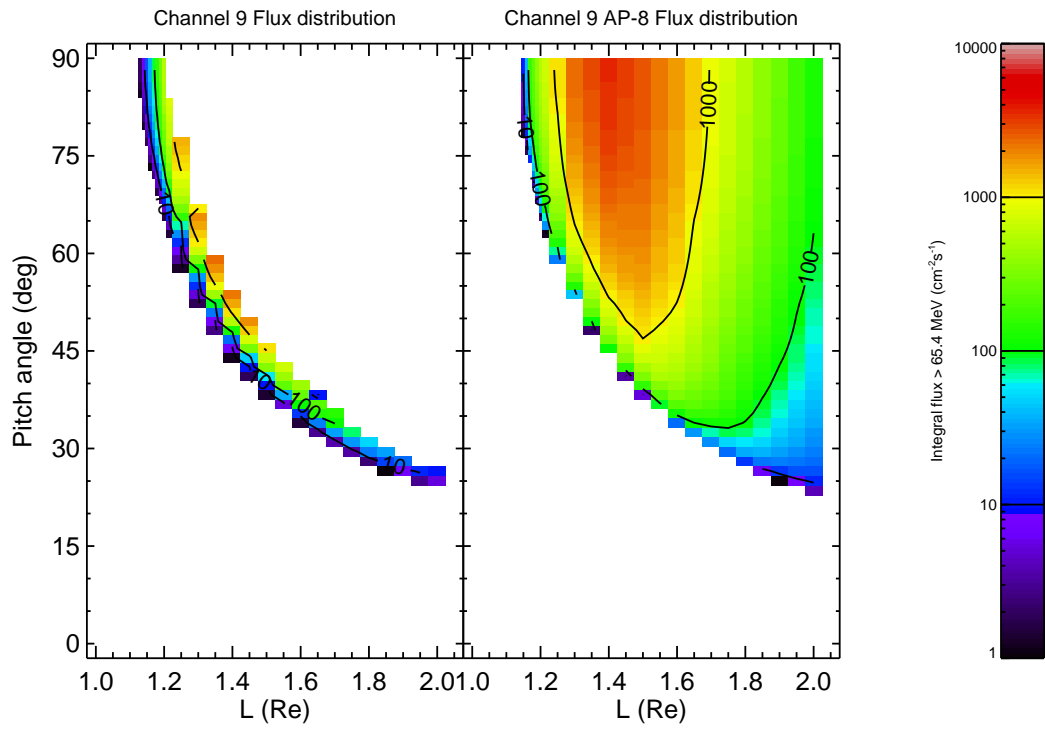


Figure 6.10. (L, α_0) Map of the PSB97 model and AP-8 MIN for channel 9

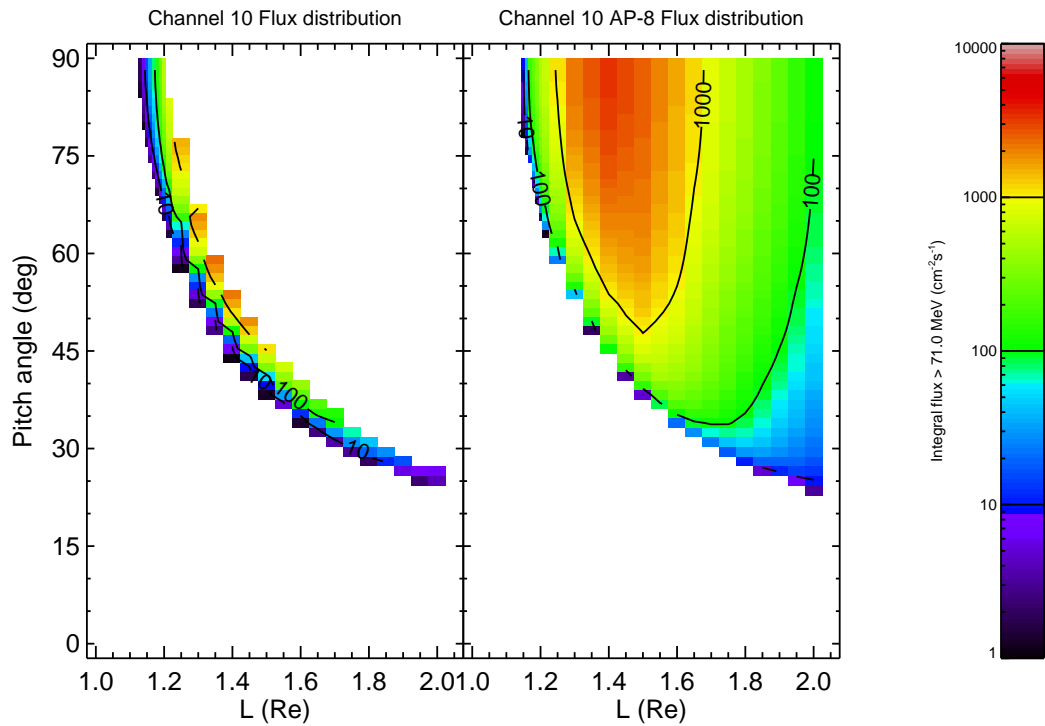


Figure 6.11. (L, α_0) Map of the PSB97 model and AP-8 MIN for channel 10

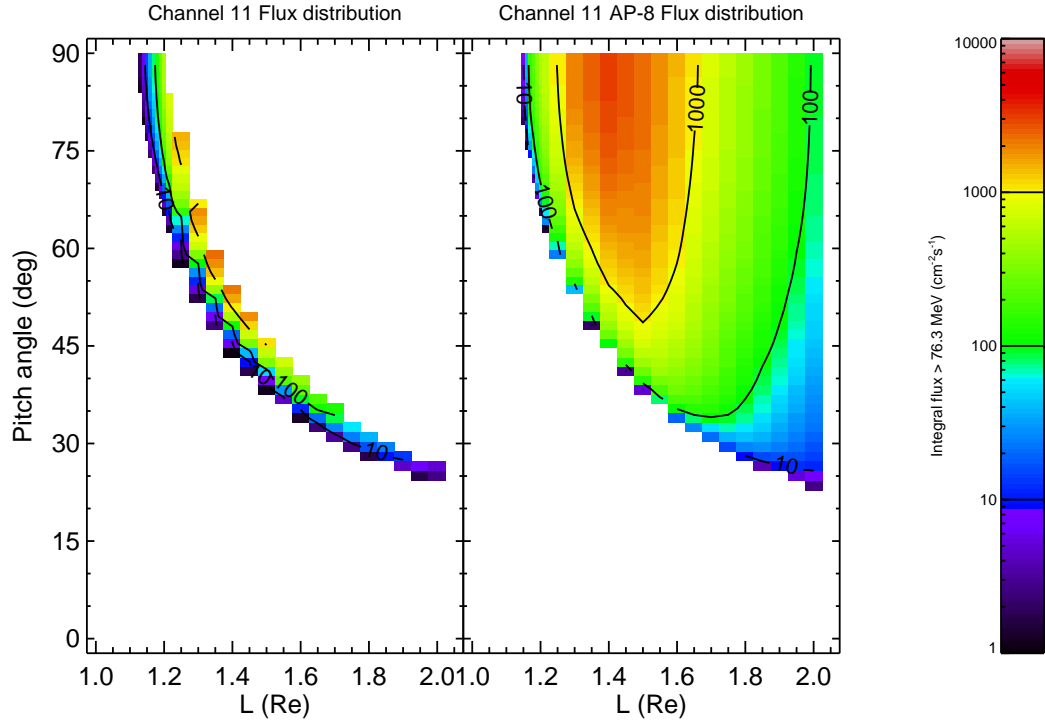


Figure 6.12. (L, α_0) Map of the PSB97 model and AP-8 MIN for channel 11

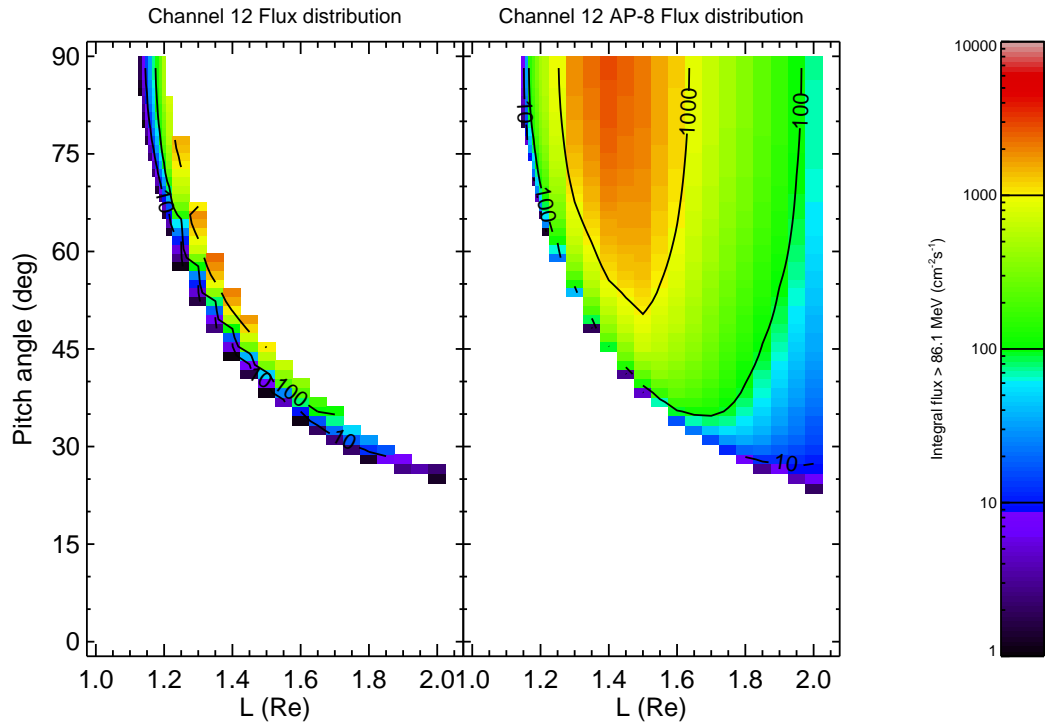


Figure 6.13. (L, α_0) Map of the PSB97 model and AP-8 MIN for channel 12

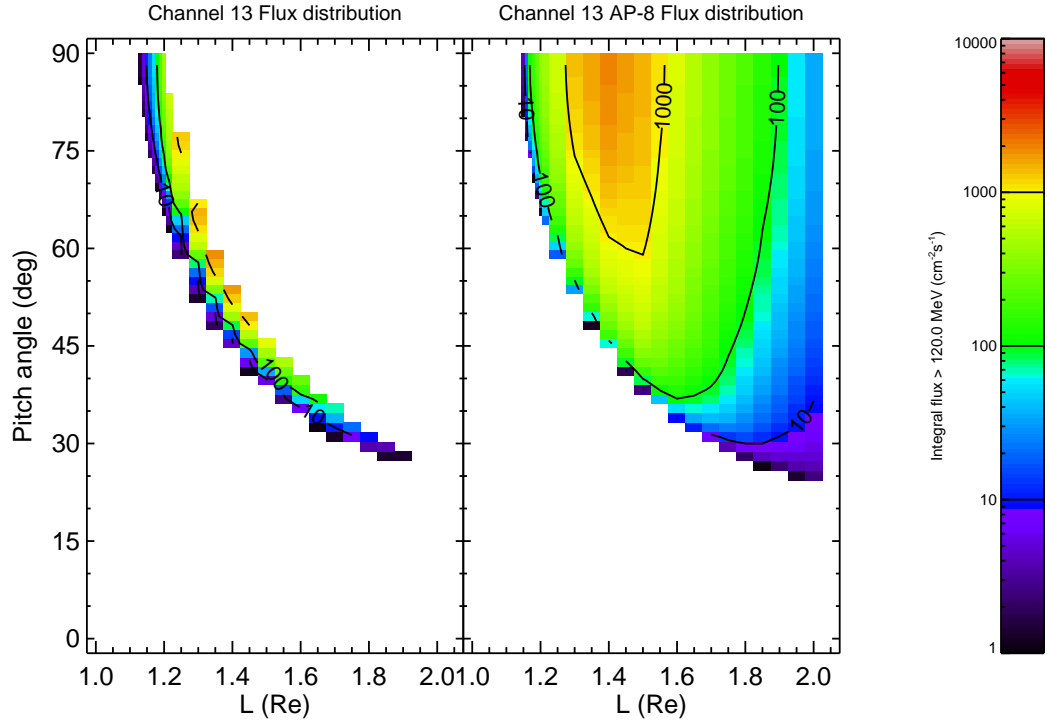


Figure 6.14. (L, α_0) Map of the PSB97 model and AP-8 MIN for channel 13

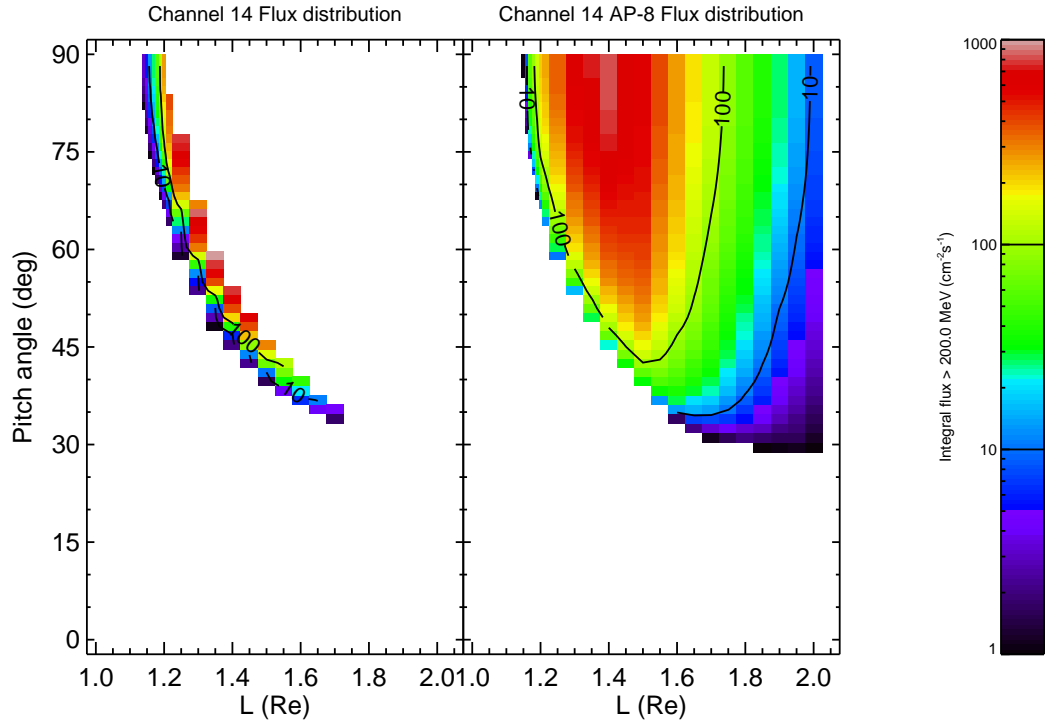


Figure 6.15. (L, α_0) Map of the PSB97 model and AP-8 MIN for channel 14

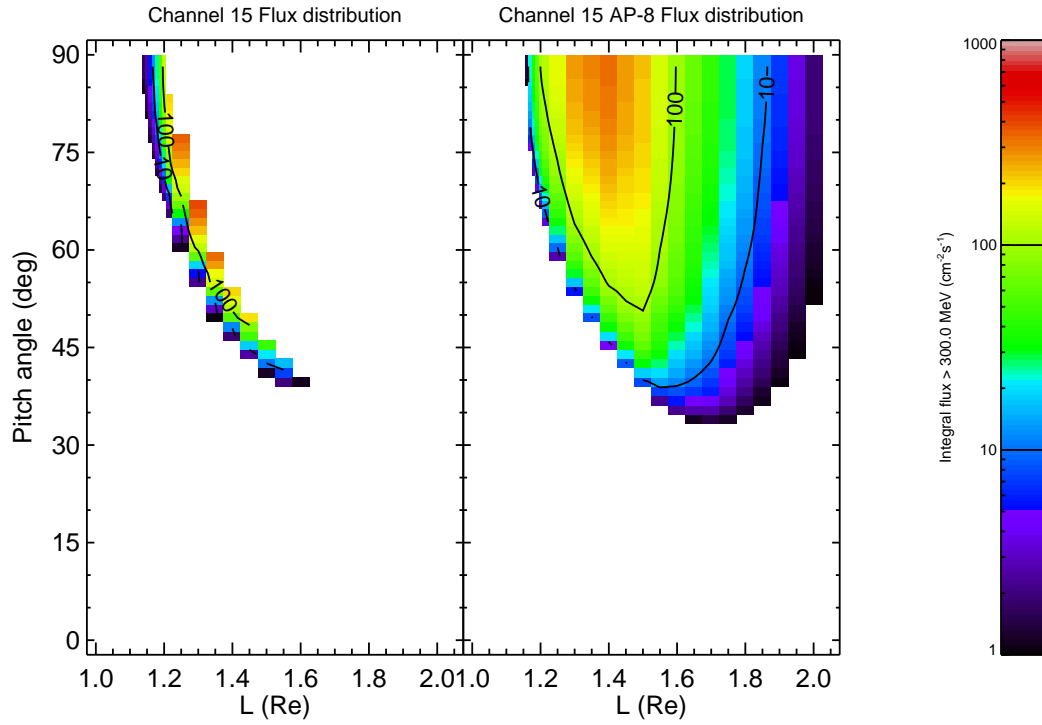


Figure 6.16. (L, α_0) Map of the PSB97 model and AP-8 MIN for channel 15

MODTOBD.FOR. This programme also transforms differential into integral fluxes. The implementation of the new SAMPEX model (called PSB97) in UNIRAD is described in Technical Note 10.

6.3.1 Comparison to AP-8

Figures 6.2–6.16 show the flux maps of the PSB97 model in (L, α_0) space, together with the directional AP-8 MIN maps for the same grid values. It can be seen that for the lowest L values the PSB97 fluxes are smaller than the corresponding AP-8 MIN fluxes by a factor of about two.

Another way of comparing the PSB97 model to AP-8 consists of drawing world maps of fluxes at fixed altitude. Figures 6.17 and 6.18 show the distributions of the PSB97 and AP-8 MIN proton flux >50 MeV at an altitude of 500 km, respectively. Again, the PSB97 flux is lower than the AP-8 MIN flux.

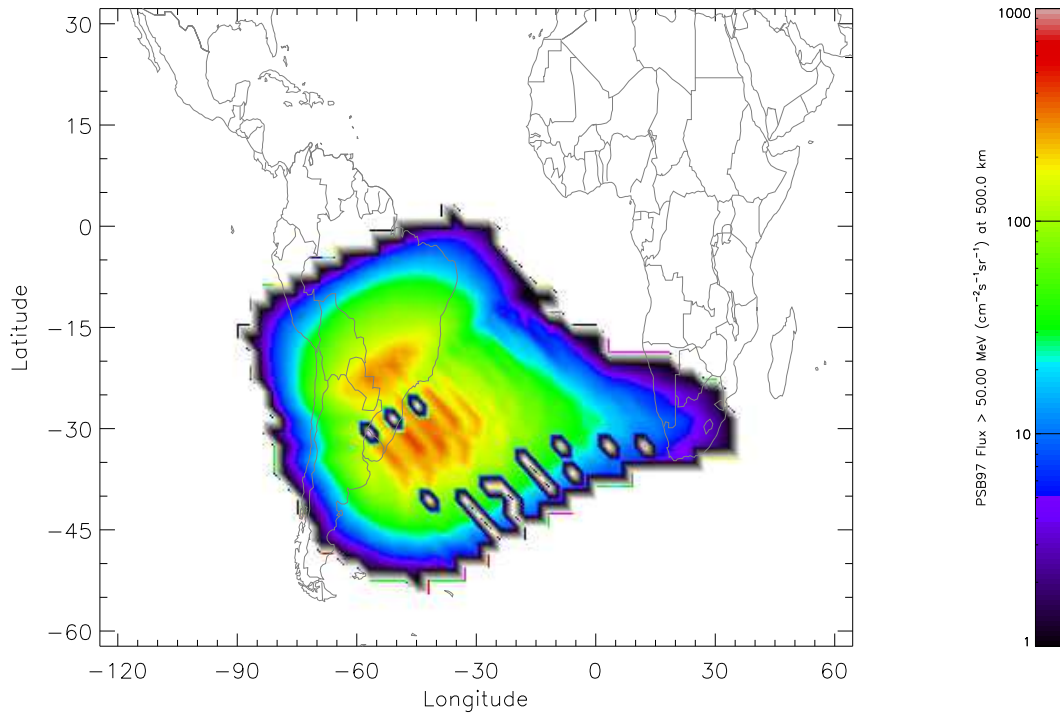


Figure 6.17. World map of the PSB97 >50 MeV proton flux at 500 km

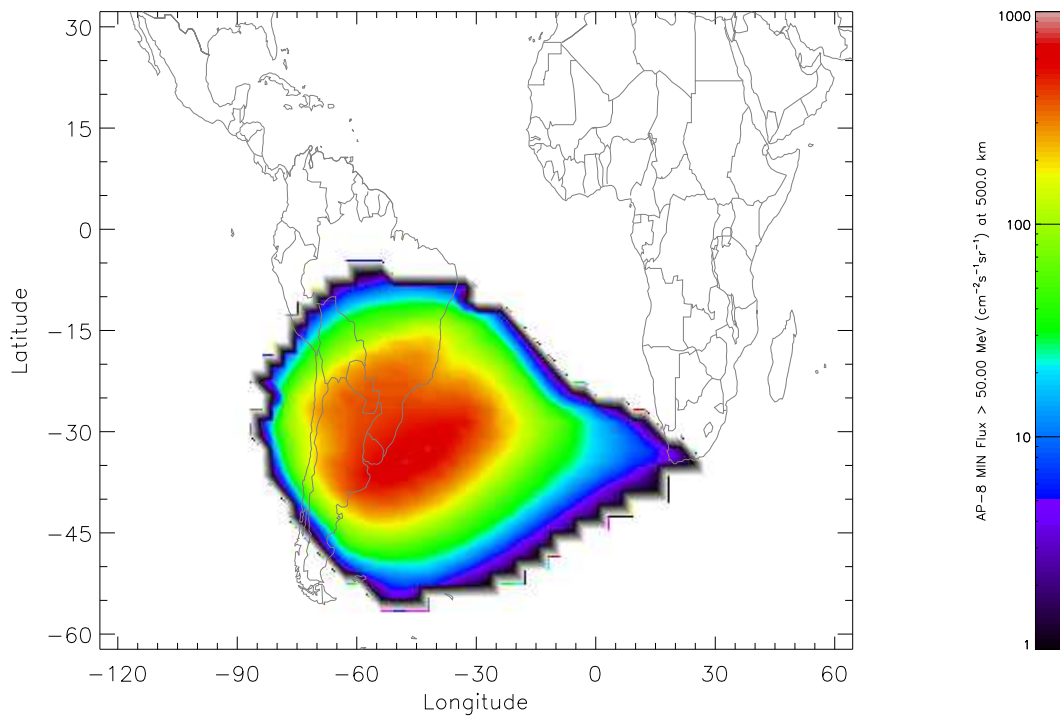


Figure 6.18. World map of the AP-8 MAX >50 MeV proton flux at 500 km

Chapter 7

Statistical analysis of the SAMPEX/PET data

This chapter contains a statistical analysis of the SAMPEX/PET proton counts and countrates. In Sect. 7.1, we show that the countrates measured over 6 second periods in a given spatial bin are very variable due to the wide variability of livetimes. Histograms of the countrates (i.e. counts over livetimes) often have a maximum around zero in regions where the particle fluxes are large. Indeed, in these regions, the livetimes are often very short and paradoxally many zero counts are then recorded. This is discussed in Sects. 7.2 and 7.3 where an analysis of the measured proton counts and of the livetimes is provided. Due to the variability of livetimes, the count histograms obtained during one month of measurements are not always Poisson distributed. By reducing the dispersion of livetimes, the count histograms are closely fitted with Poisson distributions. This confirms that the difference between the observed count histograms and the Poisson distribution is principally due to the dispersion of the livetimes in the PET measurements rather than to the time variation of the flux during the period of observation (i.e. one month in this case study).

Finally, in Sect. 7.4, a comparison between different methods for the calculation of the mean countrate is provided. We show that the simplest method, consisting of calculating the ratio of the sum of the counts and the sum of the livetimes over one month of observations, can safely be used to calculate the mean countrate for long observation periods.

7.1 Analysis of the countrate

We have studied the PET proton measurements in 6 (B, L) bins. The locations of the bins in (B, L) space are illustrated in Fig. 7.1, which represents the average countrate observed in the PET energy channel PHI32 (37.4–45.8 MeV) from Jul 1992 to Dec 1995, for times when the instrument was looking within 10° of the direction perpendicular to the local magnetic field vector.

One can see in Fig. 7.1 that the first bin is situated at low L and B where the spatial gradients

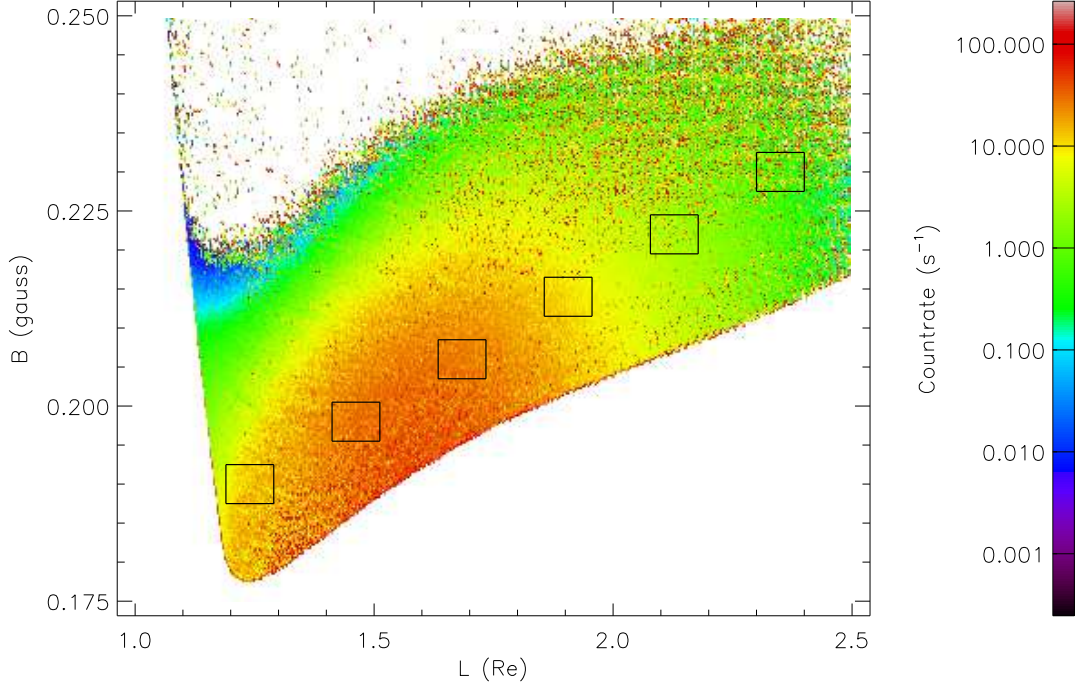


Figure 7.1. Distribution in (B, L) space of the average countrate observed in PET energy channel PHI32 from Jul 1992 to Dec 1995. Only measurements when the instrument was looking within 10° of the direction perpendicular to the local magnetic field vector are shown. The open rectangles represent the 6 bins selected for the statistical analysis.

in count rate are large. The second and third bins are near the South Atlantic Anomaly (SAA) where the flux of particles is large. The other bins are in regions where the countrate and flux are decreasing with L and B . The (B, L) coordinates of the centres of the bins are listed in Table 7.1. The bin dimensions are 0.0025 nT and $0.05 R_E$ in B and L , respectively. The spatial extent of these bins corresponds approximatively to 600 km in equatorial distance ($2\Delta L \simeq 600$ km) and about 40 km in altitude [$2\Delta h \simeq 2/3(\Delta B/B)R_E \simeq 40$ km].

Figure 7.2 shows the histograms of proton countrates (CR) obtained for each of the 6 bins during one month (Jul 1994). These histograms show that the individual countrates measured in a given bin are very variable. In regions where the fluxes are large (mainly the first three cells), there are two peaks (maxima), one at zero countrate and another at large countrates. This is due to the counting system making the livetimes shorter when the fluxes are large in a non linear manner. Many zero counts are then recorded during these very short livetimes. The zero counts may have an influence on the evaluation of the mean countrate. It is thus useful to carefully analyse the proton counts and livetimes.

Table 7.1. Probability P (in %) that the histogram of counts is distributed according to a Poisson law (null hypothesis) for six (B, L) bins and for the 15 energy channels of the PET telescope. The hypothesis that the histograms of proton counts are distributed following a Poisson law is rejected when $P < 5\%$. When the number of detected protons is not sufficient to perform a valid χ^2 test, -1 is listed.

B (Gauss)		0.190	0.198	0.206	0.214	0.222	0.230
L (R_E)		1.240	1.462	1.648	1.906	2.128	2.350
Detector	Energy range (MeV)	Bin 1	Bin 2	Bin 3	Bin 4	Bin 5	Bin 6
PLO21	18.5–20.5	100.0	100.0	27.6	50.4	97.6	11.3
PLO22	20.5–22.5	98.8	78.8	8.2	59.2	19.8	62.7
PLO23	22.5–24.5	22.3	84.9	82.8	62.1	5.0	41.4
PLO24	24.5–27.2	0.9	87.3	85.9	52.8	20.9	7.6
PHI31	27.2–37.4	0.0	1.1	77.0	30.4	52.6	0.0
PHI32	37.4–45.8	0.0	67.2	53.1	75.5	10.4	10.1
PHI33	45.8–53.0	0.8	99.3	95.0	46.1	61.3	14.9
PHI34	53.0–65.4	0.0	34.0	86.2	99.9	26.1	29.9
RNG04	65.4–71.0	25.1	55.4	98.7	89.4	47.9	76.6
RNG05	71.0–76.3	99.6	56.4	90.9	42.0	99.3	–1
RNG67	76.3–86.1	94.6	45.4	92.1	89.5	76.3	88.1
PEN81	86.1–120.0	0.0	54.8	90.0	86.3	99.1	–1
PEN82	120.0–200.0	1.6	54.3	40.2	–1	–1	–1
PEN83	200.0–300.0	0.0	32.8	83.8	–1	–1	–1
PEN84	300.0–500.0	0.0	78.1	–1	–1	–1	–1

7.2 Analysis of the counts

If the flux in a fixed location is constant in time (i.e. when there is no time variation of the environment over the period of observation) and if the probability of detection during a constant time of measurement is small, the detected counts are distributed following a Poisson distribution (Knoll 1989). We can test the following null hypothesis H for the PET measurements: the histograms of proton counts measured in a given (B, L) bin during a whole month are distributed following a Poisson law.

In the case of the PET detector, the probability p of detection in one energy channel is weak when compared to the total counts in the whole energy range. We have verified that the bins are small enough so that the flux is nearly uniform everywhere inside these bins. Nevertheless, it can be seen in Table 7.1 that the histograms of proton counts accumulated during one month are sometimes very different from a Poisson distribution. We will check whether the departure from Poisson distributions of the counts histograms are due to time variation of the flux or to the spread of livetimes.

For a Poisson distribution, the probability that the number of proton counts is equal to the

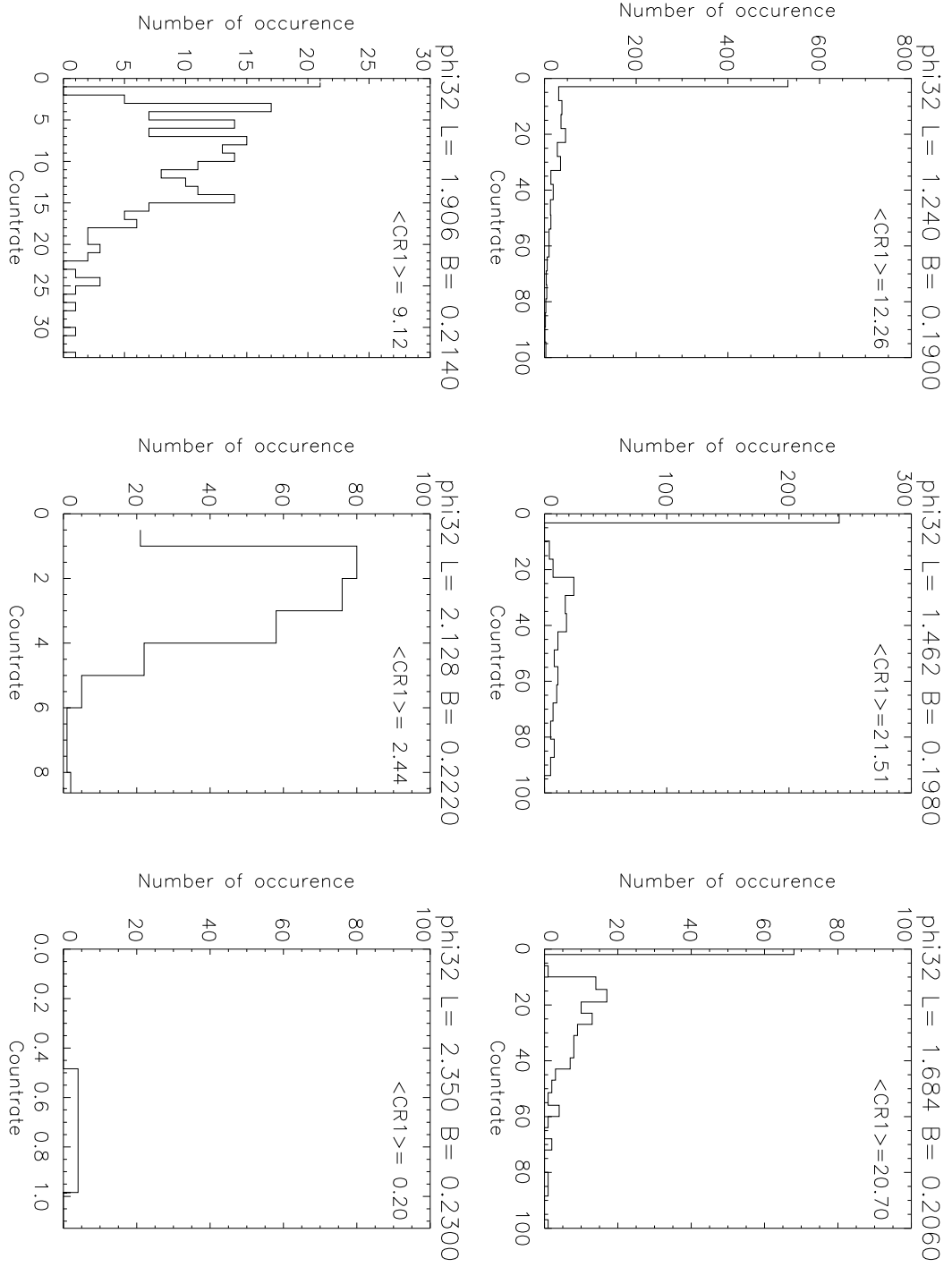


Figure 7.2. Histograms of PET proton count rates in the energy channel 37.4–45.8 MeV (PHI32) for the 6 bins shown in Fig. 7.1

integer value x_i is determined by:

$$p_i = \frac{\lambda^{x_i}}{x_i!} \exp(-\lambda) \quad (7.1)$$

where λ is the Poisson parameter. To test the hypothesis H , we can evaluate the difference between y_i , the actual number of time that x_i counts are recorded, and the corresponding number predicted by the Poisson distribution, i.e. np_i , where $n = \sum_{i=1}^r y_i$ the total number of counts over the period of one month assumed in our case study. To test H , the χ^2 function must be calculated:

$$\chi^2 = \sum_{i=1}^r \frac{(y_i - np_i)^2}{np_i} \quad (7.2)$$

where r is the maximum number of measured counts. A minimum of χ^2 is reached when λ corresponds to the mean of the observed counts i.e. when λ is equal to:

$$\lambda = \frac{1}{n} \sum_{i=1}^r y_i x_i. \quad (7.3)$$

The degree of freedom of this χ^2 test is $r - 2$. The level of significance P for the χ^2 test is obtained by comparing the values of χ^2 calculated by (7.2) with the values of the χ^2 function given in statistical tables (Burlington & May 1970). The probability that the y_i are distributed following a Poisson distribution with the parameter λ is P . One may consider that the hypothesis H has to be rejected when $P < 5\%$.

The values of P resulting from the H test are given in % in Table 7.1 for one month of measurements (July 1994) for all 15 energy channels and for the 6 (B, L) bins. When $r < 3$, the value of χ^2 is not significant since the number of counts is not large enough to form a statistically significant sample. This happens often for protons of very high energy (> 100 MeV). In this case, -1 is indicated in Table 7.1.

We can see that the hypothesis H is generally satisfied at the probability level of 5% in most bins and for most energy channels. Nevertheless, it has to be rejected in a few cases. For instance in bin 1 ($B = 0.19, L = 1.24$), the null hypothesis is rejected 9 times out of 15. This bin corresponds to a region where gradients in proton and electron countrates are important (see Fig. 7.1).

Figure 7.3 illustrates the histograms of counts for energy channel PHI32 (37.4–45.8 MeV) (solid line) as well as the best fit by a Poisson distribution (dashed line). On each graph the total number of counts n_{el} is indicated. The range of the livetimes τ , the mean livetime $\langle \tau \rangle$ and its standard deviation σ_τ , and the value of P in % are also indicated on each panel. In this example, the hypothesis H is accepted in each bin except in bin 1 where $P < 5\%$ (see also the row corresponding to PHI32 in Table 7.1). The probability that the proton counts are distributed following a Poisson law is not very high either in bins 5 and 6 since $P \simeq 10\%$ in both of these cases. To check whether these departures from the Poisson distribution is a consequence of time variations of the fluxes over the one month period considered, or whether it is due to the spread of livetimes, we analyse the distribution of livetimes in Sect. 7.3.

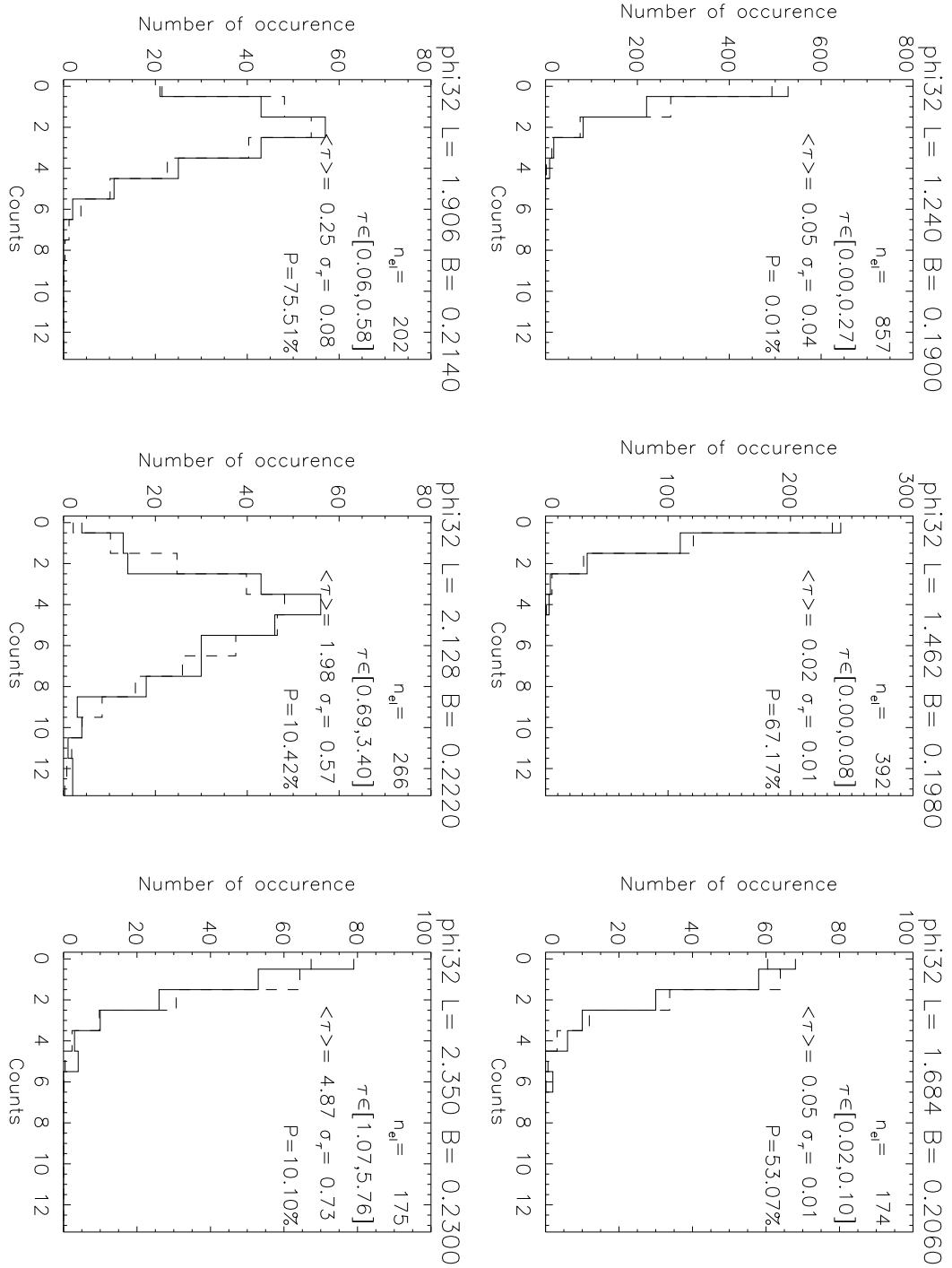


Figure 7.3. Histograms of PET PHI32 proton counts (solid lines) fitted by Poisson distributions (dashed line) with the χ^2 method, for the 6 (B , L) bins shown in Fig. 7.1

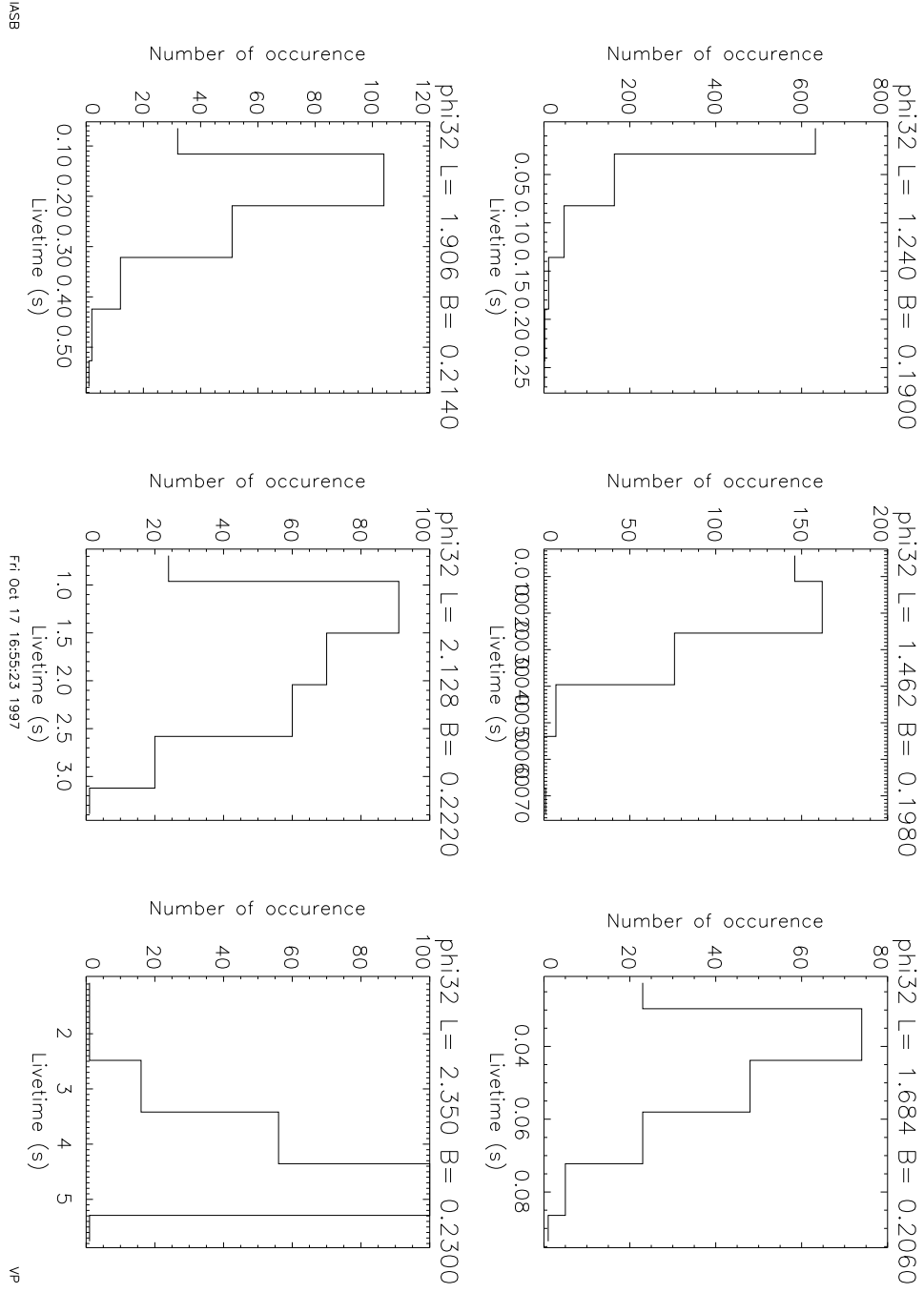


Figure 7.4. Histograms of livetimes in the PET PHI32 channel for the 6 (B, L) bins shown in Fig. 7.1

7.3 Analysis of the livetimes

In regions of large flux, the dispersion of the livetimes is particularly large compared to their mean value. This results from the characteristics of the instrument but it may also indicate a time variation of the flux over the period of observation. Indeed, another possible reason for the histograms to depart significantly from a Poisson distribution may be that the value of λ (i.e. the mean of the counts) has changed during the period of sampling, i.e. during Jul 1994. The initial aim of this study was to verify whether or not the histograms of counts do not reveal the superposition of two (or more) Poisson distributions with two (or more) different values of λ corresponding to a temporal evolution of the proton energy spectrum over a period of one month. This study is made difficult by the variability of the livetimes.

Note that the difference between a Poisson distribution and the observed distributions can also be due to a flux gradient inside the (B, L) bin. This could be the case in bin 1 where the gradient of counts is large as shown in Fig. 7.1. This problem can be eliminated by taking a smaller bin but the number of measurements will then become too low to be a statistically significant sample. The relatively good agreement between the histograms and the Poisson distributions in most of the bins indicates however that the size of the bins is generally small enough.

The livetimes are variable due to the characteristics of the instrument. In regions where the flux of electrons and protons is low, the mean livetime is close to 6 s (for instance bin 6). But in regions where the flux is large (for instance in bin 1), the livetimes can be reduced to less than 0.1 s. This is illustrated in Fig. 7.4 where we show the histograms of livetimes for all 6 bins for the detector PHI32. Note that the livetimes are neither constant nor uniformly distributed.

When the mean livetime is close to 6 s, the standard deviation of livetimes is generally smaller than 50% of the mean livetime $\langle \tau \rangle$. But when the livetimes are small, the standard deviation is as large as the mean value itself. To check if the deviation of the count histograms from Poisson distributions is due to the dispersion of the livetimes, we have subdivided the livetimes in smaller intervals so that they can be considered as approximately constant in each of these smaller intervals. We then calculate then count histograms associated to these subintervals and we test again the hypothesis H , with the additional condition that the number of measurements is sufficient for a statistical study. We disregard samples for which the number of measurements n_{el} in the subinterval is less than 10.

An example is shown in Fig. 7.5 for the detector PHI32 in bin 1. Figure 7.5 shows the histograms of counts when the dispersion of the ranges of livetimes is reduced by subdividing the whole livetime interval $[0, 0.27]$ in five subintervals with equal spacing. While the test of hypothesis H had to be rejected for the whole livetime interval ($P < 5\%$), the test is satisfied when the livetimes are distributed in livetime subintervals with lower dispersion. Note that the histograms corresponding to the intervals $[0.16, 0.21]$ and $[0.21, 0.27]$ are not shown due to a too small number of counts.

We have verified that for each bin and energy channel in Table 7.1 the null hypothesis H becomes accepted for all subintervals since now the dispersion in livetime has been reduced, i.e. the livetime in each subinterval is almost the same for each measurement in the smaller

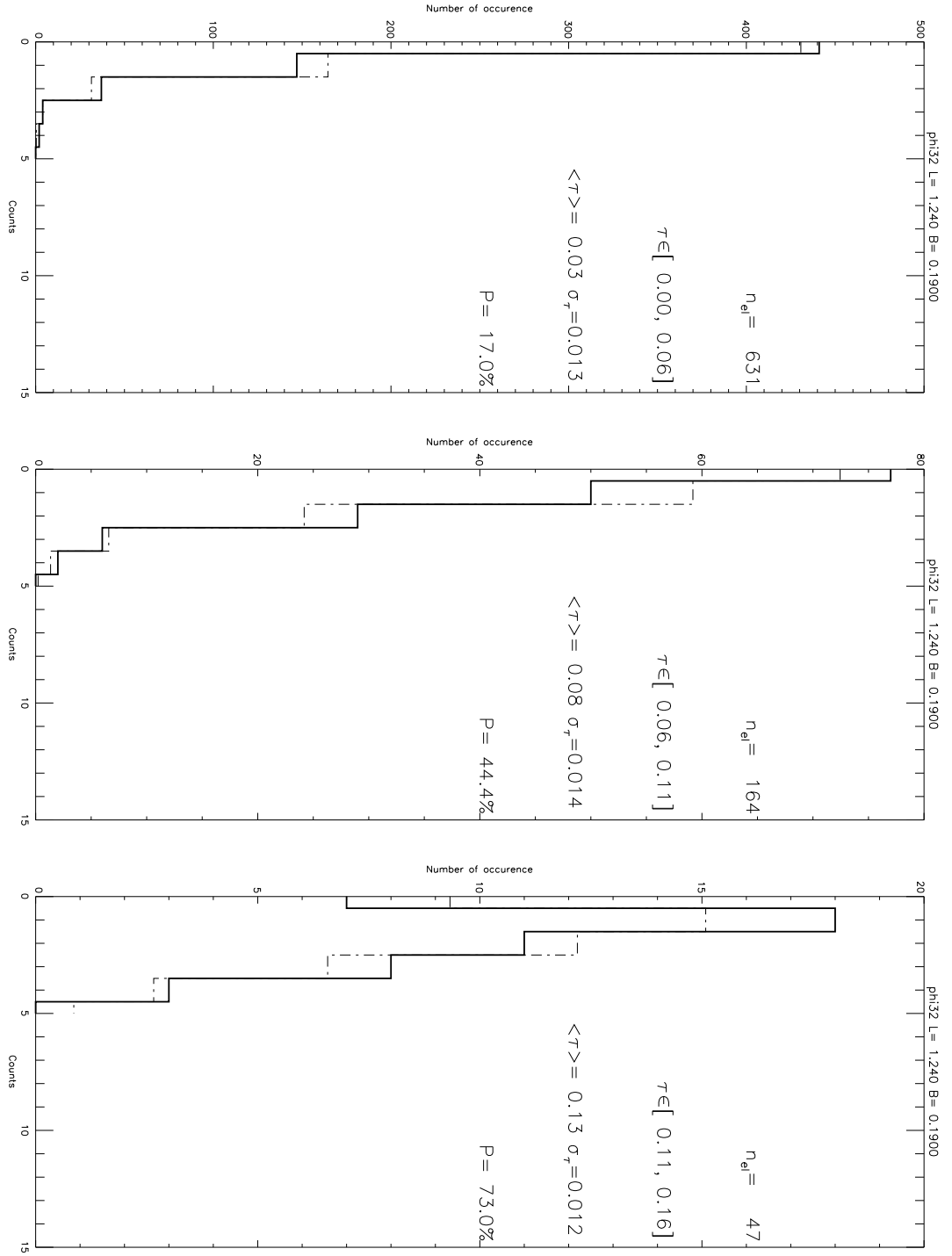


Figure 7.5. Histograms of PET PHI32 proton counts in bin 1 ($B = 0.19, L = 1.24$) when the livetime interval is subdivided in 5 equal subintervals. The probability that the count histograms are Poisson distributed increases in this case. P is now always larger than 5%. The histograms corresponding to the intervals $[0.16, 0.21]$ and $[0.21, 0.27]$ are not shown due to the too small number of counts.

samples. This is the case even for (B, L) bins where the hypothesis H had to be rejected for the total livetime interval. Note however that the value of P is not always larger for the subintervals than it was in the total livetime interval.

We demonstrated that the variations of the livetimes prevent the proton counts to be Poisson distributed. Therefore, the deviations from the Poisson distribution should be attributed to the non-constancy of the livetimes rather than to a variation of λ or p_i over the sampling period time.

7.4 Calculation of the mean countrate

There are different ways to calculate the mean countrates during one month in a bin. The question we try to answer now is which of these methods is the most reliable when the livetimes are not constant but are widely dispersed. Three different methods have been used to calculate mean countrates and to test the effects of the division into livetime subintervals on the evaluation of the mean countrate. The algorithms of these three methods are:

$$\langle \text{CR1} \rangle = \frac{\sum_{i=1}^n \text{COUNTS}}{\sum_{i=1}^n \text{LIVETIMES}}, \quad (7.4)$$

$$\langle \text{CR2} \rangle = \frac{\sum_{i=1}^n \frac{\text{COUNTS}}{\text{LIVETIMES}}}{n}, \quad (7.5)$$

$$\langle \text{CR3} \rangle = \frac{\sum_{j=1}^5 \langle \text{CR2} \rangle_j}{\sum_{j=1}^5 1}, \quad (7.6)$$

where j is considered in $\langle \text{CR3} \rangle$ only if $P > 5\%$.

$\langle \text{CR1} \rangle$ Is the ratio of all counts over one month of time and the sum of the livetimes over the same period of time. $\langle \text{CR1} \rangle$ Is generally used when the livetimes are not constant.

$\langle \text{CR2} \rangle$ Is the average of countrates for each individual measurement. The histograms of these countrates are shown in Fig. 7.2. It can be seen that they depart even more significantly from Poisson distributions than the histograms of counts shown in Fig. 7.3. Note that the number of elementary arithmetic operations involved in the calculation of $\langle \text{CR2} \rangle$ is larger than for $\langle \text{CR1} \rangle$.

$\langle \text{CR3} \rangle$ Is an average of countrates $\langle \text{CR2} \rangle_j$ calculated for 5 subintervals of livetimes. When the number of measurements in a subinterval is lower than 10, the sample is statistically not significant and P can not be calculated with the χ^2 test. In this case, the subinterval j is not considered, as well as subintervals where $P_j < 5\%$.

The results obtained for detector PHI32 are given in Table 7.2. The countrate values of $\langle \text{CR2} \rangle$ are not always larger than those obtained with $\langle \text{CR1} \rangle$ as in this example. The differences between $\langle \text{CR1} \rangle$ and $\langle \text{CR2} \rangle$ are generally small. A method to evaluate the difference between these two values of the mean countrate is to analyse whether the value of $\langle \text{CR1} \rangle$ is located inside the confidence interval of $\langle \text{CR2} \rangle$. $\langle \text{CR1} \rangle$ is generally inside a confidence interval of 90% of $\langle \text{CR2} \rangle$.

Table 7.2. Mean countrates calculated by different methods for the detector PHI32 during July 1994

Mean countrate (s^{-1})	Bin 1	Bin 2	Bin 3	Bin 4	Bin 5	Bin 6
$\langle \text{CR1} \rangle$	12.3	21.5	20.7	9.12	2.44	0.196
$\langle \text{CR2} \rangle$	13.3	22.5	21.1	9.66	2.56	0.196
$\langle \text{CR3} \rangle$	12.5	22.5	21.5	9.48	2.52	0.183
$\langle \text{CR2}_1 \rangle$	14.2	24.1	21.2	13.1	3.18	
$\langle \text{CR2}_2 \rangle$	10.7	22.5	22.6	9.85	2.90	
$\langle \text{CR2}_3 \rangle$	12.5	21.0	20.1	8.37	2.42	0.117
$\langle \text{CR2}_4 \rangle$			22.2	6.58	2.14	0.248
$\langle \text{CR2}_5 \rangle$					1.95	0.185
P_1 (%)	17	50	42	78	72	
P_2 (%)	44	99	36	66	62	
P_3 (%)	73	64	78	39	21	45
P_4 (%)			89	65	75	62
P_5 (%)					47	8

The mean countrates calculated for one month when the livetime interval is divided in smaller subintervals are represented by $\langle \text{CR2}_j \rangle$. Note that the subdivision of the livetime interval in equal subintervals modifies the mean value of the countrate in each subinterval. The value of $\langle \text{CR3} \rangle$ always remains in the 90% confidence interval of the countrate. It can be seen that the subdivision of the livetime interval does not drastically modify the value of the calculated mean countrate.

Since the differences between $\langle \text{CR1} \rangle$ and $\langle \text{CR2} \rangle$ or $\langle \text{CR3} \rangle$ do not generally exceed 5% of $\langle \text{CR1} \rangle$, we conclude that any of these three methods can be used to determine the particle flux with an accuracy better than 5%. But since $\langle \text{CR1} \rangle$ is the simplest and fastest to compute, we recommend this method to obtain the mean countrate. It cumulates the counts over a long active time during which a large number of counts are detected. It is also the easiest method to apply.

$\langle \text{CR2} \rangle$ Represents the mean of individual countrates. It can give a false value of the real mean countrate when the time period to calculate the mean value is too short. Indeed, in regions where fluxes are large, the livetimes become very short and many observed numbers of counts are then equal to zero. With the $\langle \text{CR2} \rangle$ method, the zero counts have the same weight independently of their associated livetime. $\langle \text{CR3} \rangle$ Permits to give different weights to the zero counts as a function of the livetime but is rather cumbersome to compute. For a sufficiently long period like one month, the three different methods give approximately similar mean values. But this may become more critical for shorter periods of time, i.e. when the total number of counts over the period of observation shrinks to small values.

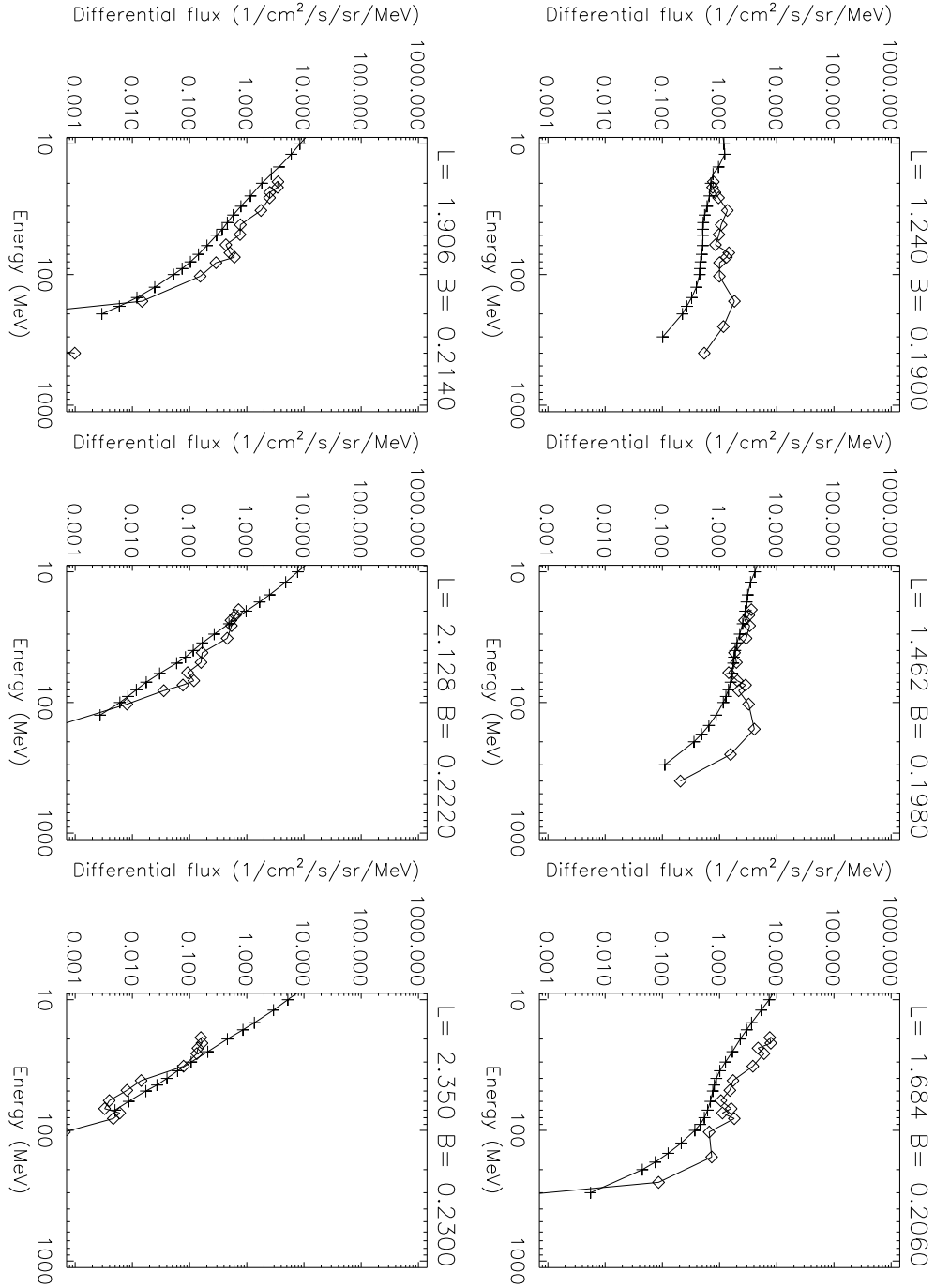


Figure 7.6. Differential unidirectional spectrum in the 6 (B, L) bins shown in Fig. 7.1. The spectra obtained with the PET measurements are represented by diamonds for July 1994. The crosses correspond to the spectrum obtained with the AP-8 empirical model divided by 4π .

7.5 Energy spectra

We have calculated the mean count rate during one month with $\langle CR1 \rangle$ for each of the 15 PET energy channels. We then divided the mean count rate by the interval in energy of the considered channel and by the geometric factor to determine the differential unidirectional energy spectra measured by PET in all 6 (B, L) bins. The spectra are shown in Fig. 7.6 for the month of July 1994 (diamonds).

A peak is observed in all bins at about 100 MeV. This population is present during more than one year and slowly decreases. This feature is absent in the unidirectional spectra of the AP-8 model, which are superimposed as crosses in Fig. 7.6. The AP-8 unidirectional fluxes in each bin are obtained from the omnidirectional flux given by the AP-8 model by dividing them by 4π , although the proton flux is generally not isotropic in the radiation belts. Moreover, the low altitude fluxes are subjected to important variations during unpredictable solar flare particle events and periods of large solar activity level, so that observed spectra can be very different from those given by the model. The peak appearing around 100 MeV on the energy spectra obtained with the PET measurements is an interesting feature which may correspond to an additional population of high energy protons injected in the inner belt before July 1994. A more specific study would permit to explain the peak in the spectra observed by PET.

7.6 Conclusions

Histograms of proton counts have been compared with Poisson distributions. We have found that the distributions of counts are sometimes very different from expected Poisson distributions, especially in regions of low L and B values where the gradients of counts and fluxes are important. We have shown that this feature is linked to the variability of the livetimes. The livetimes of the detector PET on the satellite SAMPEX are not constant but depend on the flux of electrons and protons penetrating into the particle telescope. The livetimes can become very small in the South Atlantic Anomaly due to the large numbers of electrons rapidly saturating the detector. The evaluation of the mean countrates is then affected by errors on the count measurements and on the livetime measurements. By subdividing the range of livetimes in 5 smaller subintervals, we have reduced the livetime dispersion. The null hypothesis that count histograms are Poisson distributed is then better satisfied.

The results summarised in Table 7.2 indicate that different methods to calculate the mean countrates and to determine flux of particles lead nearly to the same value. The first method generally used when the livetimes are not constant can safely be used to determine the particle flux although the third, more sophisticated but more cumbersome, method should in principle be preferred from a statistical point of view. For none of the studied cases with a sufficient number of events did we find significant differences.

Part III

The UARS data base and model

Chapter 8

Mission and detector description

J.D. Winningham, SwRI, Texas, PI for the PEM instrument on the UARS mission, was approached by the TREND project manager, in April 1995. At that time the PEM data had to be recalibrated, and the software to retrieve and process the UARS data had to be reprocessed to run with the VMS operating System installed at BIRA/IASB. Sharber et al. (1996) outline the capabilities as well as the limitations of the PEM-UARS data set for the construction of a new radiation belt models for energetic trapped protons.

In 1996, M. Kruglanski visited SwRI, Texas, to examine the PEM data and to get familiar with the existing data processing software running there on Sun stations. Thanks to the efficient collaboration of the whole PEM team at SwRI, and especially of R. Frahm, we have been able to transfer two years of PEM data to BIRA/IASB via FTP. Pre-processing of these data had to be done on the SwRI computer facilities due to computer Operating System incompatibility.

Unfortunately, the PEM detectors directional responses (geometric factor) to energetic proton has not been obtained from Lockheed Palo Alto Research Laboratory. Therefore, we had to make an educated guess to determine the sensitivity of the detectors for different angles of penetration of the energetic protons. This limits to some extent the validity of the radiation belt model obtained from the UARS data.

8.1 The UARS mission

The Upper Atmosphere Research Satellite (UARS) was launched by the space shuttle Discovery on 12 September 1991 into a near circular orbit at 585 km with 57° inclination. It operated almost continuously until April 1995 after which time the PEM coverage was considerably reduced. The satellite is three-axis stabilized and covers all the local times in approximately 36 days. About every 34 days, the spacecraft reverses its attitude by a 180° -rotation around its vertical axis (Reber 1993, Reber et al. 1993). A line drawing of the UARS spacecraft including the placement of the various experiments is presented in Fig. 8.1. The spacecraft has a length of 10.7 m and a total mass of 6,540 kg.

The goal of the UARS mission was to understand the chemistry, dynamics, and energy bal-

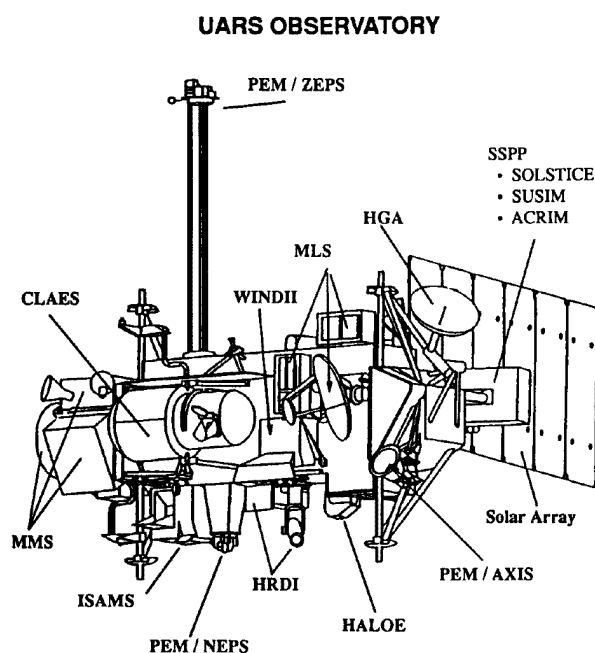


Figure 8.1. Line drawing of the UARS observatory showing the placement of the various instruments. The proton and electron sensor are designated by PEM/ ZEPS and PEM/NEPS.

ance above the troposphere as well as the coupling between these processes and atmosphere regions. The ten experiments onboard UARS, listed in Table 8.1, meet these objectives. Four experiments (CLAES, ISAMS, MLS and HALOE) are devoted to measure the altitude profiles of chemical species. Two experiments (HRDI and WINDII) are devoted to measure the atmospheric winds. Three experiments (SOLSTICE, SUSIM and ACRIM) are devoted to measure the energy inputs from the Sun. One experiment (PEM) is devoted to measure the energy input to the upper atmosphere contributed by the flux of charged particles penetrating into the Earth's magnetosphere. More extensive information can be found in the dedicated sections of the Geophysical Research Letters (Reber 1993, and following papers in the same issue) and of the Journal of Geophysical Research (Reber et al. 1993, and following papers in the same issue).

8.2 Particle Environment Monitor

The Principal Investigator (PI) of the Particle Environment Monitor (PEM) experiment is J.D. Winningham of the Southwest Research Institute (SwRI) and the collaboration includes more than thirty scientists from seven institutes. The main objective of the PEM experiment is to provide comprehensive measurements of energy inputs into the Earth's atmosphere by energetic particle precipitations (Winningham et al. 1993, Sharber et al. 1993). The four instruments which are part of the PEM experiment are listed in Table 8.2.

Table 8.1. List of the UARS experiments

CLAES	Cryogenic limb array etalon spectrometer
ISAMS	Improved stratospheric and mesospheric sounder
MLS	Microwave limb sounder
HALOE	Halogen occultation experiment
HRDI	High resolution doppler imager
WINDII	Wind imaging interferometer
SOLSTICE	Solar/stellar intercomparison experiment
SUSIM	Solar ultraviolet spectral irradiance monitor
ACRIM	Active cavity radiometer irradiance monitor
PEM	Particle environment monitor

Table 8.2. List of the PEM instruments

AXIS	Atmospheric X-ray imaging spectrometer
HEPS	High-energy particle spectrometer
MEPS	Medium-energy particle spectrometer
VMAG	Vector magnetometer

The AXIS instrument consists of an array of cooled silicon detectors. It measures the intensities of bremsstrahlung X-rays that are generated when energetic electrons penetrate the atmosphere.

The HEPS instrument consists of six silicon detector telescopes and two surface barrier detectors. These detectors measure protons in the energy range from 0.1 to 150 MeV and electrons from 0.03 to 5 MeV.

The MEPS instrument is made of eight divergent plate electrostatic analyzers. They measure particles in the energy range from 1 eV to 32 keV.

The VMAG instrument is a boom-mounted three-axis fluxgate magnetometer. Each sensor has a dynamic range of $\pm 65,000$ nT with a resolution of 2 nT and has the capability to measure disturbances in the field in the frequency range 5–50 Hz.

The HEPS and VMAG instruments of the PEM experiment provide a good opportunity to study the proton radiation belt at low altitude to an energy of 150 MeV. From here on, we will focus on the HEPS instrument of the PEM experiment and especially on the detectors dedicated to the high-energy protons.

Table 8.3. Characteristics of the HEPS detectors

Detector name	Angle [degrees]	Electron energy range [MeV]	Proton energy range [MeV]	Geometric factor [cm ² sr]
HEPS1/T1	+45	0.03 – 5.0	0.5 – 150.0	0.54
HEPS1/T2	+15	0.03 – 5.0	0.5 – 150.0	0.54
HEPS1/LEP	+15	none	0.1 – 0.5	0.07
HEPS2/T1	+90	0.03 – 5.0	0.5 – 150.0	0.54
HEPS2/T2	-15	0.03 – 5.0	0.5 – 150.0	0.54
HEPS2/LEP	-15	none	0.1 – 0.5	0.07
HEPS3/T1	+165	0.03 – 1.5	none	1.53
HEPS3/T2	-165	0.03 – 1.5	none	1.53

8.3 The HEPS instrument

The technical information on the HEPS telescopes presented in this section is mainly collected from Winningham et al. (1993) and Sharber et al. (1996).

The HEPS sensors were supplied by Lockheed Palo Alto Research Laboratory. They consist of six solid state telescopes and two low-energy proton (LEP) detectors. They are structured into three independent units (HEPS1, HEPS2 and HEPS3) and measure high energy protons and electrons in different viewing directions. They are all situated in the vertical plane that contains the spacecraft velocity vector. Four of the telescopes and the two LEP detectors measure locally downcoming protons and electrons while the two other telescopes measure locally upcoming electrons. The viewing direction, the energy range and the geometric factor of the eight detectors are listed in Table 8.3. The direction of each detector is specified by the angle from zenith to nadir in the local vertical plane. The field of view is 30°. The uncertainties in the geometric factors are 2.5% for the HEPS1 and HEPS2 telescopes, 1.5% for the HEPS3 telescopes and 3.5% for the LEP detectors.

For the study of the proton radiation belt, only the four telescopes HEPS1/T1, HEPS1/T2, HEPS2/T1 and HEPS2/T2 are useful. Except for their orientation, these telescopes are identical. The HEPS instrument operates continuously throughout the orbit.

The cross-sectional view of one of these four telescopes is shown in Fig. 8.2. The silicon detector D has a thickness of 200 μm and measures low-energy protons and electrons. High-energy electrons and medium-energy protons are stopped in detector E which is comprised of two lithium-drifted detectors of a total thickness of 1 cm. Detector E' has a thickness of 0.3 cm and differentiates medium-energy protons from the highest proton energy range. It also rejects particles penetrating from the back direction. Around the stacked E detectors lies a system of annular detectors (A) with a thickness of 0.1 cm. This system rejects high-energy particles entering from the sides.

Signals from the D and E detectors are pulse-height analyzed simultaneously by fast analog-

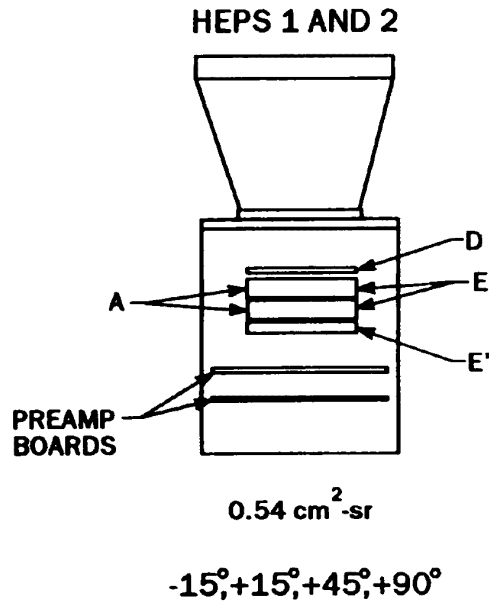


Figure 8.2. Diagram of the HEPS1 and HEPS2 telescopes showing the detector arrangements, preamplifier board location, and collimator look angles defined with respect to the zenith direction

to-digital converters. Logic analysis of the pulses by the coincidence/anticoincidence circuitry distinguishes electrons from protons and accumulates pulse-height distributions in memory. The fast parallel processing allows pulse analysis rates in each telescope of approximately 100,000 events per second. A microcomputer controls the accumulation of signals to form a 32-step logarithmic energy spectrum every four seconds for the electron channels and every 16 s for the proton channels. This compression introduces an uncertainty which varies from 3.1% at low count rates to 1.7% at higher count rates, and jumps to 10% at extremely high count rates.

For high-energy protons, a pre-flight calibration of the HEPS instrument was done on the 88-inch cyclotron of the Lawrence Berkeley Laboratories. The energy range was from 6 to 55 MeV. In the South Atlantic Anomaly (SAA) region, it is possible to obtain count rates high enough to be influenced by the processing rate capability of the HEPS counting. Therefore, the livetime as a function of counting rate was also measured during the preflight calibration. This livetime was evaluated with a set of ^{90}Sr and ^{204}Tl beta sources.

Two types of in-flight calibration are also executed periodically to monitor the instrument performance. The first type corresponds to an electronic pulser calibration mode where fixed amplitude pulses are applied to the input of the amplifier of each detector. This calibration mode tests the logic functions as well as the gain and resolution in the energy detectors. The second type of in-flight calibration utilizes a weak ^{241}Am alpha source mounted within the HEPS instrument. The energy of the most intense alpha line (5.48 MeV) is above the range of the normal operating mode, so that the background interference from the sources is minimized. This calibration provides an absolute gain calibration of the D proton detector and the E electron

Table 8.4. Differential number flux uncertainties for protons from 5 to 150 MeV

Counts/accumulation interval	Measurement uncertainties
2	74.3
10	38.9
31	29.0
32	28.9
10^2	24.9
10^3	23.1
10^4	22.8
10^5	24.7

detector during the UARS mission. Based on the two in-flight calibrations, a compensation to an electronic drift may be initiated by a ground command.

The quality of the HEPS data is influenced by the compression of accumulated data, the adjustments for dead time and the removal of a temperature-dependent background. The uncertainties on the differential number flux for protons from 5 to 150 MeV as a function of the counts per accumulation interval are presented in Table 8.4. At low count rates, the uncertainties are dominated by Poisson statistical errors. At higher count rates, the uncertainties are dominated by uncertainties on the energy channel widths of the proton detectors. At very high count rates, the uncertainties are also influenced by the errors on the dead time correction.

8.4 Data archive

The UARS data are archived at SwRI in a set of files jointly called an Instrument Data File Set (IDFS). The IDFS includes the data as well as a certain amount of metadata in order to convert telemetry values to various engineering and scientific units. For a given instrument, the information stored into an IDFS contains the telemetry of the sampled data, ancillary or engineering telemetry and a large quantity of information with all sorts of calibration and timing factors. This last type of information does not necessarily come from the spacecraft telemetry.

The archived data are accessed through a client/server system. The server subsystem provides the interface between the archive and the client subsystem. The nature of the archive devices is hidden from the server and therefore the archive can exist on different types of media. On the client side, programs based on the IDFS library (Gonzalez 1996) have to be used. The Southwest Data Display and Analysis System (SDDAS) is an example of such a program. It allows to easily display scientific data as a function of time. For other application, specific programs have to be written.

The server subsystem is common to different satellite missions and to different experiments. Therefore, all the data are organised in terms of mission, satellite, experiment, instrument, virtual data class and sensor where the virtual data class is a IDFS category that allows organiza-

Table 8.5. List of the UARS sensors used from the IDFS database

a) Experiment PEM, instrument VMAG, virtual VMMA			
Sensor number	Unit number		Description
00	5	(Gauss)	x-component of the magnetic field in the spacecraft coordinate system
01	5	(Gauss)	y-component of the magnetic field in the spacecraft coordinate system
02	5	(Gauss)	z-component of the magnetic field in the spacecraft coordinate system
b) Experiment PEM, instrument HEPS, virtual HPSB			
Sensor number	Unit number		Description
02	20	[cnts/(cm ² sr s eV)]	proton detector EP1 of the telescope HEPS1/T2
03	20	[cnts/(cm ² sr s eV)]	proton detector EP2 of the telescope HEPS1/T2
05	20	[cnts/(cm ² sr s eV)]	proton detector EP1 of the telescope HEPS1/T1
06	20	[cnts/(cm ² sr s eV)]	proton detector EP2 of the telescope HEPS1/T1
09	20	[cnts/(cm ² sr s eV)]	proton detector EP1 of the telescope HEPS2/T2
10	20	[cnts/(cm ² sr s eV)]	proton detector EP2 of the telescope HEPS2/T2
12	20	[cnts/(cm ² sr s eV)]	proton detector EP1 of the telescope HEPS2/T1
13	20	[cnts/(cm ² sr s eV)]	proton detector EP2 of the telescope HEPS2/T1
c) Experiment OAUR, instrument OAUR, virtual OAUR			
Sensor number	Unit number		Description
20	5	(no dim.)	element a_{11} of the rotation matrix between the spacecraft and GEI cartesian coordinate systems
21	5	(no dim.)	element a_{21}
22	5	(no dim.)	element a_{31}
23	5	(no dim.)	element a_{12}
24	5	(no dim.)	element a_{22}
25	5	(no dim.)	element a_{32}
26	5	(no dim.)	element a_{13}
27	5	(no dim.)	element a_{23}
28	5	(no dim.)	element a_{33}
29	6	(km)	x-component of the spacecraft position in GEI
30	6	(km)	y-component of the spacecraft position in GEI
31	6	(km)	z-component of the spacecraft position in GEI

tion of different sensors. For the present purpose, the mission and satellite names are UARS and UARS1, respectively. The experiments called PEM and OAUR provide the useful information for proton radiation belt studies. The OAUR experiment corresponds to the ephemeris, i.e. the position and attitude of the UARS satellite. The PEM experiment includes the VMAG and HEPS instruments. These instruments measure the magnetic field vector and the proton differential flux. The list of sensors useful to study the proton radiation belts and their units is shown in Table 8.5.

Table 8.6. Possible value of the IDFS quality indicator for the magnetometer and proton detectors

a) Quality variable for the magnetic field components	
Value	Description
0	No fill data
1	Fill data
2	CRC error, data questionable
3	Fill data and CRC error

b) Quality variable for the telescope proton detectors	
Value	Description
0	No fill data
1	Fill data with energy sweep
2	Possible fill data with energy sweep
4	Fill and possible fill data with energy sweep
8	Solar contaminated sensor
16	Exceeded total count for telescope
32	Exceeded total count for sensor
64	Unknown state, not enough information

For each sensor, a variable indicates the quality of the data. Generally, this quality variable is bit oriented and a zero value means good quality. The possible values of the quality indicator for the magnetometer and proton detectors are listed in Table 8.6.

Chapter 9

Data processing

To build a new proton radiation belt model, the processing of the UARS/PEM proton telescope data is realized in two separate steps. During the first step, all the basic data are retrieved from the IDFS file. The basic data include, for each point, the time of measurement, the geographic location of the spacecraft at this time, the telescope orientation and the particle fluxes for different energies. The second step consists of ordering the data in terms of geomagnetic coordinate systems.

9.1 Data retrieval

The first step is achieved by a C program (`pemextr.c`) that calls specific IDFS routines. The algorithm of the program is the following:

- select a time interval and a HPSB sensor number;
- check and promote the IDFS files for the given time interval;
- read successively each record of the virtual class HPSB;
- convert the raw data to scientific unit and get the time of measurement;
- randomly access the virtual classes VMMA and OAUR to determine the magnetic field vector, the spacecraft location and the spacecraft attitude at the time of measurement;
- check the different quality variables to reject bad data;
- compute the components of the magnetic field and the direction of the particle velocity in the GEI coordinate system;
- store the data in an ASCII file for retrieval.

During the promotion phase, the SwRI server is contacted and the needed IDFS files are automatically downloaded by an FTP session.

As input, the program `pemextr.c` reads a text file called `sens.dat` that contains the telescope code (2, 5, 9 or 12 for HEPS1/T2, HEPS1/T1, HEPS2/T2 or HEPS2/T1, respectively), the year and day number of the first date to be retrieved, and the year and day number of the last date to be retrieved. Each information has to be set on separate lines.

As output, the program `pemextr.c` produces a text file the name of which has the form `JyydddScc.NEW` where `yy` and `ddd` are the last two digits of the year and the day number of the first date, and, `cc` is the telescope code. Except the two first lines of the file, each line of the text file is related to a single flux measurement. Each line includes the date (year and day number) and Universal Time (in degrees) of the measurement, the GEI cartesian coordinates of the UARS spacecraft (in km), the GEI cartesian components of a normalized vector pointing to the mean particle velocity direction, the GEI cartesian components of the measured magnetic field vector (in Gauss) and a 16-point proton flux spectrum [counts/(cm² sr s eV)].

In the virtual class HPSB the flux spectrum measured by each telescope is spread over different sensors. The sensors DP and EP1 contain eight points of the spectrum while the sensor EP2 only contains seven points. For the sensors EP2, a dummy channel (with an energy of 2500 MeV) has been added into the IDFS files in order to get the same number of energy channels in each sensor. Since we are interested in the high energy protons, i.e. above 5 MeV, only the two sensors EP1 and EP2 are taken into account, which provides a 15-point flux spectrum for each of the four proton telescopes. The central energies and the energy widths for the four proton telescopes are listed in Table 9.1.

9.2 Geographic and geomagnetic coordinates

To make easier the following steps of the data processing, each text file produced by the program `pemextr.c` is transformed in two different IDL binary files with the same name but extensions `'.eph'` and `'.flx'`; the two files contain ephemeris data and flux data, respectively. The flow chart of this transformation is illustrated on Fig. 9.1.

The ephemeris data includes the time of measurement (in modified Julian Day), the geocentric and geodetic coordinates of the spacecraft, the spherical GEO components of the normalized velocity vector and of the measured magnetic field vector, as well as geomagnetic data obtained with the geomagnetic field model IGRF 90 (updated to 1992). The geomagnetic data include the IGRF magnetic field vector, the local normal vector to the magnetic field line, the pitch angle and azimuthal angle of the particle velocity, McIlwain's parameter L , the geocentric altitude of the lowest mirror point on the magnetic field line passing through the spacecraft location, the magnetic field intensity at the local guiding center of 100 MeV protons and McIlwain's parameter L evaluated at this guiding center.

This transformation is achieved by the IDL program `uarsprocess.pro`. The program automatically transforms all the text files with the extension `'.new'`. When a text file is processed and the two files with extensions `'.eph'` and `'.flx'` are created, the extension of the

Table 9.1. Proton energy (MeV) channels of the EP1 and EP2 sensors of the HEPS detectors

HEPS1/T2		HEPS1/T1		HEPS2/T2		HEPS2/T1	
Centre	Width	Centre	Width	Centre	Width	Centre	Width
6.7	1.5	6.2	1.3	6.6	1.5	6.1	1.3
8.0	1.2	7.4	1.1	7.9	1.2	7.3	1.1
9.9	2.6	9.2	2.5	9.7	2.4	9.1	2.5
12.5	2.7	11.7	2.7	12.4	2.9	11.6	2.7
16.0	4.2	15.1	4.2	15.9	4.2	15.1	4.2
21.7	7.2	20.8	7.2	21.7	7.2	20.8	7.2
29.0	7.3	28.1	7.3	29.0	7.4	28.0	7.3
37.9	10.4	36.9	10.4	38.3	10.4	36.9	10.4
50.9	8.9	49.5	14.6	50.8	8.9	51.8	10.1
61.7	12.9	64.1	14.6	61.7	12.9	64.1	14.5
77.9	19.4	82.7	22.6	77.8	19.4	82.7	22.7
99.3	23.6	108.2	28.5	99.4	23.7	108.4	28.6
120.3	18.3	134.1	23.4	120.0	18.2	134.2	23.1
135.3	11.9	153.4	15.1	135.3	11.9	153.3	15.3
148.4	14.8	168.0	14.0	148.4	14.2	168.0	14.0

text file is changed to ‘.pem’. The program `uarsprocess.pro` makes use of the UNIRAD library (see Technical Note 10) to evaluate the different geomagnetic data. The program also modifies the content of files called `pub02.dsc`, `pub05.dsc`, `pub09.dsc` and `pub12.dsc`. These files contain the list of the ‘.eph’ and ‘.flx’ files for the four telescope HEPS1/T2, HEPS1/T1, HEPS2/T2 and HEPS2/T1, respectively. The format of files with the extensions ‘.eph’, ‘.flx’ and ‘.dsc’ is described in Appendix A.

The algorithm of the program `uarsprocess.pro` is the following:

- select all the text files with a name of the form `JyydddScc.NEW`;
- read successively each text file;
- transform the satellite location and the different vectors to the spherical GEO coordinate system;
- evaluate the geomagnetic data by using the UNIRAD library;
- build a formatted header for the ‘.eph’ and ‘.flx’ files;
- write the ephemeris and flux files;
- modify the content of the ‘.dsc’ file;
- rename the extension of the text file.

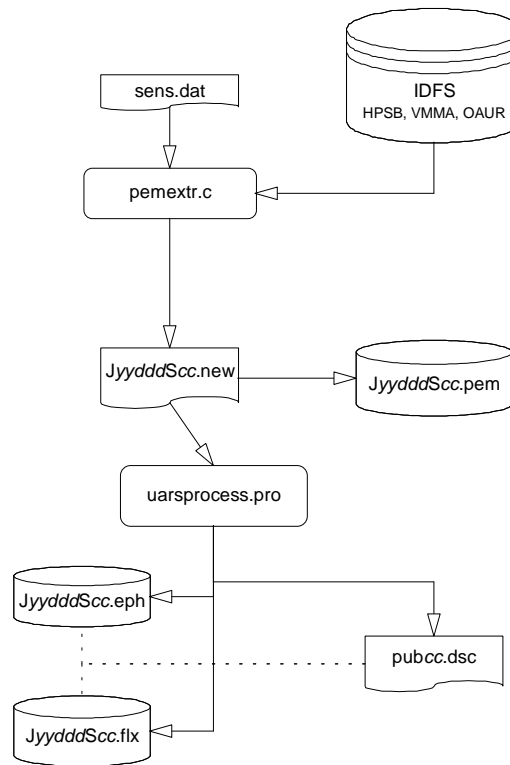


Figure 9.1. Flow chart of the transformation of IDFS files into ‘.eph’ and ‘.flx’ files

Note that the program modifies but does not create the four files `pub02.dsc`, `pub05.dsc`, `pub09.dsc`, and `pub12.dsc` which contain the list of all the processed ‘.eph’ and ‘.flx’ files.

9.2.1 Cleaning of the data sets

Not all the records in the data files are valid. In the ‘.eph’ files, a quality flag is associated to the ephemeris to identify bad records which will not be included in the model. The rejection criteria are the following:

1. when the IDFS quality variable associated to the HEPS detectors indicates data filling or contamination or overflow of the sensor (see Table 8.6);
2. when the IDFS quality variables associated to the spacecraft ephemeris indicate that data is incorrect;
3. when the IDFS quality variable associated to the magnetometer indicates data filling or questionable data (see Table 8.6);

4. when the McIlwain parameter cannot be determined by the UNIRAD library;
5. when the magnetic field vector measured by the VMAG magnetometer strongly differs from the magnetic field vector obtained from the IGRF magnetic field model.

The first three criteria are related to the IDFS quality variables. They correspond to problems which occurred onboard the spacecraft or during the telemetry sessions. The criterion related to the McIlwain parameter rejects data points where L is not defined, e.g. above the polar cap where the magnetic field lines are not closed. The last criterion is discussed below.

During the data processing, the magnetic field vector \mathbf{B}_{VMAG} as measured by the VMAG magnetometer is only used to validate the data. Records are rejected when \mathbf{B}_{VMAG} deviates significantly from the magnetic field vector \mathbf{B}_{IGRF} obtained from the magnetic field model IGRF, epoch 1992. The deviation is quantified by the two numbers Δ_θ and Δ_B defined by

$$\cos \Delta_\theta = \frac{\mathbf{B}_{\text{VMAG}} \cdot \mathbf{B}_{\text{IGRF}}}{B_{\text{VMAG}} B_{\text{IGRF}}} \quad (9.1)$$

and

$$\Delta_B = \frac{B_{\text{IGRF}} - B_{\text{VMAG}}}{B_{\text{VMAG}}}. \quad (9.2)$$

Records are flagged as bad when $\cos \Delta_\theta \leq 0.99$ or $|\Delta_B| \geq 0.03$. The limits on $\cos \Delta_\theta$ and Δ_B to rejecting data have been chosen such that they accept the data fluctuations but reject suspicious data.

In Figs. 9.2 and 9.3, the fluctuations of Δ_θ and Δ_B are illustrated for a time period of 48 hours starting 1 November 1991 and 3 November 1991, respectively. On each figure, Δ_θ and Δ_B are represented as a function of time. The polar and azimuthal angle of detector HEPS1/T1 are also given. The polar angle is measured from zenith to nadir and the azimuthal angle is measured from North to East in the local horizontal plane. In both figures, Δ_θ and Δ_B generally take values around 0° and zero, respectively. Nevertheless, in Fig. 9.2, Δ_θ deviates drastically from its normal value during 10 hours. During the same time, the polar angle of the telescope also deviated from its nominal value (45°). This behaviour is explained by corrupted data in the IDFS description of the spacecraft attitude. Note that since only the attitude data is corrupted, Δ_B remains near zero during this period of 10 hours. The IDFS quality variables associated to the spacecraft attitude warn about the data corruption during the first part of this 10-hour period. But for the end of this period where the HEPS1/T1 polar angle is about 135° , the IDFS quality variables indicate the attitude data as correct. This problem can be due to a bad transmission from the Satellite Capture Facility. In the case of Fig. 9.2, the criterion on the magnetic field vector comparison patches this problem and rejects all records of the 10-hour period. One should note that the case of Fig. 9.2 is the only one where such an error in the attitude data has been found. SwRI has been notified of this problem.

In Fig. 9.3, a 180° rotation of the spacecraft occurs during the displayed time period. During the full time period, the fluctuations of Δ_θ and Δ_B remain inside their nominal limits and the data are therefore not rejected. Nevertheless, the fluctuations of Δ_B and Δ_θ appear to be correlated to the spacecraft orientation. The correlation perhaps indicates the presence of a systematic error in the calibration of the magnetometer or in the processing of its data.

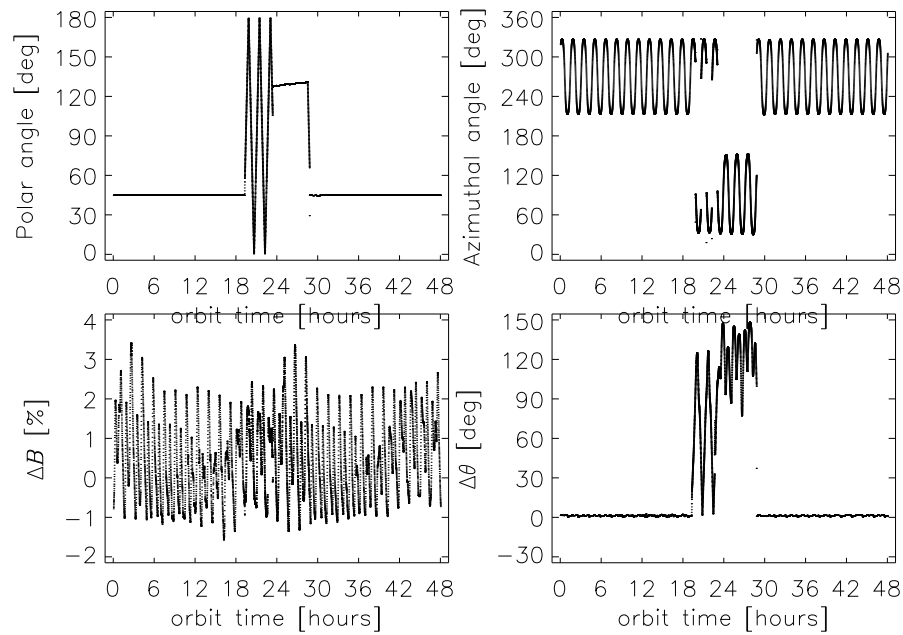


Figure 9.2. Deviation between the magnetic field vector measured by the magnetometer VMAG and the IGRF magnetic field vector for a time period of 48 hours from 1 to 2 November 1991

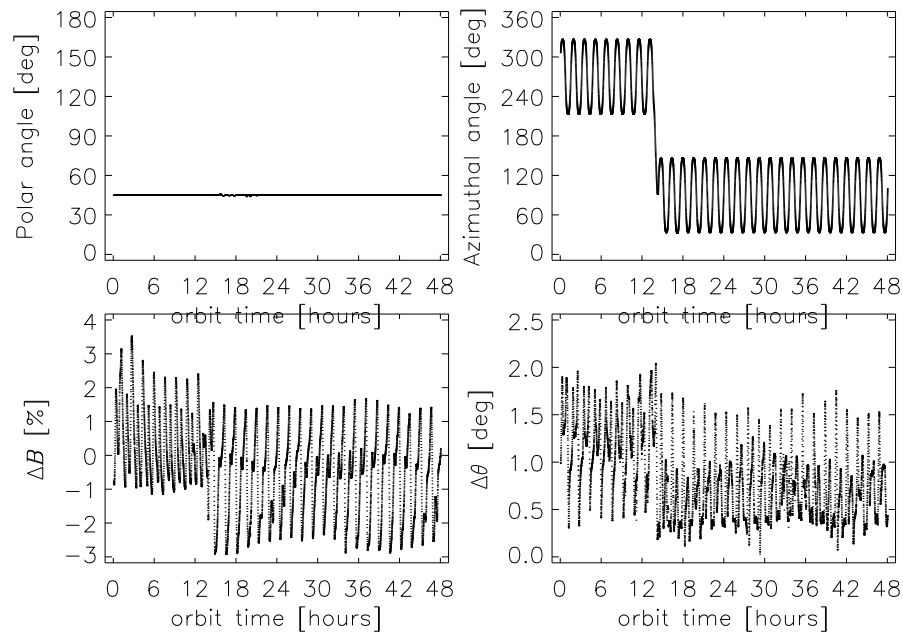


Figure 9.3. Deviation between the magnetic field vector measured by the magnetometer VMAG and the IGRF magnetic field vector for a time period of 48 hours from 3 to 4 November 1991

9.3 Geometric factor correction

The HEPS proton flux values included in the IDFS database have been obtained from constant geometric factors that do not take into account the variation of the proton flux over the opening angle of the detector. In other words, the flux values are obtained under the assumption that the detector is perfectly shielded and that the pitch angle distribution of the proton flux over its opening angle is isotropic. Since, at low altitude, the proton flux is strongly anisotropic, corrections have to be applied to the geometric factors. Indeed, the actual counting rates result from the convolution of the proton fluxes by the directional response function $h(\omega)$ of the detector, as shown by Eq. (3.4) in Sect. 3.1.

The available PEM documentation does not include the directional responses of the HEPS detectors (more information has been requested from the builder of the instrument, Lockheed Palo Alto Research Laboratory). The nominal field of view (FOV) of the HEPS detectors is equal to 30° but detailed analysis of the flux measurements shows that the effective FOV is larger and that the HEPS directional response function extends to $\theta \approx 60^\circ$ for 100 MeV protons. This FOV analysis is reported in Sect. 10.2.

Due to the large FOV and the lack of an experimental response function $h(\omega)$ of the HEPS detectors, only measurements corresponding to a local pitch angle equal to $90^\circ \pm 10^\circ$ have been used to build the UARS trapped proton model. Indeed, since the pitch angle distribution is peaked at 90° , when the local pitch angle is about 90° , most of the protons penetrate into the detector at an angle within the nominal FOV and Eq. (3.4) is expected to be well approximated by Eq. (3.1), i.e. the geometric factor correction should be small. Therefore, only a simple correction algorithm is applied. It should be kept in mind that it is not an ideal procedure to obtain fully reliable trapped proton fluxes from the PEM experiment. This situation jeopardizes the validity of the obtained radiation belt model.

The correction algorithm is described in Sect. 10.3; it is very similar to the algorithm applied to the AZUR and SAMPEX data.

9.4 Data binning

The proton UARS data are sorted in 15 energy bins, 30 McIlwain L bins and 45 equatorial pitch angle bins. The bin limits in energy correspond to the limits of the energy channels of each telescope (see Table 9.1). The bin limits in McIlwain L parameter and in equatorial pitch angle are listed in Table 9.2. The table also includes a reference value for each bin. Note that the reference value of bins generally corresponds to the mid value of the bin limits, except for the outer bins (where the reference value is set to the outer limit). From $L = 1$ to $L = 1.2$, the width of the L bins is set to $0.01 R_E$. From $L = 1.2$ to $L = 1.6$, the value of the L -bin widths is set alternatively to 0.01 and $0.04 R_E$. The alternation between small and large widths above $L = 1.2$ allows to get narrow bins without a too excessive number of bins. From $\alpha_0 = 37^\circ$ to 82° , the width of the equatorial pitch angle bins is set to 1.5° . Outside this range the widths are larger.

Table 9.2. Bin limits (L , α_0)

	McIlwain L parameter			Equatorial pitch angle		
	Min.	Max.	Ref.	Min.	Max.	Ref.
1	1.00000	1.09500	1.00000	0.0000	7.5000	0.0000
2	1.09500	1.10500	1.10000	7.5000	12.5000	10.0000
3	1.10500	1.11500	1.11000	12.5000	17.5000	15.0000
4	1.11500	1.12500	1.12000	17.5000	22.5000	20.0000
5	1.12500	1.13500	1.13000	22.5000	27.5000	25.0000
6	1.13500	1.14500	1.14000	27.5000	31.0000	30.0000
7	1.14500	1.15500	1.15000	31.0000	33.0000	32.0000
8	1.15500	1.16500	1.16000	33.0000	35.0000	34.0000
9	1.16500	1.17500	1.17000	35.0000	37.0000	36.0000
10	1.17500	1.18500	1.18000	37.0000	38.5000	37.7500
11	1.18500	1.19500	1.19000	38.5000	40.0000	39.2500
12	1.19500	1.20500	1.20000	40.0000	41.5000	40.7500
13	1.20500	1.24500	1.22500	41.5000	43.0000	42.2500
14	1.24500	1.25500	1.25000	43.0000	44.5000	43.7500
15	1.25500	1.29500	1.27500	44.5000	46.0000	45.2500
16	1.29500	1.30500	1.30000	46.0000	47.5000	46.7500
17	1.30500	1.34500	1.32500	47.5000	49.0000	48.2500
18	1.34500	1.35500	1.35000	49.0000	50.5000	49.7500
19	1.35500	1.39500	1.37500	50.5000	52.0000	51.2500
20	1.39500	1.40500	1.40000	52.0000	53.5000	52.7500
21	1.40500	1.44500	1.42500	53.5000	55.0000	54.2500
22	1.44500	1.45500	1.45000	55.0000	56.5000	55.7500
23	1.45500	1.49500	1.47500	56.5000	58.0000	57.2500
24	1.49500	1.50500	1.50000	58.0000	59.5000	58.7500
25	1.50500	1.59500	1.55000	59.5000	61.0000	60.2500
26	1.59500	1.60500	1.60000	61.0000	62.5000	61.7500
27	1.60500	1.69500	1.65000	62.5000	64.0000	63.2500
28	1.69500	1.70500	1.70000	64.0000	65.5000	64.7500
29	1.70500	1.79500	1.75000	65.5000	67.0000	66.2500
30	1.79500	1.80500	1.80000	67.0000	68.5000	67.7500
31				68.5000	70.0000	69.2500
32				70.0000	71.5000	70.7500
33				71.5000	73.0000	72.2500
34				73.0000	74.5000	73.7500
35				74.5000	76.0000	75.2500
36				76.0000	77.5000	76.7500
37				77.5000	79.0000	78.2500
38				79.0000	80.5000	79.7500
39				80.5000	82.0000	81.2500
40				82.0000	84.0000	83.0000
41				84.0000	86.0000	85.0000
42				86.0000	88.0000	87.0000
43				88.0000	90.0000	90.0000

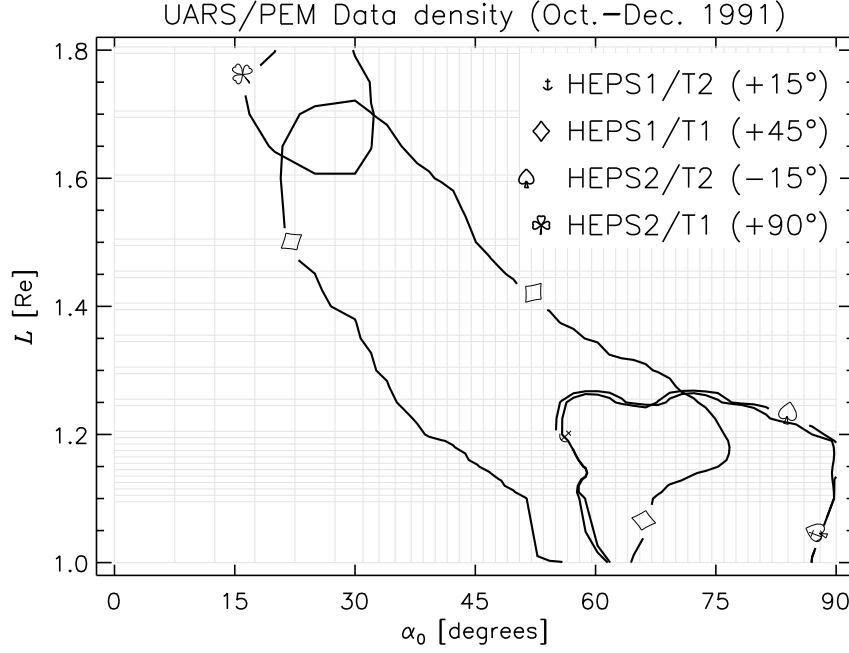


Figure 9.4. UARS/PEM data coverage in McIlwain L parameter and equatorial pitch angle for the four HEPS detectors. The solid lines delimit the area where the bins contain 35 measurements per month, per degree and per L -unit (year 1991)

The limit and reference values, listed in Table 9.2, as well as the bin widths, are stored in the text file `uarspem.lim`. This file is common to all four detectors. Since the energy channels differ slightly from one detector to the other, the values for the energy bins correspond to mean values.

The (L, α_0) mesh is represented on Fig. 9.4 as well as the data coverage for all four detectors. The data coverage is given for the whole PEM data set corresponding to the year 1991. The solid lines correspond to iso-contours of 35 measurements per month, per degree and per L -unit for the four different detectors. Equatorial pitch angles near 90 degrees are encountered only by the HEPS1/T2 and HEPS2/T2 detectors for $1 < L < 1.2$. The detector HEPS1/T1 offers the largest coverage in L . The smallest coverage is obtained by the detector HEPS2/T1. The observed difference in coverage between the detector is due to the restriction in local pitch angle and the orbit of the UARS spacecraft (see Sect. 10.1).

The UARS proton data are processed separately for different periods of time. Each year is divided in three different periods of about four months. Note, however, that for the year 1991, there is only one single period of about three months. During the binning process, the values of 15 different quantities are calculated in each bin:

- $a_0 = \sum_i F_i$;
- $a_1 = \sum_i F_i \Delta L_i$;
- $a_2 = \sum_i F_i \Delta \alpha_{0i}$;

- $a_3 = \sum_i F_i \Delta t_i$;
- $a_4 = \sum_i 1 = N$;
- $a_5 = \sum_i \Delta L_i$;
- $a_6 = \sum_i \Delta \alpha_{0i}$;
- $a_7 = \sum_i \Delta t_i$;
- $a_8 = \sum_i (\Delta L_i)^2$;
- $a_9 = \sum_i \Delta L_i \Delta \alpha_{0i}$;
- $a_{10} = \sum_i \Delta L_i \Delta t_i$;
- $a_{11} = \sum_i (\Delta \alpha_{0i})^2$;
- $a_{12} = \sum_i \Delta \alpha_{0i} \Delta t_i$;
- $a_{13} = \sum_i (\Delta t_i)^2$;
- $a_{14} = \sum_i F_i^2$.

For each quantity, the summation extends over all the data points inside the bin limits. F_i , ΔL_i , $\Delta \alpha_{0i}$ And Δt_i represent the observed flux, the deviation to the bin-reference of McIlwain's parameter, the deviation to the bin-reference of the equatorial pitch angle (in radians), and the deviation to a time reference (in day), respectively.

The 15 values evaluated in all the bins are stored for each detector in binary files, the names of which have the form `yyyySddLx.bin` where `yyyy`, `dd` and `x` represent the year, the detector number (2, 5, 9 or 12) and the period label (a, b or c), respectively. The format of the files is similar to the format of the `.eph` and `.flx` files and is described in Appendix A. The binning of the data is achieved by an IDL program called `binning_data.pro`.

9.4.1 Flux at the reference points

The 15 calculated quantities allow to evaluate for each bin the mean value ($\bar{F} = a_0/N$) and standard deviation ($\sigma = \sqrt{(a_{14} - N\bar{F}^2)/(N-1)}$) of the proton flux and also to take into account the dependences of the flux on L , α_0 , and time. The first order dependence of the flux can be expressed by the linear equation

$$F = \hat{F} + a_L \Delta L + a_\alpha \Delta \alpha_0 + a_t \Delta t \quad (9.3)$$

where \hat{F} is the flux value for the reference point of the bin. The parameters \hat{F} , a_L , a_α , and a_t can then be obtained by solving the equations:

$$\begin{cases} a_0 &= \hat{F}a_4 + a_La_5 + a_\alpha a_6 + a_ta_7 \\ a_1 &= \hat{F}a_5 + a_La_8 + a_\alpha a_9 + a_ta_{10} \\ a_2 &= \hat{F}a_6 + a_La_9 + a_\alpha a_{11} + a_ta_{12} \\ a_3 &= \hat{F}a_7 + a_La_{10} + a_\alpha a_{12} + a_ta_{13} \end{cases} \quad (9.4)$$

An evaluation of the error on \hat{F} is provided by the standard deviation

$$\hat{\sigma} = \sqrt{\frac{a_{14} - \hat{F}^2N - a_L(\hat{F}a_5 + a_1) - a_\alpha(\hat{F}a_6 + a_2) - a_t(\hat{F}a_7 + a_3)}{N - 4}}. \quad (9.5)$$

The flux \hat{F} differs from the average flux \bar{F} when

1. the bin-reference point does not lie near the centre of the bin;
2. the bin is not covered homogeneously by the satellite.

The last case occurs especially for bins located at the edge of the (L, α_0) coverage (see Fig. 9.4).

9.4.2 Processing algorithm

To build a proton radiation belt model from the UARS data, the geometric factor correction and the data binning has to be combined in an iterative process. The flow chart of this process is displayed in Fig. 9.5.

The proton fluxes and geomagnetic coordinates are stored in the ‘.eph’ and ‘.flx’ files, a catalog of which is stored in the ‘.dsc’ file. The flux data are sorted and binned by the IDL routine `binning_data.pro` according to mesh limits stored in the file `merged.lim`. The binned data are stored in a ‘.bin’ file. The IDL routine `merge_bin.pro` merges different ‘.bin’ files.

For each L value and energy channel of a ‘.bin’ file, the IDL routine `fit_mesh.pro` fits the proton flux with a 3-parameter function of the equatorial pitch angle. The function is given by

$$j(\alpha_0) = \begin{cases} f01 & \text{when } \alpha_0 < \alpha_{0c} \\ f01 + K\xi(1 + b\xi(1 + b\xi)) & \text{when } \alpha_0 > \alpha_{0c} \end{cases} \quad (9.6)$$

where $f01$ is a constant fixed at $10^{-2} \text{ cm}^{-2} \text{ sr}^{-1} \text{ s}^{-1} \text{ MeV}^{-1}$, ξ is defined as

$$\xi \equiv \sin \alpha_0 - \sin \alpha_{0c}, \quad (9.7)$$

and α_{0c} , K , and b are the three parameters to be fitted. The routine `fit_mesh.pro` allows to modify interactively the different fit parameters and to restore parameters evaluated previously. The whole set of fit parameters is stored in a ‘.cor’ file.

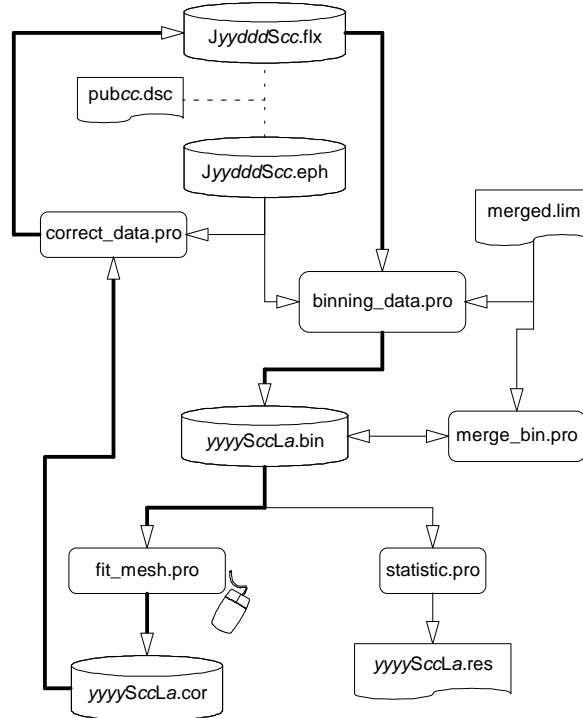


Figure 9.5. Flow chart of IDL procedures to produce the ‘.bin’, ‘.cor’ and ‘.res’ files

The geometric factor correction is applied by the IDL routine `correct_data.pro`. This routine makes use of the fitted proton fluxes to simulate the detector response and to evaluate a corrected flux. The corrected proton fluxes are stored in the ‘.flx’ files together with the raw data. Afterwards, they can be accessed by the routine `binning_data.pro` to iterate the correction process. The flow path of the iterative process is shown in Fig. 9.5

The IDL routine `statistic.pro` produces a ‘.res’ file from a ‘.bin’ file. The ‘.res’ file includes the values of \bar{F} , σ , \hat{F} and $\hat{\sigma}$ for each bin of the mesh. This file has been used to produce the figures of Sect. 10.4 as well as FORTRAN a block data for inclusion in the TREP software (see Technical Note 10).

Chapter 10

Proton PEM/UARS model

This chapter is devoted to the proton flux model derived from the HEPS measurements. The model is organized in E , L , and α_0 . The model is limited in energy from 5 to 150 MeV, in L from 1 to $1.8 R_E$, and in α_0 from 0 to 90° . As already shown in Fig. 9.4, the whole space in (L, α_0) is not covered by the available and validated measurements. The proton flux model is related only to protons whose lowest mirror-point altitude is between 500 and 585 km. This limitation results from

1. the circular orbit of UARS which is at an altitude of 585 km;
2. the restriction that the local pitch angle of the detector is equal to $90^\circ \pm 10^\circ$, i.e. for nearly locally mirroring particles.

Since, at low altitudes, the proton radiation belt is observed only in the SAA, the HEPS data included into the model corresponds to protons mirroring in the SAA close to the spacecraft altitude. Since the particles whose drift shell is passing through the SAA also have their lowest-altitude mirror point located in the SAA, this new model will correspond to protons with the lowest altitude of their mirror points equal to or slightly smaller than 585 km.

10.1 Model coverage

The coverage of the proton PEM/UARS model has been presented in Sect. 9.4. This section is focussed on the causes of this rather limited coverage.

In Figs. 10.1 and 10.2, the iso-contours of the McIlwain L parameter and of the magnetic field intensity B are represented at the altitude of the UARS orbit, respectively. The values of B and L are calculated for the IGRF magnetic field model corresponding to epoch 1992. On both figures, the dash-dotted curves indicate the location of the SAA where the NASA AP-8 MIN model predicts at 585 km a proton omnidirectional integral flux of $500 \text{ s}^{-1} \text{ cm}^{-2}$ for energies above 10 MeV. From Fig. 10.1, it can be seen that the range of L for the PEM/UARS model will not exceed $L = 2$.

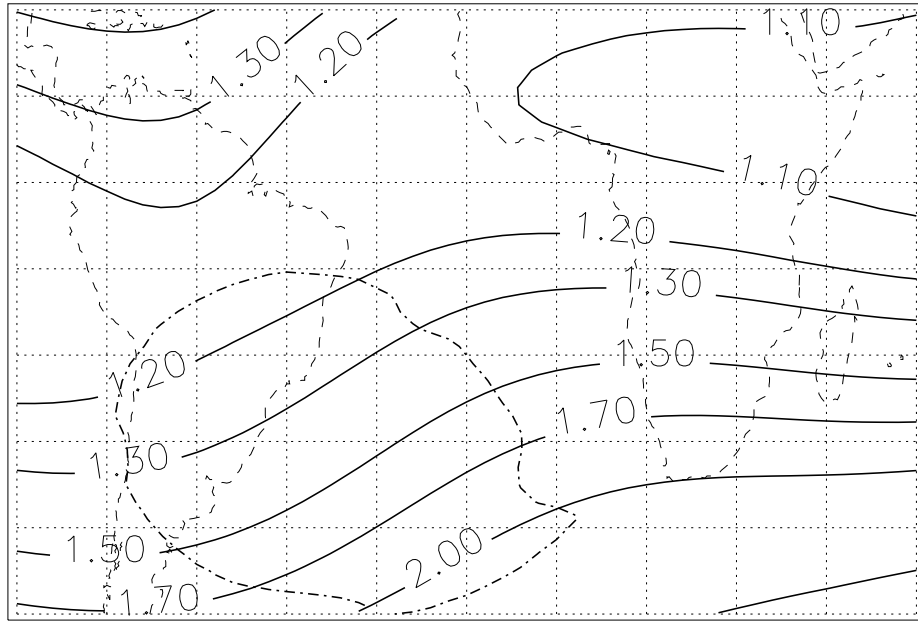


Figure 10.1. Iso-contours of L at 585 km. The dash-dotted line corresponds to an iso-contour where the AP-8 MIN omnidirectional integral proton flux above 10 MeV is equal to $500 \text{ s}^{-1} \text{ cm}^{-2}$ at 585 km. The figure demonstrates the limitation $L \leq 2$ of the PEM/UARS model

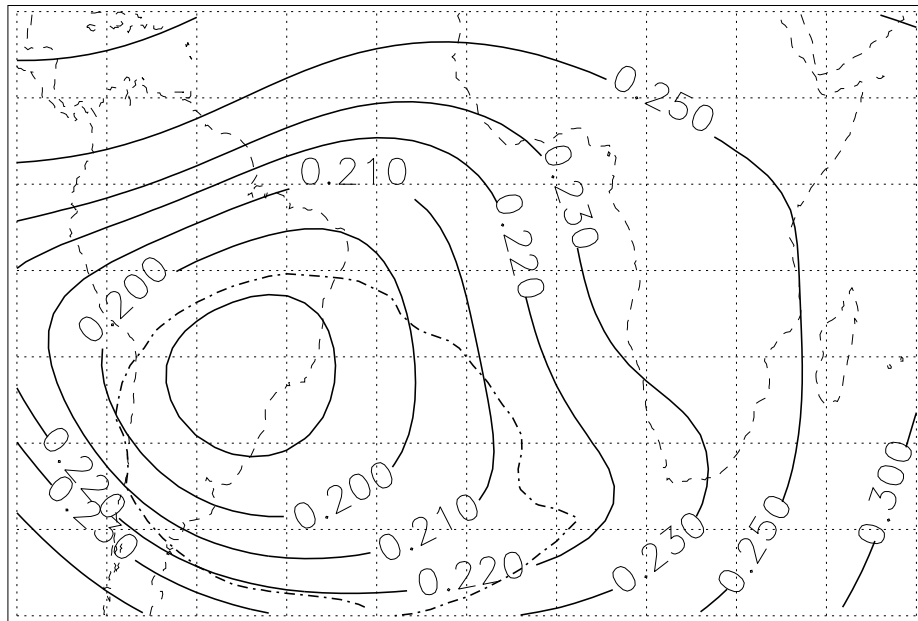


Figure 10.2. Iso-contours of the magnetic field intensity at 585 km. The dash-dotted line corresponds to an iso-contour where the AP-8 MIN omnidirectional integral proton flux above 10 MeV is equal to $500 \text{ s}^{-1} \text{ cm}^{-2}$ at 585 km. The figure demonstrates the limitation $B_m \geq 0.19$ Gauss of the PEM/UARS model

Since the observed protons have their mirror points located at the same altitude or below the point of measurement, the magnetic field intensities displayed in Fig. 10.2 correspond to the smallest mirror-point magnetic field intensities B_m for protons detected at 585 km altitude. The values of B_m in the PEM/UARS model will not be lower than 0.19 Gauss. Since the equatorial pitch angle α_0 is related to B_m and L by the relation

$$\sin \alpha_0 = \sqrt{\frac{0.311653}{B_m L^3}}, \quad (10.1)$$

in the PEM/UARS model, the maximum value of α_0 will not reach 90° for $L \geq 1.18$. Note that the data coverage in Fig. 9.4 is compatible with this statement.

Since the UARS spacecraft is three-axis stabilized, the orientations of the four HEPS detectors are only function of the spacecraft latitude ℓ . The field of view of the detectors are oriented at various angles from the spacecraft zenith to nadir in the plane containing the spacecraft velocity vector. The azimuth angle of this vertical plane is given for the ascending leg of the orbit by

$$\sin \mathcal{A} = \frac{\cos 57^\circ}{\cos \ell}, \quad (10.2)$$

where \mathcal{A} is measured from North to East in the local horizontal plane. For the descending leg of the orbit, the azimuth angle is equal to $180^\circ - \mathcal{A}$. The detector angles with respect to the zenith are listed in Table 8.3. Since the spacecraft regularly experienced a 180° rotation around its vertical axis, each HEPS detector may have four different orientations (\mathcal{A} , $\mathcal{A} + 180^\circ$, $180^\circ - \mathcal{A}$, and $360^\circ - \mathcal{A}$) for every geographic location reached by the spacecraft. Therefore, for every geographic location, each detector may see four different pitch angles.

The pitch angles seen by detector HEPS2/T2 as a function of the geographic location are displayed on Figs. 10.3–10.6. Figures 10.3 and 10.4 correspond to the ascending leg of the orbit while Figs. 10.5 and 10.6 correspond to the descending leg. Figures 10.3 and 10.5 correspond to a same orientation of the spacecraft. Figures 10.4 and 10.6 correspond to the orientation after a 180° rotation. The corresponding plots for detectors HEPS1/T2, HEPS1/T1 and HEPS2/T1 are represented on Figs. 10.7–10.10, 10.11–10.14 and 10.15–10.18, respectively. Since the PEM/UARS model is only based on measurements corresponding to local pitch angles of $90^\circ \pm 10^\circ$, these 16 figures can be used to determine when the measurements are usefull form the model.

In the SAA, the detector HEPS2/T2 has a local pitch angle of $90^\circ \pm 10^\circ$ only when the azimuth angle is equal to \mathcal{A} (Fig. 10.3) or $360^\circ - \mathcal{A}$ (Fig. 10.6). In these cases, the McIlwain L parameter does not exceed 1.23. Since the detectors HEPS1/T2 and HEPS2/T2 are positioned symetrically with respect to the zenith axis, the 180° rotation of the spacecraft switches the field of view of these two detectors. Therefore, Figs. 10.7, 10.8, 10.9 and 10.10 are identical to Figs. 10.4, 10.3, 10.6 and 10.5, respectively. Thus, pitch angles between 80° and 100° are reached in the SAA by the detector HEPS1/T2 when the azimuth angle is equal to $\mathcal{A} + 180^\circ$ (Fig. 10.8) or $180^\circ - \mathcal{A}$ (Fig. 10.9) for the same values of L . This feature explains the similarity of the data coverage for both detectors HEPS1/T2 and HEPS2/T2 in Fig. 9.4.

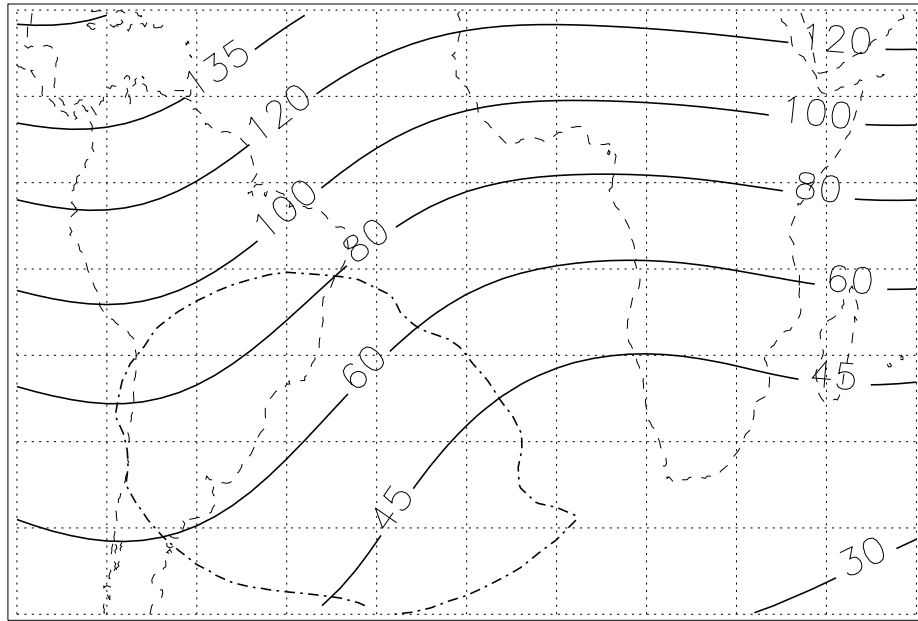


Figure 10.3. Local pitch angle of the HEPS2/T2 telescope with azimuth angle \mathcal{A} (ascending leg). Only the northern part of the SAA is covered by the α range $90^\circ \pm 10^\circ$.

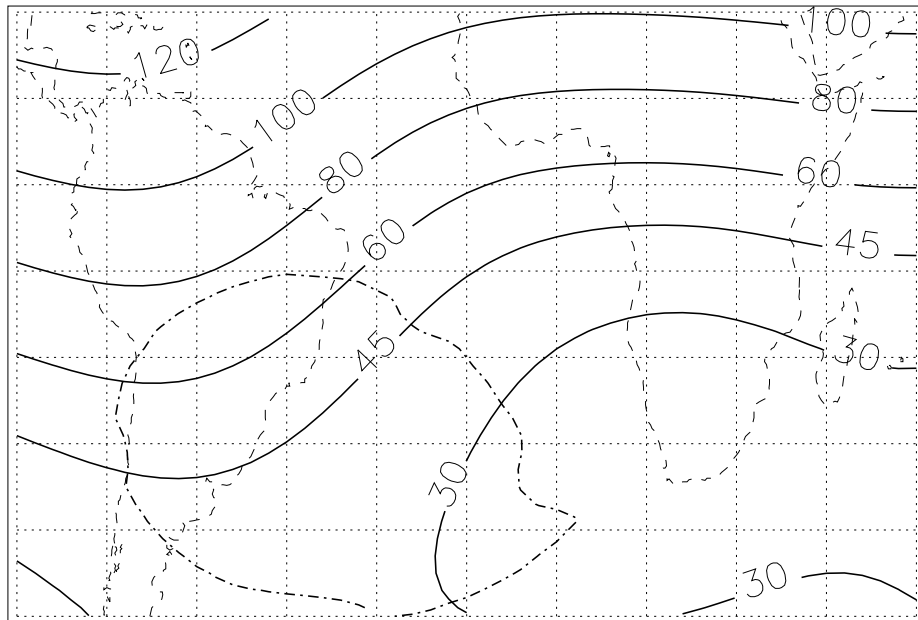


Figure 10.4. Local pitch angle of the HEPS2/T2 telescope with azimuth angle $\mathcal{A} + 180^\circ$ (ascending leg). The SAA is not covered by the α range $90^\circ \pm 10^\circ$.

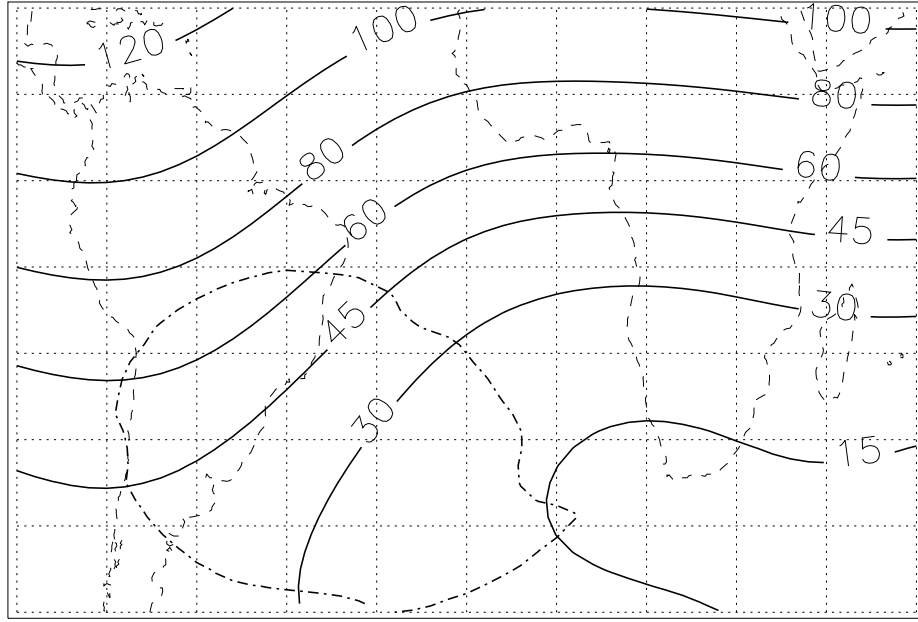


Figure 10.5. Local pitch angle of the HEPS2/T2 telescope with azimuth angle $180^\circ - \mathcal{A}$ (descending leg). The SAA is not covered by the α range $90^\circ \pm 10^\circ$.

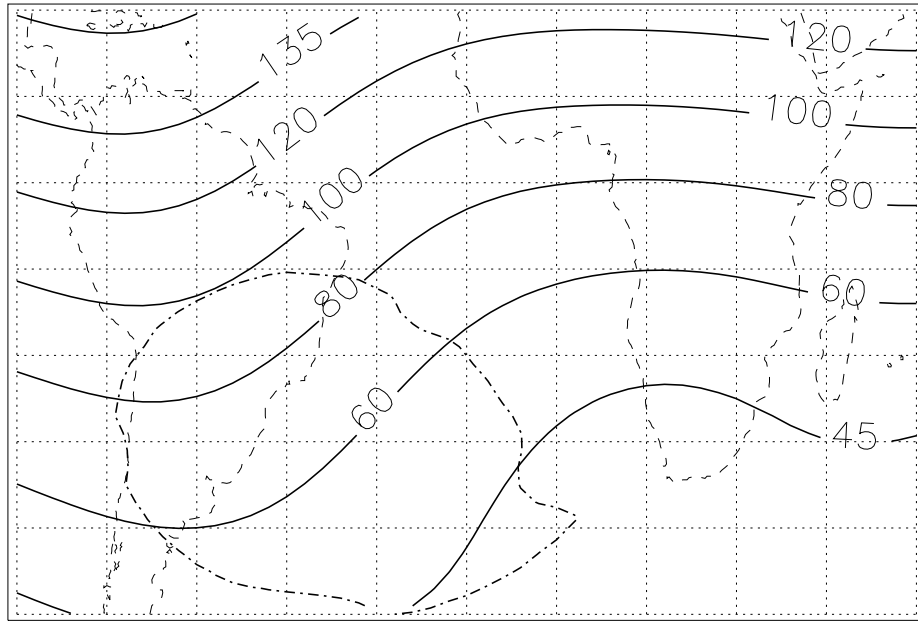


Figure 10.6. Local pitch angle of the HEPS2/T2 telescope with azimuth angle $360^\circ - \mathcal{A}$ (descending leg). Only the northern part of the SAA is covered by the α range $90^\circ \pm 10^\circ$.

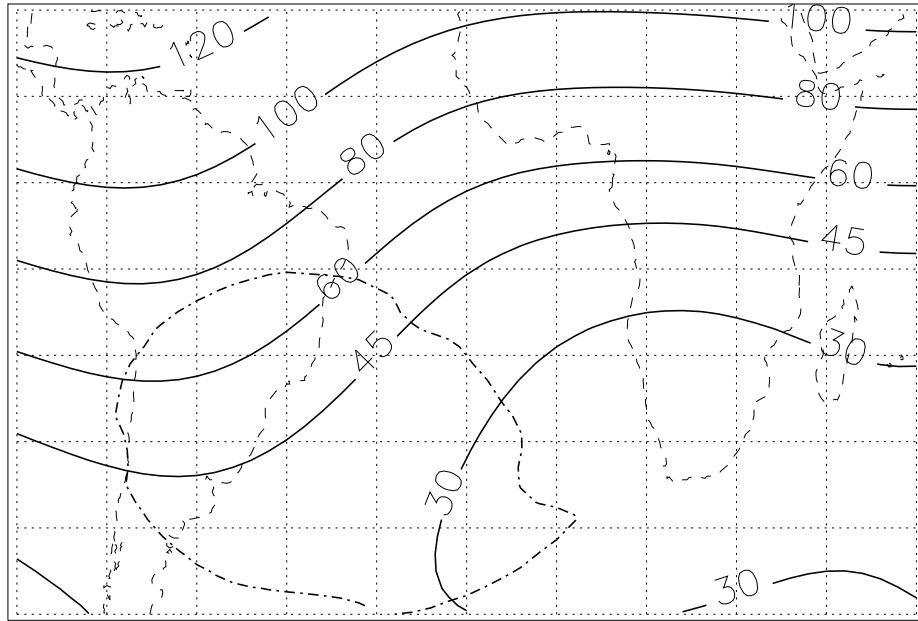


Figure 10.7. Local pitch angle of the HEPS1/T2 telescope with azimuth angle \mathcal{A} (ascending leg). The SAA is not covered by the α range $90^\circ \pm 10^\circ$.

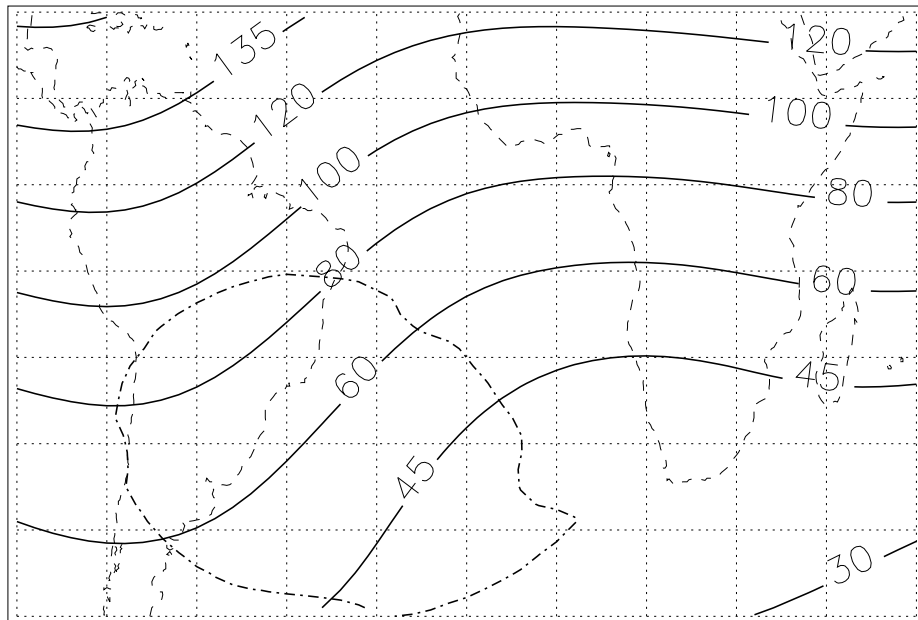


Figure 10.8. Local pitch angle of the HEPS1/T2 telescope with azimuth angle $\mathcal{A} + 180^\circ$ (ascending leg). Only the northern part of the SAA is covered by the α range $90^\circ \pm 10^\circ$.

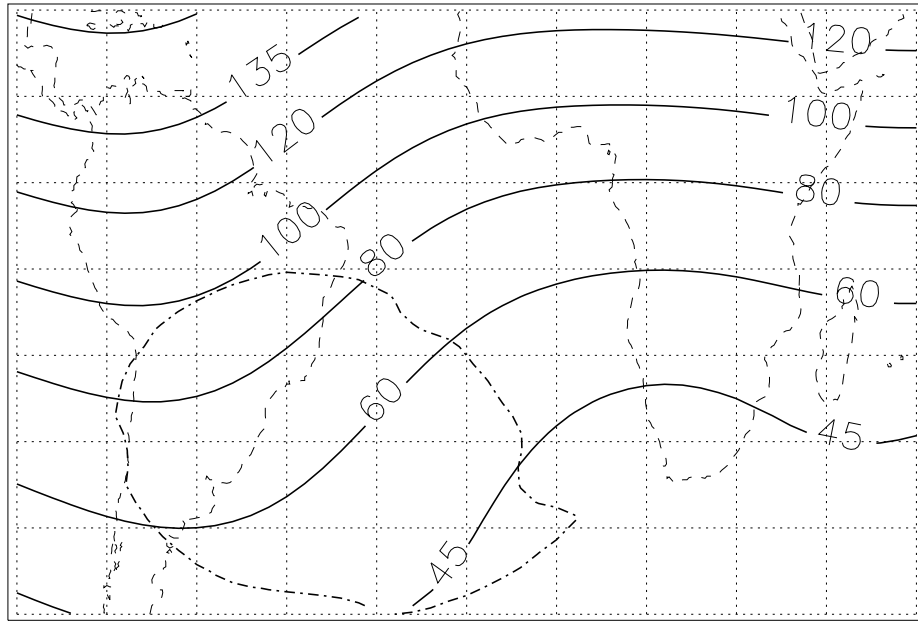


Figure 10.9. Local pitch angle of the HEPS1/T2 telescope with azimuth angle $180^\circ - \mathcal{A}$ (descending leg). Only the northern part of the SAA is covered by the α range $90^\circ \pm 10^\circ$.

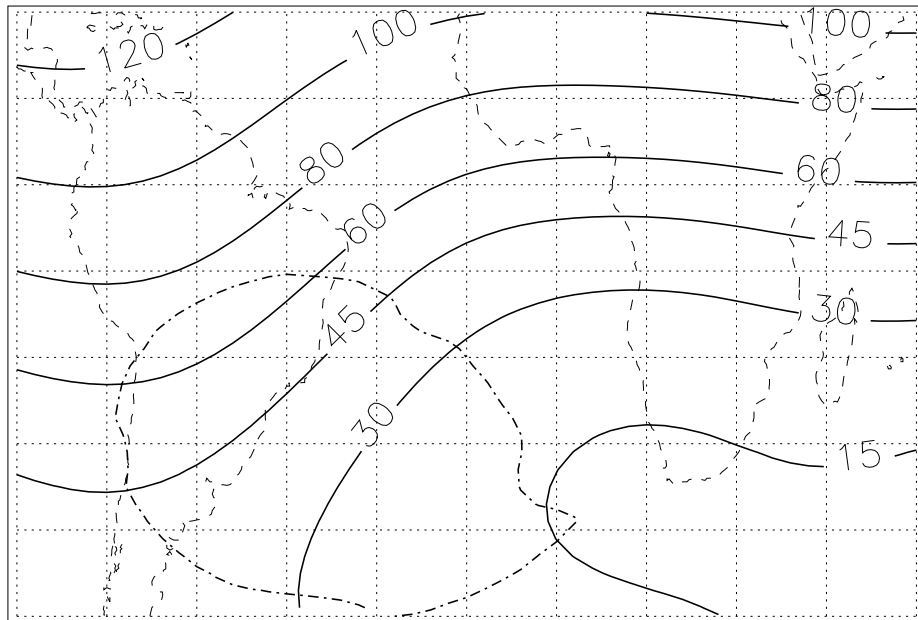


Figure 10.10. Local pitch angle of the HEPS1/T2 telescope with azimuth angle $360^\circ - \mathcal{A}$ (descending leg). The SAA is not covered by the α range $90^\circ \pm 10^\circ$.

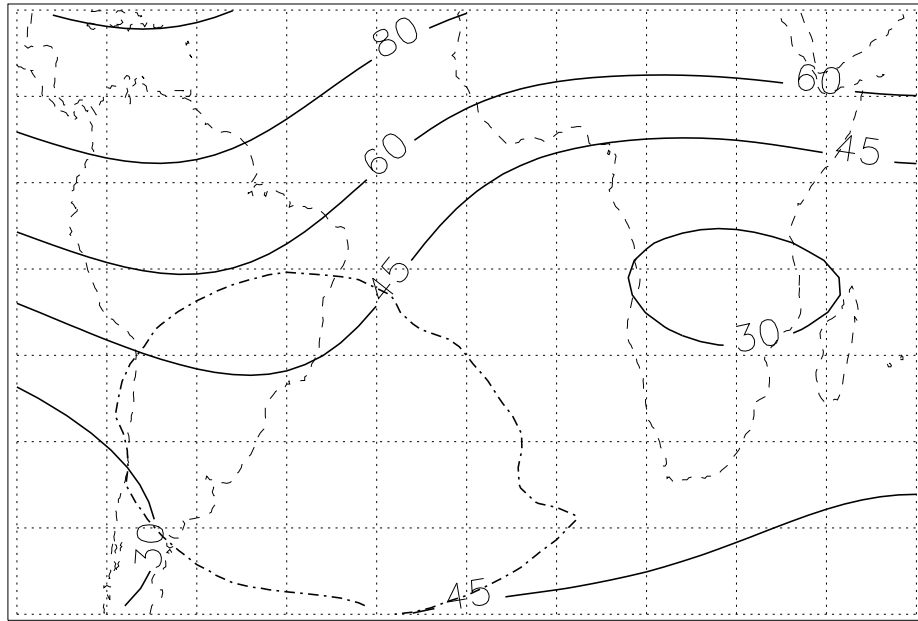


Figure 10.11. Local pitch angle of the HEPS1/T1 telescope with azimuth angle \mathcal{A} (ascending leg). The SAA is not covered by the α range $90^\circ \pm 10^\circ$.

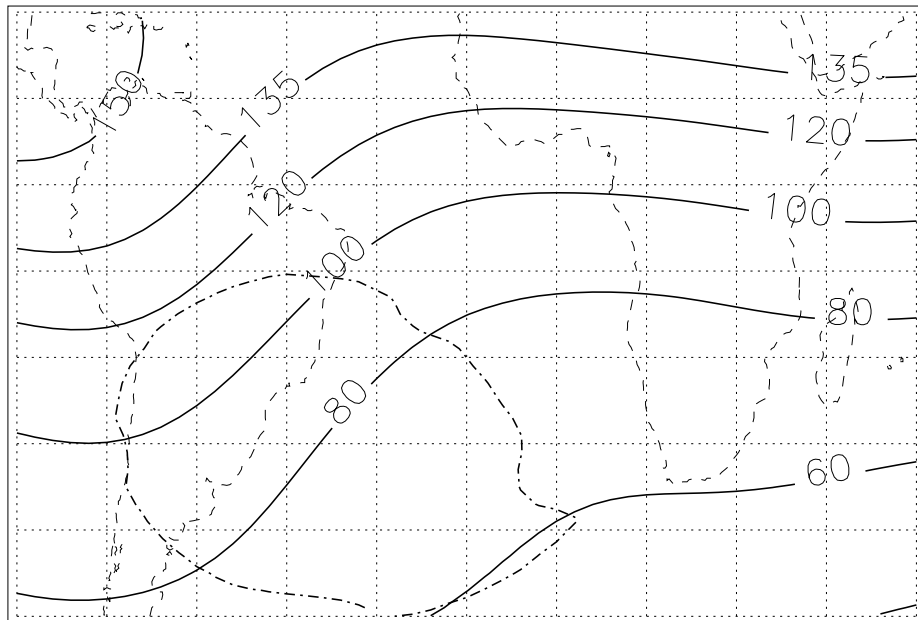


Figure 10.12. Local pitch angle of the HEPS1/T1 telescope with azimuth angle $\mathcal{A} + 180^\circ$ (ascending leg). The central part of the SAA is covered by the α range $90^\circ \pm 10^\circ$.

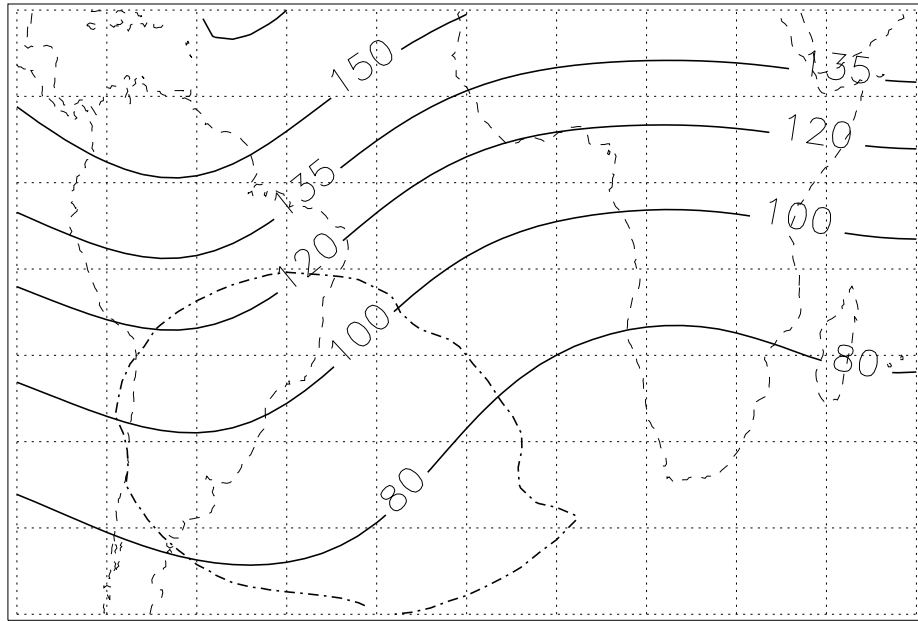


Figure 10.13. Local pitch angle of the HEPS1/T1 telescope with azimuth angle $180^\circ - \mathcal{A}$ (descending leg). A large part of the SAA is covered by the α range $90^\circ \pm 10^\circ$.

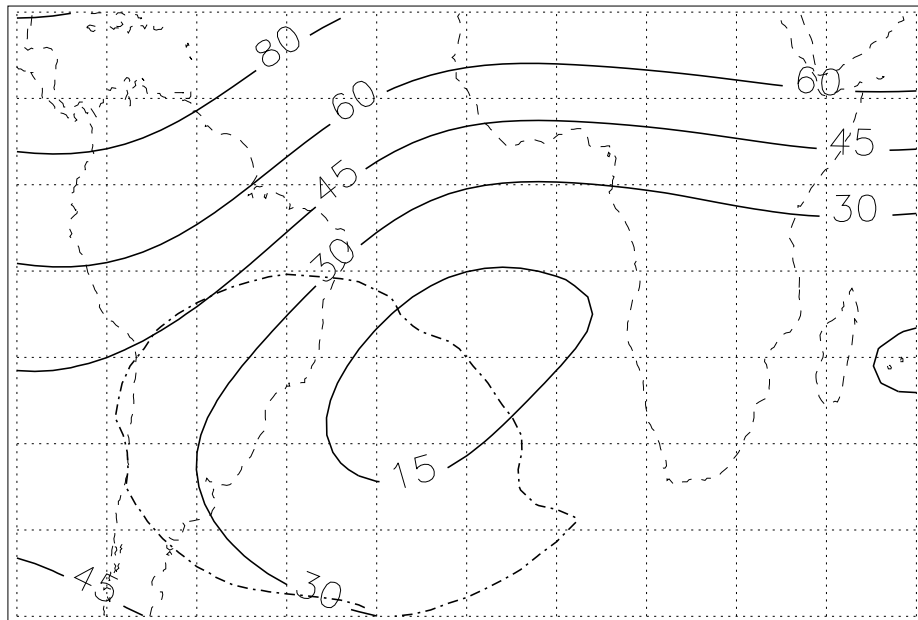


Figure 10.14. Local pitch angle of the HEPS1/T1 telescope with azimuth angle $360^\circ - \mathcal{A}$ (descending leg). The SAA is not covered by the α range $90^\circ \pm 10^\circ$.

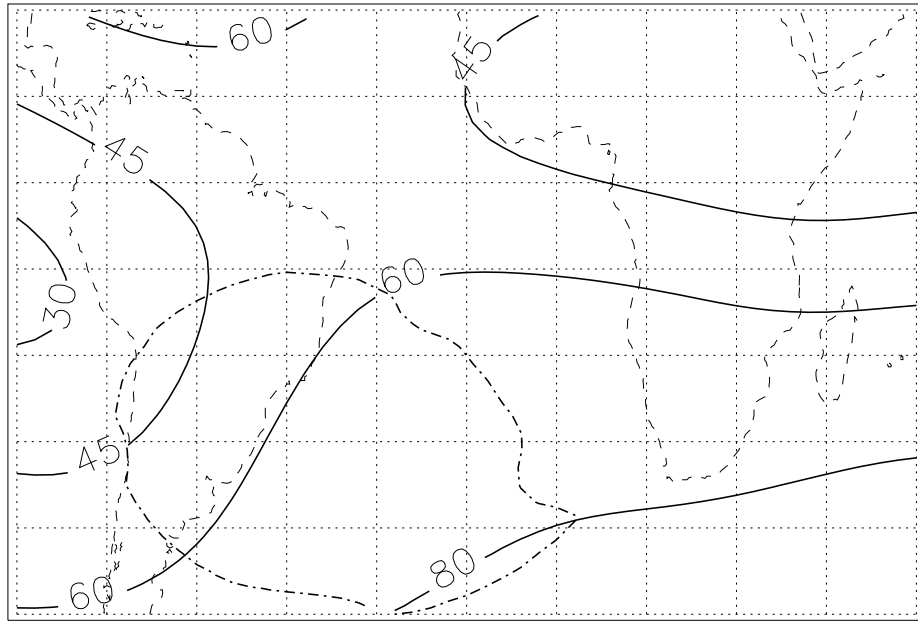


Figure 10.15. Local pitch angle of the HEPS2/T1 telescope with azimuth angle \mathcal{A} (ascending leg). Only the most southern part of the SAA is covered by the α range $90^\circ \pm 10^\circ$.

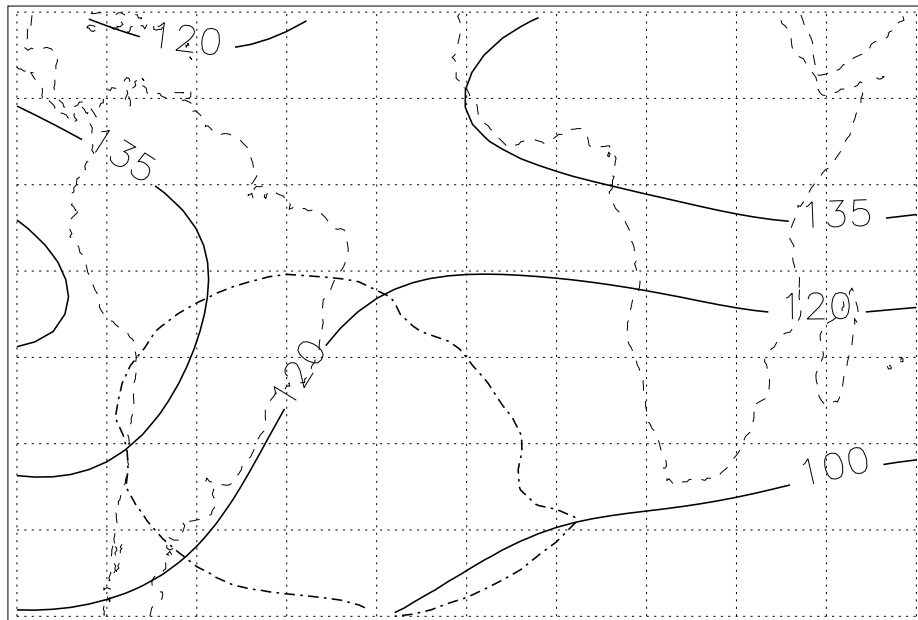


Figure 10.16. Local pitch angle of the HEPS2/T1 telescope with azimuth angle $\mathcal{A} + 180^\circ$ (ascending leg). Only the most southern part of the SAA is covered by the α range $90^\circ \pm 10^\circ$.

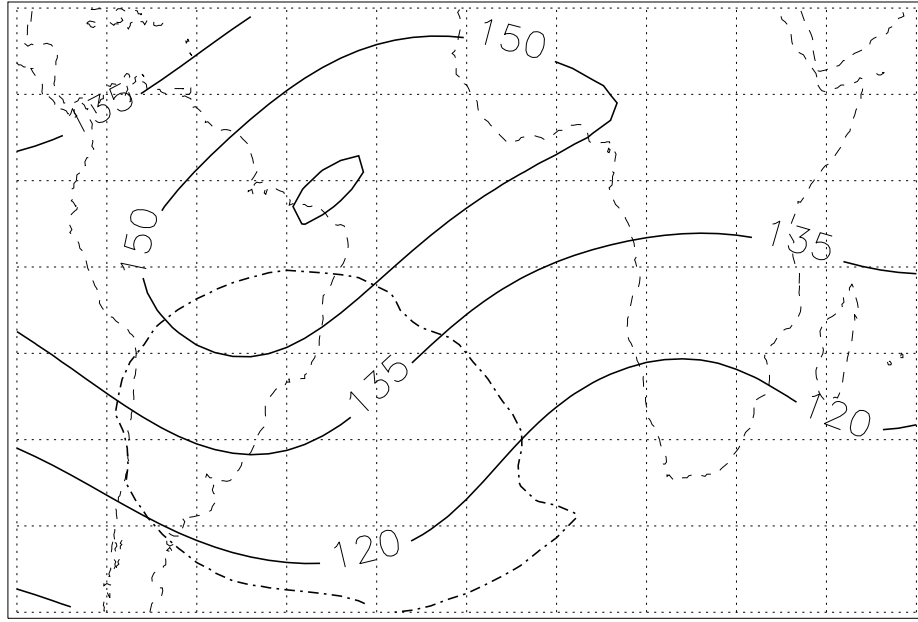


Figure 10.17. Local pitch angle of the HEPS2/T1 telescope with azimuth angle $180^\circ - \mathcal{A}$ (descending leg). The SAA is not covered by the α range $90^\circ \pm 10^\circ$.

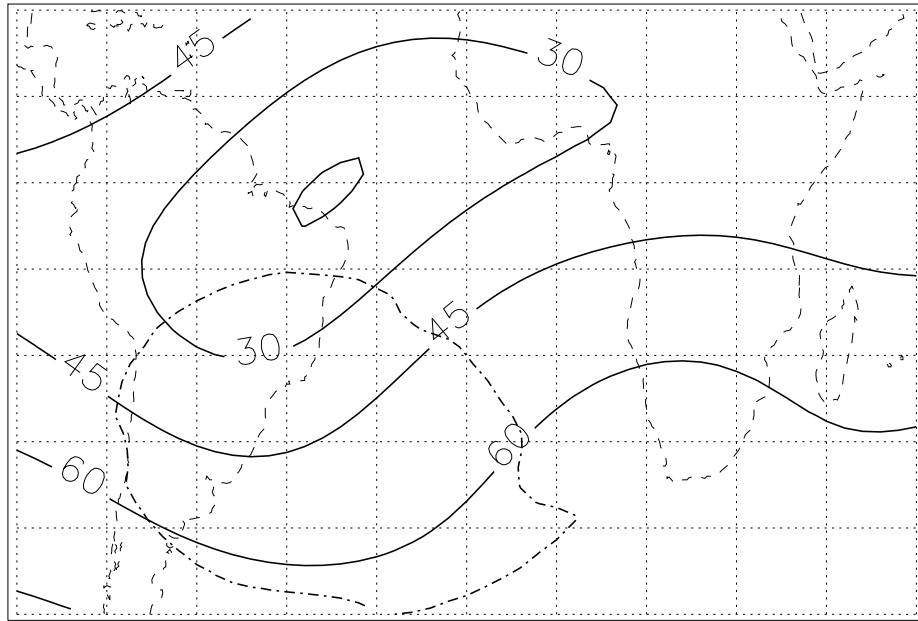


Figure 10.18. Local pitch angle of the HEPS2/T1 telescope with azimuth angle $360^\circ - \mathcal{A}$ (descending leg). The SAA is not covered by the α range $90^\circ \pm 10^\circ$.

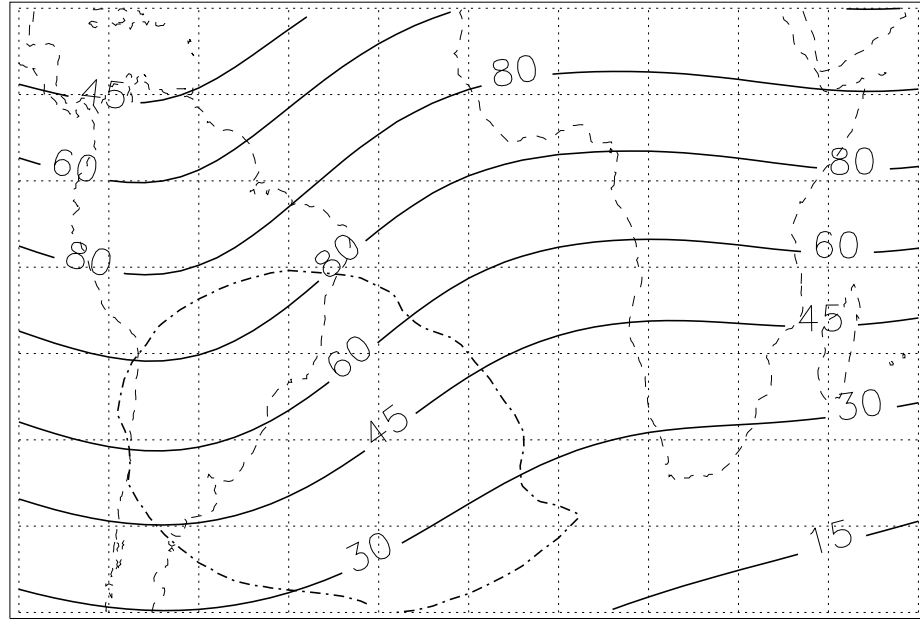


Figure 10.19. Iso-contours of the equatorial pitch angle when $\alpha = 90^\circ$ at 585 km. Equatorially mirroring particles are observable only in the northern part of the SAA.

For detector HEPS1/T1, when the azimuth angle is equal to $\mathcal{A} + 180^\circ$ (Fig. 10.12) or $180^\circ - \mathcal{A}$ (Fig. 10.13), L goes up to 1.7 when the local pitch angle is about $90^\circ \pm 10^\circ$ in the SAA. This is the reason why the detector HEPS1/T1 provides the larger coverage in Fig. 9.4

Since detector HEPS2/T1 is perpendicular to the vertical axis, the 180° rotation of the spacecraft only reverses the look direction of the detector. Therefore, the pitch angles in Figs. 10.16 and 10.18 are the supplement of the angles presented in Figs. 10.15 and 10.17, respectively. Detector HEPS2/T1 crosses the SAA with a pitch angle about $90^\circ \pm 10^\circ$ only for $L > 2.0$. The measurement data of this detector will thus be less useful for the PEM/UARS proton model than the data of the other detectors. The data coverage of detector HEPS2/T1 displayed in Fig. 9.4 corresponds to geographic locations outside the SAA, i.e. where trapped proton flux has dropped to negligible values.

In summary, Figs. 10.3–10.18 demonstrate that mostly only half of the HEPS1/T1 measurements can be used to derive a new proton flux model from the PEM instrument.

In Fig. 10.19, the equatorial pitch angle corresponding to a local pitch angle of 90° is shown as a function of the geographic location. The equatorial pitch angle is deduced from Figs. 10.1 and 10.2 with the help of Eq. (10.2). Values of α_0 greater than 80° are reached only when $L < 1.2$. Note that a better coverage cannot be obtained even when other local pitch angles are taken into account. The coverage displayed in Fig. 9.4 is mainly a function of the spacecraft attitude. When local pitch angles less than 80° are taken into account, smaller equatorial pitch angles can be reached but they correspond to directions inside the loss cone.

10.2 Detector field of view

In this section, we illustrate the effect of a finite field of view on the proton flux measurements in the case of the HEPS detectors. The formulae used below have been presented and discussed in Sect. 3.1.

The flux measurements for the time period from 7 Oct to 31 Dec for $1.295 < L < 1.305$ are displayed on Fig. 10.20 as a function of the equatorial pitch angle for each HEPS detector. In each panel, the proton fluxes have a strange distribution. Moreover, since the coordinates L and α_0 are related to the adiabatic invariants, the proton flux should have the same distribution for all the detectors. The HEPS1/T1 data at $\alpha_0 > 38^\circ$ are as expected, whilst fluxes measured for $\alpha_0 < 38^\circ$ seem to be spurious at first glance. Note that the detectors HEPS1/T2 and HEPS2/T2 provide very similar results. The result of detector HEPS2/T1 is the strangest one. The measurements displayed in Fig. 10.20 indicate clearly that at least one assumption we have made is not satisfied. At this point, different checks have been made:

- each step of the data processing has been checked carefully;
- the validity of the UARS ephemeris stored in the IDFS database has been verified by the comparison between the measured and IGRF magnetic fields (see Section 9.2.1);
- the HEPS measurements appeared to be valid according to the quality factors;
- the proton fluxes vanish when the spacecraft is outside the SAA;
- inside the SAA, the time evolution of the proton fluxes is very much like what is expected;
- ...

The only aspect not taken into account for the data in Fig. 10.20 is the opening angle correction, i.e the geometric factor correction described in Sect. 3.1. The raw data of Fig. 10.20 does not include this correction since the correction needs an iterative process and is generally assumed to be sufficiently small to be ignored in a first analysis.

The geometric factor correction is generally supposed to be small for detectors like HEPS where the field of view is equal to 30° . No field of view correction is needed when the particle flux is isotropic but can be very important when the proton flux becomes highly anisotropic. In Fig. 10.21, the local pitch angles of HEPS detectors are displayed for the same conditions as Fig. 10.20. The distribution in α is different for each detector except for HEPS1/T2 and HEPS2/T2 for which the distributions are similar. The coverage in local pitch angle has been already explained in Sect. 10.1. When Figs. 10.20 and 10.21 are compared, a correlation seems to appear between the proton flux behaviour and the local pitch angle distribution. For the detector HEPS1/T1, there are mainly two sets of local/equatorial pitch angles. The separation is near $\alpha_0 = 38^\circ$ which is also a separation in the HEPS1/T1 proton flux behaviour. At $\alpha_0 > 38^\circ$, $\alpha \approx 90^\circ$ and the proton flux behaviour is the mostly credible. For the detectors HEPS1/T2 and HEPS2/T2, the two sets of local/equatorial pitch angles overlap for $\alpha_0 < 47^\circ$. This angle also seems to be a separation in the proton flux behaviour of these detectors. Finally, for detector

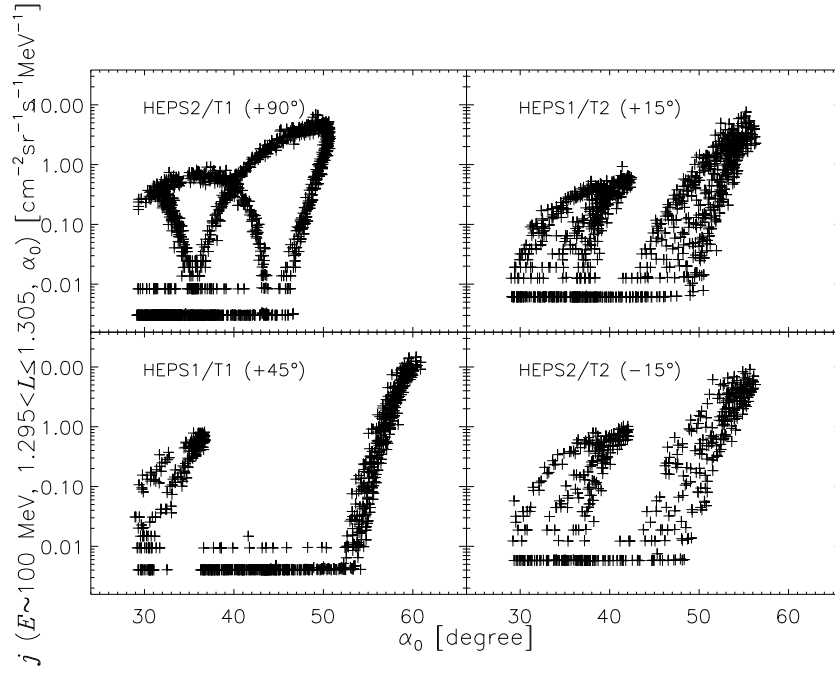


Figure 10.20. Raw $E \approx 100$ MeV proton flux at $1.295 < L < 1.305$ measured by the HEPS1/T2, HEPS1/T1, HEPS2/T2 and HEPS2/T1 telescopes as a function of the equatorial pitch angle for the period of time from October to December 1991

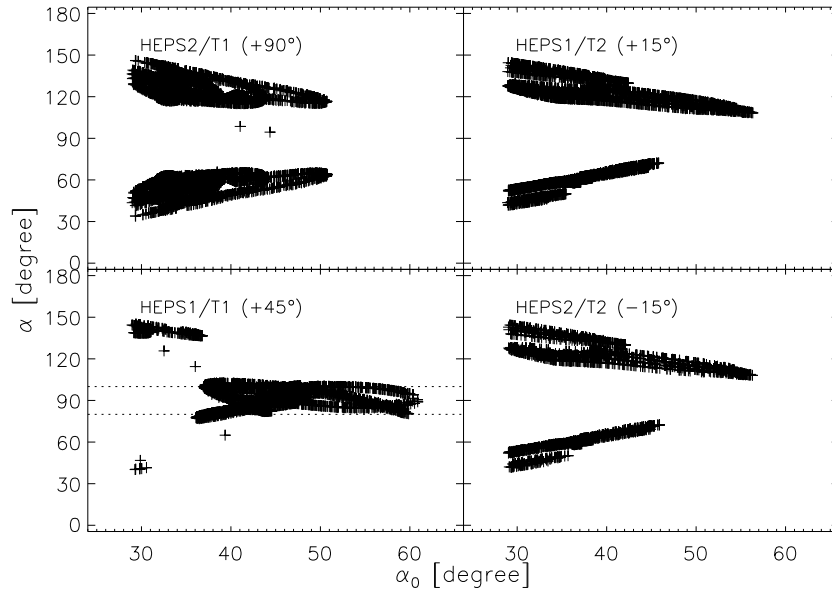


Figure 10.21. Distribution of the local pitch angle of the HEPS1/T2, HEPS1/T1, HEPS2/T2 and HEPS2/T1 telescopes as a function of α_0 at $1.295 < L < 1.305$ for the period of time from October to December 1991

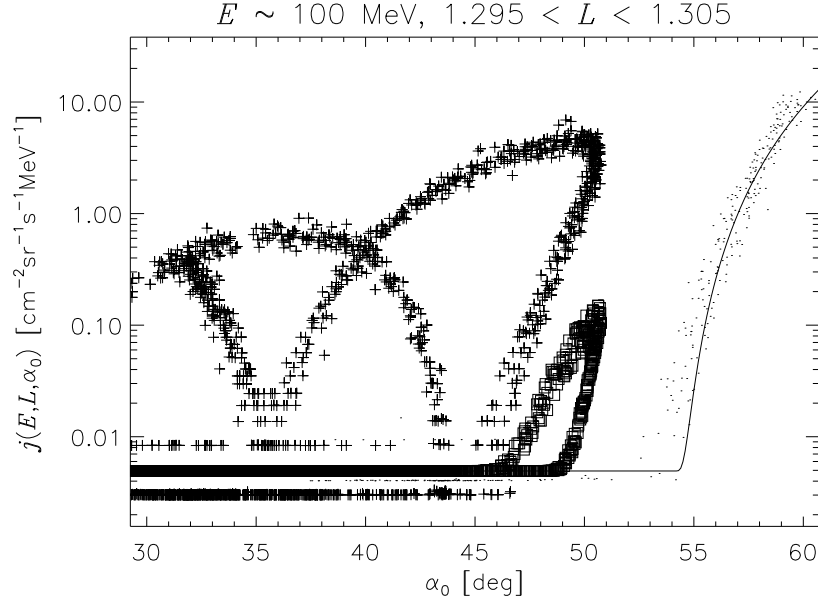


Figure 10.22. Simulation of the detector HEPS2/T1 in the same conditions as Fig. 10.20 when its angular response corresponds to a FOV of 30° . The dots correspond to the raw measurements of detector HEPS1/T1 for which $80^\circ \leq \alpha \leq 100^\circ$ whose have been used to fit the true flux j represented by the solid line. The plus signs correspond to the raw measurements of detector HEPS2/T1 while the square signs are the result of the simulation based on the flux j and the angular response h_1 .

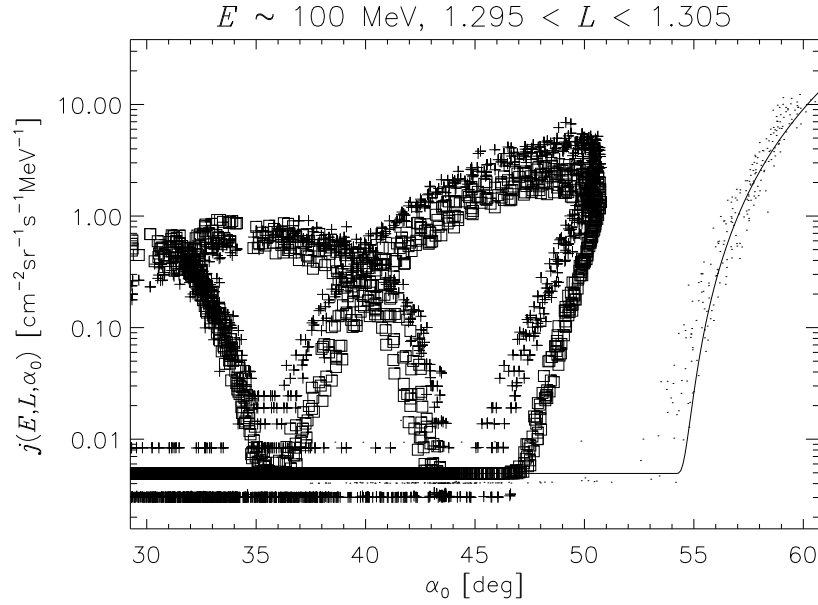


Figure 10.23. Simulation of the detector HEPS2/T1 in the same conditions as Fig. 10.20 when the FOV is extended to 130° . The dots, the solid line and the plus signs are the same as Fig. 10.22. But the square signs are the result of the simulation based on the flux j and the angular response h_2 .

HEPS2/T1 which has the strangest proton flux behaviour, the two sets of local/equatorial pitch angles overlap on the whole range of α_0 . So, for all cases, the proton flux has a stranger distribution when the local pitch angle deviates from 90° . Neglecting of the view-angle correction may explain this fact. When the local pitch angle is different from 90° , the detector is looking inside the loss cone where the proton flux is very low. But, due to the finite size of the FOV, locally mirroring protons (for which the flux is much higher) can be seen by the edge of the detector FOV. In that case, the observed flux cannot be associated simply to the look direction of the detector axis.

To test the effect of the view-angle correction on the UARS data, we have simulated the response of the detector HEPS2/T1. The proton flux measurements j^* are related to the true local flux j by

$$Gj^* = \int_0^\pi d\theta \int_0^{2\pi} d\phi j(\alpha') h(\theta) \cos \theta \sin \theta \quad (10.3)$$

where α' corresponds to the local pitch angle of the direction (θ, ϕ) and is obtained from Eq. (3.20), $h(\theta)$ is the angular response of the detector and the geometric factor G is given by

$$G = 2\pi \int_0^\pi d\theta h(\theta) \cos \theta \sin \theta. \quad (10.4)$$

The simulation of j^* for the detector HEPS2/T1 at $1.295 < L < 1.305$ has been computed for two different response functions $h(\theta)$:

1. $h_1(\theta)$ is equal to 1 when $\theta < 15^\circ$ and to 0 otherwise;
2. $h_2(\theta)$ is equal to 1 when $\theta < 15^\circ$, decreases linearly from 1 to 0 when $15^\circ < \theta < 65^\circ$, and is equal to 0 otherwise.

The first function corresponds to a detector with a FOV of 30° while the second function corresponds to a detector with a larger FOV but where the angular response is weaker on the edge of the FOV, e.g. due to a passive shielding. For the simulation, the true local flux j is evaluated from a fit to the data of detector HEPS1/T1 for which $80^\circ \leq \alpha \leq 100^\circ$ (data located between the dotted lines in Fig. 10.21). The results of both simulation are presented in Figs. 10.22 and 10.23.

In Figs. 10.22 and 10.23 the 100 MeV proton measurements of detector HEPS2/T1 are compared to two different simulations as a function of the equatorial pitch angle at $L = 3$. In both figures, the dots correspond to the HEPS1/T1 data from which the true flux j represented by a solid line has been fitted. The plus and square signs correspond to the HEPS2/T1 measurements and simulated measurements, respectively. The simulation of Fig. 10.22 does not reproduce all the detector measurements very well. According to the simulation, when the equatorial pitch angle associated to the detector axis is less than 45° at $L = 3$, a telescope with a FOV of 30° should not detect 100 MeV trapped protons. On the contrary, the simulation of Fig. 10.23 with a wider FOV fits better the measurements. Note that when the FOV extends to a value smaller than 130° , the measurements around $\alpha_0 = 30^\circ$ are not well fitted. The simulations of Figs. 10.22 and 10.23 demonstrate that the effective field of view of the HEPS detectors is probably about

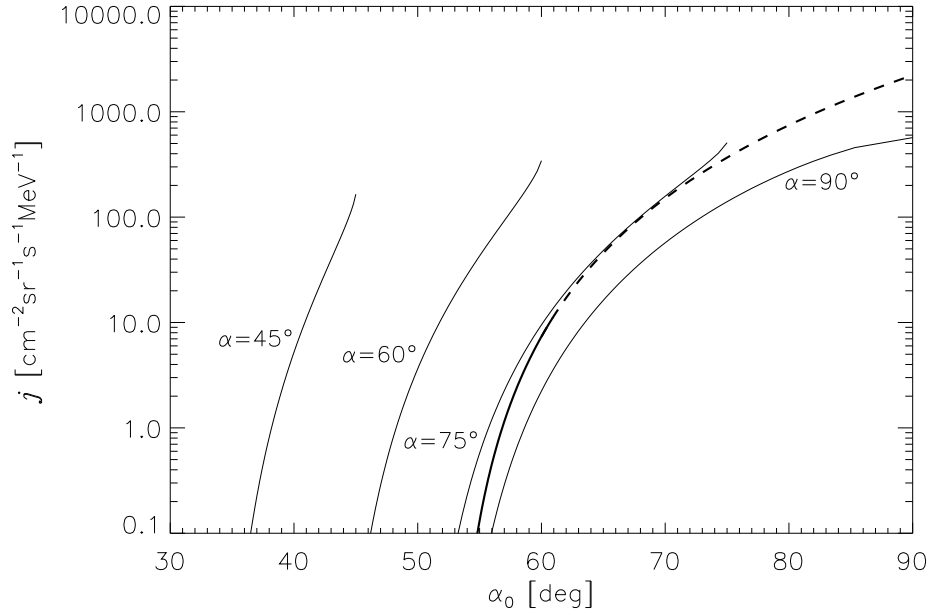


Figure 10.24. Simulation of detector measurements as a function of α_0 at different local pitch angles. The solid-dashed line corresponds to the true flux j . The thin solid lines are the results of simulations.

130°. To provide an even better simulation, one would have to know the real angular response of the detector.

The differences between j (the solid curve in Figs. 10.22 and 10.23) and j^* (square signs) clearly show that it is difficult to deduce j from j^* when the orientation of the detector deviates from an angle of 90° with respect to the local magnetic field direction. This problem is illustrated in Fig. 10.24 where the solid-dashed curve represents the true flux j , i.e. the flux that should be seen by an ideal detector with an infinitely small FOV. The solid part of the curve corresponds to the fit used in Figs. 10.22 and 10.23 while the dashed part is an extrapolation to 90°. The angular response of the detector is set to h_2 , the same function as in Fig. 10.23. The thin solid lines of Fig. 10.24 are the results of simulations when the orientation of the detector is set to $\alpha = 45^\circ, 60^\circ, 75^\circ$ and 90° , respectively. One should note that Fig. 10.24 does not depend on L nor on E (for different values of L or E , the function j is of course different, of course). When $\alpha = 90^\circ$, the proton flux is underestimated. The ratio j/j^* is equal to 4.7 at its maximum near $\alpha_0 = 55^\circ$; it decreases to 2.6 at $\alpha_0 = 73\frac{1}{2}^\circ$, and is equal to 3.9 at $\alpha_0 = 90^\circ$. When $\alpha = 75^\circ, 60^\circ$ or 45° , the proton flux is overestimated and the data does not cover the whole range of α_0 . For $\alpha = 75^\circ$, the ratio j/j^* is minimum at $\alpha_0 = 53^\circ$; it increases to 1 at $\alpha_0 = 68^\circ$, and is equal to 0.7 at $\alpha_0 = 75^\circ$.

The ratio j/j^* can be used to correct the measurements a posteriori when the measurements and the simulations cover the same equatorial pitch angle range. This type of correction was applied to the AZUR data (see Sect. 3.4) for which $\alpha \approx 90^\circ$. In the case of the UARS data, it appears clearly from Fig. 10.24 that a correction is not possible for local pitch angles less than

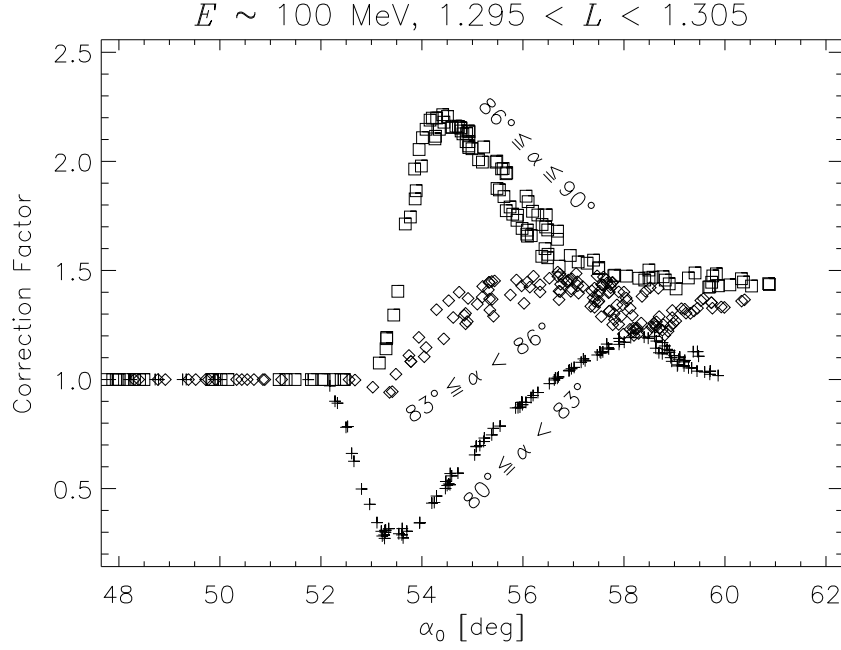


Figure 10.25. Correction factor of the HEPS1/T1 measurements for the same conditions as Fig. 10.20

75°. Note that since we do not know exactly the angular response of the HEPS detector, such a correction can only be applied approximatively.

One should note also that the flux j used to produce the simulation of Fig. 10.23 is deduced from raw measurements, i.e. uncorrected data, and can be wrong by a factor of 5. Therefore, the good agreement between the measurement and the simulation does not mean that $h_2(\theta)$ corresponds exactly to the angular response of the HEPS detectors. Indeed, other angular response function may give similar agreement, if not better.

10.3 Corrected flux

The flux correction has only been applied to the measurements of the HEPS1/T1 telescope since it is the telescope that covers the largest part of the (α_0, L) space and that has its local pitch angle near 90° when the spacecraft passes through the SAA. To apply the correction, the proton fluxes have been fitted for each L value to a 3-parameter function given by

$$j(\alpha_0) = \begin{cases} f01 & \text{when } \alpha_0 < \alpha_{0c} \\ f01 + K\xi[1 + b\xi(1 + b\xi)] & \text{when } \alpha_0 > \alpha_{0c} \end{cases} \quad (10.5)$$

where α_{0c} , K , b are parameters to be fitted, $f01$ is a constant fixed at $10^{-2} \text{ cm}^{-2} \text{ sr}^{-1} \text{ s}^{-1} \text{ MeV}^{-1}$ and ξ is defined by Eq. 9.7. Since the correct effective area has not yet been communicated by Lockheed Palo Alto Research Laboratory, a simple guess function has been used for the

correction. This function is defined by

$$h(\alpha) = \begin{cases} \cos \alpha & \text{when } \alpha < 16^\circ \\ 0 & \text{when } \alpha > 16^\circ \end{cases} \quad (10.6)$$

The correction factors for the measurements corresponding to $1.295 < L < 1.305$ are displayed in Fig. 10.25 as a function of the equatorial pitch angle. On the figure, the measurements have been splitted in three data sets according to the orientation of the detector:

- $86^\circ \leq \alpha \leq 90^\circ$ (\square symbols);
- $83^\circ \leq \alpha < 86^\circ$ (\diamond symbols);
- $80^\circ \leq \alpha < 83^\circ$ (+ symbols).

The correction factor varies between 0.3 and 2.2. It can be seen that its behaviour highly depends on the orientation (i.e. local pitch angle) of the detector. When $\alpha > 83^\circ$, the proton flux is underestimated while, when $\alpha < 83^\circ$, the proton flux is overestimated. For $\alpha_0 \ll \alpha_{0c}^\circ$ the correction factor is equal to 1 and no correction are applied.

10.4 Proton flux model

The trapped proton flux model PUB97¹ obtained from the UARS/HEPS data is illustrated on Figures 10.26–10.35. The PUB97 model is based on the HEPS1/T1 measurements from 12 September 1991 till 1 September 1992 for which the angle between the sensor axis and the local magnetic field vector was near 90° . The PUB97 model is organized in terms of energy, McIlwain's shell parameter and equatorial pitch angle. It includes 15 energy channels from 6 to 168 MeV, 41 α_0 bins and 36 L bins. The effective coverage of the model is limited to the space below 600 km where $40^\circ < \alpha_0 < 75^\circ$ and $1.12 < L < 1.52$. The coverage is restricted therefore to the innermost edge of the proton radiation belt. This restriction is due to the fact that the PEM instrument was designed to catch the precipitating flux. Note that PEM data exist at times beyond September 1992.

The dependence of the proton differential flux on the equatorial pitch angle for three energy channels and different L values is shown on Figs. 10.26 and 10.28. The vertical bars represent the flux value plus/minus one standard deviation [as defined in Eq. (9.5)]. In both figures, the PUB97 model never reaches equatorial pitch angle near 90° : only the region in the vicinity of the atmospheric loss cone is properly covered in the model. Both figures show that the flux varies about one order of magnitude on the range of few degrees in equatorial pitch angle. It indicates also a slight dependence in energy of the cut-off location.

The proton energy spectra are displayed for different values of the equatorial pitch angle in Figs. 10.29 to 10.32 for $L = 1.2, 1.3, 1.4$ and 1.5 , respectively. It can be seen that the different

¹PUB is the acronym of Proton UARS BIRA

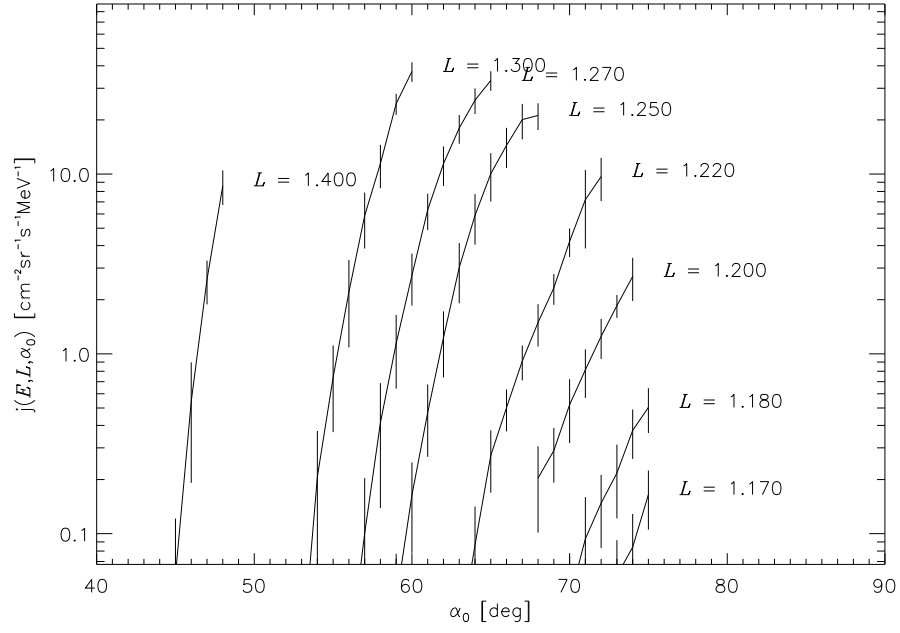


Figure 10.26. UARS/HEPS Differential flux as a function of the equatorial pitch angle for 17.2–24.4 MeV protons for different L values. The error bars correspond to one standard deviation ($\hat{\sigma}$).

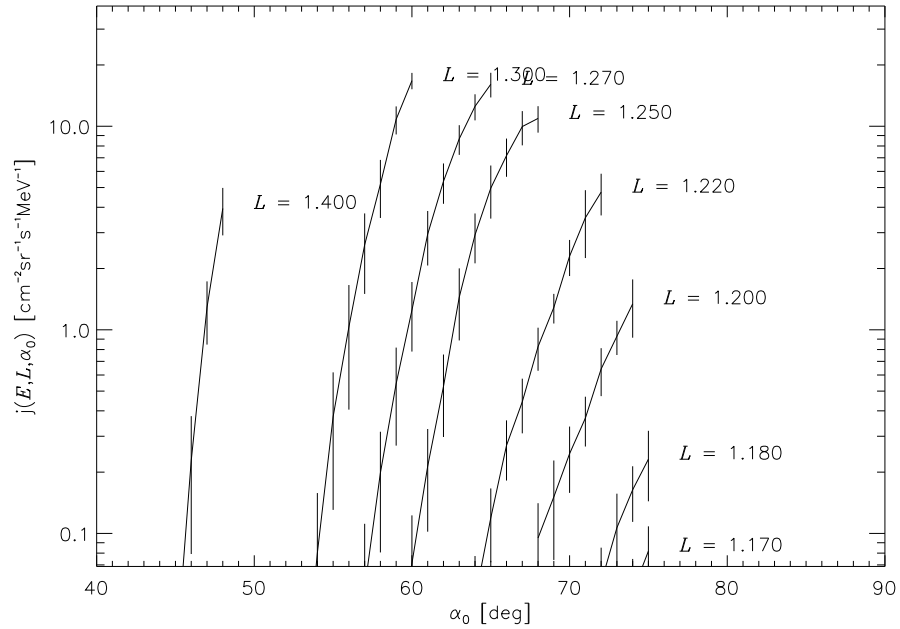


Figure 10.27. UARS/HEPS Differential flux as a function of the equatorial pitch angle for 31.7–42.1 MeV protons for different L values. The error bars correspond to one standard deviation ($\hat{\sigma}$).

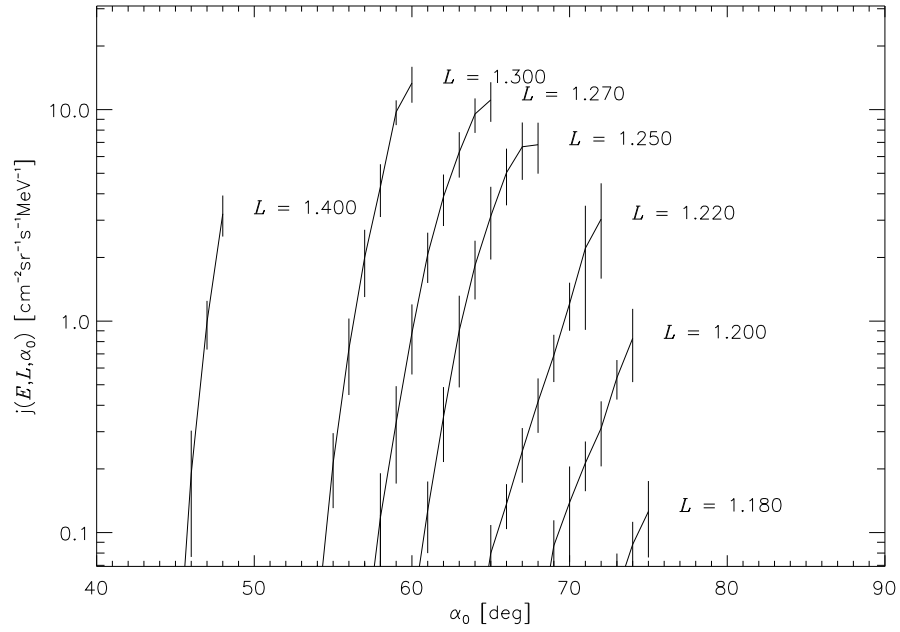


Figure 10.28. UARS/HEPS Differential flux as a function of the equatorial pitch angle for 94.0–122.5 MeV protons for different L values. The error bars correspond to one standard deviation ($\hat{\sigma}$).

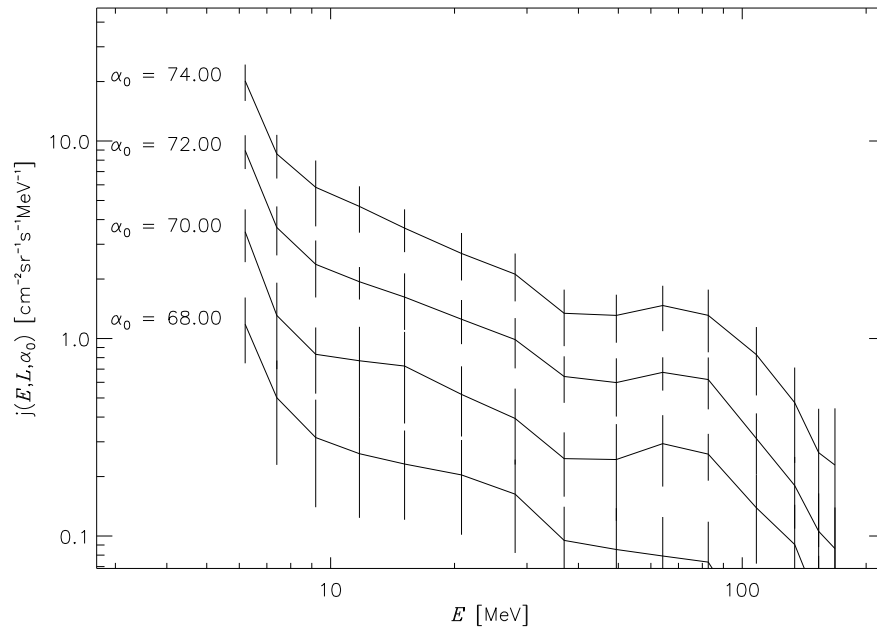


Figure 10.29. UARS/HEPS Differential proton flux spectra at $L = 1.2$ for different values of the equatorial pitch angle. The error bars correspond to one standard deviation ($\hat{\sigma}$).

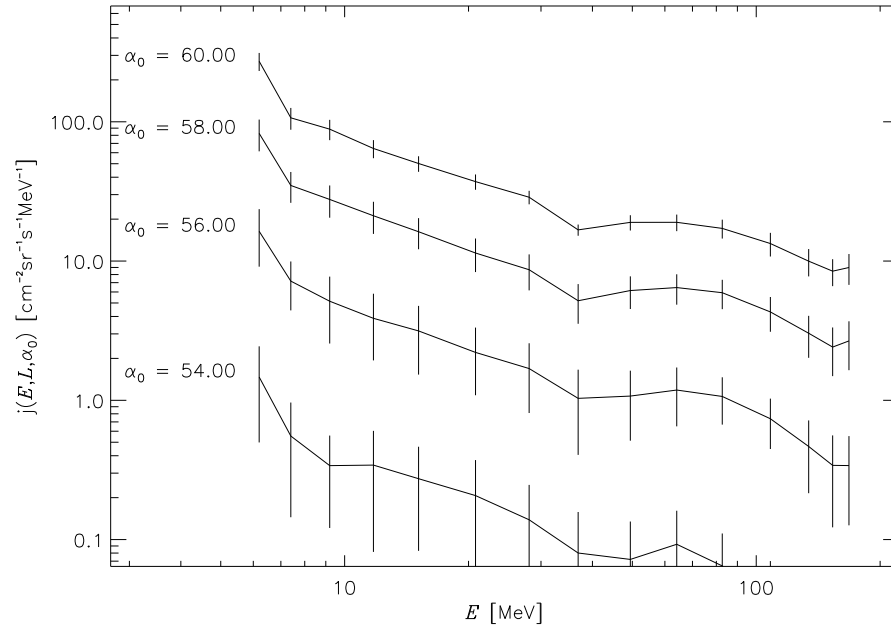


Figure 10.30. UARS/HEPS Differential proton flux spectra at $L = 1.3$ for different values of the equatorial pitch angle. The error bars correspond to one standard deviation ($\hat{\sigma}$).

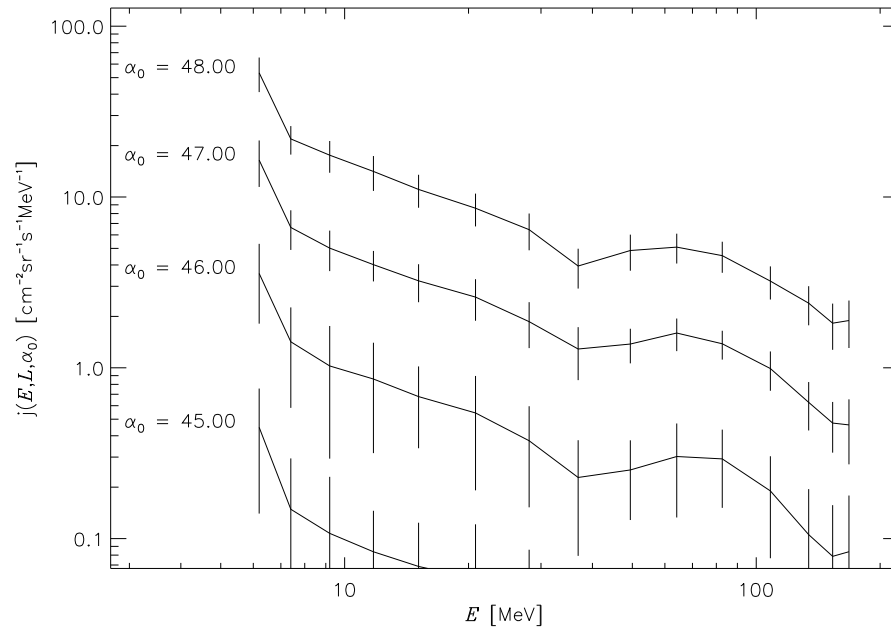


Figure 10.31. UARS/HEPS Differential proton flux spectra at $L = 1.4$ for different values of the equatorial pitch angle. The error bars correspond to one standard deviation ($\hat{\sigma}$).

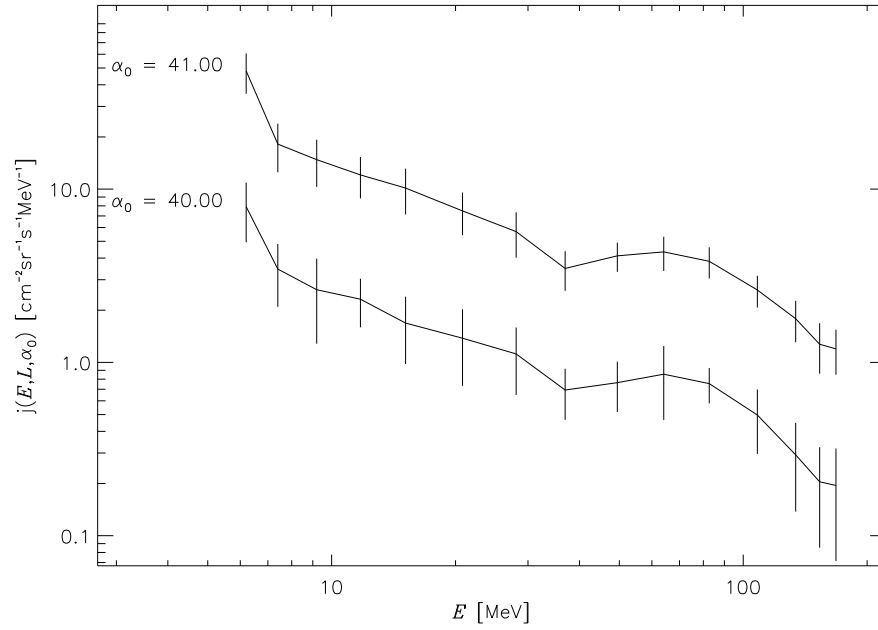


Figure 10.32. UARS/HEPS Differential proton flux spectra at $L = 1.5$ for different values of the equatorial pitch angle. The error bars correspond to one standard deviation ($\hat{\sigma}$).

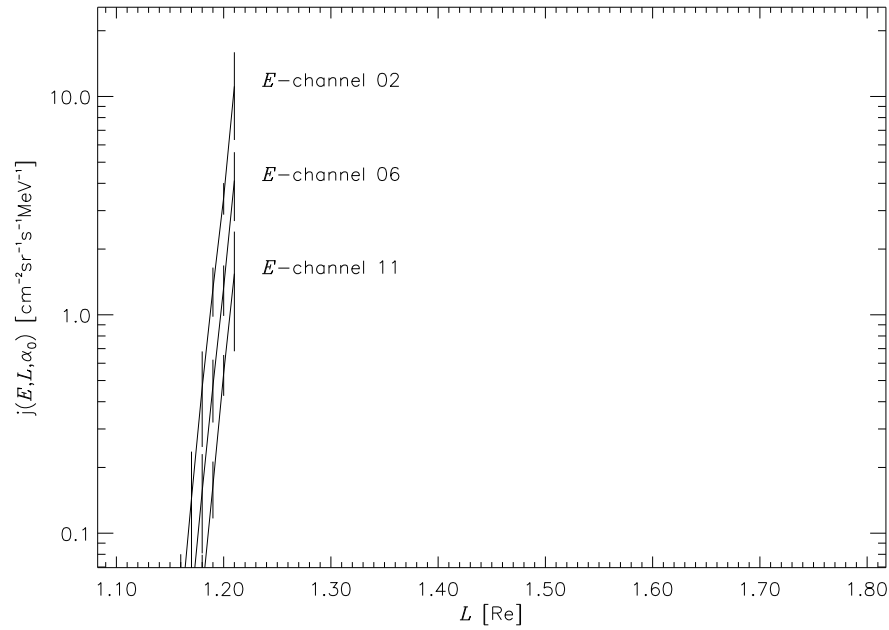


Figure 10.33. UARS/HEPS Differential proton flux as a function of the parameter L at $\alpha_0 = 73^\circ$ for different energy channels. The channels correspond to the energy ranges 8.0–10.5, 24.5–31.8 and 94.0–122.5 MeV, respectively. The error bars correspond to one standard deviation ($\hat{\sigma}$).

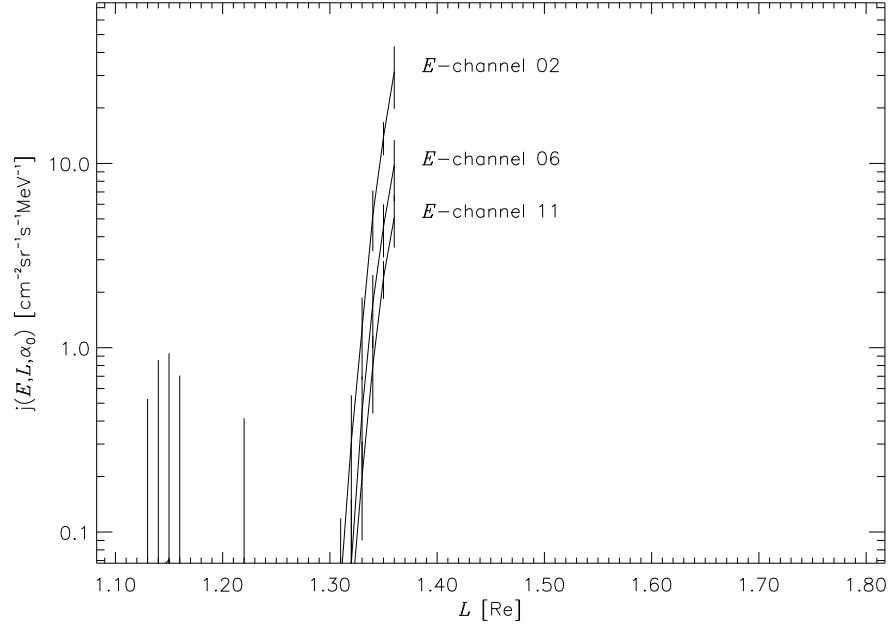


Figure 10.34. UARS/HEPS Differential proton flux as a function of the parameter L at $\alpha_0 = 52^\circ$ for different energy channels. The channels correspond to the energy ranges 8.0–10.5, 24.5–31.8 and 94.0–122.5 MeV, respectively. The error bars correspond to one standard deviation ($\hat{\sigma}$).

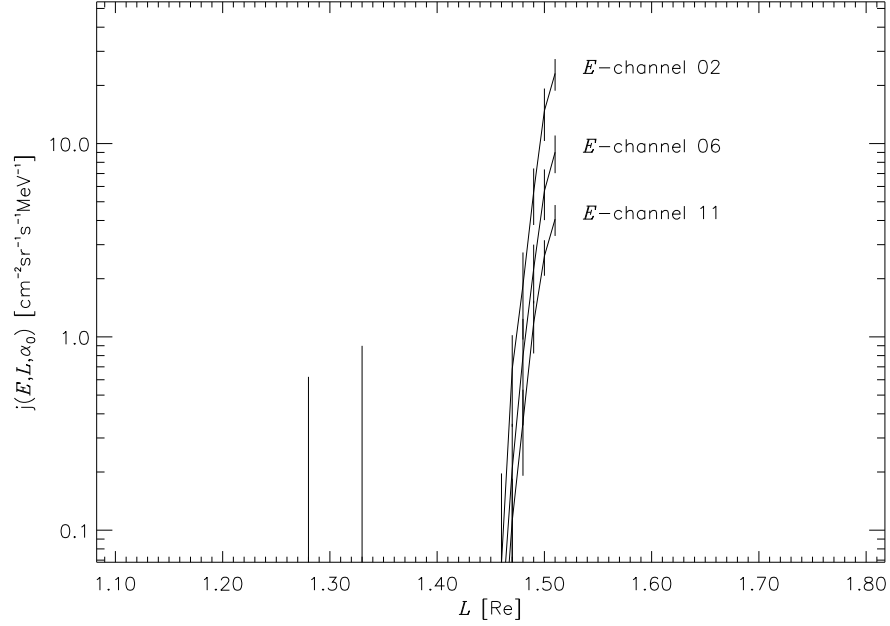


Figure 10.35. UARS/HEPS Differential proton flux as a function of the parameter L at $\alpha_0 = 41^\circ$ for different energy channels. The channels correspond to the energy ranges 8.0–10.5, 24.5–31.8 and 94.0–122.5 MeV, respectively. The error bars correspond to one standard deviation ($\hat{\sigma}$).

spectra have very similar slopes. Most of the spectra display a hump near 60 MeV, which is not present in AP-8 MAX energy spectra. Note that, due to the coverage of the model, spectra related to different equatorial pitch angles have been displayed for a set of L value. For $L = 1.2$, 1.3, 1.4 and 1.5, the coverage of the PUB97 model is limited to equatorial pitch angles about 74, 60, 48 and 41 degrees, respectively.

The dependence of the differential proton flux on the shell parameter is shown in Figs. 10.33, 10.34 and 10.35 at $\alpha_0 = 73^\circ$, 52° and 41° , respectively, for three different energy channels: 8.0–10.5 MeV, 24.5–31.8 MeV and 94.0–122.5 MeV. On each figure, the curves are closed to one another due to the slight dependence in energy of the cut-off location. Both figures show clearly that the coverage of the PUB97 model is restricted to the innermost edge of the proton radiation belt.

To be included in the UNIRAD programme TREP, the differential fluxes of the PUB97 model have been transformed into integral fluxes. The transformation has been applied with the assumption that the proton flux above 175 MeV can be neglected. The integral perpendicular proton fluxes for the 15 energy channels are shown on Figs. 10.36 to 10.50. On each figure, the fluxes of the PUB97 model are compared to the fluxes obtained with the NASA model AP-8 MAX. In order to facilitate the comparison, flux iso-contours and Vette's cutoff have been drawn on each panel. The Vette (1991a) cutoff B_c does not depend on the energy and is defined by

$$\frac{B_c}{B_0} = 0.65 L^{3.452}. \quad (10.7)$$

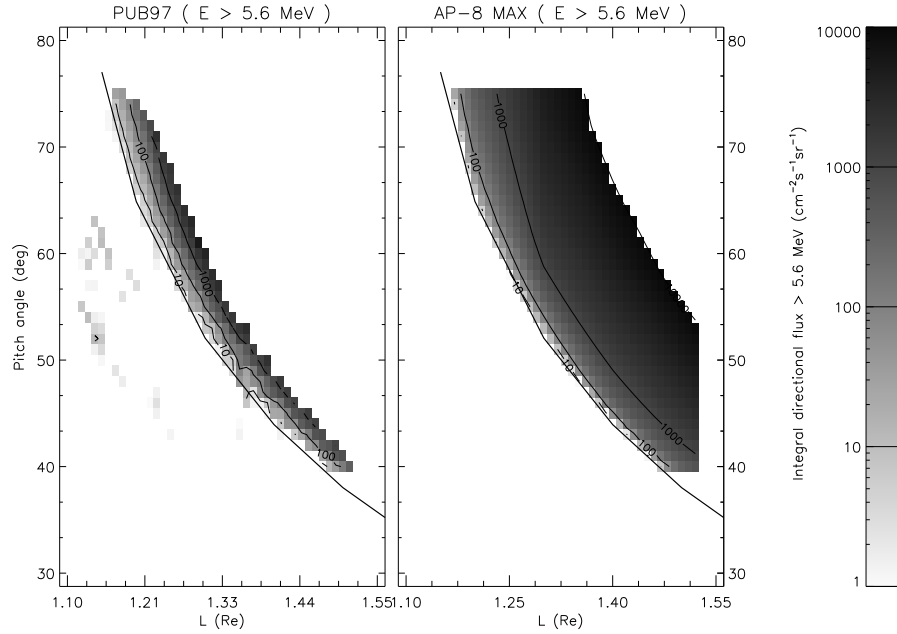


Figure 10.36. The integral perpendicular proton flux map of the PUB97 model compared to the NASA model AP-8 MAX at $E > 5.6$ MeV. The solid curves correspond to Vette's cutoff.

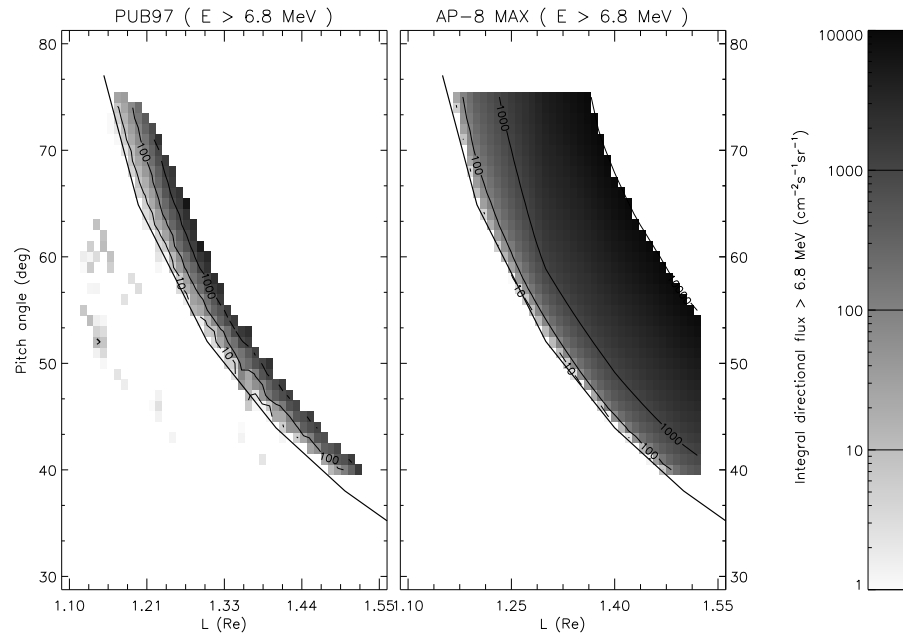


Figure 10.37. The integral perpendicular proton flux map of the PUB97 model compared to the NASA model AP-8 MAX at $E > 6.8$ MeV. The solid curves correspond to Vette's cutoff.

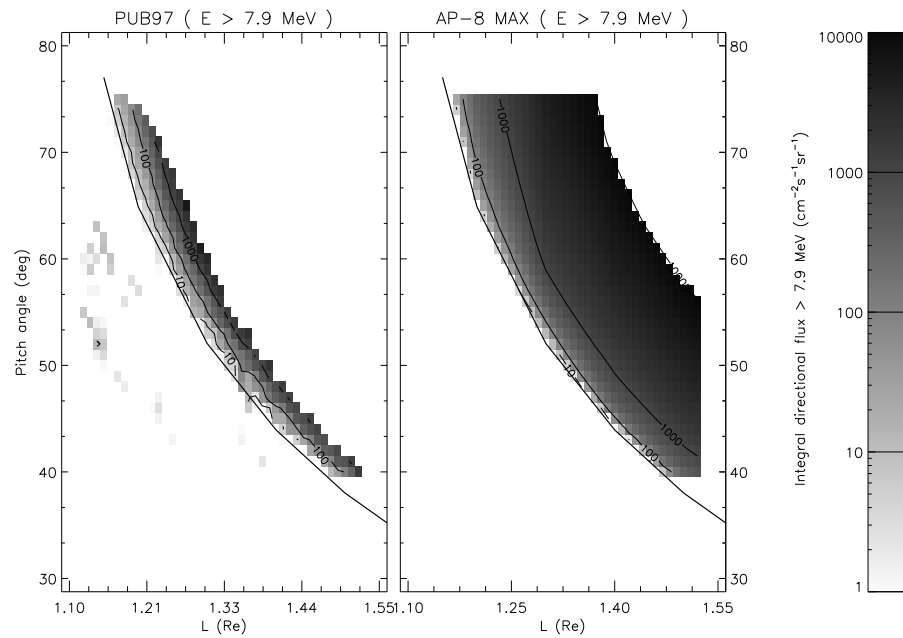


Figure 10.38. The integral perpendicular proton flux map of the PUB97 model compared to the NASA model AP-8 MAX at $E > 7.9$ MeV. The solid curves correspond to Vette's cutoff.

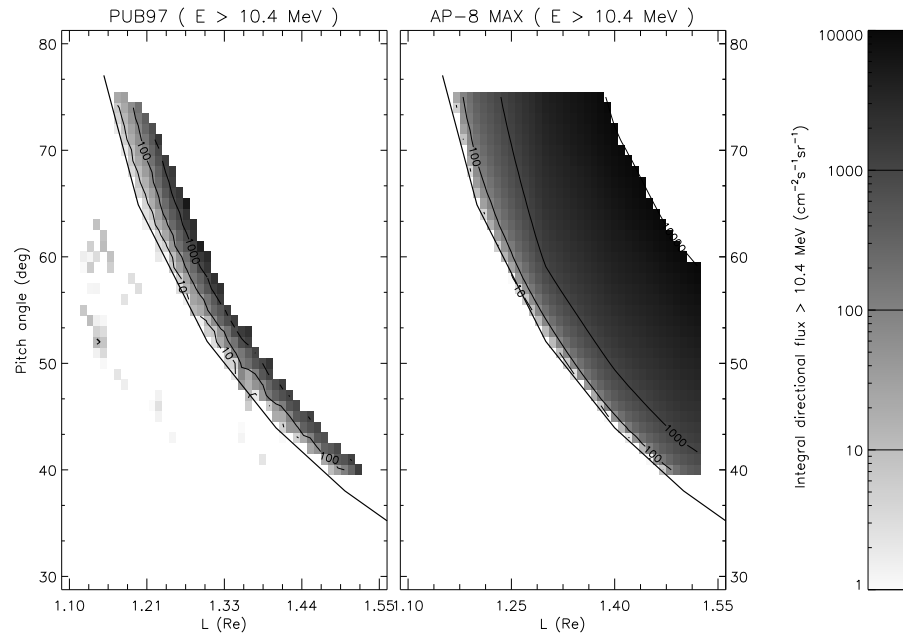


Figure 10.39. The integral perpendicular proton flux map of the PUB97 model compared to the NASA model AP-8 MAX at $E > 10.4$ MeV. The solid curves correspond to Vette's cutoff.

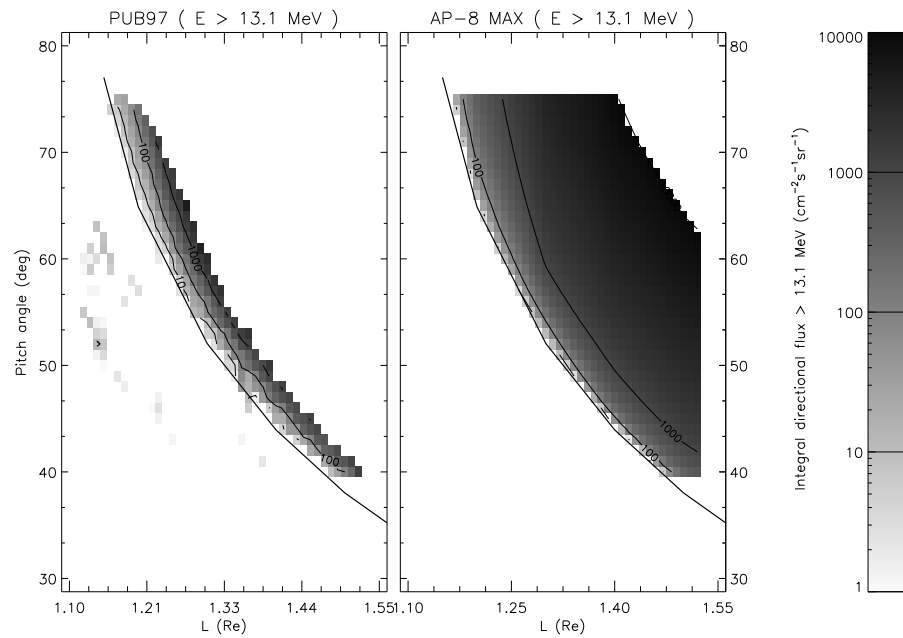


Figure 10.40. The integral perpendicular proton flux map of the PUB97 model compared to the NASA model AP-8 MAX at $E > 13.1$ MeV. The solid curves correspond to Vette's cutoff.

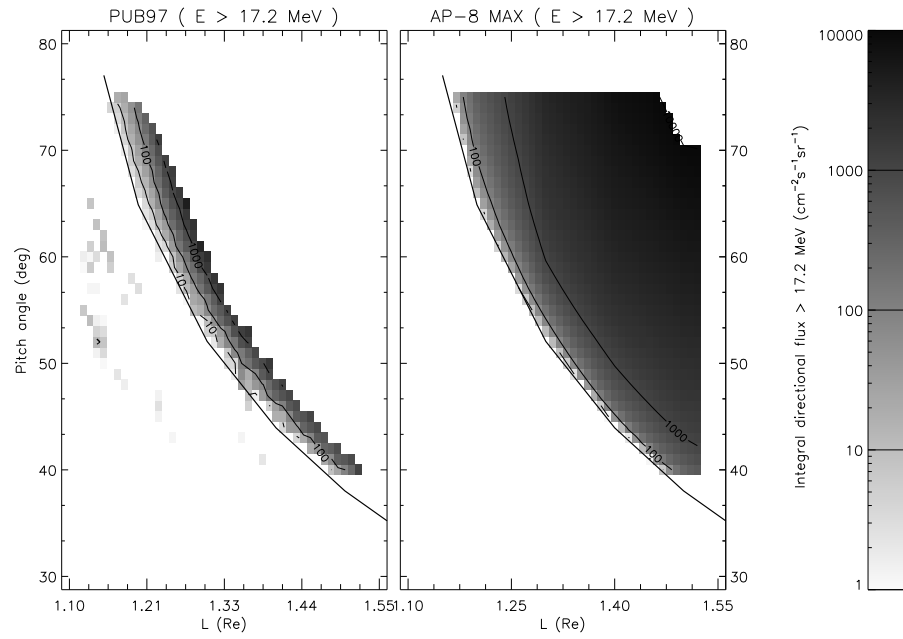


Figure 10.41. The integral perpendicular proton flux map of the PUB97 model compared to the NASA model AP-8 MAX at $E > 17.2$ MeV. The solid curves correspond to Vette's cutoff.

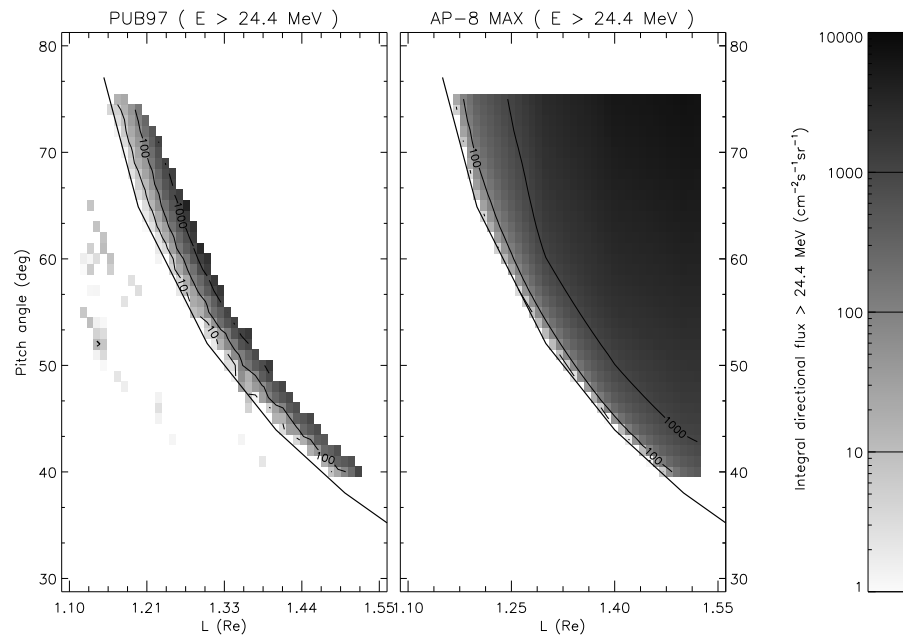


Figure 10.42. The integral perpendicular proton flux map of the PUB97 model compared to the NASA model AP-8 MAX at $E > 24.4$ MeV. The solid curves correspond to Vette's cutoff.

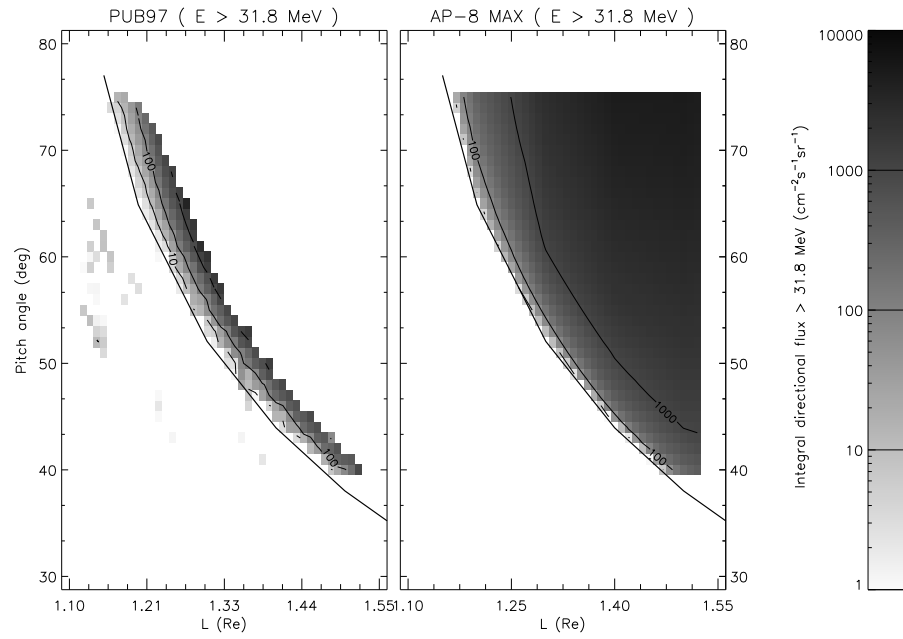


Figure 10.43. The integral perpendicular proton flux map of the PUB97 model compared to the NASA model AP-8 MAX at $E > 31.8$ MeV. The solid curves correspond to Vette's cutoff.

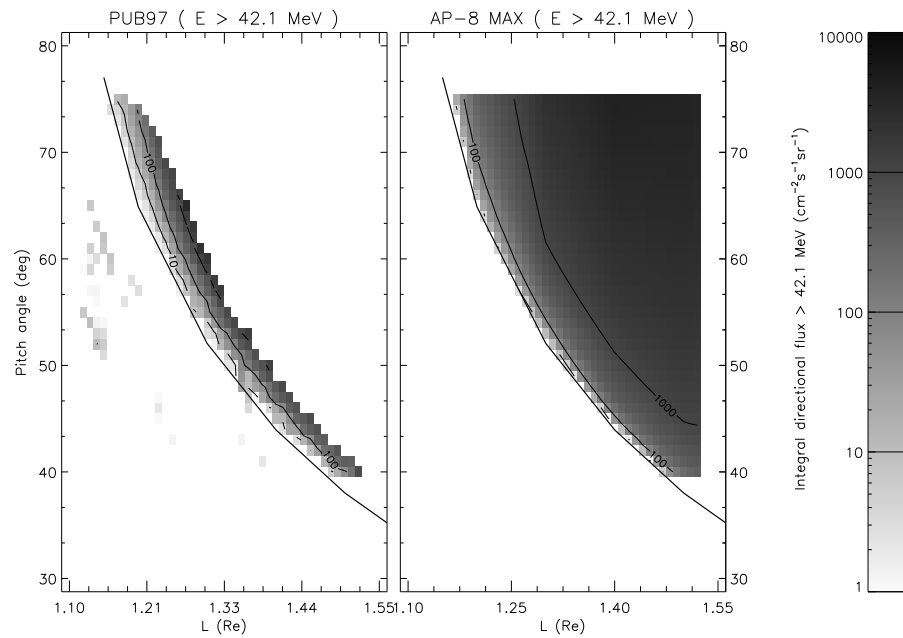


Figure 10.44. The integral perpendicular proton flux map of the PUB97 model compared to the NASA model AP-8 MAX at $E > 42.1$ MeV. The solid curves correspond to Vette's cutoff.

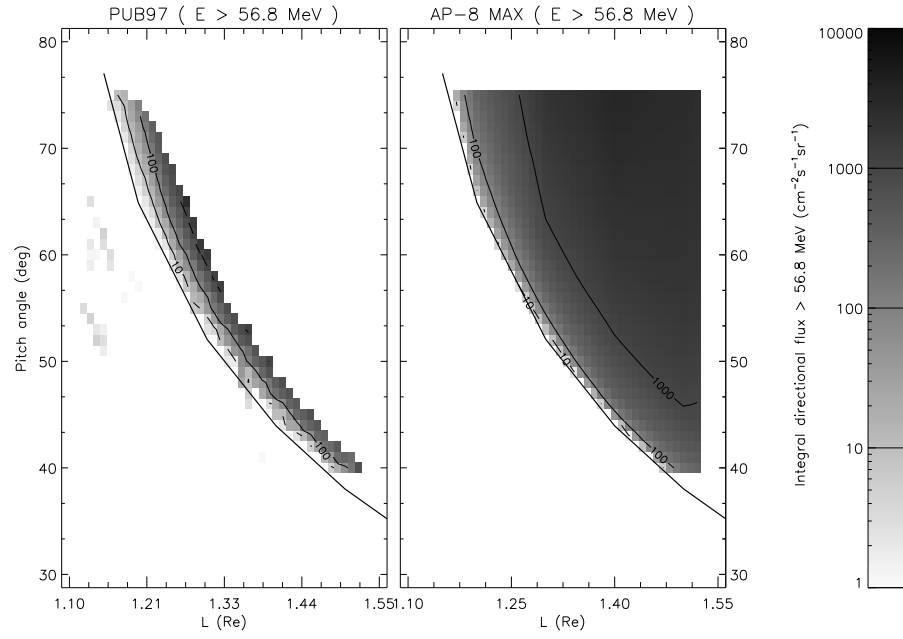


Figure 10.45. The integral perpendicular proton flux map of the PUB97 model compared to the NASA model AP-8 MAX at $E > 56.8$ MeV. The solid curves correspond to Vette's cutoff.

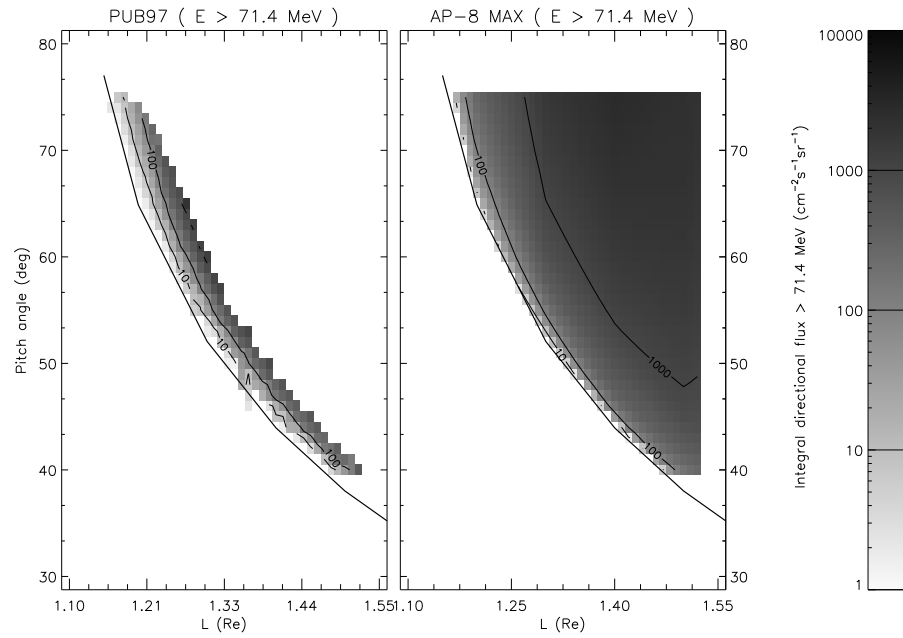


Figure 10.46. The integral perpendicular proton flux map of the PUB97 model compared to the NASA model AP-8 MAX at $E > 71.4$ MeV. The solid curves correspond to Vette's cutoff.

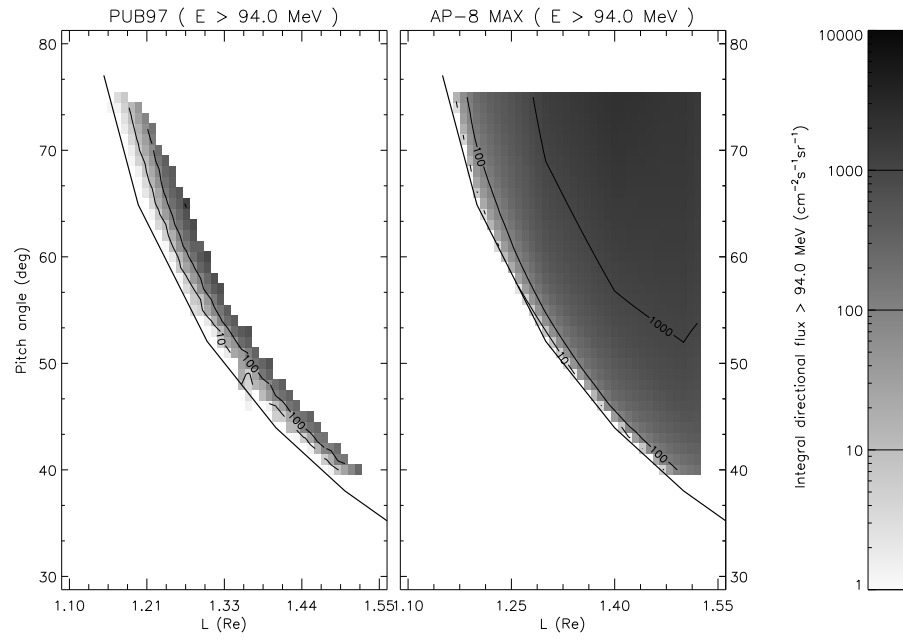


Figure 10.47. The integral perpendicular proton flux map of the PUB97 model compared to the NASA model AP-8 MAX at $E > 94.0$ MeV. The solid curves correspond to Vette's cutoff.

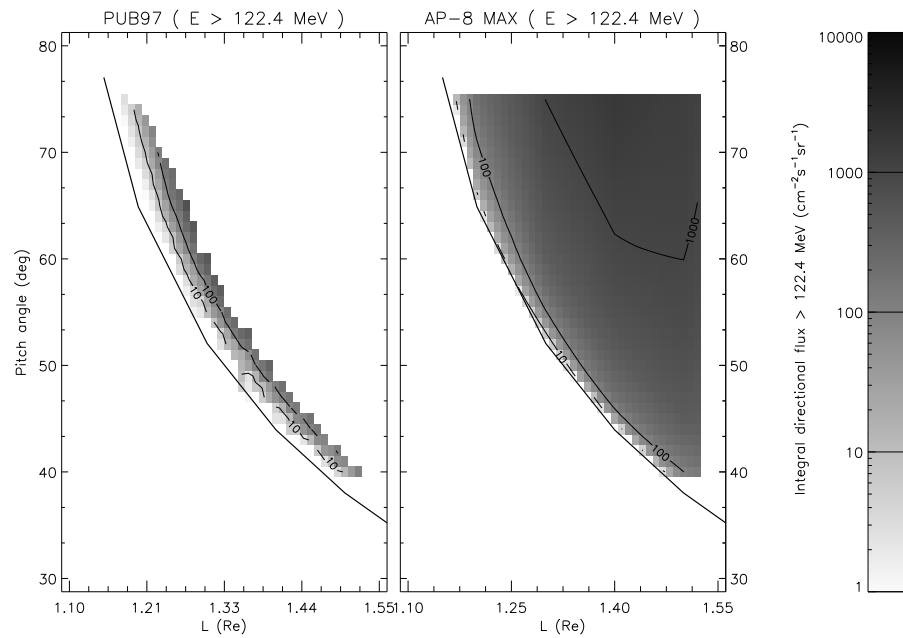


Figure 10.48. The integral perpendicular proton flux map of the PUB97 model compared to the NASA model AP-8 MAX at $E > 122.4$ MeV. The solid curves correspond to Vette's cutoff.

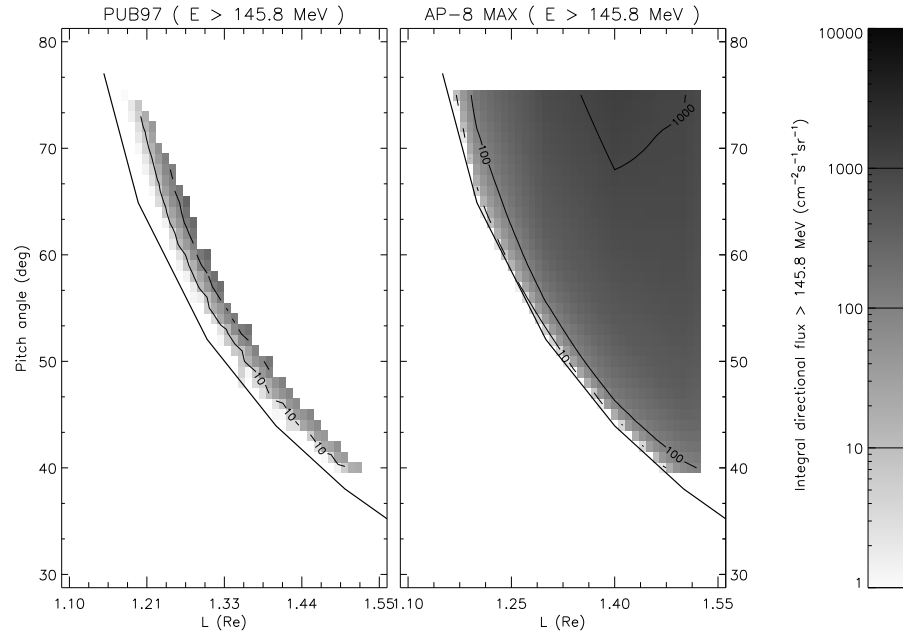


Figure 10.49. The integral perpendicular proton flux map of the PUB97 model compared to the NASA model AP-8 MAX at $E > 145.8$ MeV. The solid curves correspond to Vette's cutoff.

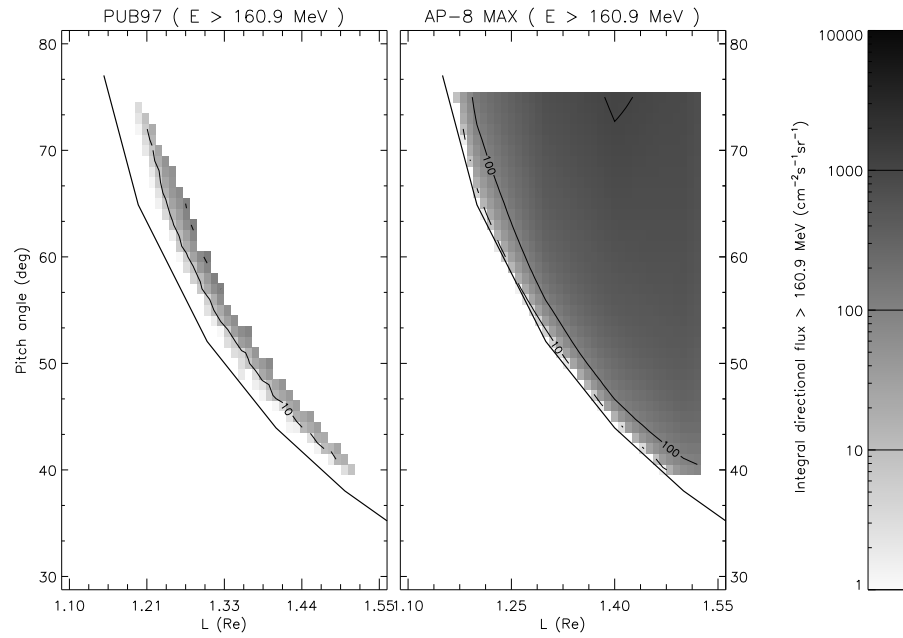


Figure 10.50. The integral perpendicular proton flux map of the PUB97 model compared to the NASA model AP-8 MAX at $E > 160.9$ MeV. The solid curves correspond to Vette's cutoff.

Since the PUB97 model and the NASA model do not correspond to the same epoch, (α_0, L) maps of both models are not directly comparable (Kruglanski 1996). Note also that the PUB97 model has not been extrapolated to higher equatorial pitch angles than available from the data set nor to L values beyond the region sampled.

On both figures, the cutoff of the PUB97 model appears at higher equatorial pitch angle, i.e. lower B , than AP-8 MAX for all energies. On the other hand, the PUB97 integral fluxes have a higher gradient than the AP-8 MAX fluxes. The origin of the weak fluxes present inside the loss cone of the PUB97 model has not been clearly identified. These weak fluxes are more prominent at the lower energies.

In Part 4 of this Technical Note, the TREP implementation of the PUB97 model is compared to other proton integral flux models.

Further details on the implementation of the PUB97 model in the TREP programme are provided in Technical Note 10. Note that when the PUB97 model is applied in the TREP programme, a warning is issued when the satellite ephemeris corresponds to L or α_0 values out of the validity range of the model.

Part IV

Model comparisons

Chapter 11

Intercomparisons of the models

In this Chapter, we intercompare the flux maps obtained from the AZUR, SAMPEX and UARS data. The AP-8 directional fluxes are added to the comparisons to put into perspective the results. The usage of the models derived from the flux maps, i.e. their implementation in TREP, is described in Technical Note 10.

As the new trapped proton models are based on data from low altitude satellites, their use is limited to predictions for low altitude missions. In Sect. 11.1, the new models, as well as the AP-8 models, are applied to a typical MIR or Space Station orbit. The model limitations are demonstrated in Sect. 11.2, where the models are applied to a GTO orbit. All model calculations were made with the UNIRAD programme suite.

11.1 Comparisons of the models for a LEO mission

The LEO mission selected for the model comparisons is a circular orbit at altitude 400 km and inclination 50° . We generated 14 orbits with SAPRE, and then ran TREP 5 times, once for each new model plus two runs with the directional versions of AP-8 MAX and AP-8 MIN. The resulting positional trapped proton unidirectional integral fluxes above 30 MeV are shown on the world maps in Figs. 11.1–11.5. On these maps, the filled squares represent non-zero fluxes. Orbital points where the flux is zero are not shown. The open squares represent orbital positions which are outside the validity range of the respective models (fluxes outside the model range are given a value -1.0 by TREP). The PAB97 and PUB97 models represent solar maximum conditions (for two different solar cycles), while the PSB97 model represents solar minimum conditions.

The first feature to note when comparing the world maps is the difference in coverage of the models. The nominal range of the AP-8 models extends over the whole region covered by the LEO orbit. This was achieved in the construction of the NASA models by extrapolating the models beyond the actual coverage of the satellite data that were used. For the new models, we decided not to extend their validity range by extrapolation, as this procedure can induce very large uncertainties in the extrapolated fluxes. The model coverage is further influenced by the

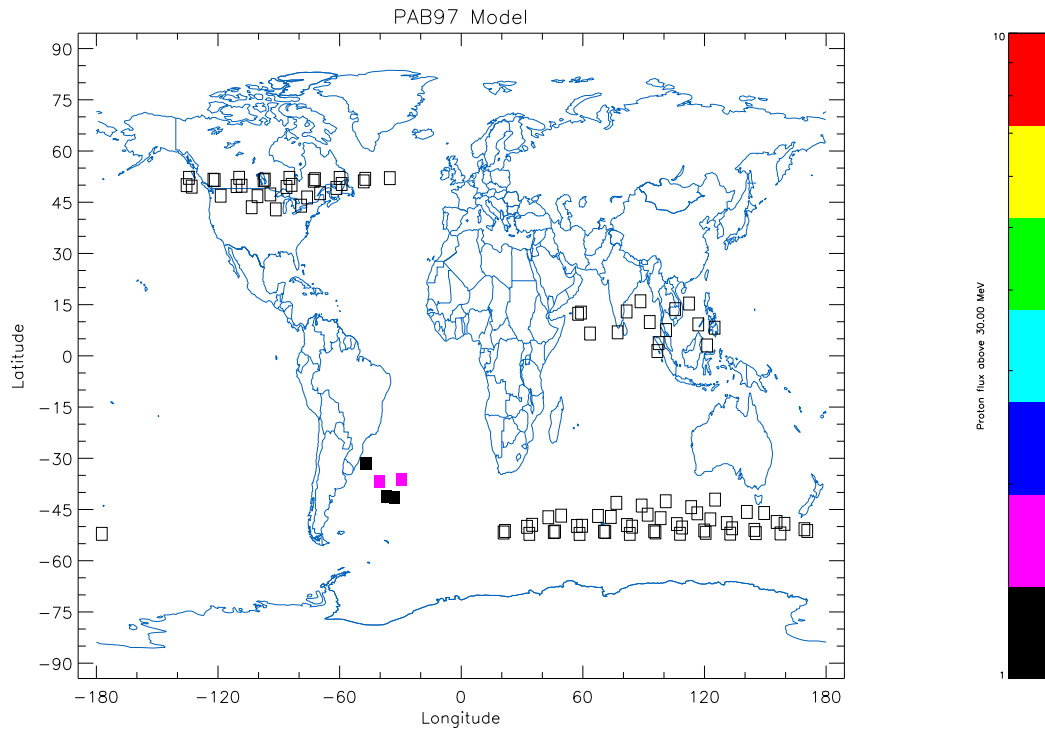


Figure 11.1. World map of the PAB97 directional proton flux above 30 MeV for the LEO orbit described in the text. The open squares represent orbital positions which are outside the validity range of the model.

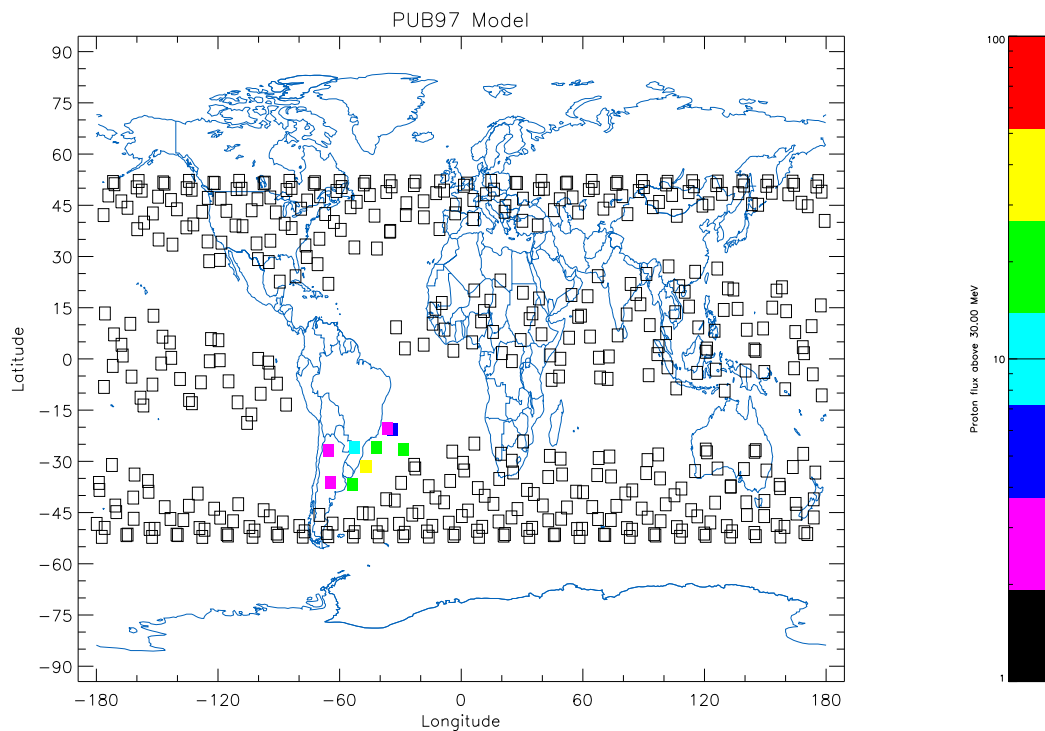


Figure 11.2. World map of the PUB97 directional proton flux above 30 MeV for the LEO orbit described in the text. The open squares represent orbital positions which are outside the validity range of the model.

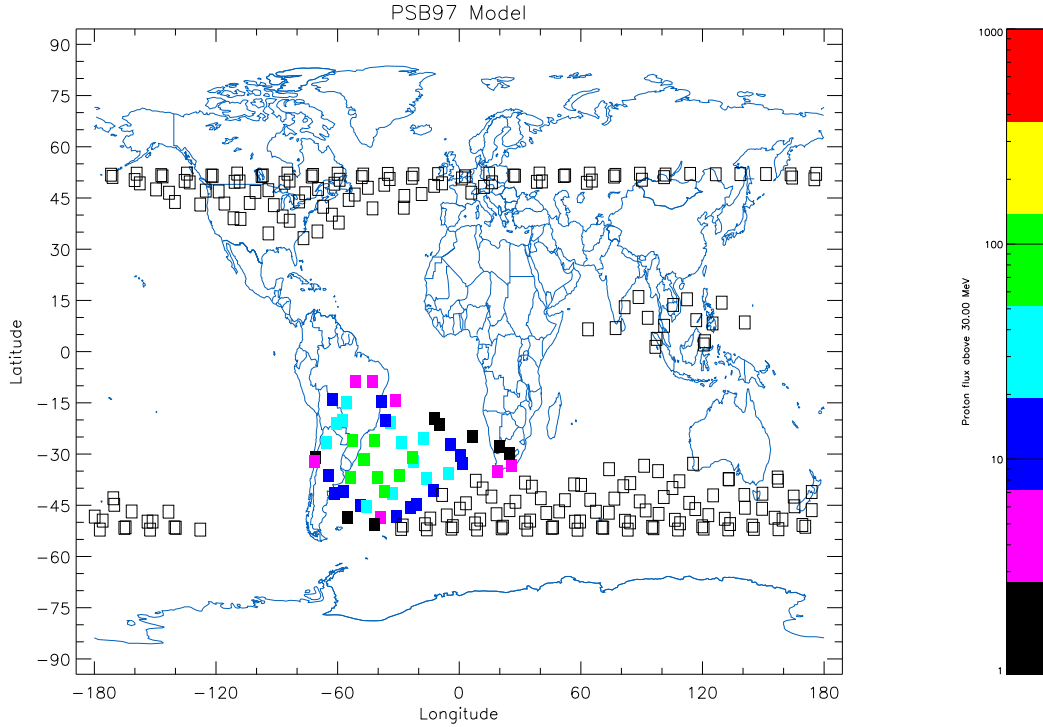


Figure 11.3. World map of the PSB97 directional proton flux above 30 MeV for the LEO orbit described in the text. The open squares represent orbital positions which are outside the validity range of the model.

fact that the respective models use different magnetic field models, with different epochs.

Secondly, the non-zero flux values at the orbital points where the models overlap differ significantly between the models. For the new models, this is due to the difference in solar conditions for which they were constructed. The differences between the new models and the AP-8 models have already been discussed in the sections of this document that cover the model descriptions.

Figures 11.6–11.10 show the integral proton flux above 30 MeV obtained with the different models as a function of orbital time. These plots further highlight the differences in model coverage, and provide a more quantitative comparison between the non-zero values. The differential and integral trapped proton spectra integrated over the full trajectory are shown in Figs. 11.11–11.15.

11.2 Comparisons of the models for a GTO mission

In order to illustrate the dangers of applying trapped particle models outside their validity range, we repeated the calculations presented in Sect. 11.1 for a GTO orbit with inclination 18° . Figures 11.16–11.20 represent the world maps obtained for this trajectory with the five different models.

As was the case for the LEO trajectory, the AP-8 model covers the whole GTO orbit, while

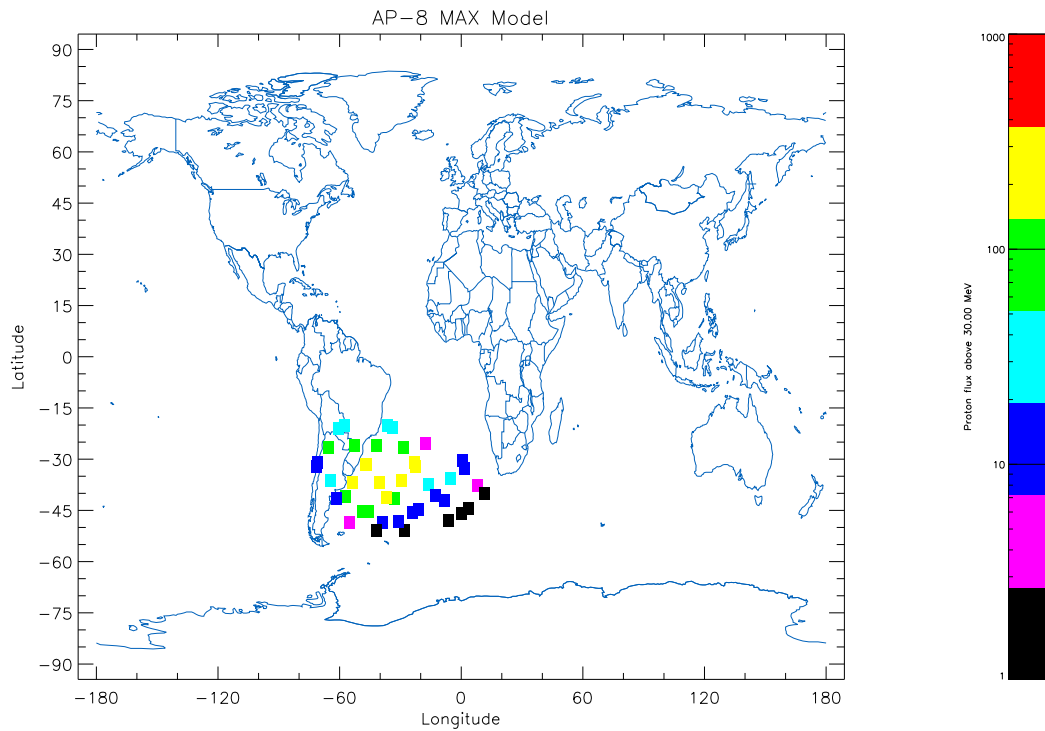


Figure 11.4. World map of the AP-8MAX directional proton flux above 30 MeV for the LEO orbit described in the text

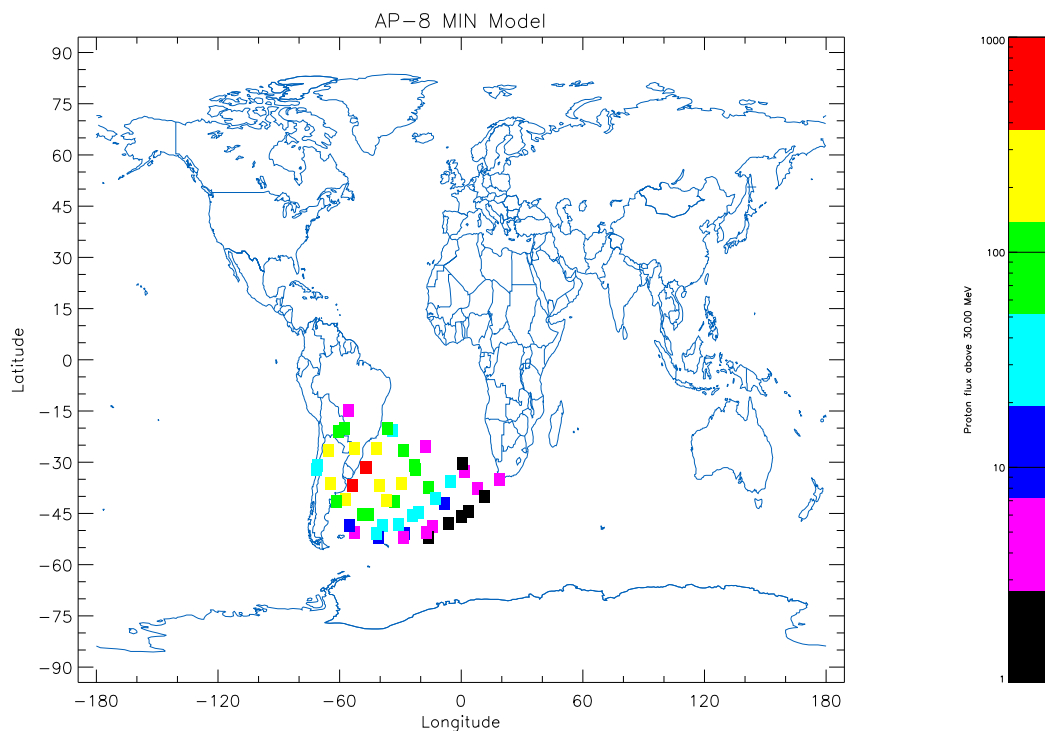


Figure 11.5. World map of the AP-8MIN directional proton flux above 30 MeV for the LEO orbit described in the text

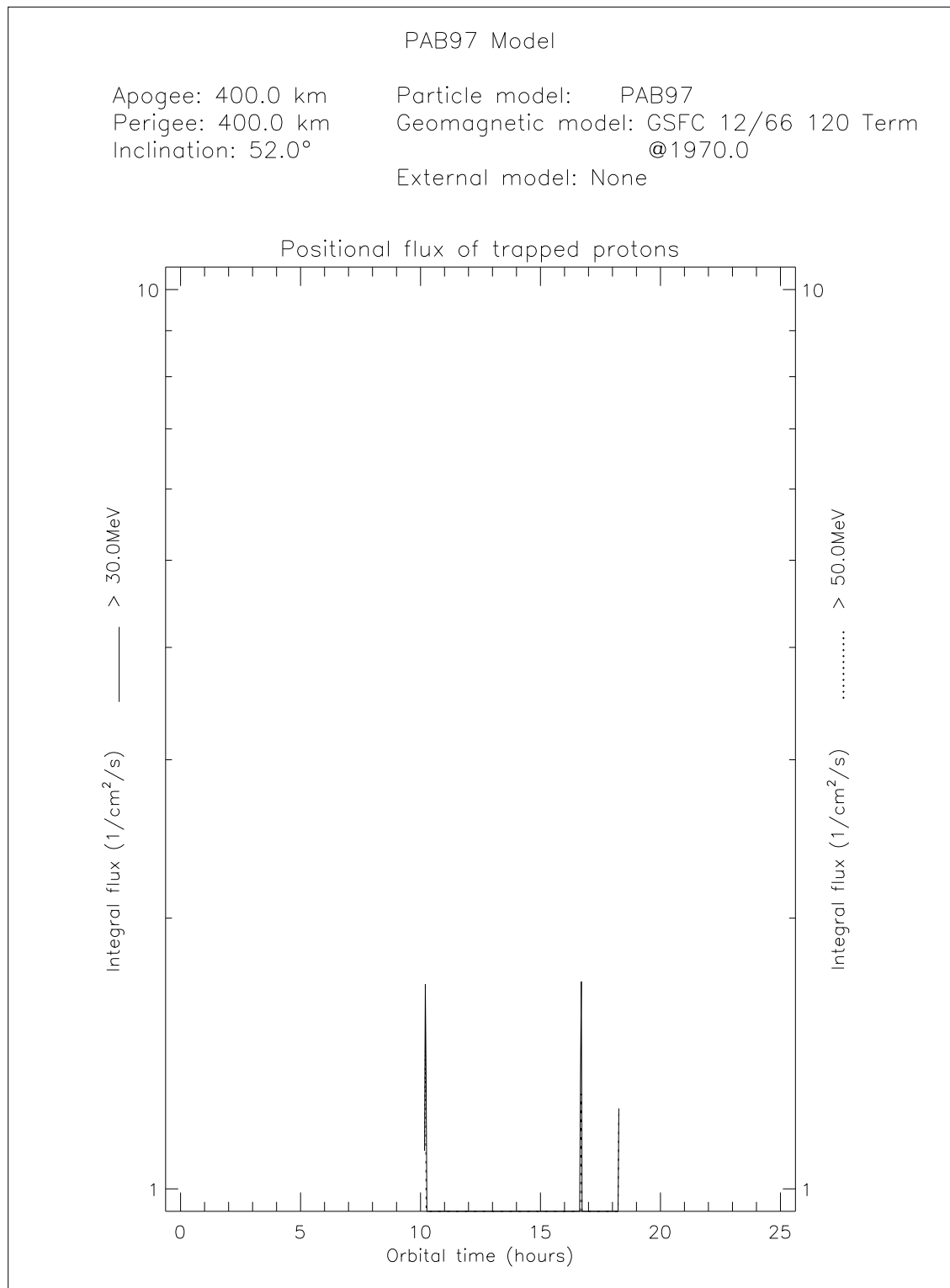


Figure 11.6. Integral PAB97 trapped proton fluxes above 30 MeV for the LEO orbit described in the text

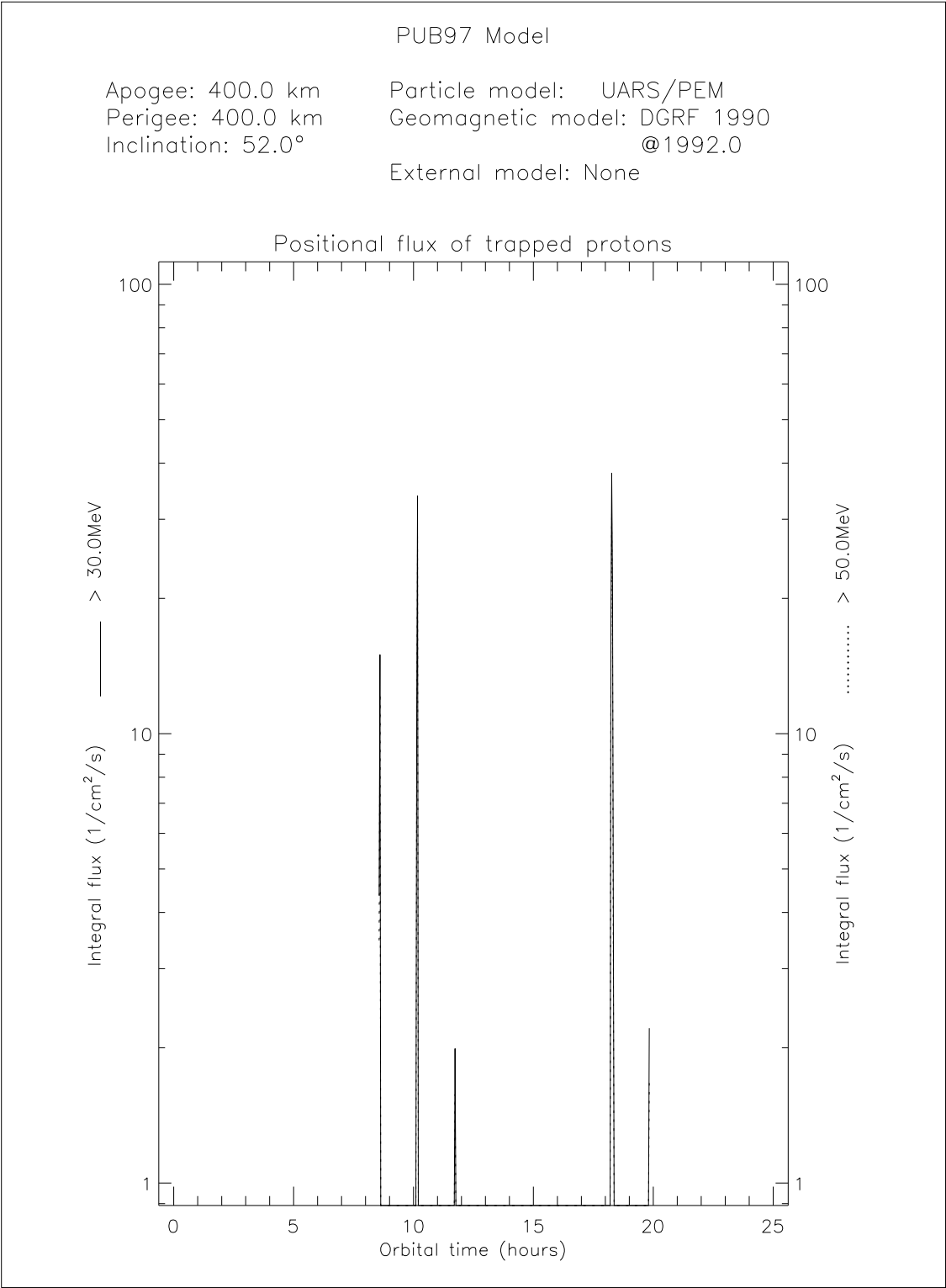


Figure 11.7. Integral PUB97 trapped proton fluxes above 30 MeV for the LEO orbit described in the text

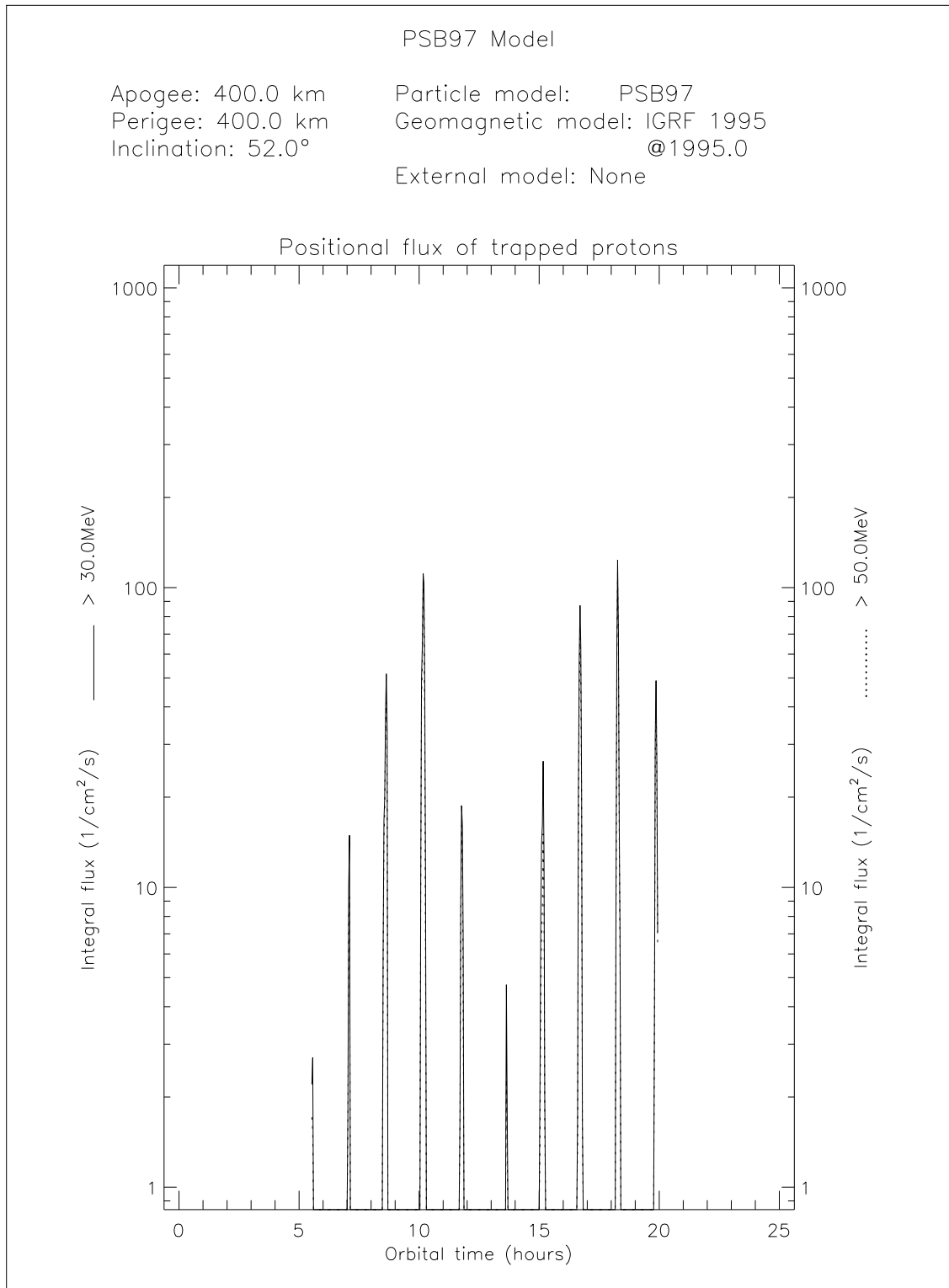


Figure 11.8. Integral PSB97 trapped proton fluxes above 30 MeV for the LEO orbit described in the text

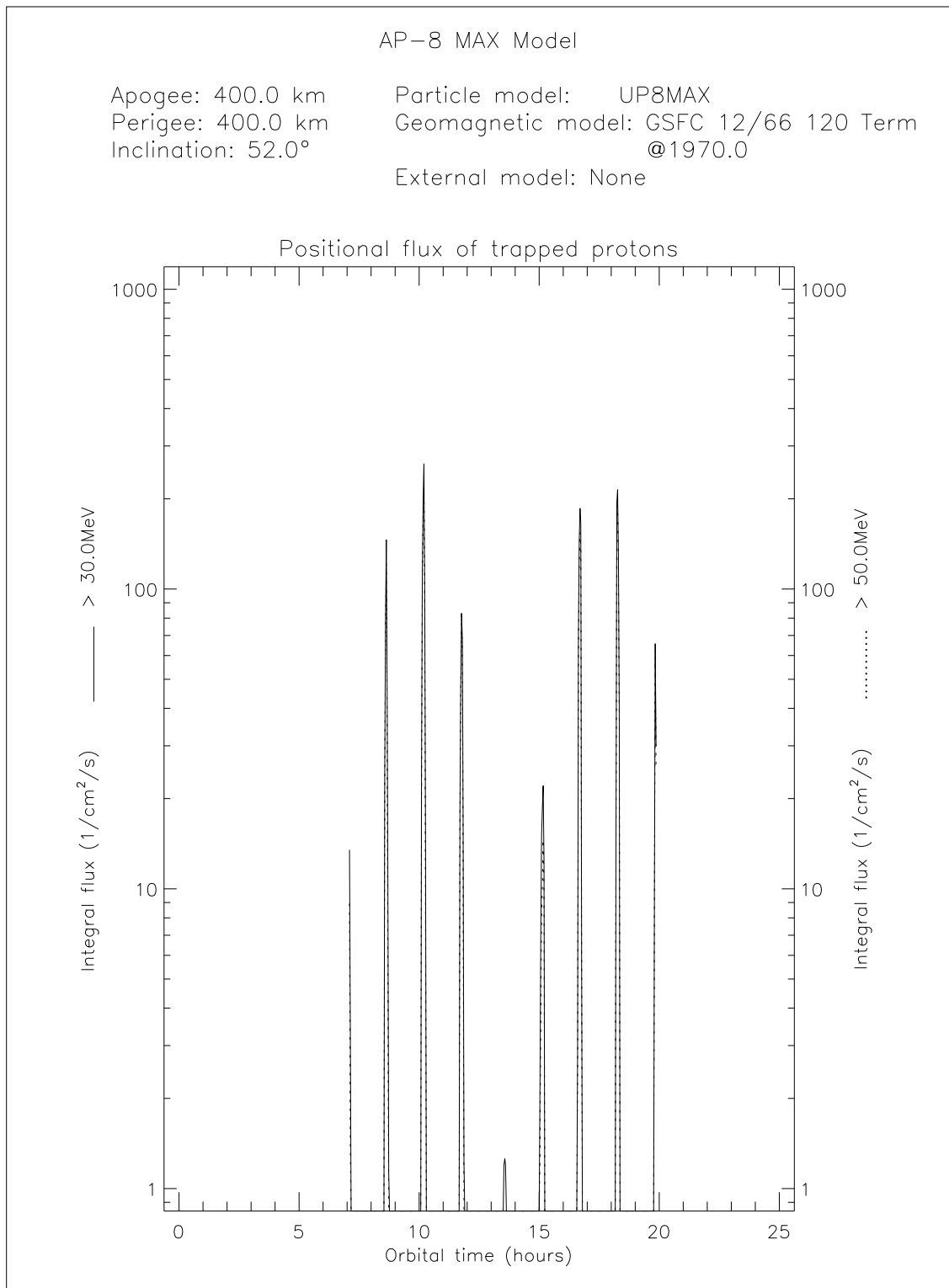


Figure 11.9. Integral AP-8 MAX trapped proton fluxes above 30 MeV for the LEO orbit described in the text

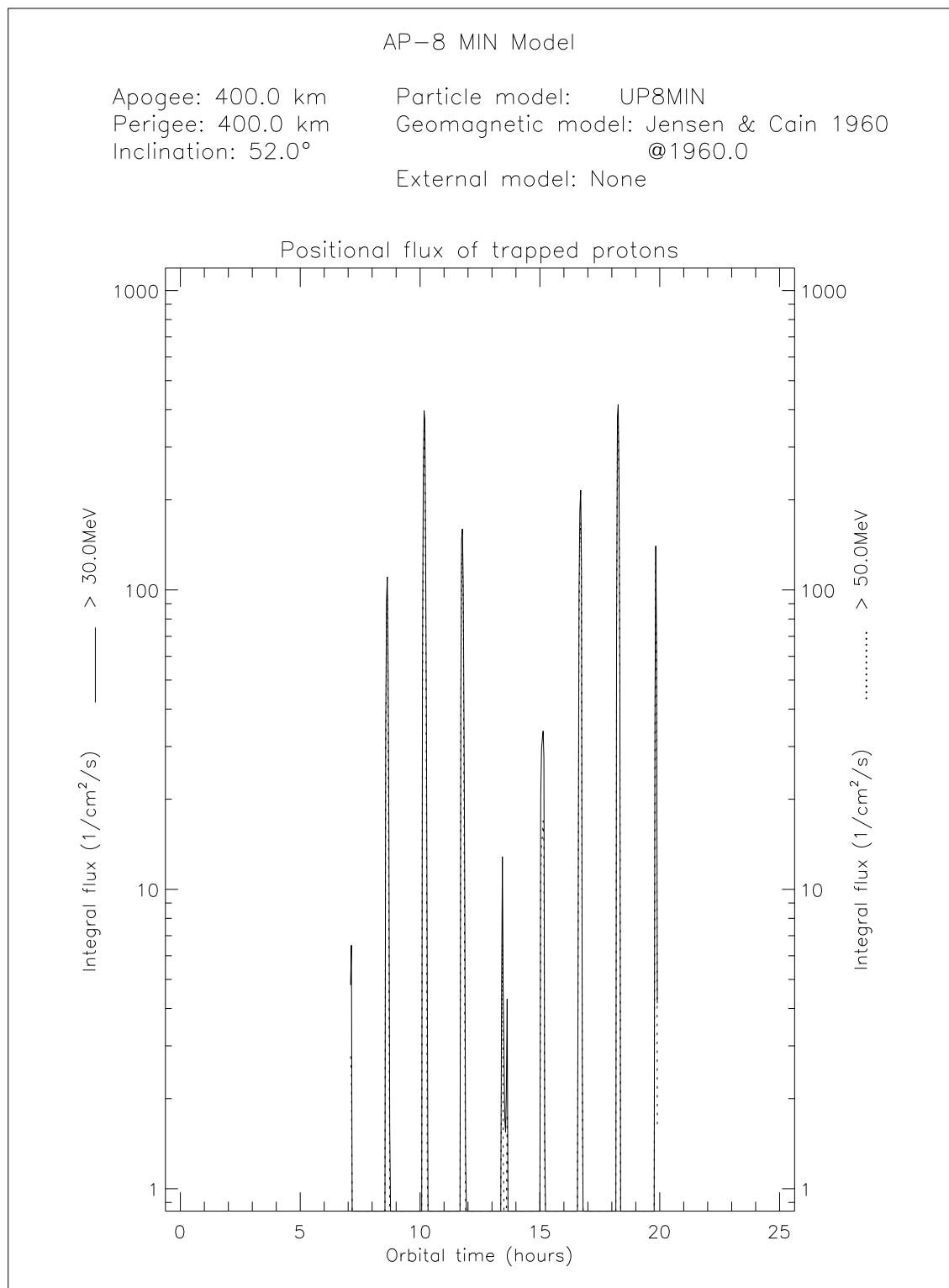


Figure 11.10. Integral AP-8 MIN trapped proton fluxes above 30 MeV for the LEO orbit described in the text

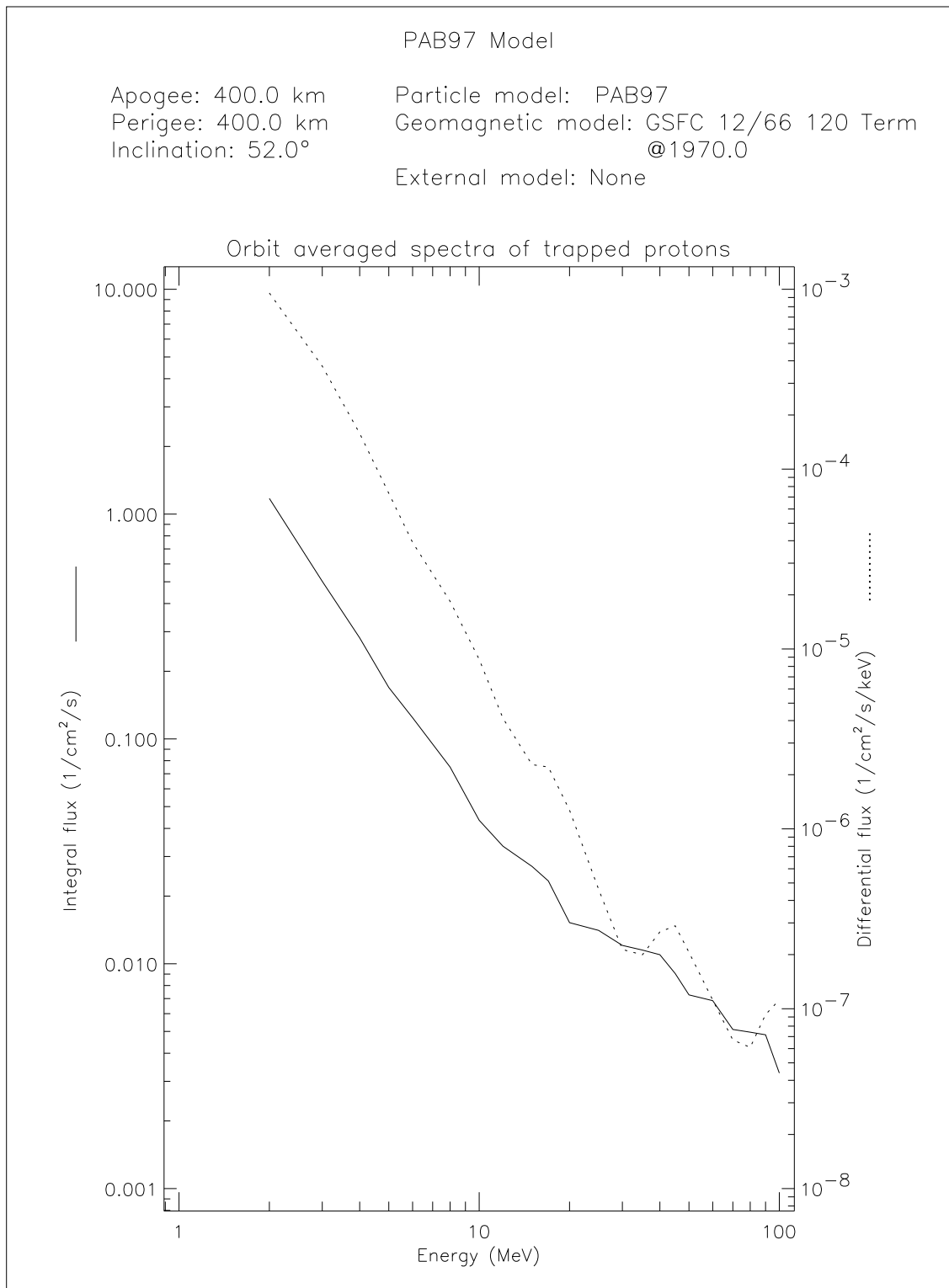


Figure 11.11. PAB97 Integral and differential trapped proton spectrum for the LEO orbit described in the text

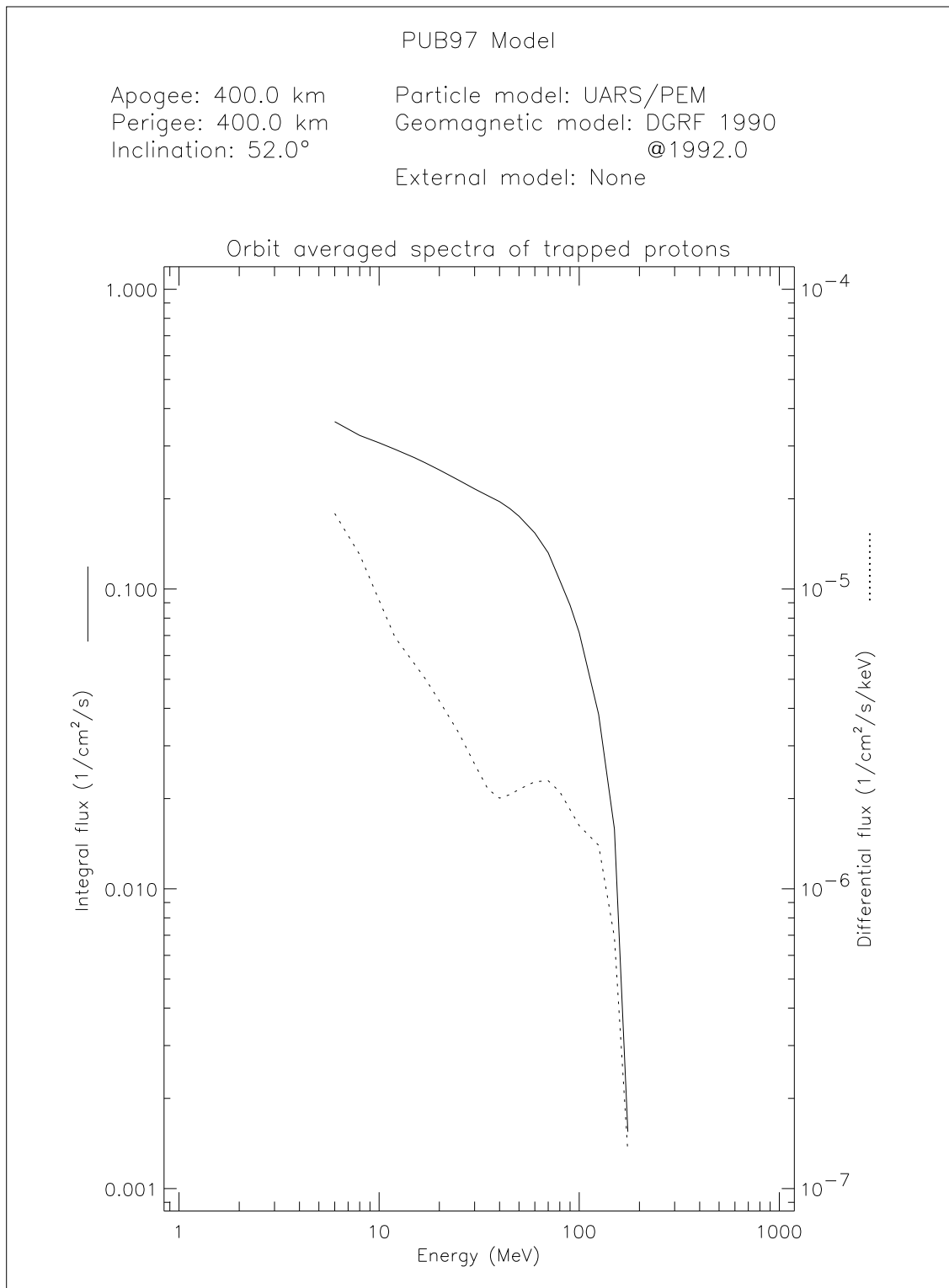


Figure 11.12. PUB97 Integral and differential trapped proton spectrum for the LEO orbit described in the text

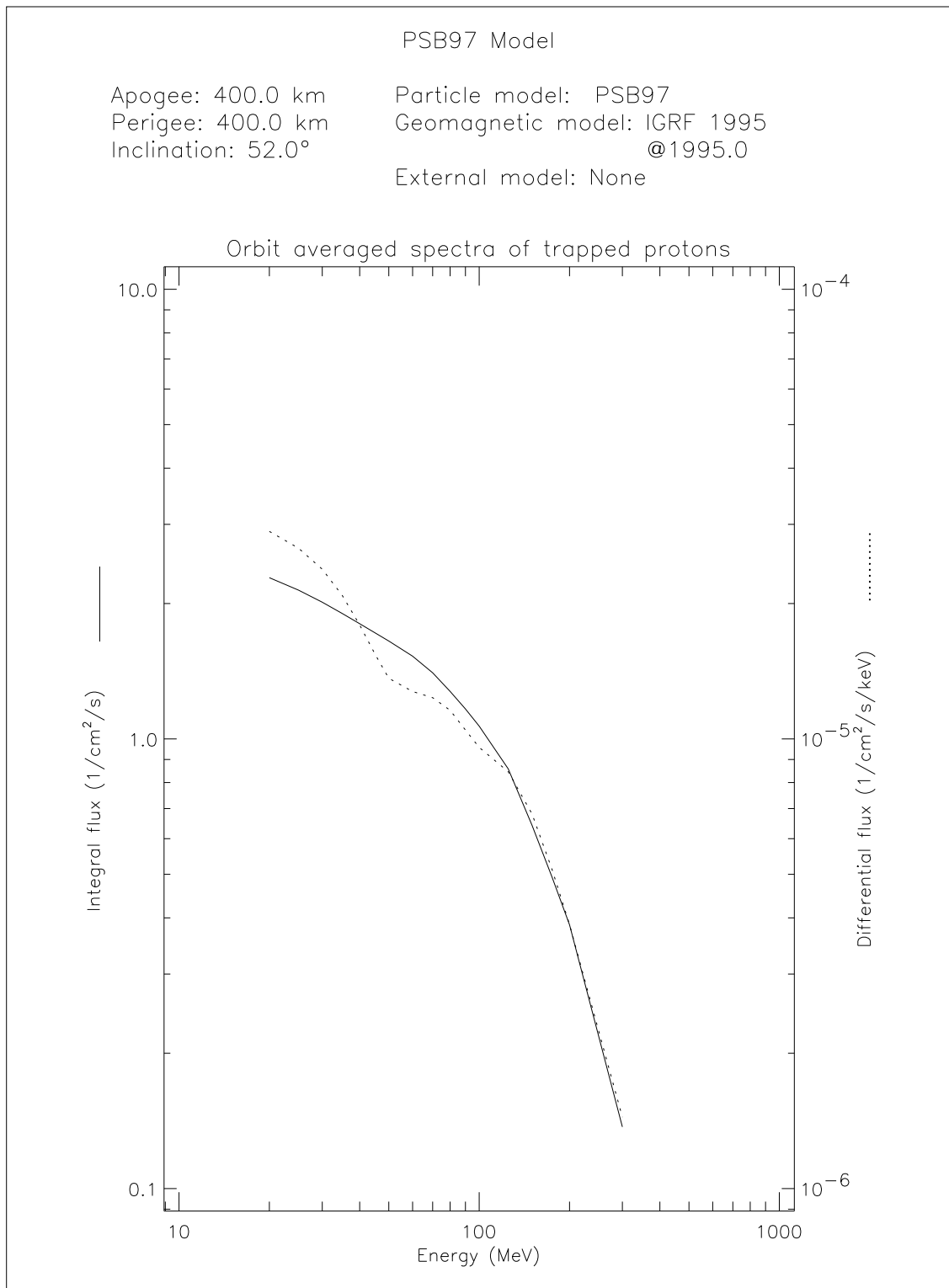


Figure 11.13. PSB97 Integral and differential trapped proton spectrum for the LEO orbit described in the text

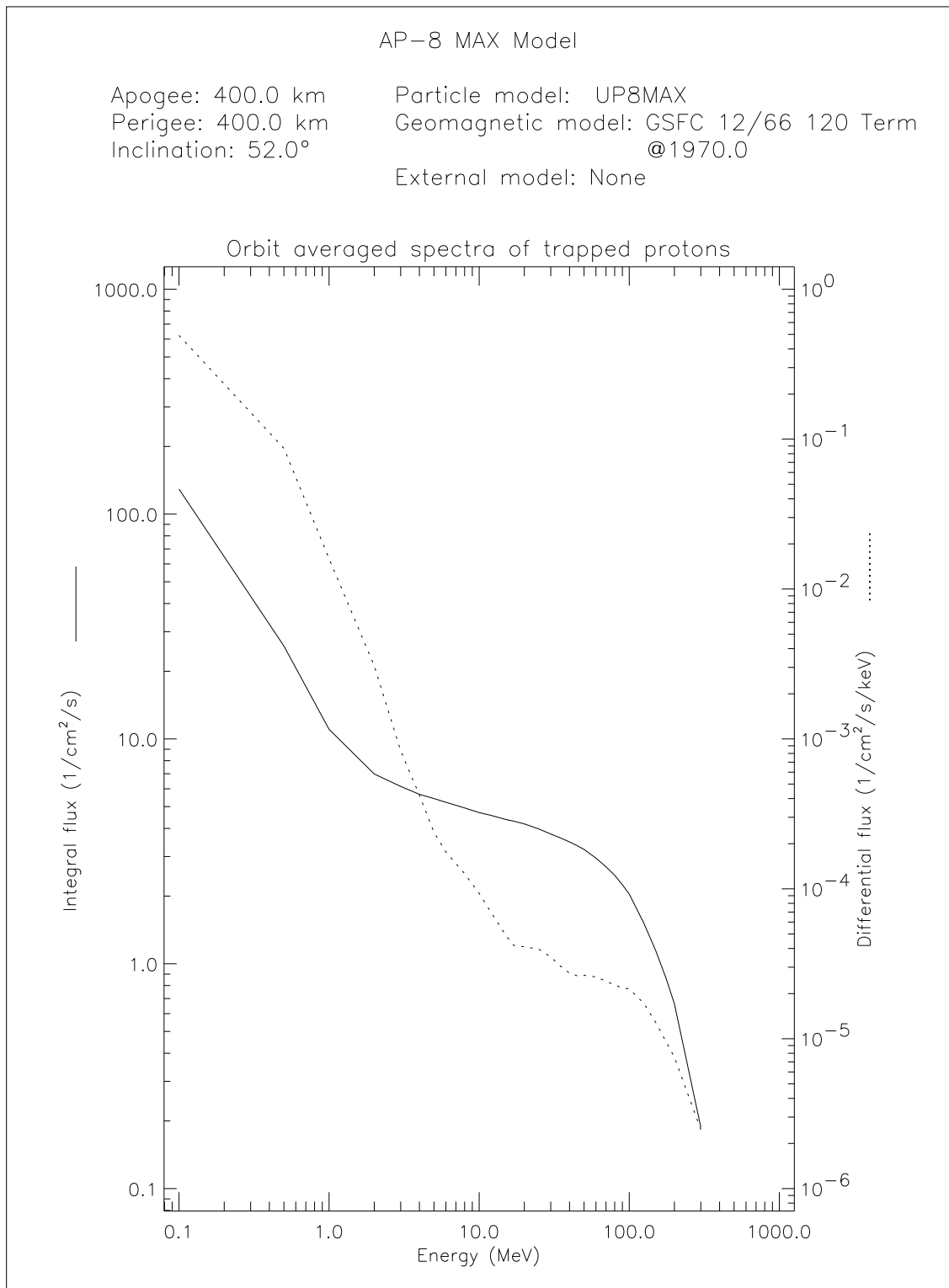


Figure 11.14. AP-8 MAX Integral and differential trapped proton spectrum for the LEO orbit described in the text

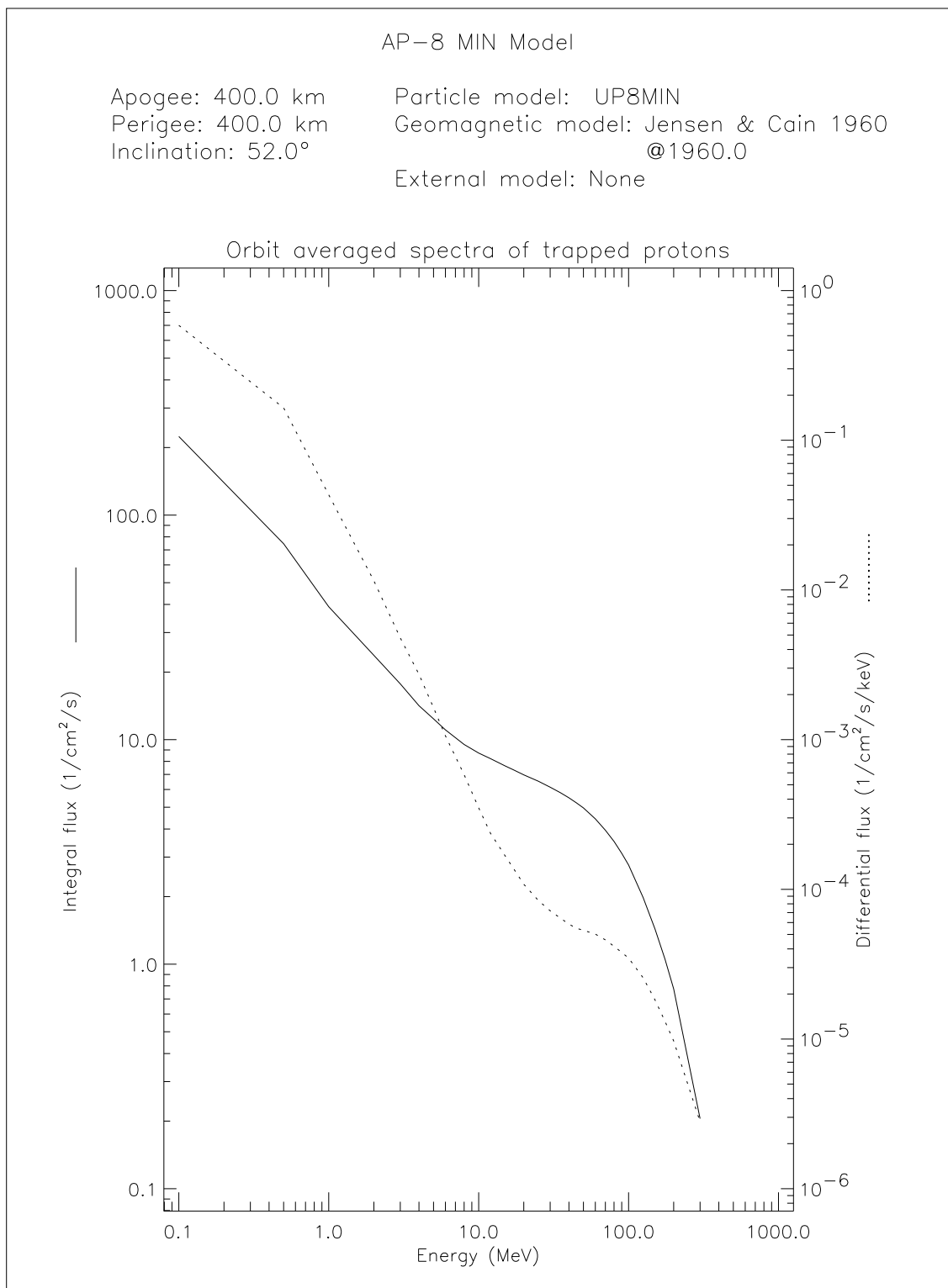


Figure 11.15. AP-8 MIN Integral and differential trapped proton spectrum for the LEO orbit described in the text

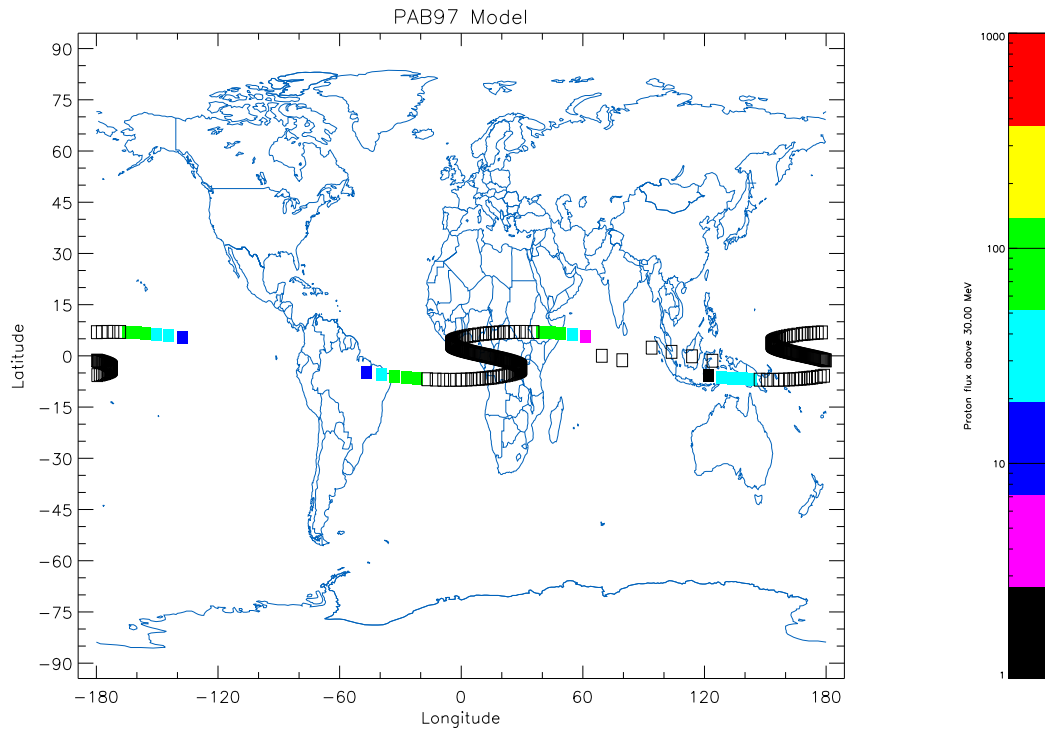


Figure 11.16. World map of the PAB97 directional proton flux > 30 MeV for the GTO orbit described in the text. The open squares represent orbital positions which are outside the validity range of the model.

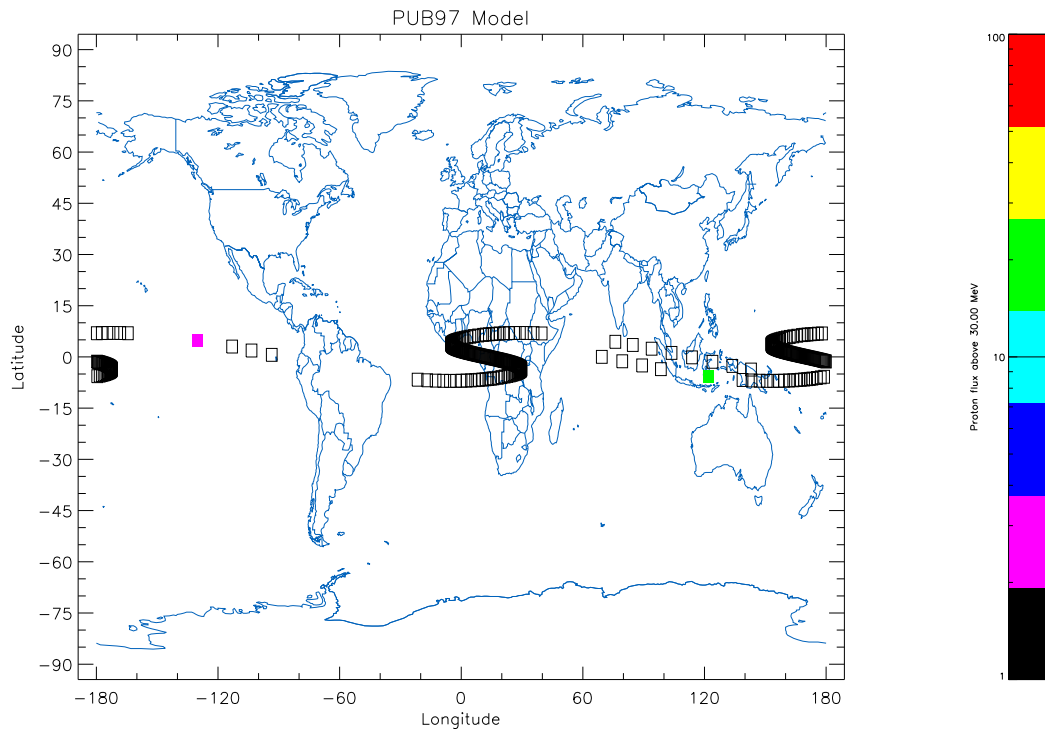


Figure 11.17. World map of the PUB97 directional proton flux > 30 MeV for the GTO orbit described in the text. The open squares represent orbital positions which are outside the validity range of the model.

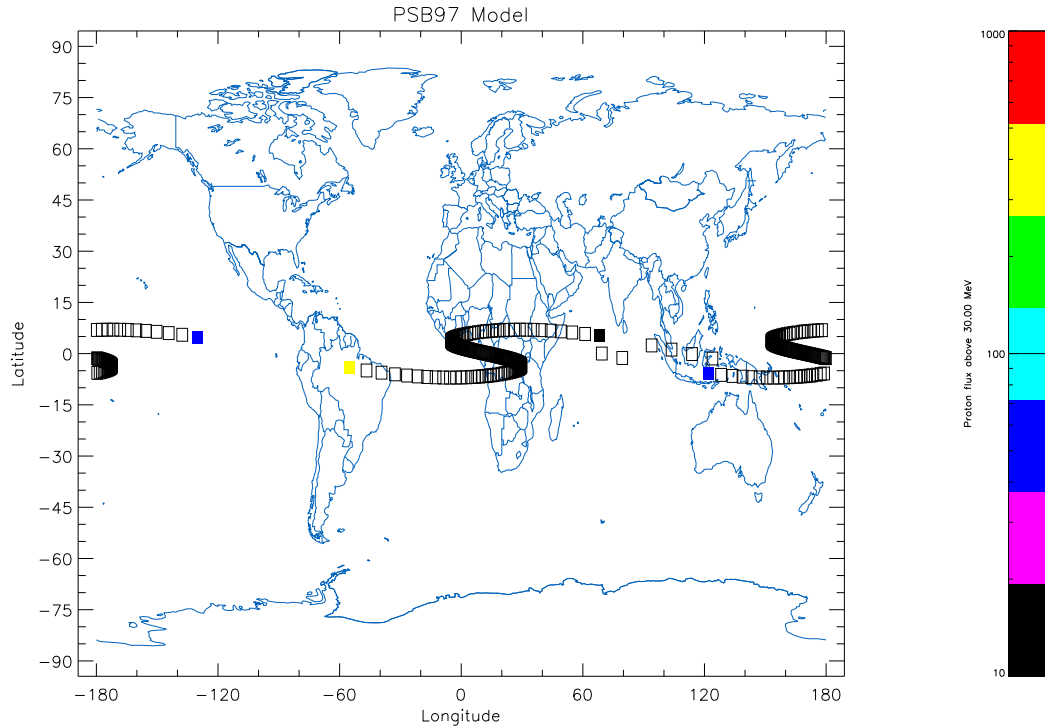


Figure 11.18. World map of the PSB97 directional proton flux > 30 MeV for the GTO orbit described in the text. The open squares represent orbital positions which are outside the validity range of the model.

the new proton models only cover the low altitude part. The new models are clearly not suited to evaluate the trapped proton flux over orbits with high apogees (for which, of course, they were not intended).

11.3 Conclusions

From the comparisons presented in this chapter, it is clear that the new trapped proton models PAB97, PSB97, and PUB97 should only be used for low altitude regimes. TREP Issues a warning when a trajectory contains geographical points that are outside the trapped particle model ranges, and outputs the number of such points. This helps the user to evaluate the validity of the model calculation. By producing a world map with the UNIRAD IDL programmes, the orbital points outside the model range can be identified.

We believe that the new models represent the low altitude trapped proton environment better than the AP-8 models for several reasons:

1. the models were constructed using only one high quality satellite data base per model, while the AP-8 models are based on data from different satellites;
2. the new models were built with directional data;

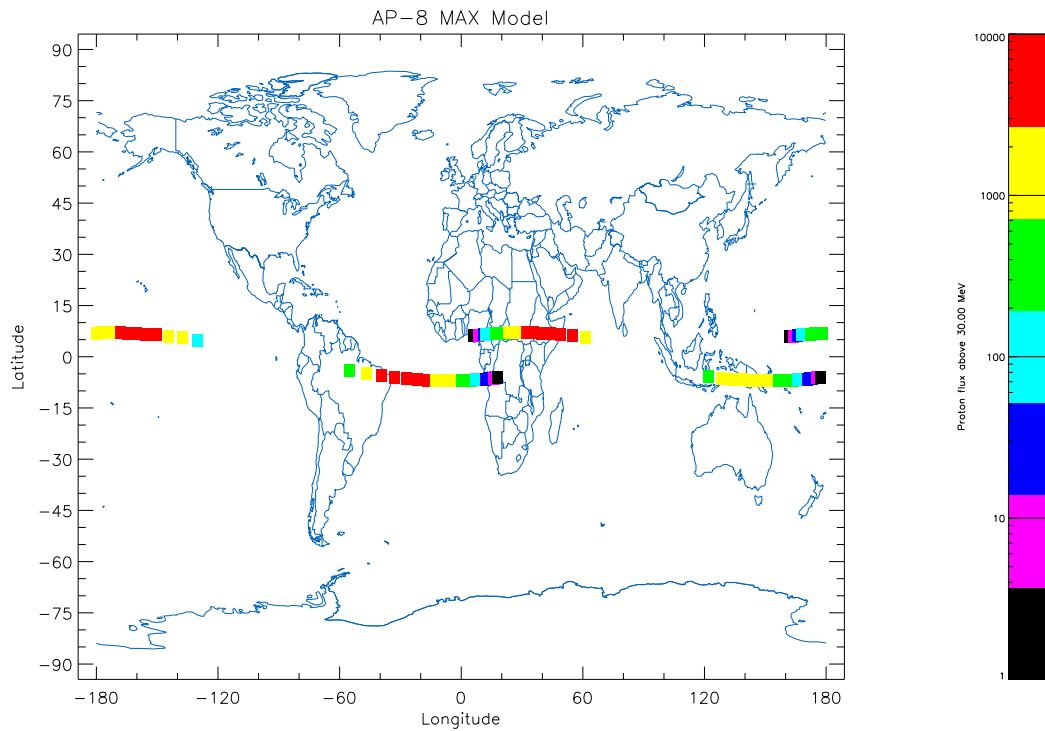


Figure 11.19. World map of the AP-8 MAX directional proton flux > 30 MeV for the GTO orbit described in the text

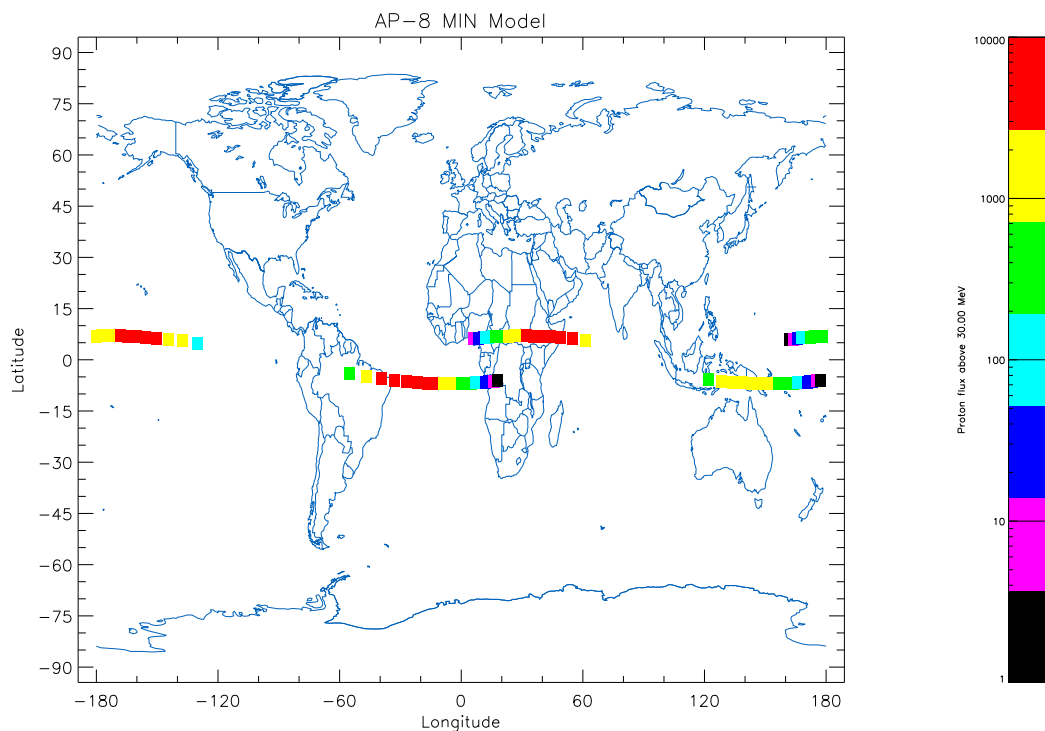


Figure 11.20. World map of the AP-8 MIN directional proton flux > 30 MeV for the GTO orbit described in the text

3. the three models represent conditions during three different solar cycle phases.

References

- Achtermann, E., Häusler, B., Hovestadt, D., Paschmann, G.: 1970, *Die Experimente EI 88 und EI 93 zur Messung von energiereichen Elektronen, Protonen und Alphateilchen im Satelliten AZUR. Physikalische Eigenschaften und Testmessungen*, BMBW-FB W 70-67
- Althouse, W.E., Cummings, A.C., Garrard, T.L., Mewaldt, R.A., Stone, E.C.: 1978, *A cosmic ray isotope spectrometer*, *Geoscience Electronics* **16**, 204–207
- Badhwar, G.D., Konradi, A.: 1990, *Conversion of Omnidirectional Proton Fluxes into a Pitch Angle Distribution*, *J. Spacecraft and Rockets* **27**, 350–352
- Baker, D.N., Mason, G.M., Figueroa, O., Colon, G., Watzin, J.G., Aleman, R.M.: 1993, *An Overview of the Solar, Anomalous, and Magnetospheric Particle Explorer (SAMPEX) Mission*, *IEEE Trans. Geosci. Remote Sensing* **31**, 531–541
- Burington, R.S., May, C.D., Jr.: 1970, *Handbook of probability and statistics with tables*, McGraw-Hill Book Company
- Cain, J.C., Hendricks, S.J., Langel, R.A., Hudson, W.V.: 1967, *A Proposed Model for the International Geomagnetic Reference Field-1965*, *J. Geomag. Geoelectr.* **19**, 335–355
- Carpenter, D.L., Anderson, R.R.: 1992, *An ISEE/Whistler Model of Equatorial Electron Density in the Magnetosphere*, *J. Geophys. Res.* **97**, 1097–1108
- Cook, W.R., Cummings, A.C., Cummings, J.R., Garrard, T.L., Kecman, B., Mewaldt, R.A., Selesnick, R.S., Stone, E.C., von Rosenvinge, T.T. : 1993a, *MAST: A Mass Spectrometer Telescope for Isotope Studies of Solar, Anomalous, and Galactic Cosmic Rays*, *IEEE Trans. Geosci. Remote Sensing* **31**, 557–564
- Cook, W.R., Cummings, A.C., Cummings, J.R., Garrard, T.L., Kecman, B., Mewaldt, R.A., Selesnick, R.S., Stone, E.C., Baker, D.N., von Rosenvinge, T.T., Blake, J.B., Callis, L.B.: 1993b, *PET: A Proton/Electron Telescope for Studies of Magnetospheric, Solar and Galactic Particles*, *IEEE Trans. Geosci. Remote Sensing* **31**, 565–571
- Daly, E.J., Evans, H.D.R.: 1993, *Problems in Radiation Environment Models at Low Altitudes*, Memorandum ESA/ESTEC/WMA/93-067/ED
- Gonzalez, C.A.: 1996, *IDFS Programmers Manual Version 15.0*, Southwest Research Institute, San Antonio, Texas
- Häusler, B.: 1972, *Untersuchungen des Verhaltens hochenergetischer Protonen und Elektronen in der inneren Magnetosphäre*, MPI-PAE/Extraterr. **66**

- Heynderickx, D., Lemaire, J.: 1993, *Improvements to Trapped Radiation Software*, Technical Note 1 of the TREND-2 Project, ESA/ESTEC/WMA TRP Contract No. 9828/92/NL/FM
- Heynderickx, D., Lemaire, J., Pierrard, V.: 1995, *Atmospheric Cut-Off*, Technical Note 2 of the TREND-3 Project, ESA/ESTEC/WMA TRP Contract No. 9828/92/NL/FM
- Heynderickx, D., Lemaire, J., Daly, E.J.: 1996a, *Historical Review of the Different Procedures Used to Compute the L-Parameter*, Radiat. Meas. **26**, 325–331
- Heynderickx, D., Lemaire, J., Daly, E.J., Evans, H.D.R.: 1996b, *Calculating Low-Altitude Trapped Particle Fluxes With the NASA Models AP-8 and AE-8*, Radiat. Meas. **26**, 947–952
- Heynderickx, D., Kruglanski, M., Lemaire, J.F., Daly, E.J.: 1996c, *A New Tool for Calculating Drift Shell Averaged Atmospheric Density*, Proc. Workshop on Radiation Belts: Models & Standards, Brussels, October 17–20, 1995 (eds. J.F. Lemaire, D. Heynderickx, D.N. Baker), Geophysical Monograph 97, 173–178
- Klecker, B., Hovestadt, D., Scholer, M., Arbing, H., Ertl, M., Kästle, H., Künne, E., Laeverenz, P., Seidenschwang, E., Blake, J.B., Katz, N., Mabry, D.: 1993, *HILT: A Heavy Ion Large Area Proportional Counter Telescope for Solar and Anomalous Cosmic Rays*, IEEE Trans. Geosci. Remote Sensing **31**, 542–548
- Knoll, G.F., Radiation detection and measurement, John Wiley and sons, 1989
- Kruglanski, M.: 1996, *Use of (B, L) Coordinates in Radiation Dose Models*, Proc. of Workshop on Radiation Belts: Models & Standards, Brussels, October 17–20, 1995, Geophysical Monograph **97**, 195–199
- Lemaire, J., Roth, M., Wisenberg, J., Domange, P., Fonteyn, D., Lesceux, J.M., Loh, G., Ferrante, G., Garres, C., Bordes, J., McKenna-Lawlor, S., Vette, J.I.: 1990, Final Report of the TREND Project, ESA/ESTEC/WMA TRP Contract No. 9011/88/NL/MAC
- Lemaire, J., Johnstone, A.D., Heynderickx, D., Rodgers, D.J., Szita, S., Pierrard, V.: 1995, Final Report of the TREND-2 Project, ESA/ESTEC/WMA TRP Contract No. 9828/92/NL/FM
- Mason, G.M., Hamilton, D.C., Walpole, P.H., Heuerman, K.F., James, T.L., Lennard, M.H., Mazur, J.E.: 1993, *LEICA: A Low Energy Ion Composition Analyzer for the Study of Solar and Magnetospheric Heavy Ions*, IEEE Trans. Geosci. Remote Sensing **31**, 549–556
- McIlwain, C.E.: 1961, *Coordinates for Mapping the Distribution of Magnetically Trapped Particles*, J. Geophys. Res. **66**, 3681–3691
- Reber, C.A.: 1993, *The Upper Atmosphere Research Satellite (UARS)*, Geophys. Res. Lett. **20**, 1215–1218
- Reber, C.A., C.E. Trevathan, R.J. McNeal and M.R. Luther: 1993, *The Upper Atmosphere Research Satellite (UARS) Mission*, J. Geophys. Res. **98**, 10643–10647
- Sawyer, D.M., Vette, J.I.: 1976, *AP-8 Trapped Proton Environment for Solar Maximum and Solar Minimum*, NSSDC/WDC-A-R&S 76-06

- Sharber, J.R., R.A. Frahm, J.D. Winningham, J.C. Biard, D. Lummerzheim et al.: 1993, *Observations of the UARS Particle Environment Monitor and Computation of Ionization Rates in the Middle and Upper Atmosphere During a Geomagnetic Storm*, Geophys. Res. Let. **20**, 1319–1322
- Sharber, J.R., R. Link, R.A. Frahm, J.D. Winningham, D. Lummerzheim et al.: 1996, *Validation of UARS particle environment monitor electron energy deposition*, J. Geophys. Res. **101**, 9571–9582
- Stone, E.C., Vogt, R.E., McDonald, F.B., Teegarden, B.J., Trainor, J.H., Jokipii, J.R., Webber, W.R.: 1977, *Cosmic ray investigation for the Voyager missions; Energetic particle studies in the outer heliosphere—and beyond*, Space Sci. Rev. **21**, 355–376
- Sullivan, J.D.: 1971, *Geometrical factor and directional response of single and multi-element particle telescopes*, Nucl. Instr. Meth. **95**, 5–11
- Vette, J.I.: 1991a, *The AE-8 Trapped Electron Model Environment*, NSSDC/WDC-A-R&S 91-24
- Vette, J.I.: 1991b, *The NASA/National Space Science Data Center Trapped Radiation Environment Model Program (1964–1991)*, NSSDC/WDC-A-R&S 91-29
- Winningham, J.D., J.R. Sharber, R.A. Frahm, J.L. Burch, N. Eaker et al.: 1993, *The UARS Particle Environment Monitor*, J. Geophys. Res. **98**, 10649–10666

Appendix A

Telemetry file for the HEPS/PEM/UARS data

This appendix describes a common format to store and retrieve the processed telemetry data. The format includes all information needed to study the trapped proton flux in the radiation belts. The current format has been designed to allow the data analysis of the PEM instrument onboard the UARS satellite. Other data sets can easily be accommodated.

The data is organised in two levels. The first level refers to general information on the mission and instrument, as well as information on the availability of the data. The second level includes the ephemeris and flux data. Generally, the second level corresponds to a large set of files while the first level corresponds to a single file. All the files consist of two parts: header and body. The header part is formatted while the body part is unformatted binary with fixed-length records.

The format is defined for easy use by IDL programs under the Digital OpenVMS operating system.

A.1 Header format

The header is placed at the beginning of the file and consists of a set of string records. The size and number of the records are not fixed. The header is separated from the file body by a record that contains one character only: a minus sign (–). Each record of the header includes a name field and a content field, separated by a colon (:) and a space. The name field consists of alphabetical characters, numerical digits or the underscore sign (_). This field is not case sensitive and identifies a metavariable. The content field consists of any printable ASCII characters and corresponds to an ASCII description of the metavariable content.

The number of metavariables defined in the header is not limited or fixed. The metavariables may appear in the header part in any order. The list of the mandatory metavariables is shown in Table A.1.

The metavariable ‘Content’ specifies the file type. The value ‘INDEX’ refers to a first-level

Table A.1. List of metavariables

Metavariable	Description
Content	Type of the file (INDEX, EPHEMERIS or MEASUREMENT)
Body_Size	Number of records in body part of the file ($1-2^3 1 - 1$)
Number_Field	Number of fields in each body record (1–99)
Fld_01	Description of the first field including its dimensions, type, name, unit, ...
Fld_##	Idem for the other fields of the body records

Note: the hash sign (#) represents a numerical digit

Table A.2. List of type codes for the record field

Code	IDL type	Number of byte
1	Byte	1
2	Integer	2
3	Longword integer	4
4	Floating point	4
5	Double-precision floating	8
6	Complex floating	8
7	String	80
9	Double-precision complex	16

file. The values ‘EPHEMERIS’ and ‘MEASUREMENT’ refer to a second-level file. The other mandatory metavariables describe the body part of the file. The content field of the metavariables ‘Body_Size’ and ‘Number_Field’ has to consist of integer values. For the metavariables of the form ‘Fld_##’ where the hash sign (#) represents a numerical digit, the content field is divided in sub-fields separated by a comma (,) and is used to describe each field of the body records. The first sub-field is equal to the number of dimensions of the record field (zero for scalar). The next sub-fields contain the size of each dimension, one sub-field per dimension (none if scalar). The number of dimensions is limited to 5. After the dimension sizes, the last seven sub-fields contain the type code, the number of elements, the name, the unit, the minimum value, the maximum value, and the error code of the record field, respectively. The possible values of the type-code sub-field are listed in Table A.2. The error code is the value assigned to the record field when this field is not available.

A.2 Body format

The body starts just after the minus sign (–) which ends the file header. It consists of a set of binary records of fixed lengths. The number of records is defined by the metavariable

Table A.3. List of additional first-level metavariables

Metavariable	Description
Mission	Name of the spacecraft (AZUR, UARS, SAMPEX,...)
Instrument	Name of the instrument and/or sensor
Orbit	Main orbit parameters separated by a comma (,): apogee, perigee in km and inclination in degrees, respectively
First_Date	First date for which data are available: year, month, day separated by a comma (,)
Last_Date	Last date for which data are available: year, month, day separated by a comma (,)
View_Angle	Half opening angle of the detector in degrees
G_Factor	Geometric factor in cm ² sr
Acc_Time	Time of accumulation in seconds
Data_Type	Set of keywords separated by spaces to describe the type of data (PROT, DOSE, FLUX, DIFF, INTG, DIRE, OMNI, CNTS,...)
N_Sensor	Number of sensors. The sensors may only differ by their orientations (look direction)
N_Channel	Number of energy channel for each sensor
Energy	List of the center energies of the channels in MeV separated by a comma (,)
E_Width	List of the energy width of the channels in MeV separated by a comma (,)

‘Body_Size’. The record length is determined by the types of the included fields. The number of field per record is defined by the metavariable ‘Number_Field’. The metavariables of the form ‘Fld_##’ include the description of the different fields.

A.3 First level file

Generally, a single first-level file should be defined for each mission and instrument. Since the PEM instrument includes different telescopes, a first level file has been defined per telescope. The first level file includes additional mandatory metavariables and the structure of its body part is predefined. The additional mandatory metavariables of the first-level file are described in Table A.3. Other metavariables may be present such as ‘Date_of_creation’, ‘P_Investigator’,

The metavariables that define the body structure are shown in the first part of Table A.4. Each body record corresponds to a time range in modified Julian Day (January 1, 1950 is day zero). The time range is specified by the two longword-integer variables ‘firstdate’ and ‘lastdate’. At each time range corresponds a set of n second-levels files the names of which are stored in the string array ‘file’. The byte array ‘status’ indicates the status of each files. The possible values of the file status are listed in the second part of Table A.4.

Table A.4. Definition of the first-level body structure

Metavariable	Content								
Number_Field:	4								
Fld_01:	0,	3,	1,	firstdate,	MJD,	0,	100000,	– 1	
Fld_02:	0,	3,	1,	lastdate,	MJD,	0,	100000,	– 1	
Fld_03:	1,	<i>n</i> ,	1,	<i>n</i> ,	status,	,	32,	127,	255
Fld_04:	1,	<i>n</i> ,	7,	<i>n</i> ,	file,	,	0,	0,	0

Decimal code	ASCII code	Description
67	C	The file is corrupted
73	I	The file is uncomplete
77	M	The file is complete but not directly accessible
82	R	The file is complete and accessible
88	X	The file has been deleted or does not exist

A.4 Second level

At least two second-level types of files should be defined for each mission and instrument. One of the second-level file types (generally the first one) correspond to ephemeris data. The structure of this file is predefined. The other second-level files are dedicated to the proton measurement data. For the PEM/UARS data only two second-level files are defined with extensions ‘.eph’ and ‘.flx’, respectively.

A.4.1 Ephemeris data

The second-level file dedicated to the ephemeris data includes additional mandatory metavariables and the structure of its body part is predefined. The mandatory metavariables and the body structure are described in parts one and two of Table A.5, respectively. For the PEM/UARS data the metavariable ‘Description_field’ has been added. This metavariable contains a short description of each variable. The descriptions are separated by a semi-colon (;).

Each body record of the ephemeris files contains 18 variables which specify the time of measurement, the spacecraft location, the local magnetic field vector, geomagnetic coordinates, etc. The meaning of the body-record variables listed in Table A.5 is the following:

‘time ’ the time of the ephemeris in modified Julian Day;

‘elong ’ the East geographic longitude;

‘gdalt ’ the geodetic altitude;

‘gdlat ’ the geodetic latitude;

Table A.5. Description of the metavariables and body structure for the ephemeris files

Metavariable	Description
First_Record	Date and time of the first record (year, month, day, hour, minute and second) in a free format, e.g. YYYY/MM/DD HH:MM:SS
Last_Record	Date and time of the last record in a free format
Mag_Internal	Description of the geomagnetic field used
Mag_External	Description of the external magnetic field used
Ref_Energy	Energy in MeV used to determine a reference proton gyroradius
Delta_Time	Elapsed time in seconds between ephemeris time and the centre of the accumulation period; for example, -Acc_Time/2 when the ephemeris time corresponds to the begin of the accumulation period
Flag_Value	Set of short descriptions separated by a comma (,) that describes the possible value of the variable ‘flag’

Metavariable	Content
Number_Field:	18
Fld_01:	0, 5, 1, time, MJD, 0.0, 10 ⁵ , -1.0
Fld_02:	0, 4, 1, elong, deg, 0.0, 360.0, -999.0
Fld_03:	0, 4, 1, gdalt, km, ?(*), ?(*), -999.0
Fld_04:	0, 4, 1, gdlat, deg, -90.0, 90.0, -999.0
Fld_05:	0, 4, 1, colat, deg, 0.0, 180.0, -999.0
Fld_06:	0, 4, 1, radius, km, 6370.0, ?(*), -1.0
Fld_07:	2, 3, N_s , 4, $3N_s$, velo, 1, -1.0, 1.0, -999.0
Fld_08:	1, 3, 4, 3, bmes, Gauss, -1.0, 1.0, -999.0
Fld_09:	1, 3, 4, 3, bcal, Gauss, -1.0, 1.0, -999.0
Fld_10:	1, 3, 4, 3, ncal, 1, -1.0, 1.0, -999.0
Fld_11:	1, N_s , 4, N_s , alpha, deg, 0.0, 180.0, -999.0
Fld_12:	1, N_s , 4, N_s , beta, deg, 0.0, 360.0, -999.0
Fld_13:	0, 4, 1, bsat, Gauss, 0.0, 1.0, -999.0
Fld_14:	1, N_s , 4, N_s , lm, Re, 0.0, ?(*), -50.0
Fld_15:	1, N_s , 4, N_s , altmin, km, 0.0, ?(*), -999.0
Fld_16:	1, N_s , 4, N_s , bgdc, Gauss, 0.0, 1.0, -999.0
Fld_17:	1, N_s , 4, N_s , lmgdc, Re, 0.0, ?(*), -50.0
Fld_18:	0, 3, 1, flag, , 0, 0, -1

(*) the value of these sub-fields depends on the mission orbit

‘colat’ the geocentric co-latitude;

‘radius’ the geocentric radius;

‘velo’ the spherical geocentric components (according to 1_ρ , 1_θ , 1_ϕ) of normalized vectors pointing, for each sensor, to the mean direction of the detected particle velocity, i.e. vectors pointing to the opposite viewing direction of the different sensors;

‘bmes’ the spherical geocentric components of the measured magnetic field vector;

‘bcal’ the spherical geocentric components of the local magnetic field vector evaluated with the help of the models described in the metavariables ‘Mag_Internal’ and ‘Mag_External’;

‘ncal’ the spherical geocentric components (according to 1_ρ , 1_θ , 1_ϕ) of the normal to the computed magnetic field line;

‘alpha’ the mean pitch angle of the detected particle velocity for the different sensors, generally obtained from ‘bcal’ and ‘velo’;

‘beta’ the mean azimuthal angle of the detected particle velocity;

‘bsat’ the computed magnetic field intensity at the spacecraft location;

‘lm’ McIlwain’s parameter L evaluated for each pitch angle ‘alpha’ on the magnetic field line passing through the spacecraft location;

‘altmin’ the geocentric altitude of the lowest mirror points on the magnetic field line passing through the spacecraft location for the different pitch angles ‘alpha’;

‘bgdc’ for each pointing direction ‘velo’, the magnetic field intensity at the local guiding center of protons of the energy specified in the metavariable ‘Ref_Energy’;

‘lmgdc’ McIlwain’s parameter L evaluated at the guiding center for each pitch angle ‘alpha’;

‘flag’ a bit-oriented quality indicator the meaning of which is described in the metavariable ‘Flag_Value’.

Note that the variables ‘velo’, ‘alpha’, ‘beta’, ‘lm’, ‘altmin’, ‘bgdc’ and ‘lmgdc’ are arrays one dimension of which is set to the number N_s of sensors specified by the metavariable ‘N_Sensor’ of the first level.

For the PEM/UARS data, eleven significant bits are use for the quality indicator ‘flag’. The first seven bits are related to the telescope measurement. The 8th and 9th bits validate the spacecraft coordinates and the magnetometer measurement, respectively. The last two bits are related to the geomagnetic coordinates.

Table A.6. Description of the body structure for the measurement files

Metavariable	Content
Number_Field:	2
Fld_01:	1, 16, 4, 16, rawflx, cnts/(cm ² sr s eV), 0.0, 10 ⁻³ , -1.0
Fld_02:	1, 16, 4, 16, modflx, cnts/(cm ² sr s eV), 0.0, 10 ⁻³ , -1.0

Table A.7. Metavariables for the binned data files

Metavariable	Description
Content:	Type of the file (BIN_DATA)
Title:	Title of the binning
Used_Var:	List separated by commas (,) of body-record variables or constants used in the binning process
Mesh_limit:	Name of the text file where the limits, reference value and width of the different bins are stored
First_dim:	Title of the first dimension (e.g. Proton energy [MeV])
Second_dim:	Title of the second dimension (e.g. Local McIlwain L parameter [Re])
Third_dim:	Title of the third dimension (e.g. Equatorial pitch angle [deg])
First_date:	Begin date of the binning
Last_date:	Last date of the binning
Ref_MJD:	Time reference for the binning in modified Julian days
Data_field:	Output of the SIZE function, i.e. '4, 15, 30, 43, 15, 5, 290250'
Remark:	Comments

A.4.2 Measurement data

Generally, the second-level files dedicated to the proton flux data will be specific to the mission and instrument.

In the case of the PEM/UARS data, there is only one kind of second-level file. It includes three additional metavariables: 'SensId', 'Correction' and 'Description.Field'. The two first metavariable contain a description of the used telescope and of the correction applied to the proton flux data, respectively. Initially the correction should concern the finite view angle of the telescope but since the telescope angular responses is unknown, no correction is applied (see Section 9.3). The last metavariable is the same one as in the ephemeris file.

The body structure is described in Table A.6. The body records contain two one-dimension floating arrays the size of which corresponds to the number of energies in the flux spectrum. The variable 'rawflx' contains the raw proton flux spectrum as retrieved by the program `pe-mextr.c` from the IDFS files of the PEM instrument. The variable 'modflx' contains the

proton flux spectrum corrected for the finite view angle of the telescope.

A.5 Binned data

The files, where are stored the binned values in energy, McIlwain parameter and equatorial pitch angle of the UARS proton data, are organised in the same way as the `.dsc`, `.eph` or `.flx` files. The metavariables include in the header part of each files are listed and explained in Table A.7. The body part includes a single 4-dimension double-precision array. The first dimension corresponds to the 15 energies, the second one to 30 McIlwain parameters, the third one to 43 equatorial pitch angle and the last one to the 15 values accumulated during the binning (see Tables 9.1 and 9.2). The body can be read also as a 1-dimensional array of a 15-element structure.

Appendix B

List of IDL subroutines related to UARS data

The subroutines used in the treatment of UARS data are listed in the Table below. All the subroutines are included in the file `uarsidl.pro`. One should note that

1. the IDL subroutines marked with a (*) access the UNIRAD library;
2. the IDL subroutine `select_igrf` has to be executed once before any calls to the IDL subroutines marked with a (+).

In order that IDL can access the UNIRAD library, a logical `unilib` has to be defined (e.g. `$ define unilib UNILIB.EXE`).

Table B.1. List of IDL subroutines related to UARS data

Procedure name	Type	Nbr.arg.	Option	Description
str80	FUN	1	0	Force a string to be 80 character long
metavalue	FUN	2	0	Return the value of a metavariable
get_header	PRO	4	0	Read the header of a DSC, EPH, FLX, LIM or BIN file
put_header	PRO	4	0	Write the header of a DSC, EPH, FLX, LIM or BIN file
make_struct	PRO	2	1	Create a structure from a variable description
geo2geodetic	PRO	1	0	Evaluate geodetic coordinates (*)
geodetic2geo	PRO	1	0	Evaluate geocentric coordinates (*)
alpha_beta	PRO	1	1	Evaluate the pitch and beta angles
select_igrf	PRO	1	0	Initialize the magnetic field model (*)
magn_vector	PRO	1	1	Evaluate the magnetic field vector (*) ⁽⁺⁾
magn_coord	PRO	1	1	Evaluate the L coordinate (*) ⁽⁺⁾
gyroradius	PRO	2	1	Evaluate B,L at the guiding centre (*) ⁽⁺⁾
readuars	PRO	3	0	Read the content of a NEW file
uarsheader	PRO	6	0	Produce information to build the different metas
uarsfirst	PRO	3	0	Transform the pemrac data into the ephemeris format used in EPH files
uarsephem	PRO	1	0	Complete the ephemeris data (*)
uarsprocess	PRO	0	1	Transform a set of NEW files to EPH, FLX and PEM files. Update the DSC files. (= "PEMRAC.PRO") (*)
show_meta	PRO	1	0	Display a meta description
file_select	PRO	1	2	Select file from a menu window
select_data	PRO	2	1	Select a data set from a DSC list
display_info	PRO	0	2	Display the DSC files and their meta descriptions
open_data	PRO	7	7	Read ephemeride and flux data for a (small) period of time
read_lim	PRO	11	0	Read the mesh limits
init_gall_lim	PRO	0	0	Create a 'galley' for the LIM file
binning_data	PRO	0	2	Bin the data into a mesh
open_mesh	PRO	5	5	Read a BIN file
merge_bin	PRO	0	3	Merge different BIN files
tobefit	PRO	3	0	Function used by fit_mesh
make_corr	PRO	7	1	Fit flux data
fit_mesh	PRO	0	1	Fit merged data with simple function
open_corr	PRO	6	4	Read a COR file
prepare_fov	PRO	2	0	Build a common block for the FOV correction
use_fov	PRO	6	1	Compute the detector simulation
uars_hache	FUN	2	0	Angular response of the detector
corr_flux	FUN	3	0	Evaluate the flux from the COR data
correct_data	PRO	0	1	Transform the raw flux with the help of the COR data